In vivo Assessment of Structural Components of Retinal Degeneration in Animal Models

Dissertation

der Mathematisch-Naturwissenschaftlichen Fakultät

der Eberhard Karls Universität Tübingen

zur Erlangung des Grades eines

Doktors der Naturwissenschaften

(Dr. rer. nat.)

vorgelegt von

Marina García Garrido

aus Salamanca, Spanien

Tübingen

2015

Gedruckt mit Genehmigung der Mathematisch-Naturwissenschaftlichen Fakultät
der Eberhard Karls Universität Tübingen.

Tag der mündlichen Qualifikation:	10.09.2015
Dekan:	Prof. Dr. Wolfgang Rosenstiel
1. Berichterstatter:	Prof. Dr. rer. nat. Peter Ruth
2. Berichterstatter:	Prof. Dr. med. Dipl.-Ing. Mathias Seeliger

To my family

II. Abbreviations

ARVO	Association for Research in Vision and Ophthalmology
BM	Bruch Membrane
CNG	CyclicNucleotide-Gated
CNS	Central Nervous System
CRB	Crumbs protein
cSLO	confocal Scanning Laser Ophthalmoscopy
ERG	Electroretinography
GCL	Ganglion Cell Layer
I/OS	Inner/Outer Segment border
ILM	Inner Limiting Membrane
INL	Inner Nuclear Layer
IPL	Inner Plexiform Layer
IS	Inner Segment
KO	Knock-Out
LCA	Leber's Congenital Amaurosis
NHP	Non-human primates
OLM	Outer Limiting Membrane
ONL	Outer Nuclear Layer
OPL	Outer Plexiform Layer
OS	Outer Segment
PN	Post-Natal day
RP	Retinitis Pigmentosa
RPE	Retinal Pigmented Epithelium
SD-OCT	Spectral Domain Optical Coherence Tomography
WT	Wild-Type

III. SUMMARY

Human inherited retinal degenerative disorders exhibit a large genetic and phenotypic heterogeneity. Retinitis Pigmentosa (RP), one of the most severe forms, denotes a group of hereditary disorders of the rod system that cause progressive retinal degeneration and may eventually lead to blindness. Achromatopsia is characterized by a total loss of function of all cone photoreceptors in the retina, leading to a severe visual impairment. So far, no cure or scientifically proven symptomatic treatment has been found for neither RP nor Achromatopsia. Because the full course of the disease is difficult to follow in patients, the availability of genetically engineered animal models is instrumental to uncover the pathophysiological mechanisms underlying the disease.

The aim of this project was to apply and further develop retinal imaging technology in order to refine in vivo structural information as a basis to better understand the mechanisms of the pathophysiology associated with inherited retinal diseases. Particularly within the scope of this thesis, major advances have been made in an early-onset form of RP called Leber's Congenital Amaurosis (LCA) and two photoreceptor channelopathies that affect the rod and the cone system, respectively. This is complemented by the development of novel structural biomarkers for the follow-up of therapeutic strategies in both rod- and cone-centered disease classes.

The **first part** of the thesis introduces recent insights in the mechanisms of interaction of Crumbs proteins and the potential exchangeability of the different forms by means of respective mouse models: *Crb1*$^{-/-}$, *Crb2*$^{-/-}$ and the *Crb1Crb2* double knock-out mouse. It has been found that the lack of Crb1 resulted in a partial degeneration of the retina, whereas the lack of Crb2 induced a severe retinal degeneration similar to that of Retinitis Pigmentosa. The simultaneous ablation of both proteins mimics the characteristic retinal degeneration pattern showed by Leber Congenital Amarosis type (LCA) patients. This work has led to substantial progress in the field and several publications in a number of high-ranking journals (publication list 2,5,9,17,18).

The **second part** addresses the work on the restoration of function and morphology in a mouse model of Retinitis Pigmentosa or Achromatopsia, lacking the Cngb1 and Cnga3 proteins, respectively. Both approaches were performed by means of an adeno-associated viral (AAV) therapy. For the short –and long term assessment of therapeutic effects, novel morphological biomarkers based on optical coherence (OCT) data were develop. This work was documented in Koch et. al. 2012 and in Mühlfriedel et al. 2013.

The **third part** is devoted to the expansion of the diagnostic repertoire by improved, more informative biomarkers for therapy assessment beyond the state-of-the-art. The work is based on OCT, a novel technique for the *in vivo* visualization of retinal layers. Here, a quantitative method for a more detailed description of the retinal structure by means of reflectivity profiles was designed. This method was verified in three common laboratory species with differences in retinal architechture. Finally, the problem of unequal scales for the measurement of two-dimensional structures was resolved. Intraocular objects of known dimensions in the murine eye were used for the equal calibration of axes in OCT images. This work was reported in Garcia Garrido et al. 2014 and Garcia Garrido et al. 2015.

IV. ZUSAMMENFASSUNG

Erbliche Neutzhauterkrankungen weisen eine umfangreiche genetische und phänotypische Heterogenität auf. Als eine der häufigsten und schwersten Formen umfasst Retinitis Pigmentosa (RP) eine Gruppe von erblichen Erkrankungen, die zur progressiven Degeneration der Netzhaut und zur totalen Erblindung führen können. Achromatopsie ist charakterisiert durch einen totalen Funktionsverlust der Zapfen in der Netzhaut, der zu einer schweren visuellen Beeinträchtigung führt. Bisher konnte weder für RP noch für Achromatopsie eine erfolgreiche Therapie entwickelt werden. Aufgrund der Komplexität des Krankheitsverlaufs gestaltet sich eine Untersuchung am Menschen als sehr schwierig. Daher wurden in den letzten Jahren genetisch veränderte Tiermodelle eingesetzt, die maßgeblich dazu beigetragen haben, die zugrunde liegenden pathophysiologischen Mechanismen zu verstehen.

Das Ziel dieser Dissertation ist die Anwendung und Weiterentwicklung der retinalen Bildgebungstechnologie, um detailliertere *in vivo* Strukturinformationen zu erhalten, die das Verständnis der Pathophysiologie von erblichen Netzhauterkrankungen erweitern. Im Rahmen dieser Arbeit wurden sowohl große Fortschritte auf dem Forschungsgebiet der Leber'schen kongenitalen Amaurose (LCA), eine frühzeitig einsetzende Form der RP, als auch auf dem Gebiet der Erforschung defekter Kanalfunktionen, die sowohl das Stäbchen- als auch das Zapfensystem betreffen, gemacht. Zusätzlich wurden während der Dissertation neuartige strukturelle *in vivo* Biomarker generiert, die für die Evaluation von therapeutischen Strategien bei verschiedenen Stäbchen- und Zapfenerkrankungen angewendet werden können.

Der **erste Teil** der Arbeit befasst sich mit der Interaktion von Membranproteinen aus der Crumbsfamilie bei Netzhauterkrankungen. Dabei wurde spezifisch die Redundanz der unterschiedlichen Crumbsvarianten anhand entsprechender Mausmodelle (*Crb1*$^{-/-}$, *Crb2*$^{-/-}$ und die *Crb1Crb2* Doppelmutante) untersucht. Es wurde bereits gezeigt, dass der Verlust von Crb1 zu einer partiellen Netzhautdegeneration führt, wohingegen der Mangel an Crb2 eine RP ähnliche Netzhautdegeneration zur Folge hat. Der gleichzeitige Verlust von beiden Proteinen ähnelt dem Degenerationsmuster, das bei LCA Patienten beobachtet wurde. Die vorliegende Arbeit hat bedeutende Erkenntnisse zur Erforschung dieser Erkrankungen beigetragen und zu einer Vielzahl an hochrangigen Veröffentlichungen geführt (Publikationsliste 2,5,9,17,18).

Im **zweiten Teil** der Arbeit stehen gentherapeutische Ansätze bei Mausmutanten, die den Phänotyp der RP bzw. Achromatopsie aufweisen, im Fokus. Dabei wurde eine Adenovirus-assoziierte (AAV) Therapie eingesetzt, die jeweils die Kanalproteine Cngb1 bzw. Cnga3 exprimieren und zur Wiederherstellung der Funktion und Morphologie der Photorezeptoren in den entsprechenden Mausmutanten führen. Zur Bewertung der kurz- und langfristigen therapeutischen Effekte wurden neuartige morphologische Biomarker, die auf Daten der Optischen Kohärenztomographie (OCT) basieren entwickelt. Ein Großteil der Ergebnisse wurde bereits in Koch et al. 2012 und in Mühlfriedel et al. 2013 beschrieben.

Der **dritte Teil** beinhaltet die Weiterentwicklung von aufschlussreicheren Biomarkern für die Bewertung von Therapieansätzen, um die aktuelle Diagnostik-Technologie zu erweitern. Dafür wurde die OCT um eine quantitative Methode erweitert, die die Struktur der Netzhaut mittels Reflektivitätsprofile beschreibt. Die Methode wurde in drei experimentellen Spezies mit einem unterschiedlichen Retinaaufbau verifiziert. In einem abschließenden Ansatz wurde die Problematik der geräteabhängigen ungleichen Maßstäbe für die Messung zweidimensionaler Objekte gelöst. Dafür wurden intraokulare Objekte im Mausauge mit bekannten Abmessungen verwendet, um eine gleichmäßige Kalibrierung der Achsen im OCT-Bild zu erreichen. Die Ergebnisse wurden in Garcia Garrido et al. 2014 und in Garcia Garrido et al. 2015 beschrieben.

INTRODUCTION

Vision starts in the retina which is located at the posterior part of the eye. “Rete”, the Latin origin of its name standing for “net”, connotes with two important properties, a two-dimensional layer structure and a multitude of connections. Vision begins when the light hits the retinal photoreceptors - rods and cones – and they transform it into an electrical signal which is rapidly processed by a network of horizontal, bipolar and amacrine cells and is further sent it to the brain along the optic nerve. Information from the optic nerve (of each eye) is then combined at the level of the chiasm and is afterwards divided, according to the visual field in a right and left optic tract. The optic tract reaches the neurons at the lateral geniculate nucleus in the thalamus which finally conducts the visual information to the primary visual cortex in the brain (Rodieck 1998).

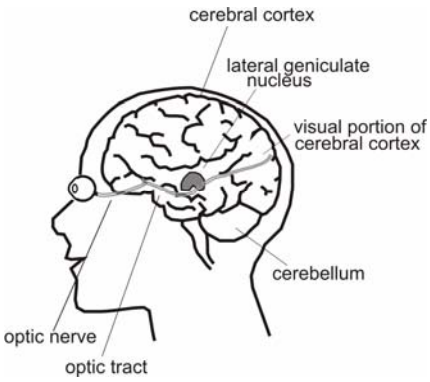

Figure 1. From the retina to the visual cortex

1.1. Anatomy of the eye

The human eye has a very similar structure to that of other vertebrate animals. It possesses a lens, adjustable depending on the distance, and a pupil, which acts as a diaphragm regulated by the iris. The retina is the light-sensitive tissue.

The anterior part of the eye is divided in two compartments: the anterior chamber, located between the cornea and the iris, and the posterior chamber, located between the iris and the lens. The pressure in these chambers is regulated by the presence of a clear liquid called humour aqueous. Between the lens and the retina there is the vitreous body which has the consistency of a gel. These structures are finally coated by three layers. The most external layer is known as the fibrous tunic and it is composed by the cornea and the sclera. The layer in the middle is known as the vascular tunic or uvea and consists of the choroid, ciliary

body and the iris. The most internal layer is the nervous tunic or retina (Levin and Kaufman 2011, Dowling 2012).

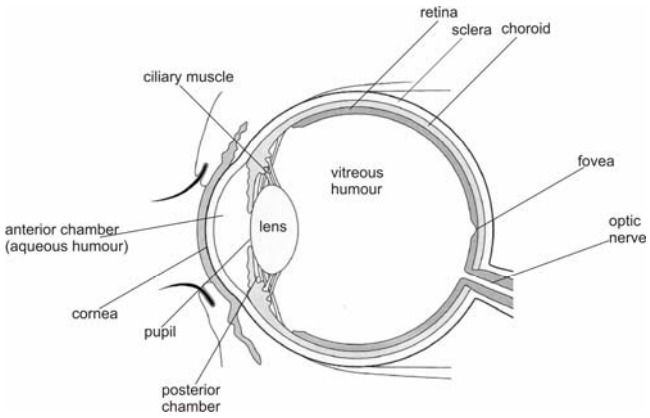

Figure 2. The human eye (modified from Novartis Pharma Schweiz AG)

1.2. Anatomy of the retina

The retina is a transparent layered tissue composed by ten underlying layers, and these from the most external to the most internal part are: (Ebrey and Koutalos 2001) (Anatomia Ocular p.24, Dr. E. Garcia Garrido).

- **Retinal Pigmented Epithelium (RPE):** The RPE is a single layer of cuboidal cells that serves some of the metabolic needs of the photoreceptors and acts as a barrier to ions and many molecules. The basal site is in touch with the Bruch's membrane (BM) and the apical site sends out microvilli towards the outer segments of the photoreceptors (PR). These cells contain a pigment called melanin (in the apical side) which strongly absorbs the light through the visible spectrum, and lipofuscine, which is originated from the phagocytic activity of these cells.
- **Photoreceptor layer:** Photoceptors are light-sensitive cells and they contain a chromophore (11-cis retinal) bound to a cell membrane protein, opsin, and this enables the visual phototransduction. There are two types of photoreceptors: cones and rods. **Rods** are very sensitive to light and are the primary source of visual information in darkness (scotopic vision). They are spread over the fundus except of the fovea. Their opsin is called rhodopsin. **Cones** are less sensitive to light than rods but they are responsible for color vision. They are densely located in the fovea but their number diminishes when reaching the periphery. There are three types of cones, each of them with a different pigment, namely: L, M and S-cones, sensitive at

different wavelengths (long, mid and short wavelengths correspond to red, green and blue, respectively).

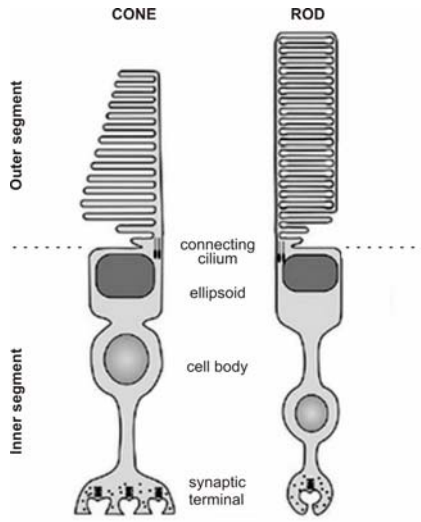

Figure 3. Photoreceptor cells (modified from (Werner and Chalupa 2014)

- **Outer Limiting Membrane (OLM):** is not a real membrane, it represents the adherens junctions between photoceptor cells and Müller glia cells and it separates the inner segment from the photoceptor nuclei.
- **Outer Nuclear Layer (ONL):** is the layer that contains the nuclear bodies of rod and cone photoreceptor cells.
- **Outer Plexiform Layer (OPL):** represents the synaptic connections between photoceptor projections and the dentrites of bipolar and horizontal cells.
- **Inner Nuclear Layer (INL):** contains the nuclei of bipolar, horizontal and amacrine cells.
- **Inner Plexiform Layer (IPL):** contains the synapse between the axons of the bipolar cells and the dendrites of the ganglion cells.
- **Ganglion Cell Layer (GCL):** contains the nuclei of the ganglion cells.
- **Nerve Fibre Layer (NFL):** contains the axons of the ganglion cells which form the optic nerve.
- **Inner Limiting Membrane (ILM):** basement membrane that separates the retina from the vitreous.

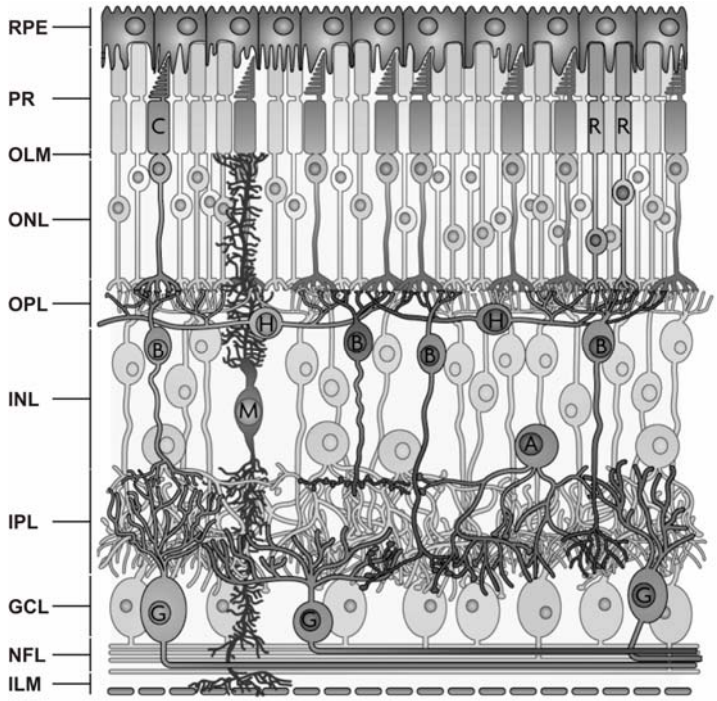

Figure 4. Schematic organization of the retina (modified from (Swaroop et al. 2010) A: amacrine; B: bipolar; C: cone; G: ganglion; H: horizontal; M: Müller; R: rod.

1.3. Inherited retinal disorders

Human inherited retinal degenerative disorders exhibit a large genetic and phenotypic heterogeneity. **Retinitis Pigmentosa** (RP), one of the most severe forms and with a prevalence of 1:4000 (Zobor and Zrenner 2012), belongs to the group of hereditary disorders of the rod system that cause progressive retinal degeneration and can lead to blindness (Hamel 2006). So far, more than 45 genes have been associated to RP. Mutations in those genes can lead to a reduction or abolishment of the functionality of the corresponding protein which is necessary for the photoreceptor cells, the RPE, the intracellular transduction cascade, the cilliary transport or the ion exchange. The onset of the disease, the progression and the magnitude of the affected retinal area, mostly depend on the inheritance pattern and the genotype of the individual (Kellner et al. 2004). RP can arise as an autosomal-dominant, autosomal recessive, x-chromosomic, mitochondrial isolated disease or syndromic e.g. Usher-Syndrome or Bardet-Biel-Syndrome (Zobor and Zrenner 2012). The clinical profile in affected individuals may further vary depending on the size and location of the damage in the retina. However, some of the common symptoms are:

- Nyctalopia or night blindness

- Loss of mid-peripheral vision, which progressively extends to both centre and periphery
- Aversion to glare
- Reduced colour vision
- Slow adaptation time
- Blurred vision and poor colour separation

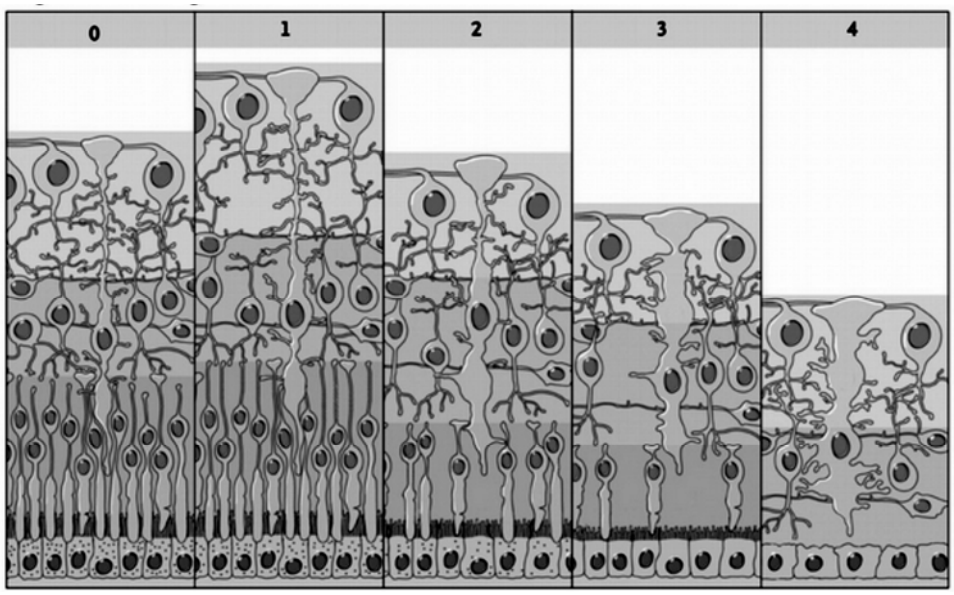

Figure 5. Different stages in RP. Changes in retinal architecture of the retina (modified from Jacobson et al. N ENG J MED 363; 17.(Jacobson and Cideciyan 2010))

Leber's Congenital Amaurosis denotes a group of inherited retinal disorders that appear at birth or within the first months of life and it has a prevalence of 1 to 80000 (Stone 2007). It can be associated with different genes, and those encode proteins with different functions as photoreceptor morphogenesis, photransduction and ciliary transport (Walia et al. 2010). Patients typically suffer from nystagmus, non-detectable or severely reduced rod and cone electroretinogram , and a poor visual acuity.

1.4. Retinal imaging methods

The retina is an offshoot of the developing brain and it is considered as a component of the central nervous system (CNS). However, it is the only part of the brain that can be visualized non-invasively. (Sensory reception: Human vision: structure and function of the human eye" vol 27, Encyclopaedia Britannica, 1987).
Thus, the retina –as part of the brain- can serve to visualize not only ocular diseases, such as age-related macular degeneration, glaucoma or retinitis pigmentosa but also systemic diseases that may also show manifestations in the retina, as for example diabetes or hypertension (Dowling 2012). For this reason, several imaging diagnostic techniques are available (Abramoff et al. 2010).

1.4.1. Scanning laser ophthalmoscopy (SLO)

SLO is an *in vivo* diagnostic technique for imaging the eye which uses specific laser wavelengths. Shorter wavelengths (blue-green) are generally more strongly absorbed by ocular structures -especially melanin granules in the retinal pigment epithelium (RPE) and choroid- than longer wavelengths (near infrared) (Preece and Claridge 2002). In consequence, lasers in the short wavelength range provide higher contrast images of the retina but are unable to penetrate the RPE/choroid, whereas the infrared lasers give less retinal details but can pass through the choroid down to the sclera (Seeliger et al. 2005). The 488 nm wavelength is used for fundus autofluorescence (FAF) analyses, which reveals the presence of natural fluorophores in the retina and the RPE (Schmitz-Valckenberg et al. 2008).

In addition, fluorescent dyes excitable in the blue and infrared range offer a unique access to the vascular structures associated with the eye. Fluorescein (FL) is a dye that emits light when excited at a wavelength of 488 nm. To allow only the light emitted by the dye upon stimulation to become visible, a barrier filter at 500 nm is used to remove the light associated with the excitation. Fluorescein angiography (FLA) provides the most detailed images of retinal capillaries (Seeliger et al. 2005). Indocyanine green (ICG) is a dye that emits light at 800 nm and above when excited at a wavelength of 795 nm. Similar to FLA, a barrier filter at 800 nm is used to remove the light associated with the excitation. Therefore, ICGA provides information about choroidal vessels.

In this research work, a HRA I system from Heidelberg Engineering GmbH (Heidelberg, Germany) was used. The HRA I device features lasers in the short (visible) wavelength

range (488 nm and 514 nm), and also in the long (infrared) wavelength range (785/815 nm). The 488 and 795 nm lasers are used for fluorescein (FLA) and indocyanine green (ICG) angiography, respectively. GFP excitation was detected in the autofluorescence mode at 488 nm with a 500 nm barrier filter.

1.4.2. Optical coherence tomography (OCT)

OCT is a retinal imaging technology that provides micrometer-scale, cross-sectional imaging in biological systems (Fujimoto et al. 1995, Drexler et al. 2001, Fujimoto 2003). In ophthalmology, it is used to assess the thickness, morphology, and vascular layers of the retina and choroid of healthy and diseased eyes. OCT is a non-invasive imaging method that uses low coherence reflectometry to obtain cross-sectional images of the retina on a micrometer scale by measuring the echo time delay and intensity of the reflected and backscattered light (Frohman et al. 2008).

OCT acquires all information in one single axial scan simultaneously by evaluating the frequency spectrum of the interference between the reflected light and a stationary reference mirror. Therefore, the interference pattern is decoded and split into its frequency components by a Fourier transformation. Each detected frequency corresponds to a certain depth within the tissue, and all of these components are simultaneously detected. The use of broadband light sources instead of low-coherent ones enables a higher depth resolution (Born and Wolf 1999, Drexler et al. 2001). Commercial OCT is one of the new standards for *in vivo* non-invasive ophthalmic imaging and is widely used for diagnosis and treatment monitoring of various ocular diseases in humans and experimental assets (Ruggeri et al. 2007). Several companies have commercialized stand-alone units and a third generation system from Heidelberg Engineering (Spectralis™, Heidelberg Engineering GmbH, Heidelberg, Germany) combining spectral-domain OCT with angiography has been used for this thesis.

2. AIMS OF THE STUDY

In this thesis, I address our contribution to the understanding of the mechanisms of the pathophysiology associated with inherited retinal diseases (genes marked with red). This particularly concerns an early-onset form of RP called Leber's Congenital Amaurosis (LCA) and two photoreceptor channelopathies that affect the rod and the cone system, respectively. A further part of the work concerns corresponding therapeutic approaches we have established and the development of novel structural in vivo biomarkers for the follow-up of the therapeutic outcome. Because the full course of the disease is difficult to analyze in patients, respective transgenic animal models were studied for this work.

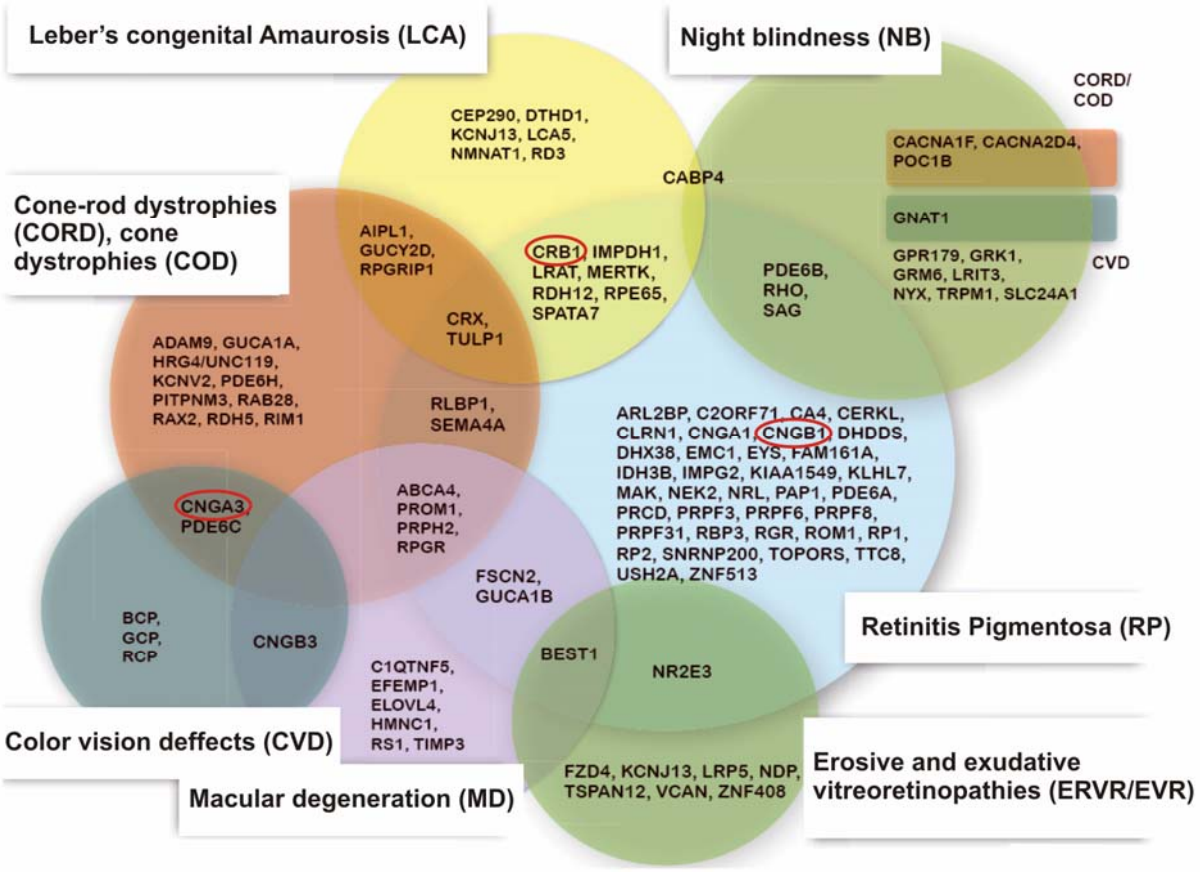

Figure 5. Clinical symptoms of non-syndromic monogenic retinal and vitreoretinal diseases and their causative genes (modified from (Berger et al. 2010) update 2014).

3. RESULTS

3.1. MANUSCRIPTS INCLUDED IN THIS THESIS

Paper I Loss of CRB2 in the mouse retina mimics human retinitis pigmentosa due to mutations in the CRB1 gene. Alves CH, Sanz AS, Park B, Pellissier LP, Tanimoto N, Beck SC, Huber G, Murtaza M, Richard F, Sridevi Gurubaran I, **Garcia Garrido M**, Levelt CN, Rashbass P, Le Bivic A, Seeliger MW, Wijnholds J. (2013) Human Molecular Genetics; 22(1):35-50.

Paper II Targeted ablation of CRB1 and CRB2 in retinal progenitor cells mimics Leber congenital amaurosis. Pellissier LP, Alves CH, Quinn PM, Vos RM, Tanimoto N, Lundvig DM, Dudok JJ, Hooibrink B, Richard F, Beck SC, Huber G, Sothilingam V, **Garcia Garrido M**, Le Bivic A, Seeliger MW, Wijnholds J. (2013) PLOS Genetics; 9(12):e1003976.

Paper III Gene therapy restores vision and delays degeneration in the CNGB1(-/-) mouse model of retinitis pigmentosa. Koch S, Sothilingam V, **Garcia Garrido M**, Tanimoto N, Becirovic E, Koch F, Seide C, Beck SC, Seeliger MW, Biel M, Mühlfriedel R, Michalakis S. (2012) Human Molecular Genetics; 21(20):4486-96.

Paper IV Optimized technique for subretinal injections in mice. Mühlfriedel R, Michalakis S, **Garcia Garrido M**, Biel M, Seeliger MW. (2013) Methods in Molecular Biology; 935:343-9.

Paper V Towards a quantitative OCT image analysis. **Garcia Garrido M**, Beck SC, Mühlfriedel R, Julien S, Schraermeyer U, Seeliger MW. (2014) PLOS One; 9(6):e100080.

Paper VI Two-dimensional measurements in OCT images. **Garcia Garrido M**, Mühlfriedel R, Beck S, Wallrapp C, Seeliger MW (2015) PLOS One. *Accepted*

3.2. Part I: Rodent models of RP based on Crumbs protein deficiency

3.2.1. Background (Paper I and II)

The Crumbs (CRB) protein complex locates to the subapical region adjacent to the adherence junctions between photoreceptors and Müller glia cells and plays a critical role in the establishment and maintenance of the apico-basal polarity in photoreceptor cells (Mehalow et al. 2003, van de Pavert et al. 2004, van de Pavert et al. 2007b). In mammals, the CRB family consists of four members: CRB1, CRB2, CRB3A and CRB3B. The Crb protein is a transmembrane protein with a large extracellular domain with epidermal growth factor (EGF) and laminin-globular domains, a single transmembrane domain, and an intracellular C-terminus of 37 amino acids with single FERM and PDZ protein-binding motifs (Tepass et al. 1990). In the adult mouse retina, CRB2 is present in photoreceptors and Müller glia cells, whereas CRB1 protein is only expressed in Müller glia cells (van Rossum et al. 2006). Mutations in the human CRB1 gene cause autosomal-recessive Retinitis Pigmentosa and Leber's Congenital Amaurosis (Richard et al. 2006). In previous studies, it was demonstrated that in Crb1 knockout ($Crb1^{-/-}$) mice, the loss of CRB1 expression led to photoreceptor displacement and was accompanied by the appearance of (half-) rosettes due to focal loss of adhesion between photoreceptors and Müller glial cells in the inferior quadrant of the retina (van de Pavert et al. 2004, van de Pavert et al. 2007a). Based on these investigations, we studied the effects of the loss of CRB2 in the mouse (**Paper I**) as well as the simultaneous loss of CRB1 and CRB2 and their potential overlapping functions (**Paper II**).

3.2.2. Results (Paper I)

A conditional *Crb2* knock-out (cKO) mouse driven by the Chx10 promoter was generated by our collaboration partners in Amsterdam and it was later in vivo functionally and morphologically characterized here in Tübingen. Heterozygous mutant mice were examined up to 18 months of age by means of electroretinography as well as SLO and OCT imaging. However, we did not find any differences in comparison to control animals **(Fig 2 and 3, Paper I)**. In contrast, we found that *Crb2Chx10* cKO mice had already at the age of 1 month an impairment of retinal function, depicting a strong photoreceptor dysfunction. Examinations were performed at several timepoints and we could show that with age, the amplitude of the signals further decreased and was severely reduced at 18 months **(Fig 2, Paper I)**. During the *in vivo* morphological assessment we found several fundus abnormalities, and in contrast to the previously reported *Crb1* mouse (van der Pavert et al. 2004), these effects were seen along the fundus. At the age of three months, mice presented a spotty fundus which turned into larger lesion areas with increasing age. We also visualized several hypo- and

hyperflourescent areas correlating with the presence of lipofuscin, whose presence is an indicator of retinal degeneration. In the angiographical work-up, we further detected fluorescein leakages which are usually related to sites of neovascularization. The retinal structure looked significantly disturbed: we observed several misplaced cells and an important loss in the retinal thickness was further visualized **(Fig 4, Paper I)**. Histological analyses were later performed and they correlated well with our *in vivo* findings. In addition, disruptions in the outer limiting membrane, rosettes and ectopic nuclei in the subretinal space could be also detected **(Fig 5, Paper I)**. In the immunohistochemistry analysis we observed an increase in GFAP expression and an abnormal expression of SOX9 and glutamine synthetase, indicating the presence of activated Müller glia cells **(Fig 6 and 7, Paper I)**.

Taken together, our data suggested that the retinal CRB2 protein plays important roles in maintaining the cell adhesion, photoreceptor polarity and retinal lamination. The progressive retinal degeneration described in depth in this study mimics that of Retinitis Pigmentosa due to mutations in the CRB1 gene.

3.2.3. Results (Paper II)

A *Crb1Crb2* double knock-out (DKO) mouse was generated in Amsterdam and we assessed the retinal function and morphology over time. In this case, whereas the Crb2 deficient mouse was a conditional knock-out (cKO) driven by the Chx10 promoter, the Crb1 was a constitutive KO mouse. In these DKO mice, we found that the ERG responses were decreased from the very first examination point and were rapidly no more detectable at the age of 3 months **(Fig 1, Paper II)**. However, progression of the degeneration was followed until later stages and in parallel, we further characterized the combination of the different genetic variants of the Crb1 and Crb2 proteins ($Crb2^{-/-}$Chx10-Cre, $Crb2^{+/-}$Chx10-Cre, $Crb1^{-/-}Crb2^{+/-}$Chx10Cre, $Crb1^{-/-}Crb2^{-/-}$Chx10Cre, $Crb1^{+/-}Crb2^{-/-}$Chx10Cre and $Crb1^{+/-}Crb2^{+/-}$Chx10Cre). The effects of the simultaneous deficiency of Crb1 and Crb2 proteins were also studied by in vivo retinal imaging. Striking results were observed by OCT imaging, where we visualized an abnormally thick retina with an aberrant layering, very similar to that of *CRB1*-LCA patients **(Fig 3, Paper II)**. However, retinal thickness promptly decreased already at the age of 3 months and a further reduction was visualized at the age of 6 months. SLO imaging depicted a strongly degenerated fundus and large areas of fluorescent material were detectable in the autofluorescent mode (Fig 3, Paper II). Using specific markers for the different cell types, it was found that all cell types formed although several of them localized ectopically **(Fig 5, Paper II)**. Furthermore, quantification of cleaved caspase 3 positive cells showed an increase in the number of apoptotic cells **(Fig 6, Paper II)**.

In summary, our data showed that levels of CRB protein control the lamination and proliferation of progenitor retinal cells and further demonstrate that Crb1 and Crb2 proteins may have overlapping functions. The unique clinical features displayed by this model imitate well the human LCA due to mutations in the CRB1 gene.

3.2.4. Contribution to Paper I and II

For this work, I performed the *in vivo* morphological analysis by means of SLO and OCT in all of the Crumbs mutant variants ($Crb2^{-/-}$Chx10-Cre, $Crb2^{+/-}$Chx10-Cre, $Crb1^{-/-}Crb2^{+/-}$Chx10Cre, $Crb1^{-/-}Crb2^{-/-}$Chx10Cre, $Crb1^{+/-}Crb2^{-/-}$Chx10Cre and $Crb1^{+/-}Crb2^{+/-}$Chx10Cre). Animals groups of 3-5 animals were examined at the age of 1, 3, 6, 12 and 18 months. I also analysed the data and contributed on writing respective manuscripts, their revised versions until their final acceptance.

3.3. Part II: Development of morphological biomarkers for the short– and long term assessment of therapeutic effects (Summary of Paper III and IV)

3.3.1. Background (Paper III and IV)

Cyclic nucleotide-gated (CNG) channels locate to the plasma membrane of rod and cone photoreceptors and play a very important role in the phototransduction cascade. The cone CNG channel is a heterotetramer composed of two CNGA3 and two CNGB3 subunits whereas the rod CNG channel is formed by three CNGA1 and one CNGB1 subunit (Biel and Michalakis 2007).

Mutations in the genes that encode either CNGA3 or CNGB3 subunits account together for ~75% of all cases of complete Achromatopsia. Achromatopsia is a hereditary autosomal recessive disorder characterized by a total lack of cone photoreceptor function. Achromatopsia patients suffer from colour blindness, poor visual acuity, nystagmus, and photophobia (Michalakis et al. 2010). Mutations in the CNGB1 subunit are found in about 4% of the patients with autosomal recessive Retinitis Pigmentosa (arRP) (Hartong and Kooijman 2006). Classical clinical symptoms of Retinitis Pigmentosa have been already described in detail in the Introduction Chapter of this thesis.

Since the clinical impact of both diseases is very high and a vast knowledge is available, it is for this reason that our group has been working in the last years towards a retinal gene therapy which can restore the function and morphology in a mouse model of Achromatopsia and Retinitis Pigmentosa, lacking the Cnga3 and Cngb1 proteins, respectively. The first milestone was already addressed and it included a rAAV-mediated gene replacement strategy in the Cnga3 deficient mouse. In this work, we decided to deliver our viral vector via subretinal injection since our target were the photoreceptors and it resulted that after this approach not only photoreceptors cells were functionally rescued but also the functionality at ganglion cell level was restored, which implied that the visual information was sent to the brain (Michalakis et al. 2010).

Since the outcome of a gene therapy in short- and long term is highly influenced by vector administration procedures it is necessary to ensure a good practice in this type of approaches. These aspects are included in the second part of this thesis.

3.3.2. Results (Paper III)

In this work, we described our methodology for optimized subretinal injections on the base of the Cnga3 gene therapy **(Fig 1, Paper III)** and defined structural biomarkers for the assessment of the intervention in the short time **(Fig 2, Paper III)**. Subretinal injections took place in anesthetized animals and ten minutes after injection, we performed SLO and OCT examinations which allowed for a non-invasive *in vivo* visualization of the retinal structure.

Firstly, SLO allowed us to assess the overall integrity of the anterior and posterior part of the eye. Should a mouse have some primary ocular defects (e. g. developmental), the animal could have been excluded from our study. Furthermore, the exact location of the injected material in the fundus in reference to the location of the injection bleb became visible **(Fig 2, Paper III)**. This is of high importance due to the anatomical properties of the retina (e.g. cell distribution, opsin gradient, etc). Besides, we could rule out adverse effects such as retinal detachment (due to an excess of the injected amount) or haemorrhages (due to vascular damage).

OCT imaging provided us with additional information in regard of the retinal layer composition. The acquired data served to allocate the injection within the layers, for instance, we could distinguish between subretinal and intravitreal injections. Additionally, we were able to visualize the height of the injection bleb and the size of the transduced area **(Fig 2, Paper III)**.

After defining our structural biomarkers, we then established and applied new criteria for the performance of this kind of approaches. These biomarkers complement well with other established techniques such as histology and electroretinography and provide the study with valuable information about the current appearance of the retina and influence the course of the selected approach.

3.3.3. Results (Paper IV)

This work is a joint project between our collaboration partners in Munich and our lab in Tübingen. Our aim here was to restore the functionality as well as the morphology in the *Cngb1* mouse, a RP model, and define novel *in vivo* structural biomarkers which may be used in the assessment of long time effects of therapeutic interventions.

This treatment was done similarly to the *Cnga3* gene therapy based on subretinal application of rAAVs (Koch et al. 2012). For this purpose, a specific viral vector was designed in Munich and we injected it subretinally in young *Cngb1* mice. The injection site was directly *in vivo* monitored 10 minutes after injection and respective structural biomarkers in the short term were considered **(Paper III)**. Later, the course of our intervention was followed at several post-injection timepoints by means of retinal imaging and electroretinography **(Fig 3 and 4, Paper IV)**. Here, based on the retinal layering visualized by OCT, we were able to distinguish between a treated and an untreated region within the same eye, meaning that with a single vector application we were able to transfect one third of the retina **(Fig 3, Paper IV)**. These findings correlated well with subsequent protein expression analyses and further revealed that the protein was mostly located to the rod outer segment, suggesting that our approach restored the correct expression and localization of the CNG channel. **(Fig 2, Paper IV)**. Within transfected (treated) areas, a proper retinal lamination was found in comparison to

non-transfected areas and/or untreated eyes (which served as control). Furthermore, in the functional assessment, we found significant differences between the treated and the untreated eye, and we reported a substantial increase in the b-wave amplitude especially at low light intensities **(Fig 4, Paper IV)**. These rescue effects were of course proportional to that of the extension of the injected area. Finally, we performed a behavioural test to check whether the ERG responses were forwarded to the brain and we obtained positive results **(Fig 5, Paper IV)**. Rescue effects were further under observation until the age of 12 months and confirmed our established morphological biomarkers in the long term. We were additionally able to show, as typical of RP models where cones degenerate secondary to rods, that cone photoreceptors at least in part benefit from the effects of the rod rescue **(Fig 6, Paper IV)**.

In order to standardize and convert the information provided by long term biomarkers into numerical data, I attempted to process the information contained in the OCT image data **(Paper V)**. For this, I plotted the reflectivity values (in form of pixel intensity in a greyscale) vs. depth (in terms of OCT, a so-called A-scan) at one specific location. As location, I chose the treated vs. untreated areas (or vs. the untreated eye). With this procedure, each OCT band can be correlated with a retinal layer, and valuable details such as size and tissue-specific reflective properties may be obtained. Within effectively treated areas, an additional OCT band was distinguishable in comparison to that of untreated areas. This band represented the border between the inner and outer segment of the photoreceptor (I/OS). In the untreated eye this band was significantly smaller or missing. This means that the organization of the outer retina partially recovered in treated areas in comparison to an untreated eye. This information was compiled and presented in **Paper V** of this thesis.

3.3.4. Contribution to Paper III and IV

The work in **Paper III** highlights the value of morphological analyses shortly after subretinal injection as well as at 2, 4, 8 and 12 months of age, using several vectors and/or other regulatory elements. Furthermore, I also contributed with substantial text passages to both manuscripts (**Paper III** & **IV**). During the data collection for **Paper III**, I assisted Dr. Mühlfriedel with the subretinal injections. After analyzing the data, I designed the structural biomarkers described above, which set up the basis for my subsequent work to improve the understanding and follow up of retinal gene therapy.

3.4. Part III: Development of morphological biomarkers beyond the state-of-the-art of the diagnostic technology

3.4.1. Background (Paper V)

In the past, fundus photography and angiography have been the traditional imaging techniques in order to assess macroscopic changes in retinal disease, whereas histology and immunohistochemistry were chosen with the aim of visualize fine details *ex vivo*. Therefore, it was a major breakthrough in ophthalmic diagnostics when OCT was first introduced as a novel tool for *in vivo* visualization of retinal layers (Fujimoto et al. 1995, Drexler et al. 2003). The resolution of third generation models of OCT equipment that became available a few years later finally turned out to be sufficient for use in rodent models of retinal disease (Fischer et al. 2009). This is of particular advantage for experimental research since it gives the option to follow the course of disease and/or monitor the effects of a therapeutic intervention over time in individual eyes (Ruggeri et al. 2007, Fischer et al. 2009). Technically, OCT provides cross-sectional images based on the reflective properties of the investigated sample (Fujimoto et al. 1995). A single measurement of the reflectivity versus depth at one specific location is called A-scan, whereas the composition of an image by alignment of several consecutive A-scans is called B-scan (van Velthoven et al. 2007). A typical B-scan shows several, often alternating bands of low and high reflectivity, as plexiform layers have a higher level of reflectivity than nuclear layers (Jacobson et al. 2003). However, these bands and the retinal layers associated with them vary in their extent with the topographical position in the retina, and this is additionally species-dependent as mentioned above. Besides, automated segmentation procedures have still not reached a satisfactory level of performance, which is why in the majority of cases simply a qualitative evaluation is performed. In order to address these issues, we attempted to investigate the retinal structure by means of OCT reflectivity profiles in a number of experimental models commonly used in research.

3.4.2. Results (Paper V)

In this work, we used the layer reflectivity in OCT images as a function of scan depth (similar to A-scan data) for a quantitative analysis of the retina of three laboratory species with a different degree of topographic structuring **(Figs 1-4, Paper V)**. These species included: *Mus musculus* (mouse), *Meriones unguiculatus* (gerbil) and *Macaca fascicularis* (cynomolgus monkey). Firstly, we started with the less topographically structured retina, which belonged to the mouse. Since it was already reported that within the mouse retina several anatomical differences are found (e.g. cell distribution, opsin gradient) (Peichl et al. 2005), we wanted to know if those differences were visible in OCT. Since we found that along the retina all the

reflectivity profiles were practically identical, we were able to generate a standard reflectivity profile in the mouse where the retinal layers were easily identified **(Supp Fig 1, Paper V)**. In the second place, we further compared two commonly used control mouse lines, the *C57BL/6* line representing pigmented strains, and the *BALB/c* line representing non-pigmented ones **(Fig 2, Paper V)**. The difference between these both lines is the melanin content which locates mainly to the retinal pigmented epithelium and the choroid. Here, we found that variations in the pigment content do influence the detection of the underlying anatomical structures and their representation in the reflectivity profile. Albino animals showed a more detailed representation of the outer retina where structures like the choriocapillaries were visible **(Fig 2, Paper V)**. Then we studied another rodent model, the gerbil. These animals are characterized by the presence of a visual streak (Huber et al. 2010). In our representation, this region presented as an elongation of the crest corresponding to the photoreceptor outer segments **(Fig 3, Paper V).** In addition, SLO was complementary performed and here we observed a unique disposition of retinal vessels at the level of the visual streak, together with a hyperreflective representation of it in the normal native imaging mode **(Fig 3, Paper V)**. Finally, we switched to a more specialised retina characterized by the presence of a fovea. This structure is limited to primates and is also present in the human eye. The reflectivity data acquired in the model allow to relate retinal layers in foveal and non-foveal regions to that of the human counterparts **(Figs 4 and 5, Paper V),** which further demonstrates the potential of this method. In conclusion, this work proofs that this kind of image processing method is valid for an inter-species evaluation of the data and may help to optimize OCT segmentation algorithms.

3.4.3. Contribution (Paper V)

As the first author of this manuscript, I designed the study and performed all experiments under the supervision of Prof. Seeliger In addition, I analysed the data and assembled the manuscript and its revision until final acceptance.

3.4.4. Background (Paper VI)

OCT imaging plays a very important role in clinical ophthalmology. However, little progress has been made in the development of methods for exact calibration of OCT image data and it is maybe for this reason that most of the reported results are limited to qualitative data. Besides, interpretation of the data have been complicated within the last years in part due to the variety of OCT manufactures, as they all provide their own software (Wolf-Schnurrbusch et al. 2009, Sull et al. 2010). Additionally, differences in their segmentation algorithms on which retinal thickness measurements based on (Odell et al. 2011, Krebs et al. 2010), axial resolution in tissue (Folgar et al. 2014), scan density variations (Sadda et al. 2010) and anatomic variations between individual patients as well as inter-species (Cook et al. 2008, Huber et al. 2010) are the most reported obstacles to deal with in the development of methods for exact calibration of OCT image data.

Several groups worldwide, including our group, verified retinal layer thickness in OCT scans, measured on a single dimension along the Y axis of images, on the basis of matching histological sections, and established respective correlation coefficients (Fischer et al. 2009, Huber et al. 2009, Ferguson et al. 2014). However, two-dimensional OCT images (B-scan) are generated via an alignment of separate one-dimensional scans (A-scan). In such B-scans, the Y axis reflects properties of the scan, whereas the X axis is a product of internal post processing based on a number of inferences.

Another approach that eliminates intra- and intersubject variabilities and provides new insights to the field is the use of a model eye. Agrawal and other groups worked towards the development of such an *in vitro* retina phantom for the evaluation of OCT devices (Zawadzki et al. 2010, Agrawal et al. 2012, Lozano et al. 2013).

In this work, we were looking for a more direct and reliable way to obtain equal scales for X and Y *in vivo* that permit two-dimensional measurements in OCT images that are otherwise distorted.

3.4.5. Results (Paper VI)

For the realisation of this work, we based our approach on dimensionally stable alginate capsules (Cellbeads®) as an *in vivo* calibration tool. Since a spherical body has equal dimensions along the X, Y and Z axis, it appeared to be a suitable gauge for scaling. These beads contained human mesenchymal stem cells transformed to produce green fluorescent protein (GFP) and they were placed both in the subretinal and intravitreal space of murine eyes. Later, intravitreal as well as subretinal transplanted beads were visualized by means of SLO and OCT **(Fig 3, Paper VI)** and an estimation of the resulting scaling errors was provided **(Fig 3, Paper VI)**. Based on those errors, a correction factor of about 3.3 was found for both subretinal and epiretinally located beads. Further, we developed a mathematical

description that allows to correct measurements of targets contained within an OCT scan in an arbitrary direction.

We demonstrated this approach with the help of two examples of defined geometrical shapes. First, we addressed the behaviour of a circular shape assuming the same diameter along X and Y axes (a/b=1). When the scale of the X axis changes up to a radio of a/b=5, our circle became an ellipse. This effect will be therefore applicable to retinal structures like e.g. vessels which will then show an elliptical cross section in the OCT scan. And when attempting to measure the diameter of the structure, this is only straightforward at 0° or 90°, i.e. entirely along the X or Y axis. While in case of the (original) circle the diameter is independent of the angle of the section, this is not so in case of an ellipse **(Fig 1, Paper VI)**. Depending on the angle of the section (α) and the ratio between X and Y scales (a/b), the measured result has to be divided by the relative diameter (d_r) to reflect the correct distance. The second example was a rectangle at an angle of 45°, which could e.g. reflect a vessel running in the X-Y plane **(Fig 2, Paper VI)**. Again, the scale of the X axis was changed up to ratio b/a=5. It is clear that a change in the scale of X will increase or reduce the angle of the structure; the actual formula for that angle being α=arctan(a/b). This effect will lead to an underestimation of the angle when the X scale is larger than the Y scale, and will be a particular problem for any analysis by visual inspection **(Fig 5, Paper VI)**.

The establishment of equal scales for OCT appears to be essential as it influences both qualitative and quantitative image analysis that often guides diagnosis and treatment in eye diseases.

3.4.6. Contribution (Paper VI)

For this work I performed all the experiments in mice and the analysis of the acquired data. I wrote the manuscript under the supervision of Prof. Seeliger and took care of the submission and revision until final acceptance.

4. DISCUSSION

This thesis relates recent discoveries about the underlying mechanisms in common and very important retinal diseases such as an early onset form of RP called LCA and two photoreceptor channelopathies affecting either rod or cone cells. Other primary aspects treated in this thesis are the development of novel and more informative morphological biomarkers for use in the assessment of therapeutic intervention, and the diagnostic improvement and optimization of OCT technology.

Mutations in the *CRB1* gene have been described to cause RP and LCA. Mutations in *CRB2* have been also associated with the disease but so far, they have not been described as the single cause leading to disease (van den Hurk et al. 2005). The retina in *CRB1*-associated retinal degeneration patients is characterized by the lack of ordered retinal layers and is notably thicker than that of healthy subjects (Jacobson et al. 2003). However, the phenotype of a *Crb1* KO mouse was very different to that of human patients. Although a retinal degeneration could be observed, this was only located to one quadrant of the retina and did not therefore represent the retinal degeneration seen in patients (van de Pavert et al. 2007b). These findings were confirmed later on the *rd8*-Crumbs mutant mouse in which the mutation (citosine deletion in Exon 9) occured naturally (Aleman et al. 2011). Our continuing investigations in the *Crb2Chx10* mouse revealed novel aspects of the disease. This model developed an early retinal disorganization and retinal degeneration that extended all over the fundus and reminded of that of *CRB1*-related RP patients (Alves et al. 2013) (**Paper I**). It was then suggested that *CRB2* had a more relevant role than *CRB1*, and that it was responsible for the correct retinal lamination and proliferation of progenitors. However, this aberrant retinal thickness found in patients could not be explained until we studied an additional mouse model: the *Crb1Crb2* DKO (Pellissier et al. 2013) (**Paper II**). This mouse mimicked the human LCA phenotype in a much better way. The results obtained in these studies suggest that the severity of the disease in mice is inversely proportional to amount of Crb protein and, that Crb1 and Crb2 proteins might have overlapping functions, so that only a combinational DKO produces a human-like result.

In both **Paper I** and **II**, we were able to report these important mechanistic insights to the pathophysiology of RP and LCA. Recently, by means of several genetic variants and/or new generated mutant mice, the role of the Crb1 and Crb2 protein was further studied as well as the role of other proteins which are also part of the Crumbs complex such as Mpp3. In those approaches, the protein expression was regulated by different specific promotors as for example the Crx (which targets both photoreceptor cell types) or the PdgFrα (for the MGC).

These results were reported in Manuscripts #9, 17 and 18 as listed at the end of this thesis. Since our mouse models had several similarities with the human disease, they offer great possibilities for the development of new therapeutic strategies. First steps to evaluate the potential of a therapy that restores retinal structure and function in a Crb1-RP model have been done already (Pellissier et al. 2015). In addition, in all of these studies we were able to demonstrate that SLO and OCT imaging are very useful diagnostic techniques in such projects. They are particularly well suited to follow the course of the disease together with functional *in vivo* techniques such as ERG.

In **Paper III,** we focused on the description of structural biomarkers which serve for the evaluation of therapeutic strategies in the short term, as the localization of the injected material and the extension and height of the bleb after injection. This study was carried out in the framework of the Cnga3 gene replacement therapy. The performance of *in vivo* imaging techniques like SLO and OCT served as a quality control of subretinal injections and provided novel insights which can notably determine the course of the intervention in individual eyes. Besides, since examinations may be repeated in relatively short periods of time, a very accurate time course of the effects of an intervention (positive and adverse) may be recorded.
In analogy, we defined relevant structural biomarkers for the Cngb1 gene replacement approach. Here, restoration of vision was obtained by means of an AAV-based gene therapy in the CNGB1 knock-out model of RP (Koch et al. 2012) (**Paper IV**). Those biomarkers included differences in the appearances of the OCT bands as well as a comprenhensive quantitative analysis of the data contained in an OCT image. Furthermore, we introduced a way to use OCT reflectivity profiles for a quantitative description of retinal layers (Garcia Garrido et al. 2014) (**Paper V**). Taking into account that current developments of molecular therapies, particularly in retinal degenerations, will undoubtedly lead to a large number of clinical trials in the near future, the *in vivo* quantification of therapeutic effects over time will almost certanly include OCT data.
Since visual inspection is usually sufficient to get an immediate overview of the contained information, this study has a broad application potential on both clinic and research.

The third part of this thesis was devoted to the improvement and optimization of OCT as diagnostic technology. In the first place, we demonstrated the potential of OCT reflectivity profiles as a basis for a quantitative characterization of the retinal morphology in a cross-species comparative study (Garcia Garrido et al. 2014) (**Paper V**). The characteristic pattern of the mammalian reflectivity profiles may also help to better fine-tune automated segmentation algorithms. It is a long-standing problem that, because retinal anatomy and

layering in health as well as in disease is complex and variable, automated segmentation procedures have not yet reached a satisfactory level of performance. Here it was shown that quantitative OCT analyses are very well suited to capture and numeralize similarities and differences in the retina of three laboratory species with a different degree of topographic structuring: mouse, gerbil and NHP. This work closely relates to human studies (Barthelmes et al. 2006, Barthelmes et al. 2008, Jacobson et al. 2009, Jacobson et al. 2012). As a first step in this study, we investigated whether the anatomical properties within the mouse retina would affect our reflectivity profile. Secondly, we studied whether differences in the retinal pigment content would somehow affect the reflectivity profile and therefore, we examined the C57BL/6 line representing pigmented strains, and the BALB/c line representing non-pigmented ones. Besides, each part of the profile was matched to a corresponding retinal structure in *ex vivo* morphology. As presumed, we found that variations in the retinal pigment content do influence the detection of the underlying anatomical structures and their representation in the reflectivity profile. By acquiring several reflectivity profiles from different fundus locations, we could demonstrate that the comparatively minor topographical differences across the mouse retina (e.g. cell distribution, opsin gradient) did not substantially manifest in OCT reflectivity profiles. In a next step, we recorded a standard reflectivity profile of another rodent model, the gerbil. Gerbils are primarily diurnal (activity during the day and sleeping at night). Their body size lies between that of mice and rats, but their retinal organisation is very different from those primarily nocturnal species. Most obvious in this regard is the well-expressed visual streak, a specialized retinal region that resembles many features of the human macula (Huber et al. 2010). The visual streak is represented in the native fundus image as a high reflective band located to the dorsal part of the retina. Based on the reflectivity profile, we were able to show that the visual streak region is characterized by an elongation of the crest corresponding to the photoreceptor outer segments. Another typical landmark in gerbils is the characteristic pattern of the retinal vasculature. The relatively high similarity of the vascular organization with the human macula may render this class of rodents suitable models for experimental therapies in diseases with a strong vascular component like *Diabetes Mellitus*. It is believed that the topographical differences in retinal morphology between different animal species have developed due to evolutionary pressure in their natural habitat. The driving force may be an advantage in the acquirement and processing of specific, vital visual information. Typical patterns associated with such an adaptation may include a difference in the number and type of retinal cells (e.g. photoreceptors, bipolar, or ganglion cells), the distribution and spectral sensitivity of visual pigments, or even variations in the vascular pattern (Peichl 2005). It is believed that preferential day- or night-activity constitutes a major determinative factor in this context, and whether the animal's role is rather prey or predator. Indeed, other day-active species like the

unstriped soudanian grass rat (*Arvicanthis ansorgei*) are known to possess a retina rich in cones and a special organisation of those in the ONL (Boudard et al. 2010), very well in agreement with our findings. More details regarding the visual streak organisation in a predator like the cat with a so-called *area centralis* may be found elsewhere (Narfstrom et al. 2011). Finally, we turned to even further specialised retinas as found in primates including humans. These retinae are characterized by the presence of a *fovea* conferring high-acuity central vision. Based on Cynomolgus monkey data, we produced a generic OCT reflectivity profile in non-human primates. All layers in foveal and non-foveal regions were successfully matched with that of human counterparts. Also, the foveal reflex, featuring a total reflection, was detected in both primates and humans. The quantification of the retinal nerve fibre layer (RNFL) via reflectivity profiles pointed out a lower density of nerve fibres in cynomolgus monkeys in comparison to human retina. In diseases where the thickness of the NFL is altered (e.g. glaucoma), the assessment of the RNFL via reflectivity profiles may nevertheless be a valuable biomarker in the follow-up of the disease.

The final part of this thesis addresses the problems in OCT image analysis induced by distortion due to unequal X and Y scales, and provides an exemplary case for an OCT image calibration based on *in vivo* data using intraocular objects (**Paper VI,** Garcia Garrido et al. 2015, *accepted*). The introduction of the OCT in the clinical practice has without question been one of the major breakthroughs of the recent years. A particular asset of imaging data in general is that a visual inspection is usually sufficient to get an immediate overview of the contained information without the need for an often intransparent numerical analysis. OCT data, however, have the appearance of histological sections, but they are generated quite differently. They are computer-generated images made of a lateral combination of a series of axial reflectivity profiles (A-scans). While the Y axis basically reflects the original A-scans, the X axis is a product of a fitting process based on a number of inferences, so that the scales for X and Y are not intrinsically identical. As scaling properties may be altered by factors like additional lenses in the optical pathway (on the equipment side or on the side of the subject), shape and size of the eye, or species differences (in experimental studies), a check of these properties may be required to ensure a system with equal scaling in X and Y (and possibly Z for ‘volume scan’ 3D stacks). It may be for this reason that two-dimensional measurements in OCT images, in contrast to e.g. ultrasound image data, are rarely used so far.
The evaluation of OCT data is in the vast majority of clinical applications done by visual inspection, and to a lesser degree also supported by quantitative analysis. Presumably since unequal scales are not part of the natural environment, our visual system is not well suited to incorporate this in the assessment process. We show here that a number of effects may lead to unwanted distortions if the scales for X and Y are not equal, which may influence any

conclusions drawn from such images. The effect of distorted proportions in a two-dimensional graph is demonstrated in this work on the basis of two examples. We showed that a circular shape turns into an ellipse if X-Y scaling is not equal. A two-dimensional measurement of such a distorted structure would require a correction dependent on the angle of the cross-section as detailed in *Appendix 1* (**Paper VI**). Further, any rectangular structure will appear at an altered angle in the X-Y plane depending on the amount of scale differences, according to the formula given that determines the size of this effect and may be used for a correction. As a conclusion, we proposed to establish an equal scaling of the axes to circumvent the need for any correction of distortion, which would both apply to visual inspection as well as to numerical two-dimensional measurements. To achieve a two-dimensional calibration of the acquired OCT raw images, a relation between X and Y axis data needs to be established, which in our hands is most reliable when using well-defined intraocular objects *in vivo*. Potentially, this can be anything temporary or persistent from surgical equipment tips, syringes, or fluid droplets to implanted devices like slow release containers or retinal prostheses. The use of natural landmarks like the optic disc has the limitation that their exact size and shape is usually not known and may thus not work as desired. In this study, we use spherical MicroBeads containing GFP-expressing mesenchymal stem cells placed either sub- or epiretinally in the retina of *Sv129* wild-type mice. We feel that an *in vivo* verification of scaling is the best option to ensure a proper calibration, as the complexity of the different tissues and pathways are hard to fully integrate in theoretical models or fabricated OCT phantoms (Agrawal et al. 2012, Baxi et al. 2014).
For our setup, a correction factor of about 3.3 was determined from that data. This factor describes the X-Y scaling differences within the same OCT scan and should not be confused with the “conversion constants” between OCT data and histology that have been established in several studies on animal models (Fischer et al. 2009, Huber et al. 2009, Ferguson et al. 2014). These studies purely compare the A-Scan data (Y axis) with ex vivo tissue morphometry, whereas the present study is to our best knowledge the first to introduce a method of how a reliable X-Y relationship may be established based on real world data. Our results demonstrated the need for a proper two-dimensional calibration of OCT data, and we expect that the consideration of equal scaling will advance the use of two-dimensional measurements and thereby help to increase the efficiency of OCT image analysis.

In summary, this thesis demonstrates the capability of *in vivo* retinal imaging techniques to unravel meaningful aspects of the retina in health and disease. Additionally, our work contributed to the further optimization and advancement of the diagnostic technology.

V. ACKNOWLEDGEMENTS

My most sincere thanks go to Prof. Seeliger for giving me the opportunity to work in his lab and for sharing his valuable scientific knowledge with me. His inquisitive disscussions have helped me to become more critical and experienced.

I would also like to thank Prof. Ruth for his interest in my work and his very uncomplicated supervision.

Thanks as well to Dr. Gesine Huber and Dr. Susanne Beck for their initial training in the lab and introduction in this research field.

My close colleagues at the institute: Vithiya, Gudrun, Susanne, Pia, Regine and Naoyuki deserve my heartfelt thanks for offering a very friendly atmosphere at work, a lot of interesting conversations and many fun moments during business trips.

Although it would be impossible to name them all, I would also like to thank all of the people around the world I have worked with during the conduction of this thesis. I have visited a lot of new cities and I have met great people! Thanks.

A special thanks goes to Julian, for his long-standing support and understanding. We make a great team together!.

Last but not least, I would like to thank my father, mother and sister for their inconditional love and encouragement. Despite the distance, I feel you very close!. Os quiero.

VI. REFERENCES

Abramoff, M. D., M. K. Garvin and M. Sonka (2010) Retinal Imaging and Image Analysis. IEEE Trans Med Imaging 3:169-208.

Agrawal, A., M. Connors, A. Beylin, C. P. Liang, D. Barton, Y. Chen, R. A. Drezek and T. J. Pfefer (2012) Characterizing the point spread function of retinal OCT devices with a model eye-based phantom. Biomed Opt Express 3(5):1116-1126.

Aleman, T. S., A. V. Cideciyan, G. K. Aguirre, W. C. Huang, C. L. Mullins, A. J. Roman, A. Sumaroka, M. B. Olivares, F. F. Tsai, S. B. Schwartz, L. H. Vandenberghe, M. P. Limberis, E. M. Stone, P. Bell, J. M. Wilson and S. G. Jacobson (2011) Human CRB1-associated retinal degeneration: comparison with the rd8 Crb1-mutant mouse model. Invest Ophthalmol Vis Sci 52(9):6898-6910.

Alves, C. H., A. S. Sanz, B. Park, L. P. Pellissier, N. Tanimoto, S. C. Beck, G. Huber, M. Murtaza, F. Richard, I. Sridevi Gurubaran, M. Garcia Garrido, C. N. Levelt, P. Rashbass, A. Le Bivic, M. W. Seeliger and J. Wijnholds (2013) Loss of CRB2 in the mouse retina mimics human retinitis pigmentosa due to mutations in the CRB1 gene. Hum Mol Genet 22(1):35-50.

Barthelmes, D., M. C. Gillies and F. K. Sutter (2008) Quantitative OCT analysis of idiopathic perifoveal telangiectasia. Invest Ophthalmol Vis Sci 49(5):2156-2162.

Barthelmes, D., F. K. Sutter, M. M. Kurz-Levin, M. M. Bosch, H. Helbig, G. Niemeyer and J. C. Fleischhauer (2006) Quantitative analysis of OCT characteristics in patients with achromatopsia and blue-cone monochromatism. Invest Ophthalmol Vis Sci 47(3):1161-1166.

Baxi, J., W. Calhoun, Y. J. Sepah, D. X. Hammer, I. Ilev, T. J. Pfefer, Q. D. Nguyen and A. Agrawal (2014) Retina-simulating phantom for optical coherence tomography. J Biomed Opt 19(2):21106.

Berger, W., B. Kloeckener-Gruissem and J. Neidhardt (2010) The molecular basis of human retinal and vitreoretinal diseases. Prog Retin Eye Res 29(5):335-375.

Biel, M. and S. Michalakis (2007) Function and dysfunction of CNG channels: insights from channelopathies and mouse models. Mol Neurobiol 35(3):266-277.

Born, M. and E. Wolf (1999). Principles of optics : electromagnetic theory of propagation, interference and diffraction of light. Cambridge ; New York, Cambridge University Press.

Boudard, D. L., N. Tanimoto, G. Huber, S. C. Beck, M. W. Seeliger and D. Hicks (2010) Cone loss is delayed relative to rod loss during induced retinal degeneration in the diurnal cone-rich rodent Arvicanthis ansorgei. Neuroscience 169(4):1815-1830.

Cook A, S. White, M. Batterbury, D. Clark (2008) Ocular growth and refractive error development in premature infants with or without retinopathy of prematurity. Invest Ophthalmol Vis Sci. 49(12):5199-207

Dowling, J. E. (2012). The retina : an approachable part of the brain. Cambridge, Mass., Belknap Press of Harvard University Press.

Drexler, W., U. Morgner, R. K. Ghanta, F. X. Kartner, J. S. Schuman and J. G. Fujimoto (2001) Ultrahigh-resolution ophthalmic optical coherence tomography. Nat Med 7(4):502-507.

Drexler, W., H. Sattmann, B. Hermann, T. H. Ko, M. Stur, A. Unterhuber, C. Scholda, O. Findl, M. Wirtitsch, J. G. Fujimoto and A. F. Fercher (2003) Enhanced visualization of macular pathology with the use of ultrahigh-resolution optical coherence tomography. Arch Ophthalmol 121(5):695-706.

Ebrey, T. and Y. Koutalos (2001) Vertebrate photoreceptors. Prog Retin Eye Res 20(1):49-94.

Ferguson, L. R., S. Grover, J. M. Dominguez, 2nd, S. Balaiya and K. V. Chalam (2014) Retinal thickness measurement obtained with spectral domain optical coherence tomography assisted optical biopsy accurately correlates with ex vivo histology. PLoS One 9(10):e111203.

Fischer, M. D., G. Huber, S. C. Beck, N. Tanimoto, R. Muehlfriedel, E. Fahl, C. Grimm, A. Wenzel, C. E. Reme, S. A. van de Pavert, J. Wijnholds, M. Pacal, R. Bremner and M. W. Seeliger (2009) Noninvasive, in vivo assessment of mouse retinal structure using optical coherence tomography. PLoS One 4(10):e7507.

Frohman, E. M., J. G. Fujimoto, T. C. Frohman, P. A. Calabresi, G. Cutter and L. J. Balcer (2008) Optical coherence tomography: a window into the mechanisms of multiple sclerosis. Nat Clin Pract Neurol 4(12):664-675.

Fujimoto, J. G. (2003) Optical coherence tomography for ultrahigh resolution in vivo imaging. Nat Biotechnol 21(11):1361-1367.

Fujimoto, J. G., M. E. Brezinski, G. J. Tearney, S. A. Boppart, B. Bouma, M. R. Hee, J. F. Southern and E. A. Swanson (1995) Optical biopsy and imaging using optical coherence tomography. Nat Med 1(9):970-972.

Garcia Garrido, M., S. C. Beck, R. Muhlfriedel, S. Julien, U. Schraermeyer and M. W. Seeliger (2014) Towards a quantitative OCT image analysis. PLoS One 9(6):e100080.

Hamel, C. (2006) Retinitis pigmentosa. Orphanet J Rare Dis 1:40.

Hartong, D. T. and A. C. Kooijman (2006) Night-vision goggles for night-blind subjects: subjective evaluation after 2 years of use. Ophthalmic Physiol Opt 26(5):490-496.

Huber, G., S. C. Beck, C. Grimm, A. Sahaboglu-Tekgoz, F. Paquet-Durand, A. Wenzel, P. Humphries, T. M. Redmond, M. W. Seeliger and M. D. Fischer (2009) Spectral domain optical coherence tomography in mouse models of retinal degeneration. Invest Ophthalmol Vis Sci 50(12):5888-5895.

Huber, G., S. Heynen, C. Imsand, F. vom Hagen, R. Muehlfriedel, N. Tanimoto, Y. Feng, H. P. Hammes, C. Grimm, L. Peichl, M. W. Seeliger and S. C. Beck (2010) Novel rodent models for macular research. PLoS One 5(10):e13403.

Jacobson, S. G., T. S. Aleman, A. V. Cideciyan, A. Sumaroka, S. B. Schwartz, E. A. Windsor, M. Swider, W. Herrera and E. M. Stone (2009) Leber congenital amaurosis caused by Lebercilin (LCA5) mutation: retained photoreceptors adjacent to retinal disorganization. Mol Vis 15:1098-1106.

Jacobson, S. G. and A. V. Cideciyan (2010) Treatment possibilities for retinitis pigmentosa. N Engl J Med 363(17):1669-1671.

Jacobson, S. G., A. V. Cideciyan, T. S. Aleman, M. J. Pianta, A. Sumaroka, S. B. Schwartz, E. E. Smilko, A. H. Milam, V. C. Sheffield and E. M. Stone (2003) Crumbs homolog 1 (CRB1) mutations result in a thick human retina with abnormal lamination. Hum Mol Genet 12(9):1073-1078.

Jacobson, S. G., A. V. Cideciyan, R. Ratnakaram, E. Heon, S. B. Schwartz, A. J. Roman, M. C. Peden, T. S. Aleman, S. L. Boye, A. Sumaroka, T. J. Conlon, R. Calcedo, J. J. Pang, K. E. Erger, M. B. Olivares, C. L. Mullins, M. Swider, S. Kaushal, W. J. Feuer, A. Iannaccone, G. A. Fishman, E. M. Stone, B. J. Byrne and W. W. Hauswirth (2012) Gene therapy for leber congenital amaurosis caused by RPE65 mutations: safety and efficacy in 15 children and adults followed up to 3 years. Arch Ophthalmol 130(1):9-24.

Folgar, F. A., E. L. Yuan, S. Farsiu, C. A. Toth (2014) Lateral and axial measurement differences between spectral-domain optical coherence tomography systems. J Biomed Opt. 19 (1):16014

Kellner, U., H. Tillack and A. B. Renner (2004) [Hereditary retinochoroidal dystrophies. Part 1: Pathogenesis, diagnosis, therapy and patient counselling]. Ophthalmologe 101(3):307-319; quiz 320.

Koch, S., V. Sothilingam, M. Garcia Garrido, N. Tanimoto, E. Becirovic, F. Koch, C. Seide, S. C. Beck, M. W. Seeliger, M. Biel, R. Muhlfriedel and S. Michalakis (2012) Gene therapy restores vision and delays degeneration in the CNGB1(-/-) mouse model of retinitis pigmentosa. Hum Mol Genet 21(20):4486-4496.

Krebs, I. S. Hagen, W. Brannath, P. Haas, I. Womastek, G. de Salvo, S. Ansari-Shahrezaei, S. Binder. (2010) Repeatability and reproducibility of retinal thickness measurements by optical coherence tomography in age-related macular degeneration. Ophthalmology; 117(8):1577-84.

Levin, L. A. and P. L. Kaufman (2011). Adler's physiology of the eye : clinical application. Edinburgh ; New York, Saunders/Elsevier.

Lozano, D. C. and Twa, M. D. (2013). Development of a rat schematic eye in vivo biometry and the correction of lateral magnification in SD-OCT imaging. Invest Ophthalmol Vis Sci. 27; 54 (9):6446-55.

Mehalow, A. K., S. Kameya, R. S. Smith, N. L. Hawes, J. M. Denegre, J. A. Young, L. Bechtold, N. B. Haider, U. Tepass, J. R. Heckenlively, B. Chang, J. K. Naggert and P. M. Nishina (2003) CRB1 is essential for external limiting membrane integrity and photoreceptor morphogenesis in the mammalian retina. Hum Mol Genet 12(17):2179-2189.

Michalakis, S., R. Muhlfriedel, N. Tanimoto, V. Krishnamoorthy, S. Koch, M. D. Fischer, E. Becirovic, L. Bai, G. Huber, S. C. Beck, E. Fahl, H. Buning, F. Paquet-Durand, X. Zong, T. Gollisch, M. Biel and M. W. Seeliger (2010) Restoration of cone vision in the CNGA3-/- mouse model of congenital complete lack of cone photoreceptor function. Mol Ther 18(12):2057-2063.

Muhlfriedel, R., S. Michalakis, M. G. Garrido, M. Biel and M. W. Seeliger (2013) Optimized technique for subretinal injections in mice. Methods Mol Biol 935:343-349.

Narfstrom, K., M. Menotti Raymond and M. Seeliger (2011) Characterization of feline hereditary retinal dystrophies using clinical, functional, structural and molecular genetic studies. Vet Ophthalmol 14 Suppl 1:30-36.

Odell D.,A. M. Dubis, J. F. Lever, K. E. Stepien, J. Carroll (2011) Assessing errors in OCT-derived macular thickness maps. J Ophthalmol 2011:692574

Peichl, L. (2005) Diversity of mammalian photoreceptor properties: adaptations to habitat and lifestyle? Anat Rec A Discov Mol Cell Evol Biol 287(1):1001-1012.

Pellissier, L. P., C. H. Alves, P. M. Quinn, R. M. Vos, N. Tanimoto, D. M. Lundvig, J. J. Dudok, B. Hooibrink, F. Richard, S. C. Beck, G. Huber, V. Sothilingam, M. Garcia Garrido, A. Le Bivic, M. W. Seeliger and J. Wijnholds (2013) Targeted ablation of CRB1 and CRB2 in retinal progenitor cells mimics Leber congenital amaurosis. PLoS Genet 9(12):e1003976.

Pellissier, L. P., P. M. Quinn, C. H. Alves, R. M. Vos, J. Klooster, J. G. Flannery, J. A. Heimel, J. Wijnholds (2015) Gene therapy into photoreceptors and Müller glial cells restores retinal structure and function in CRB1 retinitis pigmentosa mouse models. Hum Mol Genet pii: ddv062. [Epub ahead of print]

Preece, S. J. and E. Claridge (2002) Monte Carlo modelling of the spectral reflectance of the human eye. Phys Med Biol 47(16):2863-2877.

Richard, M., R. Roepman, W. M. Aartsen, A. G. van Rossum, A. I. den Hollander, E. Knust, J. Wijnholds and F. P. Cremers (2006) Towards understanding CRUMBS function in retinal dystrophies. Hum Mol Genet 15 Spec No 2:R235-243.

Rodieck, R. W. (1998). The first steps in seeing. Sunderland, Mass., Sinauer Associates.

Ruggeri, M., H. Wehbe, S. Jiao, G. Gregori, M. E. Jockovich, A. Hackam, Y. Duan and C. A. Puliafito (2007) In vivo three-dimensional high-resolution imaging of rodent retina with spectral-domain optical coherence tomography. Invest Ophthalmol Vis Sci 48(4):1808-1814.
Sadda S. R , P. A. Keane, Y. Ouyang, J.F. Updike, A.C. Walsh (2010) Impact of scanning density on measurements from spectral domain optical coherence tomography. Invest Ophthalmol Vis Sci. 51(2):1071-8.

Schmitz-Valckenberg, S., F. G. Holz, A. C. Bird and R. F. Spaide (2008) Fundus autofluorescence imaging: review and perspectives. Retina 28(3):385-409.

Seeliger, M. W., S. C. Beck, N. Pereyra-Munoz, S. Dangel, J. Y. Tsai, U. F. Luhmann, S. A. van de Pavert, J. Wijnholds, M. Samardzija, A. Wenzel, E. Zrenner, K. Narfstrom, E. Fahl, N. Tanimoto, N. Acar and F. Tonagel (2005) In vivo confocal imaging of the retina in animal models using scanning laser ophthalmoscopy. Vision Res 45(28):3512-3519.

Stone, E. M. (2007) Leber congenital amaurosis - a model for efficient genetic testing of heterogeneous disorders: LXIV Edward Jackson Memorial Lecture. Am J Ophthalmol 144(6):791-811.

Sull A. C., L. N. Vuong , L. L. Price V. J. Srinivasan, I. Gorczynska, J. G. Fujimoto, J. S. Schuman, J. S. Duker (2010) Comparison of spectral/Fourier domain optical coherence tomography instruments for assessment of normal macular thickness

Swaroop, A., D. Kim and D. Forrest (2010) Transcriptional regulation of photoreceptor development and homeostasis in the mammalian retina. Nat Rev Neurosci 11(8):563-576.

Tepass, U., C. Theres and E. Knust (1990) crumbs encodes an EGF-like protein expressed on apical membranes of Drosophila epithelial cells and required for organization of epithelia. Cell 61(5):787-799.

van de Pavert, S. A., A. Kantardzhieva, A. Malysheva, J. Meuleman, I. Versteeg, C. Levelt, J. Klooster, S. Geiger, M. W. Seeliger, P. Rashbass, A. Le Bivic and J. Wijnholds (2004) Crumbs homologue 1 is required for maintenance of photoreceptor cell polarization and adhesion during light exposure. J Cell Sci 117(Pt 18):4169-4177.

van de Pavert, S. A., J. Meuleman, A. Malysheva, W. M. Aartsen, I. Versteeg, F. Tonagel, W. Kamphuis, C. J. McCabe, M. W. Seeliger and J. Wijnholds (2007a) A single amino acid substitution (Cys249Trp) in Crb1 causes retinal degeneration and deregulates expression of pituitary tumor transforming gene Pttg1. J Neurosci 27(3):564-573.

van de Pavert, S. A., A. S. Sanz, W. M. Aartsen, R. M. Vos, I. Versteeg, S. C. Beck, J. Klooster, M. W. Seeliger and J. Wijnholds (2007b) Crb1 is a determinant of retinal apical Muller glia cell features. Glia 55(14):1486-1497.

van den Hurk, J. A., P. Rashbass, R. Roepman, J. Davis, K. E. Voesenek, M. L. Arends, M. N. Zonneveld, M. H. van Roekel, K. Cameron, K. Rohrschneider, J. R. Heckenlively, R. K. Koenekoop, C. B. Hoyng, F. P. Cremers and A. I. den Hollander (2005) Characterization of the Crumbs homolog 2 (CRB2) gene and analysis of its role in retinitis pigmentosa and Leber congenital amaurosis. Mol Vis 11:263-273.

van Rossum, A. G., W. M. Aartsen, J. Meuleman, J. Klooster, A. Malysheva, I. Versteeg, J. P. Arsanto, A. Le Bivic and J. Wijnholds (2006) Pals1/Mpp5 is required for correct localization of Crb1 at the subapical region in polarized Muller glia cells. Hum Mol Genet 15(18):2659-2672.

van Velthoven, M. E., D. J. Faber, F. D. Verbraak, T. G. van Leeuwen and M. D. de Smet (2007) Recent developments in optical coherence tomography for imaging the retina. Prog Retin Eye Res 26(1):57-77.

Walia, S., G. A. Fishman, S. G. Jacobson, T. S. Aleman, R. K. Koenekoop, E. I. Traboulsi, R. G. Weleber, M. E. Pennesi, E. Heon, A. Drack, B. L. Lam, R. Allikmets and E. M. Stone (2010) Visual acuity in patients with Leber's congenital amaurosis and early childhood-onset retinitis pigmentosa. Ophthalmology 117(6):1190-1198.

Werner, J. S. and L. M. Chalupa (2014). The new visual neurosciences. Cambridge, Massachusetts, The MIT Press.

Wolf-Schnurrbusch, U. E., Wolf-Schnurrbusch U. E., Ceklic L., Brinkmann C. K., Iliev M. E., Frey M., Rothenbuehler S. P., Enzmann V., Wolf S. (2009) Macular thickness measurements in healthy eyes using six different optical coherence tomography instruments. Invest Ophthalmol Vis Sci. 50(7):3432-7.

Zawadzki R. J., et al. (2010) Towards building an anatomically correct solid eye model with volumetric representation of retinal morphology. Proc. SPIE 7550, 75502F

Zobor, D. and E. Zrenner (2012) [Retinitis pigmentosa - a review. Pathogenesis, guidelines for diagnostics and perspectives]. Ophthalmologe 109(5):501-514;quiz 515.

Other REFERENCES

Sensory reception: Human vision: structure and function of the human eye" vol 27, Encyclopaedia Britannica, 1987.

Anatomia Ocular p.24, Dr. Encarna Garcia Garrido

VII. *CURRICULUM VITAE*

EDUCATION

2005 - 2010	Grado en Farmacia, University of Salamanca, Spain
2008 - 2009	Pharmacy studies, University of Bonn, Germany
04/ 2011	German “Approbation als Apothekerin“
11/2010 – heute	PhD candidate, Division of Ocular Neurodegeneration, Institute for Ophthalmic Research, Tübingen, Germany

MEMBERSHIPS/AWARDS

Since 2010	Member of the Association for Research in Vision and Ophthalmology (ARVO)
Since 2011	Member of the Landesapothekerkammer Baden-Württembergs (LAK)
2008/2009	Erasmus-Programm Scholarship
01/2014	Swiss Retina Award, Swiss Eye Research Meeting, Biel, Switzerland

VIII. LIST OF PUBLICATIONS

2012:

1. Lack of the sodium-driven chloride bicarbonate exchanger NCBE impairs visual function in the mouse retina. Hilgen G, Huebner AK, Tanimoto N, Sothilingam V, Seide C, *Garrido MG*, Schmidt KF, Seeliger MW, Löwel S, Weiler R, Hübner CA, Dedek K. (2012) **PLOS ONE**; 7(10):e46155.

2. Loss of CRB2 in the mouse retina mimics human retinitis pigmentosa due to mutations in the CRB1 gene. Alves CH, Sanz Sanz A, Park B, Pellissier LP, Tanimoto N, Beck SC, Huber G, Murtaza M, Richard F, Sridevi Gurubaran I, *Garcia Garrido M*, Levelt CN, Rashbass P, Le Bivic A, Seeliger MW, Wijnholds J. (2012) **Human Molecular Genetics**; 22(1):35-50.

3. Gene therapy restores vision and delays degeneration in the CNGB1(-/-) mouse model of retinitis pigmentosa. Koch S, Sothilingam V, *Garcia Garrido M*, Tanimoto N, Becirovic E, Koch F, Seide C, Beck SC, Seeliger MW, Biel M, Mühlfriedel R, Michalakis S. (2012) **Human Molecular Genetics**; 21(20):4486-96.

4. PGC-1α determines light damage susceptibility of the murine retina.
   Egger A, Samardzija M, Sothilingam V, Tanimoto N, Lange C, Salatino S, Fang L, *Garcia-Garrido M*, Beck S, Okoniewski MJ, Neutzner A, Seeliger MW, Grimm C, Handschin C. (2012) **PLOS ONE**; 7(2):e31272.

2013:

5. Targeted Ablation of Crb1 and Crb2 in Retinal Progenitor Cells Mimics Leber Congenital Amaurosis. Pellissier LP, Alves HC, Quinn PM, Vos RM, Tanimoto N, Lundvig DM, Dudok JJ, Hooibrink B, Richard F, Beck SC, Huber G, Sothilingam V, *Garcia Garrido M*, Le Bivic A, Seeliger MW and Wijnholds J. (2013) **PLOS GENETICS**; 9(12):e1003976.

6. Mosaic synaptopathy and functional defects in Cav1.4 heterozygous mice and human carriers of CSNB2. Michalakis S, Shaltiel L, Sothilingam V, Koch S, Schludi V, Krause S, Zeitz C, Audo I, Lancelot ME, Hamel C, Meunier I, Preising MN, Friedburg C, Lorenz B, Zabouri N, Haverkamp S, *Garrido MG*, Tanimoto N, Seeliger MW, Biel M, Wahl-Schott CA. (2013) **Human Molecular Genetics** 23(6):1538-50.

7. Cav1.4 IT mouse as model for vision impairment in human congenital stationary night blindness type 2. Knoflach D, Kerov V, Sartori SB, Obermair GJ, Schmuckermair C, Liu X, Sothilingam V, *Garrido MG*, Baker SA, Glösmann M, Schicker K, Seeliger M, Lee A, Koschak A. (2013) **Channels** (Austin); 19;7(6).

8. Myosin7a deficiency results in reduced retinal activity which is improved by gene therapy. Colella P, Sommella A, Marrocco E, Di Vicino U, Polishchuk E, *Garrido MG*, Seeliger MW, Polishchuk R, Auricchio A. (2013) **PLOS ONE**; 8(8):e72027.

9. MPP3 regulates levels of PALS1 and adhesion between photoreceptors and Müller cells. Dudok JJ, Sanz AS, Lundvig DM, Sothilingam V, *Garrido MG*, Klooster J, Seeliger MW, Wijnholds J. (2013) **Glia**; 61(10):1629-44.

10. Alterations of the tunica vasculosa lentis in the rat model of retinopathy of prematurity. Favazza TL, Tanimoto N, Munro RJ, Beck SC, *Garcia Garrido M*, Seide C, Sothilingam V, Hansen RM, Fulton AB, Seeliger MW, Akula JD. (2013) **Documenta Ophthalmologica**; 127(1):3-11.

11. Mice lacking Period 1 and Period 2 circadian clock genes exhibit blue cone photoreceptor defects. Ait-Hmyed O, Felder-Schmittbuhl MP, *Garcia-Garrido M*, Beck S, Seide C, Sothilingam V, Tanimoto N, Seeliger M, Bennis M, Hicks D. (2013) **European Journal of Neuroscience**; 37(7):1048-60.

12. Book chapter: Optimized technique for subretinal injections in mice. Mühlfriedel R, Michalakis S, *Garrido MG*, Biel M, Seeliger MW. (2013) **Methods in Molecular Biology**; 935:343-9.

2014:

13. Elk3 deficiency causes transient impairment in post-natal retinal vascular development and formation of tortuous arteries in adult murine retinae. Weinl C, Wasylyk C, *Garcia Garrido M*, Sothilingam V, Beck SC, Riehle H, Stritt C, Roux MJ, Seeliger MW, Wasylyk B, Nordheim A. (2014) **PLOS ONE** 9(9):e107048.

14. Towards a Quantitative OCT Image Analysis
Garcia Garrido M, Beck SC, Mühlfriedel R, Julien S, Schraermeyer U, Seeliger MW (2014) **PLOS ONE**; 9(6):e100080.

15. Knockout of PARG110 confers resistance to cGMP induced toxicity in mammalian photoreceptors. Sahaboglu A, Tanimoto N, Bolz S, *Garcia Garrido M*, Ueffing M,

Seeliger M, Löwenheim H, Ekström P, Paquet-Durand F (2014) **Cell Death and Disease**; 5:e1234.

16. Gene Therapy Restores Vision and Delays Degeneration in the CNGB1(-/-) Mouse Model of Retinitis Pigmentosa. Michalakis S, Koch S, Sothilingam V, *Garrido MG*, Tanimoto N, Schulze E, Becirovic E, Koch F, Seide C, Beck SC, Seeliger MW, Mühlfriedel R, Biel M. (2014) **Advances in Experimental Medicine and Biology**; 801:733-9.

17. CRB2 acts as a modifying factor of CRB1-related retinal dystrophies in mice. Pellissier LP, Lundvig DM, Tanimoto N, Klooster J, Vos RM, Richard F, Sothilingam V, *Garrido MG*, Le Bivic A, Seeliger MW, Wijnholds J. (2014) **Human Molecular Genetics**; 23(14):3759-71.

18. Targeted ablation of Crb2 in Photoreceptor Cells induces Retinitis Pigmentosa. Alves CH, Pellissier LP, Vos RM, *Garrido MG*, Sothilingam V, Seide C, Beck SC, Klooster J, Furukawa T, Flannery JG, Verhaagen J, Seeliger MW, Wijnholds J. (2014) **Human Molecular Genetics**; 23(13):3384-401.

2015:

19. Influence of the β2-subunit of L-type voltage-gated Cav channels on the structural and functional development of photoreceptor ribbon synapse. Katiyar R, Weissgerber P, Roth E, Dörr J , Sothilingam V, *Garcia Garrido M*, Beck SC , Seeliger MW , Beck A, Schmitz F, Flockerzi V. **Investigative Ophthalmology & Visual Science** pii: IOVS-15-16654.

20. Mutations in the Unfolded Protein Response regulator, ATF6, cause the cone dysfunction syndrome Achromatopsia. Kohl S, Zobor D, Chiang WC J, Weisschuh N, Staller J, Gonzalez Menendez I, Chang S, Beck SC, *Garcia Garrido M*, Sothilingam V, Seeliger MW, Stanzial F, Benedicenti F, Inzana F, Heon E, Vincent A, Beis J, Strom TM, Rudolph G, Roosing S, den Hollander AI, Cremers FPM, Lopez I, Ren H, Moore AT, Webster A, Michaelides M, Koenekoop RK, Zrenner E, Kaufman RJ, Tsang SH, Wissinger B, Lin JH. (2015) **Nature Genetics in press.**

21. VEGF Mediates ApoE4-Induced Neovascularization and Synaptic Pathology in the Choroid and Retina. Antes R, Salomon-Zimri S, Beck SC, *Garcia Garrido M*, Livnat T, Maharshak I, Kadar T, Seeliger M, Weinberger D, Michaelson DM. (2015) **Current Alzheimer Research** 12(4):323-34.

22. Scale adjustments to facilitate two-dimensional measurements in OCT images. *Garcia Garrido M*, Mühlfriedel R, Beck S, Wallrapp C, Seeliger MW. (2015) **PLOS One. (**accepted)

Retinitis Pigmentosa: Impact of different Pdea6a point mutations on the disease phenotype. Sothilingam V*, *Garcia Garrido M**, Jiao K*, Buena-Atienza E, Sahaboglu A, Triunfović D, Balendran S, Koepfli T, Mühlfriedel R, Schön C, Biel M, Heckmann A, Beck SC, Michalakis S, Wissinger B, Seeliger MW, Paquet-Durand F. *: equally contribution. **Under review Human Molecular Genetics**

IX. PRESENTATIONS RELATED TO THIS RESEARCH WORK

2011:

Oral presentations:
27th, 28th January, "Assessment of retinal structure and function in Crb2/Crb1 double knock-out mice". Biel, Switzerland. Swiss Eye Research Meeting.

22nd, 23rd May, "*In vivo* morphological analysis of retinal structure in Crb2 mutant mice". Amsterdam, Netherlands. Crumbs In Sight Meeting, Crumbs Consortium.

23rd, 24th August, "*In vivo* morphological analysis in Crb2/Crb1 double knock-out mice". ThromboGenics NV, Leuven, Belgium.

Poster presentation:
1st-5th May, "Crb1 and Crb2 in Retinal Development". Fort Lauderdale, Florida, USA. The Association for Research in Vision and Ophthalmology (ARVO) Annual Meeting.

2012:

Oral presentations:
26th, 27th January, "Comparison between *CRB1*- associated retinal degeneration in human patients and corresponding mouse models". Biel, Switzerland. Swiss Eye Research Meeting.

13th, 14th February, "*In vivo* morphological and functional analysis of retinal structure in *shaker1* mutant mouse". Rome, Italy. Treatrush: fighting blindness of Usher Syndrome, Treatrush Consortium.

29th, 30th March, "Morphological and functional characterization of the *Thrß2-Crb1* mutant mouse". Marseille, France. Crumbs In Sight Meeting, Crumbs Consortium.

23rd May, "The Role of Crumbs in the Retina: An Experimental Approach". Tübingen, Germany. Vorlesungsreihe: "Modelle erblicher Netzhauterkrankungen: Genetik, Pathophysiologie und Therapie"

4th-8th June, "Novel models of LCA based on Crumbs protein deficiency". Valencia, Spain. ISCEV Symposium.

Poster presentation:
6th-10th May, "Comparison Between *CRB1*-Associated Retinal Degeneration in Human Patients and Corresponding Mouse Models". Fort Lauderdale, Florida, USA. The Association for Research in Vision and Ophthalmology (ARVO) Annual Meeting.

2013:

Oral presentations:
24th, 25th January, "Rodent models for Usher syndrome: New aspects of disease severity". Biel, Switzerland. Swiss Eye Research Meeting.

13th, 14th February, "*In vivo* morphological and functional analysis of retinal structure in mouse models for Usher syndrome type I". Brussels, Belgium. Treatrush: fighting blindness of Usher Syndrome, Treatrush Consortium.

29th May, “Towards a quantitative OCT image analysis”. Tübingen, Germany. Vorlesungsreihe: “Modelle erblicher Netzhauterkrankungen: Genetik, Pathophysiologie und Therapie”

13th June, “Towards a quantitative OCT image analysis”. Tübingen, Germany. “Progress in Neuroscience Research of the Retina and Inner Ear”.

Poster presentation:
5th-9th May, “Retinal OCT Reflectivity Profiles in Three Laboratory Animal Species”. Seattle, Washington, USA. The Association for Research in Vision and Ophthalmology (ARVO) Annual Meeting.

2014:

Oral presentations:
23rd, 24th January, “Towards a quantitative OCT image analysis”. Biel, Switzerland. Swiss Eye Research Meeting. Recipient of the Swiss Retina Award for the best presentation in the category of “young scientist”

4th June, “Towards a quantitative OCT image analysis”. Tübingen, Germany. Vorlesungsreihe: “Modelle erblicher Netzhauterkrankungen: Genetik, Pathophysiologie und Therapie”

Poster presentation:
4th-8th May, “Towards a quantitative OCT image analysis”. Orlando, Florida, USA. The Association for Research in Vision and Ophthalmology (ARVO) Annual Meeting.

2015:

Oral presentations:
20th May, “Advances in the diagnostics of ocular structure”. Tübingen, Germany. Vorlesungsreihe: “Modelle erblicher Netzhauterkrankungen: Genetik, Pathophysiologie und Therapie”

X. APPENDIX

Human Molecular Genetics, 2013, Vol. 22, No. 1 **35–50**
doi:10.1093/hmg/dds398
Advance Access published on September 21, 2012

Loss of CRB2 in the mouse retina mimics human retinitis pigmentosa due to mutations in the *CRB1* gene

Celso Henrique Alves[1], Alicia Sanz Sanz[1], Bokyung Park[1], Lucie P. Pellissier[1], Naoyuki Tanimoto[3], Susanne C. Beck[3], Gesine Huber[3], Mariyam Murtaza[4], Fabrice Richard[5,6], Iswariyaraja Sridevi Gurubaran[1], Marina Garcia Garrido[3], Christiaan N. Levelt[2], Penny Rashbass[4], André Le Bivic[5,6], Mathias W. Seeliger[3] and Jan Wijnholds[1,*]

[1]Department of Neuromedical Genetics and [2]Department of Molecular Visual Plasticity, The Netherlands Institute for Neuroscience, Royal Netherlands Academy of Arts and Sciences (KNAW), Meibergdreef 47, 1105 BA Amsterdam, The Netherlands, [3]Division of Ocular Neurodegeneration, Institute for Ophthalmic Research, Centre for Ophthalmology, Eberhard Karls University of Tübingen, Tübingen D-72076, Germany, [4]University of Sheffield, Alfred Denny Building, Western Bank, S102TN Sheffield, UK, [5]Developmental Biology Institute of Marseille Luminy (IBDML), Aix-Marseille University (AMU) and [6]CNRS, UMR 6216, IBDML, Case 907, 13288 Marseille, Cedex 09, France

Received June 21, 2012; Revised and Accepted September 14, 2012

In humans, the Crumbs homolog-1 (*CRB1*) gene is mutated in progressive types of autosomal recessive retinitis pigmentosa and Leber congenital amaurosis. However, there is no clear genotype–phenotype correlation for *CRB1* mutations, which suggests that other components of the CRB complex may influence the severity of retinal disease. Therefore, to understand the physiological role of the Crumbs complex proteins, we generated and analysed conditional knockout mice lacking CRB2 in the developing retina. Progressive disorganization was detected during late retinal development. Progressive thinning of the photoreceptor layer and sites of cellular mislocalization was detected throughout the CRB2-deficient retina by confocal scanning laser ophthalmoscopy and spectral domain optical coherence tomography. Under scotopic conditions using electroretinography, the attenuation of the a-wave was relatively stronger than that of the b-wave, suggesting progressive degeneration of photoreceptors in adult animals. Histological analysis of newborn mice showed abnormal lamination of immature rod photoreceptors and disruption of adherens junctions between photoreceptors, Müller glia and progenitor cells. The number of late-born progenitor cells, rod photoreceptors and Müller glia cells was increased, concomitant with programmed cell death of rod photoreceptors. The data suggest an essential role for CRB2 in proper lamination of the photoreceptor layer and suppression of proliferation of late-born retinal progenitor cells.

INTRODUCTION

The establishment and maintenance of apical–basal polarization and adhesion is controlled by apical polarity protein complexes, which are crucial for proper lamination of mammalian photoreceptor cells (1–8). The apical Crumbs complex resides in the adult retina at a subapical region adjacent to adherens junctions between photoreceptors and Müller glia cells (2,9). In amniotes, there are four Crumbs family members, CRB1, CRB2, CRB3A and CRB3B (10). In zebrafish, the family consists of Crb1, Crb2a (Ome), Crb2b, Crb3a and Crb3b (11,12). The prototypic CRB protein has a large extracellular domain with epidermal growth factor and laminin-globular domains, a single transmembrane domain and a short 37 amino acid intracellular C-terminus containing single-FERM and -PDZ protein-binding motifs (13). The core proteins of the complex are either CRB–PALS1 (protein associated with Lin Seven 1)–PATJ (PALS1-associated tight junction

*To whom correspondence should be addressed. Tel: +31 205664597; Fax: +31 205666121; Email: j.wijnholds@nin.knaw.nl

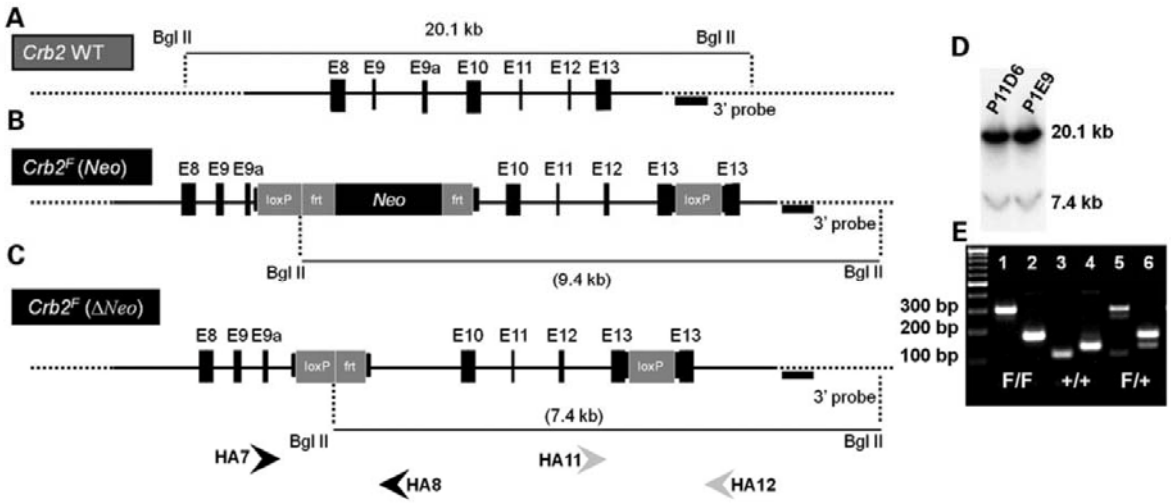

Figure 1. Schematic representation of the *Crb2* targeting construct and genotyping strategy. (**A**) *Crb2* WT gene composed of 13 exons. (**B**) *Crb2* targeting construct, the *loxP* recombination sites are located between exons 9a and 10, and in exon 13, in the 3′ untranslated region. The targeting construct also contains a neomycin cassette flanked by *frt* recombination sites. (**C**) *Crb2* targeting construct after *frt* recombination and deletion of the neomycin cassette. The localization of the 3′ end arm probe used to characterize the targeting construct, and of the pairs of primers, HA7/8 and HA11/12, located around the *loxP* recombination sites and used for genotyping, are represented in the figure. Two *Bgl*II restriction sites locate outside the targeted DNA; one extra *Bgl*II restriction site is present in the targeting construct near the 5′ end *loxP* site. (**D**) Southern blotting analysis of $Crb2^{F/+}$ embryonic stem-cell genomic DNA digested using *Bgl*II showed a 20.1 kb fragment corresponding to the WT allele and a 7.4 kb fragment corresponding to the *Crb2* floxed allele. (**E**) PCR genotyping of $Crb2^{F/F}$ (F/F), $Crb2^{+/+}$ (+/+) and $Crb2^{F/+}$ (F/+) mice. The left lane contains 100 bp DNA size markers, and the pairs of subsequent lanes contain PCR products of $Crb2^{F/F}$ (lanes 1 and 2), $Crb2^{+/+}$ (lanes 3 and 4) and $Crb2^{F/+}$ mouse DNA (lanes 5 and 6). Lanes 1, 3 and 5 contain the HA7/8 reaction product and the lanes 2, 4 and 6 contain the HA11/12 reaction product.

protein) or CRB–PALS1–MUPP1 (MUPP1—multi-PDZ domain protein 1) (2,14–18). The C-terminal PDZ motif of CRB interacts with the PDZ domain of PALS1, which in turn binds via an N-terminal L27 domain to the L27 domain of PATJ and MUPP1 (18). The PDZ motif of CRB can also interact with PAR6 (19), which can also bind to PALS1 (20). The multi-adaptor protein PALS1 recruits MPP3 and MPP4 into the apical complex (15,16). The FERM motif binds to EPB4.1L5, the mammalian homologue of *Drosophila* Yurt and zebrafish Mosaic Eyes (Moe) (21–23).

In humans, mutations have been identified in the *CRB1* gene in individuals with Leber congenital amaurosis, retinitis pigmentosa type 12, retinitis pigmentosa with Coats-like exudative vasculopathy and other early-onset retinitis pigmentosa (10,24,25). In the mouse retina, CRB1 maintains adherens junctions between photoreceptors and Müller glia cells and prevents retinal disorganization and dystrophy; moreover, the loss of CRB1 results in a phenotype limited to one retinal quadrant (1,2). However, the severity of the phenotype is strongly dependent on the genetic background, as different mutations in *CRB1/Crb1* cause various retinal phenotypes in human and mice. The lack of a clear genotype–phenotype correlation suggests that other components of the Crumbs complex have a function influencing the severity of the retinal disease. In zebrafish, the two *Crb2* genes (*Crb2a* and *Crb2b*) have been implicated in retina developmental and morphological defects. Crb2a (Ome) is a determinant of apicobasal polarity in the retina, and the loss of Crb2a causes severe basal displacement of cell junctions in neuroepithelial cells (11,12). *Ome* mutants display gross morphological abnormalities of the retina with inappropriate lamination and ectopic apical surfaces (26). Moreover, zebrafish Crb2b is essential for the determination of the size of apical membrane domain within photoreceptors. Overexpression of mouse *Crb2* in embryonic stem cells increased cell proliferation and reduced terminal neural differentiation (27).

Here, we study the effects of the loss of CRB2 from the developing mouse retinal neuroepithelium. Our findings show that conditional deletion of *Crb2* in the retina results in early retinal disorganization leading to severe and progressive retinal degeneration with a concomitant visual loss that mimics retinitis pigmentosa due to mutations in the *CRB1* gene, and suggest a role for CRB2 in suppressing proliferation of late retinal progenitors.

RESULTS

Lack of CRB2 impairs retinal function in adult mice

In mice, the degeneration due to the loss of CRB1 is limited to one quadrant of the retina, suggesting compensatory mechanisms (2). To ablate CRB2 function in the mouse, *loxP* sites were inserted in the *Crb2* gene between exons 9a and 10 and in exon 13 downstream of the stop codon (Fig. 1). *Crb2* floxed homozygous ($Crb2^{F/F}$) mice showed no identifiable phenotype, had a normal lifespan and were fully fertile. We crossed the *Crb2* conditional knockout (cKO) with Chx10-*Cre* mice to obtain *Crb2*Chx10 cKO ($Crb2^{F/F}/Chx10Cre^{+/}$)

animals. Chx10-*Cre* drives Cre-mediated recombination in neuroepithelial progenitors of the retina (28), resulting in the loss of CRB2 expression at the apical surface from embryonic day (E) 12.5 (Supplementary Material, Fig. S1).

We performed functional and structural *in vivo* analyses of 1–18-month-old *Crb2*Chx10 cKO and control mice, using electroretinography, spectral domain optical coherence tomography and scanning laser ophthalmoscopy. In electroretinography experiments under both scotopic and photopic conditions, there was no significant difference between the control animals ($Crb2^{F/+}/Chx10Cre^{+/}$ and $Crb2^{F/F}$) mice at any of the time points analysed (Fig. 2A–C). In contrast, already 1-month-old *Crb2*Chx10 cKO mice showed considerable reduction in amplitudes of both scotopic and photopic electroretinography responses, indicating alterations of both rod and cone system components (Fig. 2A). At high stimulus intensities under scotopic conditions, the attenuation of the a-wave was relatively stronger than that of the b-wave (Fig. 2A), resulting in a high b/a ratio (Fig. 2B). As the initial portion of the a-wave reflects the primary light response in photoreceptors, the remarkable attenuation of the a-wave observed in *Crb2*Chx10 cKO mice indicates a strong photoreceptor dysfunction. Furthermore, in *Crb2*Chx10 cKO mice, the signal amplitudes progressively decreased with age, until they became practically extinguished around 18 months of age (Fig. 2C).

In the *in vivo* imaging analysis using scanning laser ophthalmoscopy and spectral domain optical coherence tomography, control littermates did not show any abnormalities in fundus appearance, fundus autofluorescence, retinal vasculature and retinal morphology at any time point. Also, no differences were observed between the $Crb2^{F/+}/Chx10Cre^{+/}$ and $Crb2^{F/F}$ mice (Fig. 3A–E). In contrast, 1-month-old *Crb2*Chx10 cKO retinae revealed changes in fundus appearance as well as in retinal layer morphology, suggesting a progressive retinal degeneration (Figs 3F–J and 4A–O). With native scanning laser ophthalmoscopy, many spots and patchy areas were visible, and fundus autofluorescence revealed accumulation of autofluorescent remains from lost photoreceptor cells. Commonly, degenerative processes are characterized by accumulation of autofluorescent material, mainly break-down products of photoreceptor outer segments that contain the visual pigment chromophore 11-*cis* retinal, in the retina (29). These data were supported by spectral domain optical coherence tomography analysis. A significant reduction of retinal thickness, compared with control animals, was found in the outer retina of *Crb2*Chx10 cKOs. Furthermore, sites with cellular mislocalization were detected (Fig. 4D and I and insets E and J). In the *Crb2*Chx10 cKOs, a further progression of the retinal degeneration was observed (Fig. 4A, F and K). Most severe degeneration was found, particularly in the central retina surrounding the optic disc and at sites of cellular mislocalization.

Additionally, in the *Crb2*Chx10 cKO, the retinal vasculature was affected already at 3 months of age (Fig. 4C). With fluorescein angiography (FLA), sites of neovascularization were observed very similar to vascular abnormalities detected in *Crb1* $^{-/-}$ mice (3). At some of these sites (Fig. 4H and M), choroidal structures were visible, suggesting disruption of the retinal pigment epithelium layer. These processes were clearly visualized by spectral domain optical coherence tomography imaging (Fig. 4E, J and O). Taken together, our results indicate that *Crb2*Chx10 cKO animals have a strong retinal phenotype with severe functional consequences.

CRB2 is required in retinal development

The *in vivo* studies suggested abnormalities during retinal development. CRB2 is localized at E11.5 in retinal progenitor cells (Supplementary Material, Fig. S1) and later on in photoreceptors and Müller glia cells (30). Morphological alterations in the *Crb2*Chx10 cKO were found from E18.5 (Figs 5B and 6D and F). In the *Crb2*Chx10 cKO, sporadic disruptions of the outer limiting membrane and mislocalized cell nuclei in the subretinal space were observed at the periphery of the retina (Figs 5B and 6D and F). The *Crb2*Chx10 cKO lost CRB2 expression from the subapical region (Fig. 6B and Supplementary Material, Fig. S1) and displayed disrupted adherens junctions and subapical region (Fig. 6D, F, H, J, L and N).

At postnatal day (P) 3, the *Crb2*Chx10 cKO retinal progenitors and newly born photoreceptors had lost their normal orientation and instead formed rosettes and half-rosettes at the periphery of the retina (Fig. 5D). These rosettes consisted of immature retinal cells with adherens junctions and subapical regions positive for apical proteins such as MUPP1 and PATJ (Supplementary Material, Fig. S2D–F). Recoverin is a marker for immature as well as mature photoreceptors and some cone bipolar cells, and in regions where the adherens junctions were disrupted, recoverin-positive cells were displaced from the apical surface and localized ectopically in the centre of the neuroepithelial layer (Fig. 7B). Moreover, we observed an increase in the number of recoverin-positive cells in the *Crb2*Chx10 cKO compared with the control (24.0 ± 0.6 versus 21.9 ± 0.4 recoverin-positive cells/100 $\mu m \pm$ SEM; Supplementary Material, Fig. S3). In addition, we observed, near these rosettes, ectopic nuclei of cells in the subretinal space adjacent to the adherens junctions (Fig. 5D).

At P6, rosettes and half-rosette structures could also still be observed at the periphery of the retina. Interestingly, the rosettes contained cells positive as well as negative for the proliferation markers phospho-histone H3 (pH3), Ki67 and apical marker PATJ (which marks the apical membrane but also co-stains a subset of Ki67-positive cells at the periphery of the developing retina) (Fig. 8D). In addition, ectopic nuclei were detected in the subretinal space throughout the retina. These were situated both alone or in small clusters (Fig. 5F and 7D). Some of these nuclei were positive for recoverin but negative for rhodopsin (a marker for mature rod photoreceptors), and others were positive for both recoverin and rhodopsin (Fig. 7D). Transmission electron microscopy showed local loss of adherens junctions near these ectopic cells (Fig. 9B).

At P10, the outer limiting membrane was disrupted throughout the mutant retina. These disruptions lead to an increased number of ectopic nuclei residing in the subretinal space immediately adjacent to the retinal pigment epithelium (Fig. 5H and 7F and H; Supplementary Material, Fig. S4B). Most of these cell bodies were positive for recoverin (Fig. 7F) and rhodopsin (Fig. 7H). The ectopic photoreceptors in the subretinal space did not develop proper segments, implying that these cells were immature non-polarized

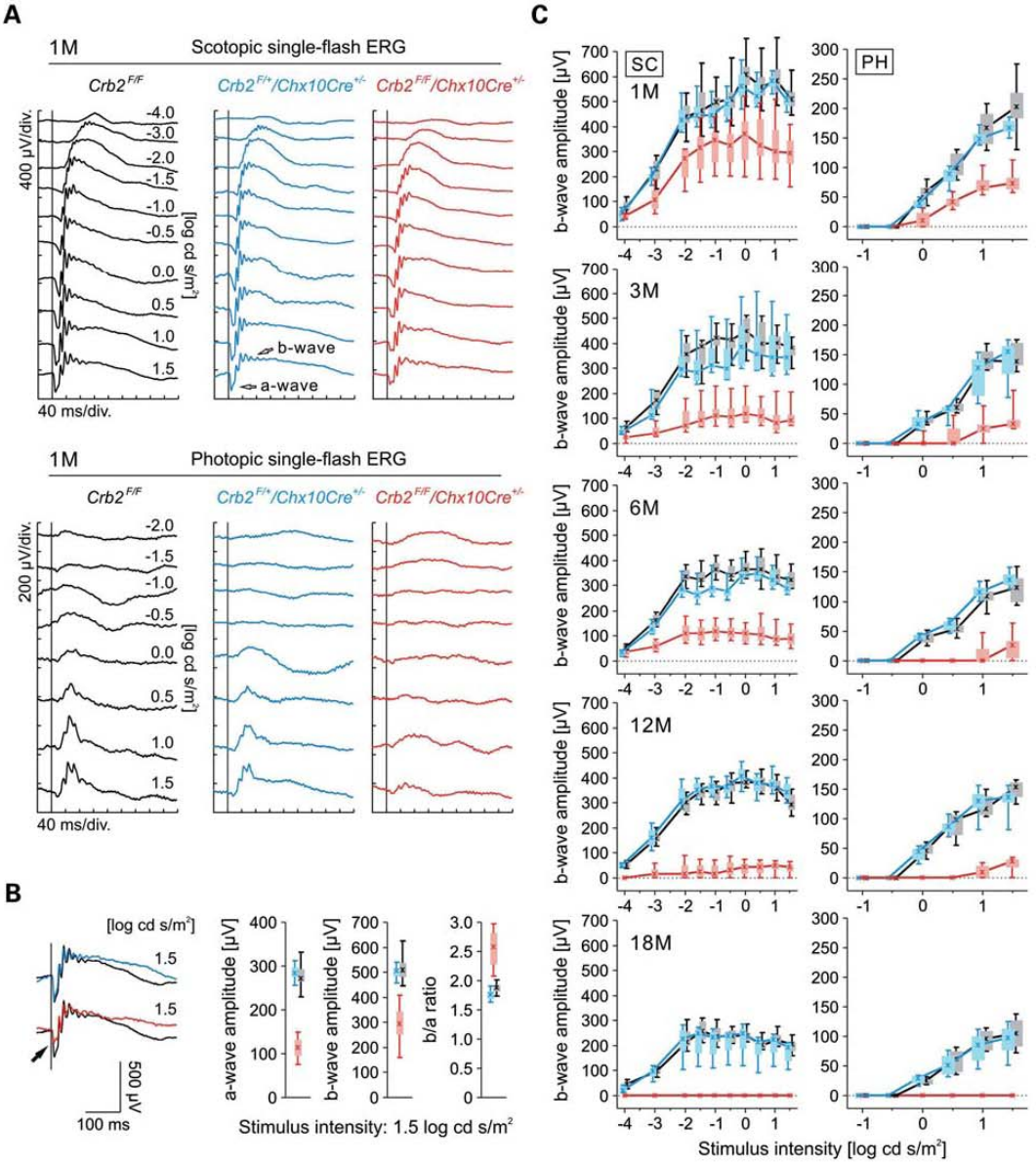

Figure 2. Progressive loss of retinal function in *Crb2*Chx10 cKO animals *in vivo*. Electroretinographic time course of retinal function in $Crb2^{F/F}$ control (black), $Crb2^{F/+}/Chx10Cre^{+/-}$ heterozygous (blue) and $Crb2^{F/F}/Chx10Cre^{+/-}$-affected mice (red). (**A**) Scotopic (top) and photopic (bottom) single-flash electroretinography responses from representative animals at the age of 1 month. The a-wave and the b-wave are indicated by open arrows. (**B**) Left: Superposition of scotopic single-flash electroretinography responses (1.5 log cd s/m^2) from (A). The arrow points to the attenuated a-wave of the affected mouse. Right: Quantitative evaluation of scotopic single-flash a-wave and b-wave amplitudes (1.5 log cd s/m^2) as well as the corresponding b-wave/a-wave amplitude ratio (b/a ratio). Boxes indicate the 25 and 75% quantile range, whiskers indicate the 5 and 95% quantiles and the asterisks indicate the median of the data (box-and-whisker plot). In affected $Crb2^{F/F}/Chx10Cre^{+/-}$ mice, the a-wave was relatively more attenuated than the b-wave, leading to a high b/a ratio and suggesting a predominant dysfunction of photoreceptors. (**C**) Time course of visual function based on single-flash electroretinography data from 1-, 3-, 6-, 12- and 18-month-old animals. For each age group, scotopic (SC, left column) and photopic (PH, right column) b-wave amplitude data are shown as box-and-whisker plot as above and were plotted as a function of the logarithm of the flash intensity (VlogI function). In affected $Crb2^{F/F}/Chx10Cre^{+/-}$ mice, the b-wave amplitude was already somewhat reduced at the age of 1 month under both scotopic and photopic conditions and declined rapidly with age. The retinal functionality of heterozygous $Crb2^{F/+}/Chx10Cre^{+/-}$ mice was not detectably decreased. Number of animals used: 1 month old (1 M): four/group; 3 months old (3 M): four of each control and five cKO; 6 months old (6 M): four $Crb2^{F/F}$, three $Crb2^{F/+}/Chx10Cre^{+/-}$ and seven cKO; 12 months old (12 M): five/group; 18 months old (18 M): four $Crb2^{F/F}$, three $Crb2^{F/+}/Chx10Cre^{+/-}$ and four cKO. ERG, electroretinography.

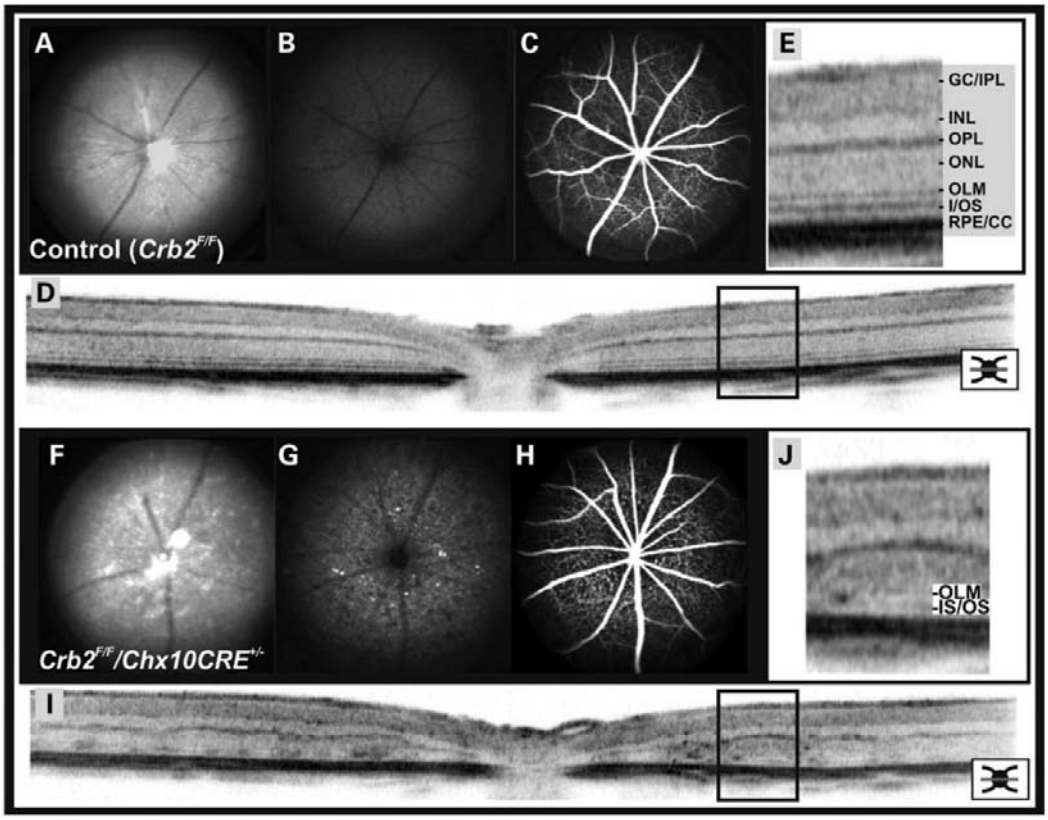

Figure 3. Retinal morphology in 1-month-old control and *Crb2*Chx10 cKO mice *in vivo*. *In vivo* imaging of the retinal phenotype in representative control ($Crb2^{F/F}$) and affected mice ($Crb2^{F/F}/Chx10Cre^{+/-}$) at 1 month after birth (1 M). Control and affected mouse retinae were examined with SLO imaging (**A** and **B** versus **F** and **G**), FLA (**C** versus **H**) and SD-OCT (**E** and **D** versus **J** and **I**). (A and F) Native fundus images at 513 nm revealed a spotty fundus appearance in the affected eye in comparison with the control, which imposed as multiple hyper- and hypofluorescences in the autofluorescence image (B and G) at 488 nm. (C and H) FLA, however, did not show apparent abnormalities of the choroidal and retinal vasculature at that point. (D and I) Horizontal spectral domain optical coherence tomography scans across the optic disc nevertheless revealed multiple indentations of the outer retina of affected eyes, presumably due to the cellular mislocalizations, disturbing retinal layering. Enlarged details (E and J) illustrate that between these indentations, intact-looking outer limiting membrane and inner/outer segment layers were detectable. GC/IPL, ganglion cell/inner plexiform layer; INL, inner nuclear layer; I/OS, inner/outer segment; OLM, outer limiting membrane; ONL, outer nuclear layer; OPL, outer plexiform layer; RPE/C, retinal pigment epithelium/choriocapillaris complex.

photoreceptors. Moreover, cone photoreceptors, stained for M-opsin (Fig. 7H and Supplementary Material, Fig. S5B–D) and cone arrestin (data not shown), were also affected and misplaced in the subretinal space. At the same stage, sporadic giant rosettes and half-rosettes in the outer nuclear layer were also observed, suggesting that there was a lack of adhesion between the cells (Supplementary Material, Fig. S4B). Transmission electron microscopy studies, performed on P10 retinas, showed disruption of the adherens junctions at the outer limiting membrane, and at these sites mislocalized photoreceptor cell nuclei were detected in the subretinal space (Fig. 9D). Furthermore, some of the cells showed polarity defects, as the segments were pointing towards the inner retina (Supplementary Material, Fig. S5C), or else were twisted (Supplementary Material, Fig. S5D) and organized in small half-rosettes around the remaining outer limiting membrane. In addition, several cone photoreceptors with abnormally long axons were detected, with axons extending from the outer plexiform layer into the ectopic nuclear layer (Supplementary Material, Fig. S5B). Ectopic PSD95 staining was detected in the photoreceptor cells misplaced in the subretinal space, suggesting the presence of ectopic synapses of these cells (data not shown). In P10 retinae, although there were no misplaced SOX9-positive cells observed in the *Crb2*Chx10 cKO (Supplementary Material, Fig. S6B), the number of Müller glia cells was 6% increased in the *Crb2*Chx10 cKO compared with the control (15.3 ± 0.2 versus 14.4 ± 0.3 SOX9-positive cells/100 μm ± SEM; Supplementary Material, Fig. S3).

Taken together, our data imply that CRB2 plays important roles in maintaining the adhesion, structural integrity, cell polarity, photoreceptor lamination, as well as controlling the differentiation of appropriate numbers of Müller glia cells and recoverin-positive cells.

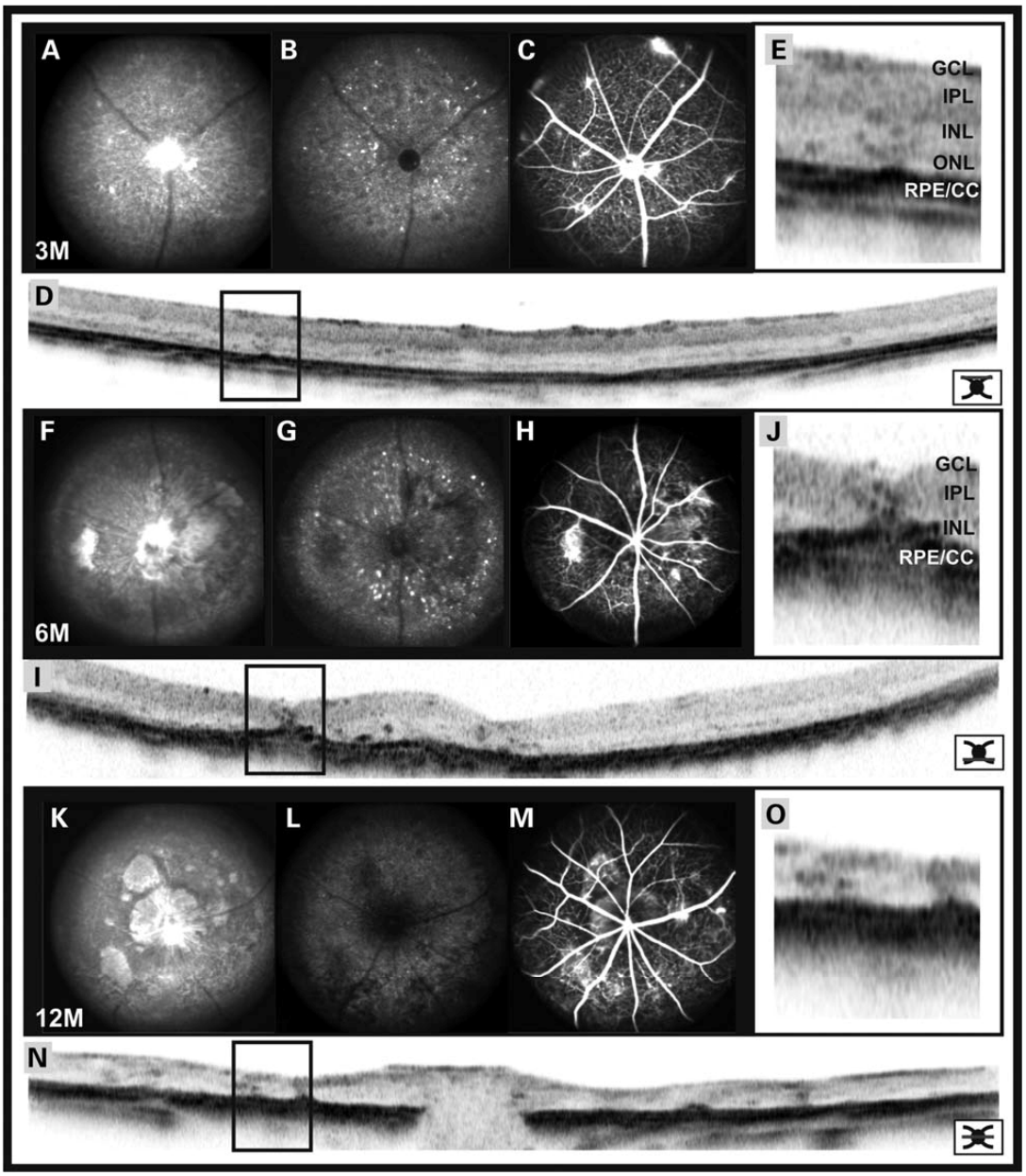

Figure 4. Progression of retinal changes in *Crb2*Chx10 cKO animals *in vivo*. Time course of retinal degeneration in representative affected mice ($Crb2^{F/F}$/$Chx10Cre^{+/-}$) up to 12 months after birth (12 M). Mouse retinae were examined with native scanning laser ophthalmoscopy imaging (**A**, **F** and **K**), fundus autofluorescence (**B**, **G** and **L**), FLA (**C**, **H** and **M**) and spectral domain optical coherence tomography (**D** and **E**, **J** and **I**, and **N** and **O**). Initially smaller, later increasingly confluent bright areas resembling retinal lesions became apparent in native imaging at 6 months (6 M) and older (F and K). Fundus autofluorescence (B, G and L) changed with age mainly in the regard that in the developing lesions described before, no fluorescence was detected, i.e. these areas remained dark. In FLA (C, H and M), sites of neovascularization developed, which were also detectable in spectral domain optical coherence tomography (D and E, J and I, and N and O). In addition, window effects led to an increased visibility of the lesion areas, particularly obvious in (M). A decrease in outer retinal thickness with disease progression was also apparent in spectral domain optical coherence tomography. GCL, ganglion cell layer; INL, inner nuclear layer; IPL, inner plexiform layer; ONL, outer nuclear layer; RPE/CC, retinal pigmented epithelium/choriocapillaris complex.

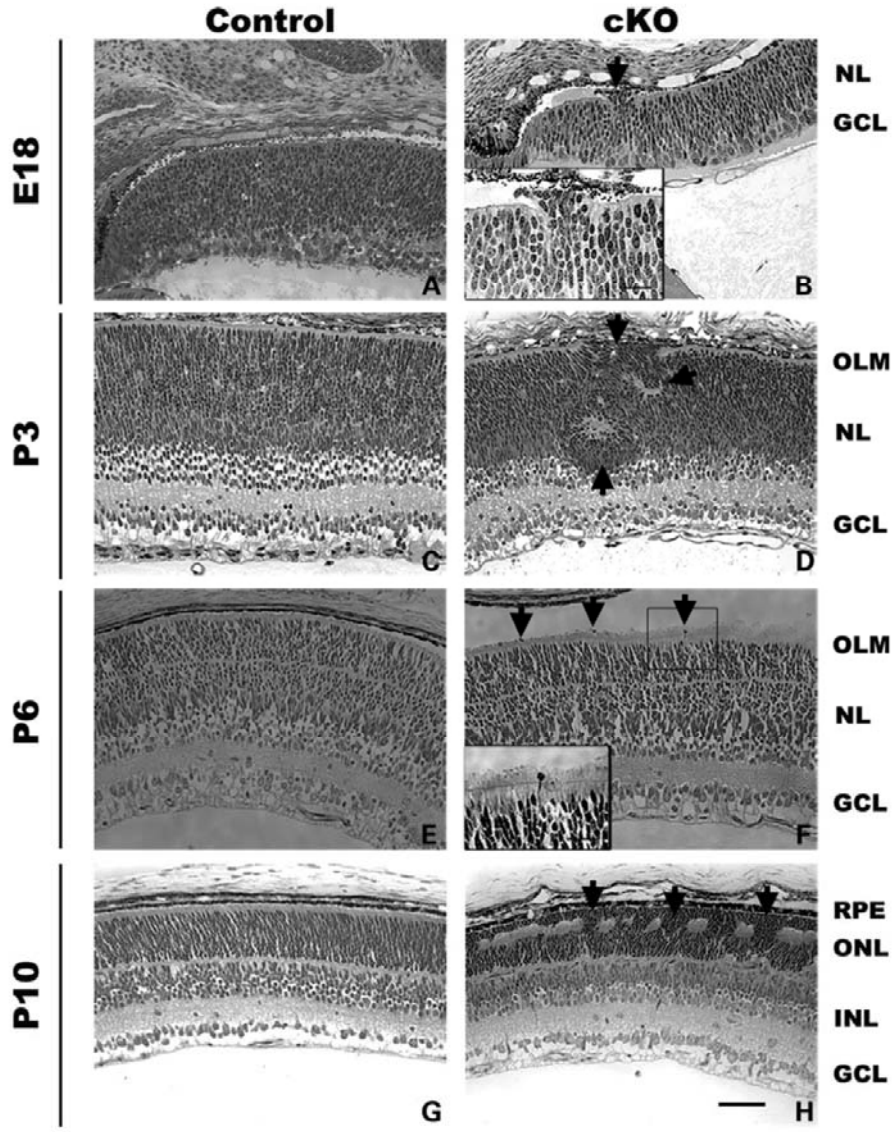

Figure 5. Loss of CRB2 results in retinal disorganization. Toluidine-stained light microscope pictures, of retina sections, from the control (**A**, **C**, **E** and **G**) and from the Crb2Chx10 cKO (**B**, **D**, **F** and **H**) at different ages: (A and B) E18; (C and D) P3; (E and F) P6; (G and H) P10. No abnormalities were observed in the control. At E18 (B) and P3 (D), gaps in the outer limiting membrane were sporadically observed in the neuroepithelial layer at the periphery. Moreover, at P3, it was also possible to detect rosettes in the neuroepithelial layer. At P6 (F), we observed some ectopic nuclei in the subretinal space. At P10 (H), a high number of nuclei were localized ectopically in the subretinal space. Disruption of the outer limiting membrane and ectopic nuclei are indicated by arrows. Scale bars: 50 μm in (A–H), and 20 μm in insets of (B) and (F). GCL, ganglion cell layer; INL, inner nuclear layer; NL, neuroepithelial layer; OLM, outer limiting membrane; ONL, outer nuclear layer; RPE, retinal pigment epithelium.

Lack of CRB2 results in progressive morphological deterioration in the adult retina

At 1 month of age, the *Crb2*Chx10 cKO retinae showed the presence of ectopic photoreceptor cell nuclei in the subretinal space and disruptions at the outer limiting membrane (Supplementary Material, Fig. S4D).

Retinal thickness gradually decreased with progressive age in the *Crb2*Chx10 cKO. This was especially apparent in the photoreceptor cell layer at the centre of the retina. At both 3

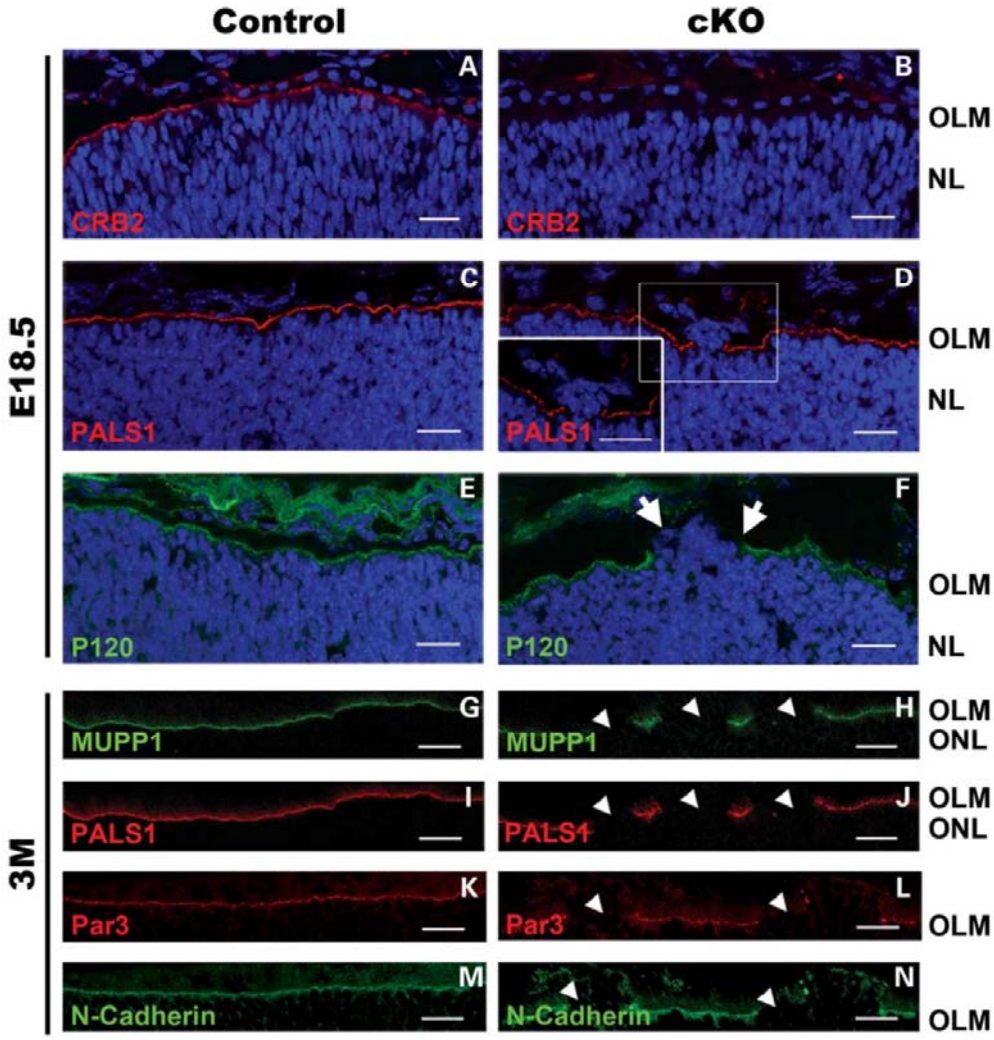

Figure 6. Lack of CRB2 leads to the disruption of the apical proteins. Immunohistochemistry pictures from the control (**A**, **C**, **E**, **G**, **I**, **K** and **M**) and from the *Crb2*Chx10 cKO (**B**, **D**, **F**, **H**, **J**, **L** and **N**) at different ages: (A–F) E18.5; (G–N) 3 months. Sections were stained with antibodies against: CRB2 (A and B), PALS1 (C, D, I and J), catenin pp120 (P120) (E and F), MUPP1 (G and H), PAR3 (K and L), N-cadherin (M and N). CRB2 was absent in the knockout retina (B), in contrast to control (A); however, it was possible to detect some signal, maybe due to cross-reactivity of the antibody with others Crumbs proteins. PALS1 and MUPP1 staining showed disruption of the Crumbs complex at the subapical region (D, H and J). PAR3 was also lost at sites of disruption (L). Staining using adherens junctions markers P120 (F) and N-cadherin (N) showed disruption of the adherens junctions. Moreover, it was also possible to visualize ectopic nuclei protruding into the subretinal space (arrows). No morphological changes were observed in the control retinae. NL, neuroepithelial layer; OLM, outer limiting membrane; ONL, outer nuclear layer. Scale bars: 20 μm.

and 6 months of age, we observed regions with several rows of photoreceptor cell nuclei protruding into the subretinal space, gaps in the outer limiting membrane and similarly protrusions of inner nuclear layer cells into the outer nuclear layer (Supplementary Material, Fig. S4F and H). We examined 3-month-old retinae in detail using immunohistochemistry. In control retinae, the Crumbs complex members MUPP1 and PALS1 (Fig. 6G and I) and CRB1 and PATJ (data not shown) stained the subapical region adjacent to the outer limiting membrane. In contrast, in *Crb2*Chx10 cKO retinae, the staining for subapical region proteins was absent in the regions with protrusions of photoreceptor nuclei into the subretinal space (Fig. 6H and J). Staining for markers of the adherens junctions at the outer limiting membrane (cadherins, β-catenin, catenin p120) and PAR3 gave similar results (Fig. 6L and N). The recoverin and rhodopsin staining indicated a clear decrease in the thickness of the *Crb2*Chx10 cKO outer nuclear layer and photoreceptor segments (Fig. 7J). Furthermore, the cone photoreceptor morphology was highly affected, with the loss of segments and incorrect

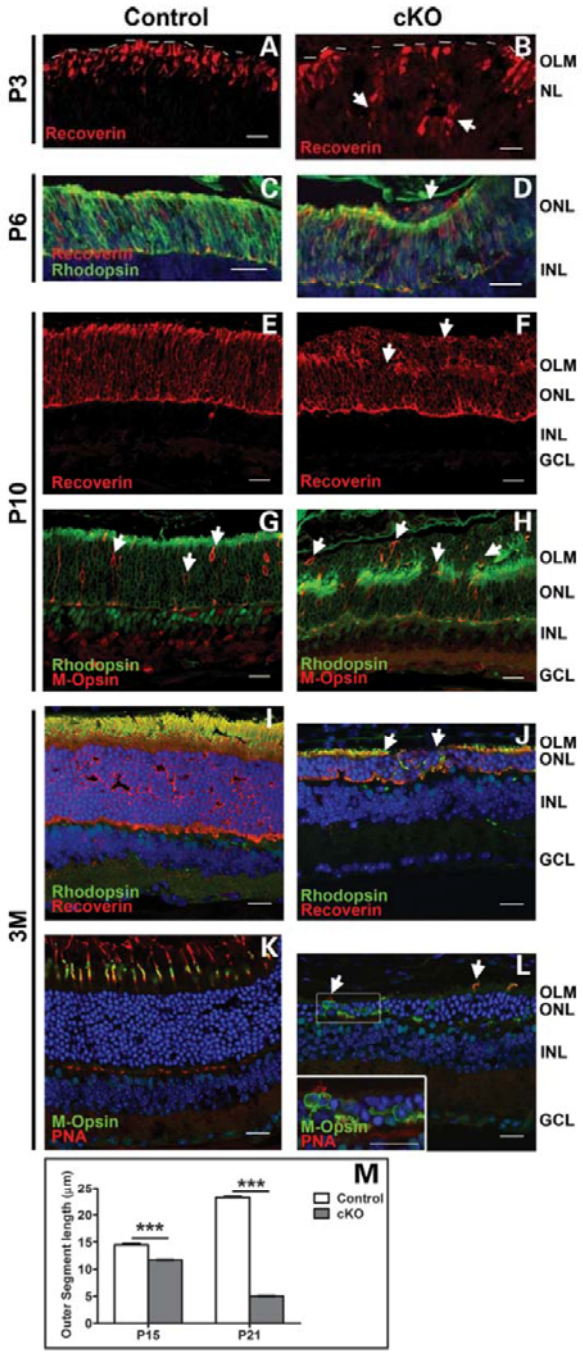

Figure 7. Loss of CRB2 affects lamination of photoreceptor cells and photoreceptor outer segment length. Immunohistochemistry pictures from mouse retinae with ages comprehended between P3 and 3 months (3 M). Retina sections of the control (**A**, **C**, **E**, **G**, **I** and **K**) and of the *Crb2*Chx10 cKO (**B**, **D**, **F**, **H**, **J** and **L**) at the different time points: (A and B) P3; (C and D) P6; (E, F, G and H) P10; (I, J, K and L) 3 months. Sections were stained with antibodies against: recoverin (A and B, E and F), recoverin and rhodopsin (C and D, I and J), rhodopsin and M-opsin (G and H), M-opsin and peanut agglutinin (K and L). At P3 and P6, the knockout retinae presented disorganization of the photoreceptor cells, stained with recoverin (B and D). Close to the periphery, we could detect photoreceptors, rosettes and half-rosettes in the neuroepithelial layer (B, arrows). Ectopic nuclei could be found in the subretinal space at P6. Some of these cells were recoverin-positive but rhodopsin-negative, a mature rod photoreceptor marker (D, arrow). At P10, most of the nuclei localized in the subretinal space were positive for recoverin (F) and rhodopsin (H). However, some of these nuclei were M-opsin-positive, showing that also cone photoreceptors were misplaced (H, arrows). At 3 months of age, the photoreceptor layer of the *Crb2*Chx10 cKO retinae was reduced to few nuclei in a row when stained with recoverin (J). Rhodopsin is normally localized in the outer segments of the photoreceptors (I), but in the knockout retinae besides the reduced length of the segments, it is possible to detect some ectopic cytoplasmic localization of this protein (J). In the control, anti-M-opsin and peanut agglutinin stain mainly the segments of the photoreceptors (K); however, in the knockout retinae, the cones are heavily affected, especially their segments, with ectopic localization of the M-opsins in the cell bodies (L, inset). No morphological changes were observed in the control retinae. (M) Histogram showing the length of cone outer segments in the retinae from littermate control (white bars) and *Crb2*Chx10 cKO (grey bars) retinae at P15 and P21. The peanut agglutinin-stained cone outer segments in the central region were measured to verify the involvement of CRB2 in the growth and maintenance of cone outer segments; significant differences were found at P15 (control = 3 mice, $n = 320$; cKO = 3 mice, $n = 352$) and P21 (control = 3 mice, $n = 606$; cKO = 3 mice, $n = 472$). Asterisks indicate a significant difference compared with the control (Student's *t*-test). Error bars indicate ± SEM. INL, inner nuclear layer; GCL, ganglion cell layer; NL, neuroepithelial layer; OLM, outer limiting membrane; ONL, outer nuclear layer. Scale bars: 20 μm.

expression of S- and M-opsins in the cell soma (Fig. 7L and Supplementary Material, Fig. S5H). Despite this severe phenotype, the cone photoreceptors survived in *Crb2*Chx10 cKO retinae, even in areas where only few photoreceptor nuclei remained.

Throughout the 3-month-old *Crb2*Chx10 cKO retina, we observed an increase in GFAP expression (a marker of intermediate filaments in Müller glia cells; Fig. 10D and F). Abnormal expression of SOX9 and glutamine synthetase in the mutant outer nuclear layer indicated the presence of ectopic Müller glia cell nuclei in this region (Fig. 10H). These cells were negative for the proliferation marker pH3 (data not shown). Interestingly, at this age, we also observed an increase of 12% in the total number of SOX9-positive cells in the *Crb2*Chx10 cKO compared with the control (17.6 ± 0.5 versus 15.5 ± 0.5 SOX9-positive cells/100 μm ± SEM; Supplementary Material, Fig. S3).

In *Crb2*Chx10 cKO retina, we observed a marked increase in CD45 and CD11b expression, two microglia cell markers (Supplementary Material, Fig. S6D and F). This expression extended into the outer retinal layers. MPP4 is present at the synapses of photoreceptors, and at lower levels at the outer limiting membrane; in control retinae, it is expressed in a continuous band at the outer limiting membrane and outer plexiform layer (Supplementary Material, Fig. S6G) (15). In the *Crb2*Chx10 cKO retinae, the outer plexiform layer was thinner and MPP4 staining was disrupted (Supplementary Material, Fig. S6H). The synapses of the photoreceptor cone cells appeared less well defined when stained with peanut agglutinin (Fig. 7L and Supplementary Material, Fig. S5H) and anti-cone arrestin (Supplementary Material, Fig. S5F).

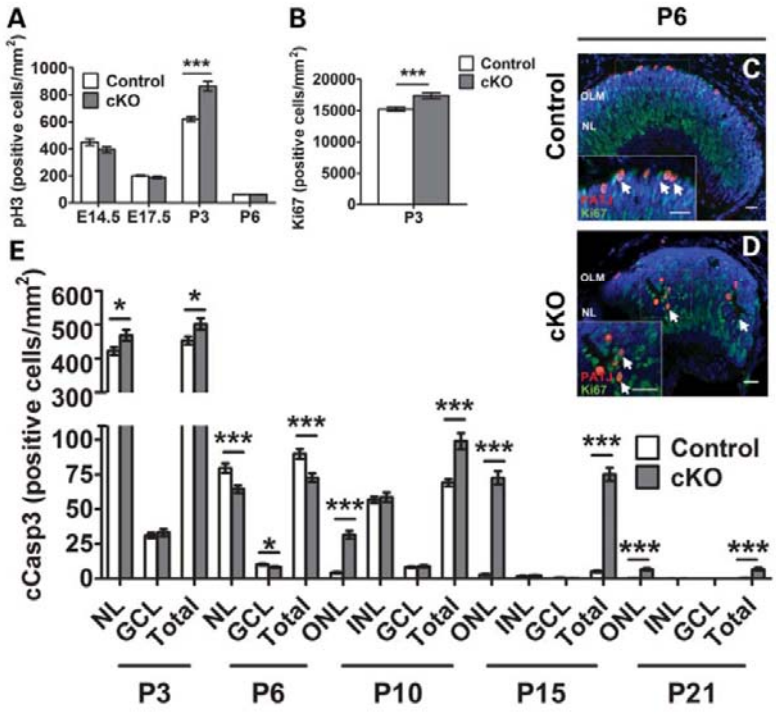

Figure 8. Loss of CRB2 affects timing of apoptosis and mitosis. (**A**) Histogram depicting the number of pH3-positive cells per square millimetre, in control and *Crb2*Chx10 cKO retinae, at E14.5 (control = 3 mice, cKO = 4 mice; $n = 31$ and $n = 26$, respectively), E17.5 (4 mice/group; $n = 118$ and $n = 93$, respectively), P3 (control = 4 mice, cKO = 3 mice; $n = 118$ and $n = 92$, respectively) and P6 (control = 3 mice, cKO = 4 mice; $n = 97$ and $n = 100$, respectively). Error bars indicate ± SEM. (**B**) Histogram depicting the number of Ki67-positive cells per square millimetre, in control and *Crb2*Chx10 cKO retinae, at P3 (3 mice/group; $n = 29$ and $n = 29$, respectively). Error bars indicate ± SEM. (**C** and **D**) Immunohistochemistry pictures from P6 mouse retinae. Retina sections of the control (C) and of the *Crb2*Chx10 cKO (D) were stained with antibodies against Ki67 and PATJ (C and D). In the knockout retina (D), misplaced Ki67-positive mitotic cells were detected. The apical marker PATJ co-stains a subset of Ki67-positive cells at the periphery of the developing retina. Scale bars: 20 μm. (**E**) Histogram depicting the number of cCasp3-positive cells, a marker for apoptosis, per square millimetre, in control and *Crb2*Chx10 cKO retinae at P3 (3 mice/group; $n = 31$ and $n = 26$, respectively), P6 (control = 3 mice, cKO = 4 mice; $n = 75$ and $n = 87$, respectively), P10 (3 mice/group; $n = 80$ and $n = 70$, respectively), P15 (3 mice/group; $n = 30$ and $n = 45$, respectively) and P21 (control = 3 mice, cKO = 4 mice; $n = 62$ and $n = 45$, respectively). Asterisks indicate a significant difference compared with the control. Student's *t*-test for P3, Mann–Whitney *U* test for P6, P10, P15 and P21. Error bars indicate ± SEM. GCL, ganglion cell layer; INL, inner nuclear layer; NL, neuroepithelial layer; OLM, outer limiting membrane; ONL, outer nuclear layer.

The morphology and location of the bipolar cells were also affected in the *Crb2*Chx10 cKO. In adult Chx10-*Cre* retinae, the Cre protein is fused with EGFP and can be detected in the nuclei of some bipolar cells (28). Using this, we could observe misplaced *Crb2*Chx10 cKO bipolar cell nuclei in the outer nuclear layer. At 3 months of age, PKCα expression indicated that these cells showed fewer dendrites (Supplementary Material, Fig. S6H). Nevertheless, in some areas in the *Crb2*Chx10 cKO retinae, we observed long dendritic projections almost up to the outer limiting membrane (data not shown). The tip of the ectopic dendrites colocalized with MPP4 expression, suggesting ectopic photoreceptor-bipolar cell synapses (data not shown). Other inner retinal cells, such as calretinin-positive amacrine cells, showed normal localization at 3 months of age (Supplementary Material, Fig. S6J).

In contrast to earlier time points, by 12 and 18 months of age the entire *Crb2*Chx10 cKO retina was affected (Supplementary Material, Fig. S4J and L). Very few photoreceptor cells remained. Large and numerous retinal blood vessels were detected. The retinal pigment epithelium was also affected; in some areas, the epithelium was disrupted and protruded into the retina.

Loss of CRB2 affects progenitor proliferation, rod photoreceptor apoptosis and cone photoreceptor outer segment size

To study whether CRB2 plays a role in determining the length of photoreceptor outer segments, we quantified the length of cone photoreceptor outer segments, marked with peanut agglutinin (a marker for the outer segments and pedicles of cone photoreceptors). In *Crb2*Chx10 cKO retinae, we observed shorter cone outer segments at P15 (11.7 ± 0.3 μm compared with the control 14.5 ± 0.2 μm ± SEM) and P21 (5 ± 0.2 μm compared with the control 23.2 ± 0.3 μm ± SEM) (Fig. 7M), suggesting that CRB2 may play a role in determining the length of cone photoreceptor outer segments.

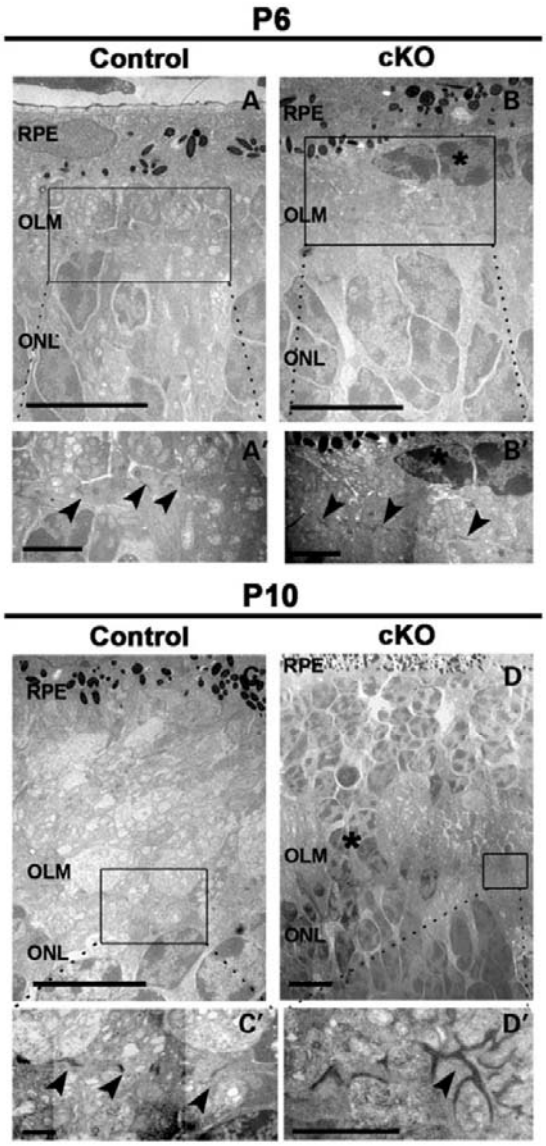

Figure 9. Loss of CRB2 results in the disruption of the adherens junctions. Transmission electron microscopy pictures of retinae sections, from the control (**A** and **C**) and from the *Crb2*Chx10 cKO (**B** and **D**), at different ages: (A and B) P6; (C and D) P10. No abnormalities were observed in the control. At P6 in the *Crb2*Chx10 cKO retinas, ectopic nuclei (asterisk) located in the subretinal space were observed (B). Disruption in the adherens junctions were observed at the level of the ectopic nuclei (**B′**). At P10, a high number of nuclei were localized ectopically in the subretinal space (D, asterisk), and clusters of the adherens junctions were also observed (**D′**). Scale bars in (A–D): 7.5 μm, and in (**A′–D′**): 2.5 μm. OLM, outer limiting membrane; ONL, outer nuclear layer; RPE, retinal pigment epithelium.

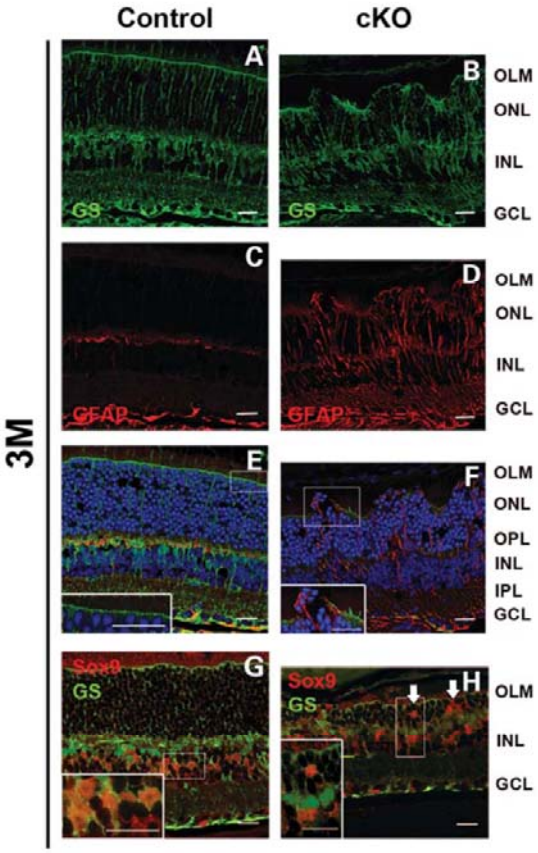

Figure 10. Lack of CRB2 results in retinal gliosis. Immunohistochemistry pictures of 3-month-old retina sections. Sections from the control (**A**, **C**, E and F) and from the *Crb2*Chx10 cKO (**B**, **D**, F and **H**) were stained with antibodies against: glutamine synthetase (GS) (A and B), glial fibrillary acidic protein (GFAP) (C and D), GS and GFAP (merged) (E and F), GS and SOX9 (**G** and H). The *Crb2*Chx10 cKO retinae showed activated Müller glia cells, detected by an increase in the GFAP staining (D and F). Some nuclei of the Müller glia cells were mislocalized in the outer nuclear layer (H). GCL, ganglion cell layer; INL, inner nuclear layer; IPL, inner plexiform layer; OLM, outer limiting membrane; ONL, outer nuclear layer; OPL, outer plexiform layer. Scale bars: 20 μm.

The number of pH3- and Ki67-positive cells was significantly increased at P3 in the *Crb2*Chx10 cKO retinae compared with the controls (Fig. 8A and B). However, no difference in the number of pH3-positive cells was detected at E14.5, E17.5 or P6, implying that the presence of CRB2 is required to control the proliferation of late-born progenitor cells around the peak of birth of Müller glia cells, rods and bipolar cells.

Programmed cell death, detected by the number of cleaved caspase-3 (cCasp3)-positive cells, was significantly higher in *Crb2*Chx10 cKO retinae at P3, P10, P15 and P21 but not at P6, where a decrease in apoptosis is observed (Fig. 8E). The decrease in apoptosis, at P6, may reflect a shift in the apoptosis timing or an increase in cell survival at this time point. Interestingly, increased apoptosis affected only cells in the photoreceptor layer and not in the inner nuclear layer or ganglion cell layer. In the mutant retina, the peak in the number of

apoptotic cells occurred around P15, where a 10-fold increase of apoptotic cells was observed. At P10 and P15, the number of apoptotic rod photoreceptors was equally divided between ectopic and correctly localized cells.

DISCUSSION

Our key findings are that retinal CRB2 is required for: (i) correct expression and/or localization of apical complex and adherens junction proteins, (ii) proper lamination of photoreceptor cells, and (iii) suppression of birth of late-born progenitor cells. Moreover, in addition to these late developmental defects, the adult *Crb2*Chx10 cKO retina undergoes progressive rod photoreceptor degeneration with associated loss of retinal function that mimics retinitis pigmentosa due to mutations in the *CRB1* gene.

We have shown that CRB2 colocalizes with other apical marker proteins in the retina. Depletion of CRB2 resulted in the loss of other apical and some adherens junction protein markers, suggesting that reduction in CRB2 levels leads to the destabilization of the whole CRB complex and its interacting complexes. Our observation is therefore consistent with the epithelial polarity and adhesion defects seen in both the *Drosophila Crb* mutant and the zebrafish *Crb2a* (*ome*) mutant (9,11,21). However, in the *Crb2*Chx10 cKO retina, the phenotype did affect the late but not the early retinal neuroepithelium despite the fact that CRB2 has been lost throughout. Our results are also partially in consonance with the phenotype detected in mice with reduced retinal levels of PALS1, a CRB interacting protein, as both show retinal degeneration affecting lamination of the photoreceptor layer (4,6). In the retinal neuroepithelium, the absence of CRB2 results in inappropriate numbers of Müller glia cells and rod photoreceptor cells, with many of the latter appearing to remain with an immature expression profile for longer than in controls. Interestingly, these retinal cell types are the ones born last from a retinal precursor that experiences a changing micro-environment (31). We found that there was a significant increase in pH3- and Ki67-positive cells at P3. This would correlate approximately with the time when the cells may be undergoing their last symmetric post-mitotic cell division (32). This suggests that CRB2 inhibits retinal progenitor proliferation in the late developing retina.

In the developing retina, we found that the loss of CRB2 during retinal development results in ectopic Ki67/PATJ-positive cells and displaced recoverin-positive photoreceptor cells. Ectopic *Crb2*Chx10 cKO bipolar cell and Müller glia cell nuclei were also apparent in the outer nuclear layer at 3 months of age. The lamination of earlier born progenitor, ganglion, horizontal, amacrine cells and Müller glia cells was not affected. Furthermore, the lamination defects seem to affect mainly late-born retinal progenitors, rod and, to some extent, cone photoreceptors and bipolar cells, suggesting a lack of adhesion between these cells. This is consistent with data that show a role for zebrafish Crb2a in retinal cell patterning and lamination (26). Moreover, reduced levels of PALS1, in mouse retinae, affected the correct patterning of newly born retinal cells, especially photoreceptors (4,6).

Zebrafish Crb2 interacts directly with the extracellular domain of Notch and inhibits its activity. Further data suggest that the zebrafish CRB–Moe complex and Notch play key roles in a positive feedback loop to maintain apicobasal polarity and the apical-high–basal-low gradient of Notch activity in neuroepithelial cells (33). For mammals, this will be further explored in forthcoming experiments.

It has been suggested that Crumbs proteins play a role in determining the length of the photoreceptor cell segments. Our data show that the loss of CRB2 results in shorter cone photoreceptor outer segments, consistent with the roles of zebrafish Crb2b in cone photoreceptors (11), of *Drosophila* Crb in determining the length of the stalk membrane, which is the functional equivalent of vertebrate inner segments (9) and of mouse CRB1 in determining the length of the apical villi of Müller glia cells (3).

The retinae of Leber congenital amaurosis patients with *CRB1* mutations are relatively thick and resemble the immature retina, suggesting a disturbance in normal development (34,35). To date, no mutations in *CRB2* or *CRB3* have been associated with retinal degeneration. However, it cannot be excluded that some sequence variants may contribute to retinal disease (36). Our previous results showed that *Crb1* $^{-/-}$ mouse retinae develop localized lesions, particularly in the inferior temporal quadrant of the mouse eye, after retinal development (3). *Crb2*Chx10 cKO mice developed early disorganization and degeneration throughout the entire retina during late retinal development, suggesting that CRB2 is required for proper lamination of the entire photoreceptor layer. Mice lacking functional CRB1 do not become blind, and since there may be functional redundancy between CRB family members (1–3,8,11,35), *Crb2* and *Crb1Crb2* double-cKO mice may become valuable in functionally testing *CRB1* gene therapy vectors *in vivo*.

MATERIALS AND METHODS

Animals

All procedures concerning animals were performed with the permission of the animal experimentation committee (DEC) of the Royal Netherlands Academy of Arts and Sciences (KNAW) (permit number NIN06–46). All mice used were maintained on a 50% C57BL/6JOlaHsd and 50% 129/Ola genetic background. Animals were maintained on a 12 h day/night cycle and supplied with food and water *ad libitum*.

Generation of the *Crb2* cKO mouse

Using recombineering in bacterial artificial chromosomes (BACs) and *Cre/loxP* technology (37), we generated a conditional gene targeting construct for *Crb2*. Details are available upon request. In short, a 3′ *loxP* site was inserted in exon 13 downstream the stop codon in the 3′ untranslated region of *Crb2*. A neomycin cassette flanked by *frt* recombination sites and a 5′ *loxP* site was inserted in intron 9 downstream exon 9a. The targeting vector was released from the BAC into a plasmid using homologous recombineering. The *Crb2* gene is expressed from two different promoters that are far apart (unpublished data); therefore, the *Crb2* targeting vector

has been designed to put *loxP* recombination sites around the last four coding exons (10–13) of the gene that encode the CRB2 transmembrane domain and the 37 amino acids of the C-terminal intracellular domain. Cre-mediated recombination deleted coding exons 10–13 and resulted in a nonsense mutation with premature truncation of CRB2 protein at amino acid 871. The Cre recombination therefore removed both the transmembrane domain and the highly conserved 37 amino acids intracellular domain that contains the functionally significant FERM and PDZ protein-binding motifs. The function of the *loxP* and *frt* recombination sites was tested by expression of the floxed *Crb2* targeting vector in bacterial cells expressing CRE or FLP recombinases. The targeting vector was used to generate $Crb2^{F/+}$ mouse 129 E14 embryonic stem cells by homologous recombination. The $Crb2^{F/+}$ cKO mice were generated by blastocyst injections of $Crb2^{F/+}$ embryonic stem cells. Chimeric mice gave germ-line transmission, then the neomycin cassette was successfully removed by crossing the $Crb2^{F/+}$ mice with a transgenic mouse that expressed FLP recombinase in the germ line (129S4/SvJaeSor-t(ROSA)26Sortm1(*FLP1*)Dym/J mice; Jackson Laboratory). Two $Crb2^{F/+}$ mouse lines were generated from two independent embryonic stem cell clones; these lines were designated P1E9 and P11D6. The two lines gave identical phenotypes.

Genotyping was performed by Southern blotting, long-distance PCR and PCR. For Southern blotting, *Bgl*II-digested genomic DNA was transferred to Hybond N+ membrane (GE Healthcare, Germany), UV-crosslinked and hybridized to radiolabelled probes. PCR genotyping of mice was performed using primers flanking the *loxP* sites. The cKO mice were crossed with Chx10-*Cre* (Jackson Laboratory) expressing CRE recombinase in the developing neuroepithelium of the retina (28).

Chromosomal DNA isolation and genotyping

Ear biopsies were incubated in lysis buffer (50 mM Tris, pH 8.0, 100 mM NaCl, 1% SDS) with Proteinase K (0.5 mg/ml) at 55°C for 16 h. The isopropanol precipitated chromosomal DNA was washed with 80% ethanol and rehydrated in TE buffer. The localization of the primers used to genotype the targeting construct is represented in Figure 1. Two different pair of primers were used to genotype the transgenic floxed offspring via PCR using genomic DNA extracted from biopsies: HA7 forward 5′-TGCATCTTCTGAGATCAGGTG-3′, HA8 reverse 5′-ACCTGCCAGACTTCTCCTAC-3′ (*Δfrt*) [*Δfrt*: 303 base pairs (bp)/wild-type (WT): 106 bp], HA11 forward 5′-TGGAGATGGACAGTGTCCTC-3′, HA12 reverse 5′-GCTCTGGAAACAGTCTCCTTG-3′ (*LoxP*) (Flox: 217 bp/WT: 185 bp). To analyse the presence of the *flp* recombinase, the following primers were used: FLP (transgenic) forward 5′-CACTGATATTGTAAGTAGTTTGC-3′, reverse 5′-CTA GTGCGAAGTAGTGATCAGG-3′ (product size 725 bp), FLP (WT) forward 5′-GGAAAATGCCAATGCTCTGT-3′, reverse 5′-ACGTTTCCGACTTGAGTTGC-3′ (product size 835 bp). The presence of the neomycin cassette was analysed using the following primers: forward 5′-CGGACAGGTC GGTCTTGACA-3′ and reverse 5′-TGAGCCTGGCGAACA GTTCG-3′ (product size 380 bp). The following primers were used to detect the transgenic *Cre* expression: Chx10-*Cre* forward 5′-GGGCACCTGGGACCAACTTCACGA-3′, reverse 5′-CGGCGGCGGTCACGAACTCC-3′ (product size 750 bp).

In vivo analysis

Scanning laser ophthalmoscopy, spectral domain optical coherence tomography and electroretinography measurements were performed in animals groups of 1, 3, 6, 12 and 18 month(s). The groups were composed of four to six animals of each genotype: controls ($Crb2^{F/F}$ and $Crb2^{F/+}/Chx10Cre^{+/}$) and *Crb2*Chx10 cKO ($Crb2^{F/F}/Chx10Cre^{+/}$).

Electroretinographic analysis

Electroretinograms were performed according to previously described procedures (38). The electroretinography equipment consisted of a Ganzfeld bowl, a direct current amplifier and a PC-based control and recording unit (Multiliner Vision). Animals were dark-adapted overnight and anaesthetized with ketamine (66.7 mg/kg body weight) and xylazine (11.7 mg/kg body weight). Pupils were dilated with tropicamide eye drops (Mydriaticum Stulln, Pharma Stulln, Stulln, Germany). Single-flash responses were obtained under dark-adapted (scotopic) and light-adapted (photopic) conditions. Light adaptation was accomplished with a background illumination of 30 candela (cd) per square metre, starting 10 min before photopic recordings. Single white-flash stimuli ranged from −4 to 1.5 log cd s/m^2 under scotopic and from −2 to 1.5 log cd s/m^2 under photopic conditions. Ten responses were averaged with inter-stimulus intervals of 5 s (for −4 to −0.5 log cd s/m^2) or 17 s (for 0–1.5 log cd s/m^2).

Scanning laser ophthalmoscopy and angiography

Retinal structures of the anaesthetized animals were visualized via scanning laser ophthalmoscopy imaging with HRA 1 and HRA 2 (Heidelberg Engineering, Heidelberg, Germany), according to previously described procedures (39). Briefly, HRA 1 and HRA 2 systems feature two lasers (488/514 nm) in the short (visible) wavelength range and two (795/830 nm and 785/815 nm) in the long (infrared) wavelength range. The 488 and 795 nm lasers are used for FLA and indocyanine green angiography, respectively.

Spectral domain optical coherence tomography

Spectral domain optical coherence tomography imaging was done in the same session as scanning laser ophthalmoscopy and it was performed with a commercially available Spectralis™ HRA + OCT device from Heidelberg Engineering, featuring a broadband superluminescent diode at $\lambda =$ 870 nm as a low-coherent light source (40). Each two-dimensional B-Scan recorded with the equipment set to 30° field of view consists of 1536 A-scans acquired at a speed of 40 000 scans per second. Optical depth resolution is ∼7 μm, with digital resolution reaching 3.5 μm. Imaging was performed using the proprietary software package Eye Explorer (version 3.2.1.0, Heidelberg Engineering).

Morphological and immunohistochemical analyses

Eyes were collected at different time points: E11.5, E12.5, E14.5, E16.5, E17.5, E18.5; P3, P6, P10, P15, P21; 1-, 3-, 6-, 12- and 18-month-old mice ($n = 3–6$/age group). For morphological analysis, eyes were enucleated and fixed at room temperature with 4% paraformaldehyde in PBS for 20 min. After fixation, the eyes were dehydrated for 30 min in 30, 50, 70, 90 and 96% ethanol and embedded in Technovit 7100 (Kulzer, Wehrheim, Germany), according to the manufacturer's instructions and sectioned (3 μm). Slides were dried, counterstained with 0.5% toluidine blue and mounted under cover slips, using Entellan (Merk, Darmstadt, Germany). For immunohistochemical analysis, eyes from the animals were enucleated and fixed during 20 min in 4% paraformaldehyde in PBS. Subsequently, the tissues were cryoprotected with 30% sucrose in PBS, embedded in Tissue-Tek O.C.T. Compound (Sakura, Finetek) and used for cryosectioning. Cryosections (7 μm) were rehydrated in PBS. For Ki67 stainings, heat-mediated antigen retrieval was performed before the blocking step, sections were boiled at 95–100°C for 2 min in 10 mM sodium citrate buffer with 0.05% Tween-20, pH 6.0, and allowed to cool down for 30 min. Samples were blocked for 1 h using 10% goat or donkey serum, 0.4% Triton X-100 and 1% bovine serum albumin (BSA) in PBS. The following primary antibodies were used: β-catenin (1:100; BD Biosciences), catenin pp120 (P120) (1:100; BD Biosciences), N-cadherin (1:100, BD Biosciences), calretinin (1:500, Chemicon), APC-conjugated CD11b (1:100; eBioscience), PE-conjugated CD45 (1:100; Emeelca), cCasp3 (1:250; Cell Signaling), cone arrestin (1:500, Millipore), CRB1 (AK2, 1:100), CRB2 (SK11; 1:700, obtained from P.R.), glial fibrilliary acidic protein (GFAP) (1:200; Dako), glutamine synthetase (1:200; BD Biosciences), Ki67 (1:50, BD Biosciences), M-opsin (1:250; Chemicon), S-opsin (1:250; Chemicon), PALS1 (1:1000; Proteintech), PAR3 (1:100, Upstate), PATJ (1:250, obtained from A.L.B.), PAX6 (1:100; Developmental Studies Hybridoma Bank), rhodamine peanut agglutinin (1:150; Vector Lab), pH3 (1:500; Millipore), PKCα (1:200; BD Biosciences), PSD-95 (1:200, Cell Signaling), recoverin (1:500; Chemicon), rhodopsin (1:250; Millipore), MPP4 (AK4, 1:300), MUPP1 (1:200; BD Biosciences), SOX9 (1:250, Millipore). The primary antibodies were diluted in 0.3% goat or donkey serum, 0.4% Triton X-100 and 1% BSA in PBS and incubated for 16 h at 4°C. Fluorescent-labelled secondary antibodies, donkey anti-chicken, goat anti-mouse or goat anti-rabbit IgGs conjugated to Cy3, Alexa 488 or Alexa 555 (1:500; Jackson ImmunoResearch, Stanford, CA, USA, and Invitrogen), were diluted in 0.1% goat or donkey serum in PBS and incubated for 1 h at room temperature. Nuclei were counterstained using the DNA dye TO-PRO-3 iodine (Invitrogen) at 1 μM. Sections were mounted under cover slips using Mowiol 4–88 (Sigma-Aldrich) to prevent fading of fluorescence. Sections were imaged on a Zeiss 510 confocal laser scanning microscope (CLSM) or on a Leica SP5 CLSM. Confocal images were processed with Adobe Photoshop CS4 extended v11.0.1.

Transmission electron microscopy

Mice of 6 and 10 days of age were perfused with 4% paraformaldehyde, 2% glutaraldehyde in 0.1 M cacodylate buffer, pH 7.4. The eyes were opened along the ora serrata. The cornea, lens and vitreous body were removed. After the retinae were dissected free, they were post-fixed for 1 h in 1% osmium tetroxide in the same buffer. Tissues were abundantly rinsed with the buffer and stained with 2% uranyl acetate in 70% ethanol for 1 h. Samples were then dehydrated in a graded series of ethanol and embedded in Epon 812 (Polysciences, Eppelheim, Germany). Ultrathin sections were examined with a Zeiss 912 electron microscope (Zeiss).

Quantification of apoptotic, mitotic and retina cells

Retina sections (P3, P6, P10, P15 and P21) were stained with cCasp3 antibody to quantify the number of apoptotic cells. To quantify the number of mitotic cells, retina sections (E14.5, E17.5, P3 and P6) were stained with pH3 antibody. The number of proliferating cells at P3 was quantified using Ki67 staining. To study defects in late-born cell specification, the number of photoreceptor cells, Müller glia cells and bipolar cells was quantified at different time points using specific antibodies. To count photoreceptor cells, a recoverin antibody was used at P3. Müller glia cells were counted at P10 and 3 M using a SOX9 antibody. Bipolar cells were counted at 3 M using a PKCα antibody. Ten to 20 retina sections from three to six different *Crb2*Chx10 cKO and control mice were used. Retina sections were counterstained and mounted with Vectashield Hard-Set Mounting Medium with DAPI (H1500, Vector Laboratories). The total number of cells was determined by manually counting the positive cells, and digital images were generated by a Leica epifluorescence microscope (DMRD), using the LAS AF v2.4.1 software (n represents the number of individual sections).

Quantification of the cone photoreceptor outer segment length

Retina sections (P15 and P21) were stained with rhodamine-conjugated peanut agglutinin to quantify the length of the cone photoreceptor outer segments. Representative sections from different animals (three animals per group) were counterstained and mounted with Vectashield Hard-Set Mounting Medium with DAPI (H1500, Vector Laboratories). Digital images were generated by a Leica epifluorescence microscope (DMRD), using the LAS AF v2.4.1 software. The ImageJ software v1.45 was used to quantify the length of the outer segments (n represents the number of individual outer segments measured).

Statistical analysis

Normality of the distribution was tested by the Kolmogorov–Smirnov test. Statistical analysis was performed using Student's t-test or the Mann–Whitney U test in case of a non-normal distribution. Values of $^{*}P < 0.05$, $^{**}P < 0.01$,

$^{***}P < 0.001$ were considered to be statistically significant. Values are expressed as means ± SEM. Calculations were made using the SPSS statistical package version 17.0.

SUPPLEMENTARY MATERIAL

Supplementary Material is available at *HMG* online.

ACKNOWLEDGEMENTS

The authors thank Marian Verhage for blastocyst injections, and Inge Versteeg, Rogier Vos, Christine Brussel, Fadime Üzel, Gudrun Utz and Pia Lacroix for technical assistance. The authors also thank all members of the Neuromedical Genetics group for advice on the manuscript.

Conflict of Interest statement. None declared.

FUNDING

This work was supported by Rotterdamse Vereniging Blindenbelangen, Landelijke St. voor Blinden en Slechtzienden, St. Blindenhulp, St. Oogfonds Nederland, St. Retina Nederland and Netherlands Institute for Neuroscience (J.W.), The Netherlands Organisation for Health Research and Development (ZonMw 43200004 to J.W.), European Union (HEALTH F2-2008-200234 to A.L.B., M.W.S., P.R., J.W.), The Deutsche Forschungsgemeinschaft (DFG Se837/5-2, Se837/6-1, Se837/6-2, Se837/7-1 to M.W.S.), the German Ministry of Education and Research (BMBF 0314106 to M.W.S.) and The French National Research Agency (ANR) (BLAN 07-2-186738 to A.L.B.).

REFERENCES

1. Mehalow, A.K., Kameya, S., Smith, R.S., Hawes, N.L., Denegre, J.M., Young, J.A., Bechtold, L., Haider, N.B., Tepass, U., Heckenlively, J.R. *et al.* (2003) CRB1 is essential for external limiting membrane integrity and photoreceptor morphogenesis in the mammalian retina. *Hum. Mol. Genet.*, **12**, 2179–2189.
2. van de Pavert, S.A., Kantardzhieva, A., Malysheva, A., Meuleman, J., Versteeg, I., Levelt, C., Klooster, J., Geiger, S., Seeliger, M.W., Rashbass, P. *et al.* (2004) Crumbs homologue 1 is required for maintenance of photoreceptor cell polarization and adhesion during light exposure. *J. Cell Sci.*, **117**, 4169–4177.
3. van de Pavert, S.A., Sanz, A.S., Aartsen, W.M., Vos, R.M., Versteeg, I., Beck, S.C., Klooster, J., Seeliger, M.W. and Wijnholds, J. (2007) Crb1 is a determinant of retinal apical Muller glia cell features. *Glia*, **55**, 1486–1497.
4. Park, B., Alves, C.H., Lundvig, D.M., Tanimoto, N., Beck, S.C., Huber, G., Richard, F., Klooster, J., Andlauer, T.F., Swindell, E.C. *et al.* (2011) PALS1 is essential for retinal pigment epithelium structure and neural retina stratification. *J. Neurosci.*, **31**, 17230–17241.
5. Sottocornola, R., Royer, C., Vives, V., Tordella, L., Zhong, S., Wang, Y., Ratnayaka, I., Shipman, M., Cheung, A., Gaston-Massuet, C. *et al.* (2010) ASPP2 binds Par-3 and controls the polarity and proliferation of neural progenitors during CNS development. *Dev. Cell*, **19**, 126–137.
6. Cho, S.H., Kim, J.Y., Simons, D.L., Song, J.Y., Le, J.H., Swindell, E.C., Jamrich, M., Wu, S.M. and Kim, S. (2012) Genetic ablation of Pals1 in retinal progenitor cells models the retinal pathology of Leber congenital amaurosis. *Hum. Mol. Genet.*, **21**, 2663–2676.
7. Koike, C., Nishida, A., Akimoto, K., Nakaya, M.A., Noda, T., Ohno, S. and Furukawa, T. (2005) Function of atypical protein kinase C lambda in differentiating photoreceptors is required for proper lamination of mouse retina. *J. Neurosci.*, **25**, 10290–10298.
8. van de Pavert, S.A., Meuleman, J., Malysheva, A., Aartsen, W.M., Versteeg, I., Tonagel, F., Kamphuis, W., McCabe, C.J., Seeliger, M.W. and Wijnholds, J. (2007) A single amino acid substitution (Cys249Trp) in Crb1 causes retinal degeneration and deregulates expression of pituitary tumor transforming gene Pttg1. *J. Neurosci.*, **27**, 564–573.
9. Pellikka, M., Tanentzapf, G., Pinto, M., Smith, C., McGlade, C.J., Ready, D.F. and Tepass, U. (2002) Crumbs, the *Drosophila* homologue of human CRB1/RP12, is essential for photoreceptor morphogenesis. *Nature*, **416**, 143–149.
10. Richard, M., Roepman, R., Aartsen, W.M., van Rossum, A.G., den Hollander, A.I., Knust, E., Wijnholds, J. and Cremers, F.P. (2006) Towards understanding CRUMBS function in retinal dystrophies. *Hum. Mol. Genet.*, **15**, 235–243.
11. Omori, Y. and Malicki, J. (2006) oko meduzy and related crumbs genes are determinants of apical cell features in the vertebrate embryo. *Curr. Biol.*, **16**, 945–957.
12. Hsu, Y.C. and Jensen, A.M. (2010) Multiple domains in the Crumbs Homolog 2a (Crb2a) protein are required for regulating rod photoreceptor size. *BMC Cell Biol.*, **11**, 60.
13. Tepass, U., Theres, C. and Knust, E. (1990) crumbs encodes an EGF-like protein expressed on apical membranes of *Drosophila* epithelial cells and required for organization of epithelia. *Cell*, **61**, 787–799.
14. Bulgakova, N.A. and Knust, E. (2009) The Crumbs complex: from epithelial-cell polarity to retinal degeneration. *J. Cell Sci.*, **122**, 2587–2596.
15. Kantardzhieva, A., Gosens, I., Alexeeva, S., Punte, I.M., Versteeg, I., Krieger, E., Neefjes-Mol, C.A., den Hollander, A.I., Letteboer, S.J., Klooster, J. *et al.* (2005) MPP5 recruits MPP4 to the CRB1 complex in photoreceptors. *Invest. Ophthalmol. Vis. Sci.*, **46**, 2192–2201.
16. Kantardzhieva, A., Alexeeva, S., Versteeg, I. and Wijnholds, J. (2006) MPP3 is recruited to the MPP5 protein scaffold at the retinal outer limiting membrane. *FEBS J.*, **273**, 1152–1165.
17. Assemat, E., Bazellieres, E., Pallesi-Pocachard, E., Le Bivic, A. and Massey-Harroche, D. (2008) Polarity complex proteins. *Biochim. Biophys. Acta*, **1778**, 614–630.
18. Roh, M.H., Makarova, O., Liu, C.J., Shin, K., Lee, S., Laurinec, S., Goyal, M., Wiggins, R. and Margolis, B. (2002) The Maguk protein, Pals1, functions as an adapter, linking mammalian homologues of Crumbs and Discs Lost. *J. Cell Biol.*, **157**, 161–172.
19. Lemmers, C., Michel, D., Lane-Guermonprez, L., Delgrossi, M.H., Medina, E., Arsanto, J.P. and Le Bivic, A. (2004) CRB3 binds directly to Par6 and regulates the morphogenesis of the tight junctions in mammalian epithelial cells. *Mol. Biol. Cell*, **15**, 1324–1333.
20. Hurd, T.W., Gao, L., Roh, M.H., Macara, I.G. and Margolis, B. (2003) Direct interaction of two polarity complexes implicated in epithelial tight junction assembly. *Nat. Cell Biol.*, **5**, 137–142.
21. Hsu, Y.C., Willoughby, J.J., Christensen, A.K. and Jensen, A.M. (2006) Mosaic Eyes is a novel component of the Crumbs complex and negatively regulates photoreceptor apical size. *Development*, **133**, 4849–4859.
22. Gosens, I., Sessa, A., den Hollander, A.I., Letteboer, S.J., Belloni, V., Arends, M.L., Le Bivic, A., Cremers, F.P., Broccoli, V. and Roepman, R. (2007) FERM protein EPB41L5 is a novel member of the mammalian CRB-MPP5 polarity complex. *Exp. Cell Res.*, **313**, 3959–3970.
23. Laprise, P., Beronja, S., Silva-Gagliardi, N.F., Pellikka, M., Jensen, A.M., McGlade, C.J. and Tepass, U. (2006) The FERM protein Yurt is a negative regulatory component of the Crumbs complex that controls epithelial polarity and apical membrane size. *Dev. Cell*, **11**, 363–374.
24. den Hollander, A.I., ten Brink, J.B., de Kok, Y.J., van Soest, S., van den Born, L.I., van Driel, M.A., van de Pol, D.J., Payne, A.M., Bhattacharya, S.S., Kellner, U. *et al.* (1999) Mutations in a human homologue of *Drosophila* crumbs cause retinitis pigmentosa (RP12). *Nat. Genet.*, **23**, 217–221.
25. den Hollander, A.I., Davis, J., van der Velde-Visser, S.D., Zonneveld, M.N., Pierrottet, C.O., Koenekoop, R.K., Kellner, U., van den Born, L.I., Heckenlively, J.R., Hoyng, C.B. *et al.* (2004) CRB1 mutation spectrum in inherited retinal dystrophies. *Hum. Mutat.*, **24**, 355–369.
26. Malicki, J. and Driever, W. (1999) oko meduzy mutations affect neuronal patterning in the zebrafish retina and reveal cell-cell interactions of the retinal neuroepithelial sheet. *Development*, **126**, 1235–1246.

27. Boroviak, T. and Rashbass, P. (2011) The apical polarity determinant Crumbs 2 is a novel regulator of ESC-derived neural progenitors. *Stem Cells*, **29**, 193–205.
28. Rowan, S. and Cepko, C.L. (2004) Genetic analysis of the homeodomain transcription factor Chx10 in the retina using a novel multifunctional BAC transgenic mouse reporter. *Dev. Biol.*, **271**, 388–402.
29. Schmitz-Valckenberg, S., Holz, F.G., Bird, A.C. and Spaide, R.F. (2008) Fundus autofluorescence imaging: review and perspectives. *Retina*, **28**, 385–409.
30. van Rossum, A.G., Aartsen, W.M., Meuleman, J., Klooster, J., Malysheva, A., Versteeg, I., Arsanto, J.P., Le Bivic, A. and Wijnholds, J. (2006) Pals1/Mpp5 is required for correct localization of Crb1 at the subapical region in polarized Muller glia cells. *Hum. Mol. Genet.*, **15**, 2659–2672.
31. Agathocleous, M. and Harris, W.A. (2009) From progenitors to differentiated cells in the vertebrate retina. *Annu. Rev. Cell Dev. Biol.*, **25**, 45–69.
32. Cepko, C.L., Austin, C.P., Yang, X., Alexiades, M. and Ezzeddine, D. (1996) Cell fate determination in the vertebrate retina. *Proc. Natl Acad. Sci. USA*, **93**, 589–595.
33. Ohata, S., Aoki, R., Kinoshita, S., Yamaguchi, M., Tsuruoka-Kinoshita, S., Tanaka, H., Wada, H., Watabe, S., Tsuboi, T., Masai, I. *et al.* (2011) Dual roles of Notch in regulation of apically restricted mitosis and apicobasal polarity of neuroepithelial cells. *Neuron*, **69**, 215–230.
34. Jacobson, S.G., Cideciyan, A.V., Aleman, T.S., Pianta, M.J., Sumaroka, A., Schwartz, S.B., Smilko, E.E., Milam, A.H., Sheffield, V.C. and Stone, E.M. (2003) Crumbs homolog 1 (CRB1) mutations result in a thick human retina with abnormal lamination. *Hum. Mol. Genet.*, **12**, 1073–1078.
35. Aleman, T.S., Cideciyan, A.V., Aguirre, G.K., Huang, W.C., Mullins, C.L., Roman, A.J., Sumaroka, A., Olivares, M.B., Tsai, F.F., Schwartz, S.B. *et al.* (2011) Human CRB1-associated retinal degeneration: comparison with the rd8 Crb1-mutant mouse model. *Invest. Ophthalmol. Vis. Sci.*, **52**, 6898–6910.
36. van den Hurk, J.A., Rashbass, P., Roepman, R., Davis, J., Voesenek, K.E., Arends, M.L., Zonneveld, M.N., van Roekel, M.H., Cameron, K., Rohrschneider, K. *et al.* (2005) Characterization of the Crumbs homolog 2 (CRB2) gene and analysis of its role in retinitis pigmentosa and Leber congenital amaurosis. *Mol. Vis.*, **11**, 263–273.
37. Warming, S., Costantino, N., Court, D.L., Jenkins, N.A. and Copeland, N.G. (2005) Simple and highly efficient BAC recombineering using galK selection. *Nucleic Acids Res.*, **33**, e36.
38. Tanimoto, N., Muehlfriedel, R.L., Fischer, M.D., Fahl, E., Humphries, P., Biel, M. and Seeliger, M.W. (2009) Vision tests in the mouse: functional phenotyping with electroretinography. *Front. Biosci.*, **14**, 2730–2737.
39. Seeliger, M.W., Beck, S.C., Pereyra-Munoz, N., Dangel, S., Tsai, J.Y., Luhmann, U.F., van de Pavert, S.A., Wijnholds, J., Samardzija, M., Wenzel, A. *et al.* (2005) In vivo confocal imaging of the retina in animal models using scanning laser ophthalmoscopy. *Vision Res.*, **45**, 3512–3519.
40. Fischer, M.D., Huber, G., Beck, S.C., Tanimoto, N., Muehlfriedel, R., Fahl, E., Grimm, C., Wenzel, A., Reme, C.E., van de Pavert, S.A. *et al.* (2009) Noninvasive, in vivo assessment of mouse retinal structure using optical coherence tomography. *PloS One*, **4**, e7507.

OPEN ACCESS Freely available online

PLOS | GENETICS

Targeted Ablation of *Crb1* and *Crb2* in Retinal Progenitor Cells Mimics Leber Congenital Amaurosis

Lucie P. Pellissier[1], Celso Henrique Alves[1], Peter M. Quinn[1], Rogier M. Vos[1], Naoyuki Tanimoto[2], Ditte M. S. Lundvig[1], Jacobus J. Dudok[1], Berend Hooibrink[3], Fabrice Richard[4], Susanne C. Beck[2], Gesine Huber[2], Vithiyanjali Sothilingam[2], Marina Garcia Garrido[2], André Le Bivic[4], Mathias W. Seeliger[2], Jan Wijnholds[1]*

1 Department of Neuromedical Genetics, The Netherlands Institute for Neuroscience, Royal Netherlands Academy of Arts and Sciences (KNAW), Amsterdam, The Netherlands, **2** Division of Ocular Neurodegeneration, Institute for Ophthalmic Research, Centre for Ophthalmology, Eberhard Karls University of Tübingen, Tübingen, Germany, **3** Department of Cell Biology and Histology, Amsterdam Medisch Centrum, Amsterdam, The Netherlands, **4** Aix-Marseille University, Developmental Biology Institute of Marseille Luminy (IBDML) and CNRS, UMR 6216, Marseille, France

Abstract

Development in the central nervous system is highly dependent on the regulation of the switch from progenitor cell proliferation to differentiation, but the molecular and cellular events controlling this process remain poorly understood. Here, we report that ablation of *Crb1* and *Crb2* genes results in severe impairment of retinal function, abnormal lamination and thickening of the retina mimicking human Leber congenital amaurosis due to loss of *CRB1* function. We show that the levels of CRB1 and CRB2 proteins are crucial for mouse retinal development, as they restrain the proliferation of retinal progenitor cells. The lack of these apical proteins results in altered cell cycle progression and increased number of mitotic cells leading to an increased number of late-born cell types such as rod photoreceptors, bipolar and Müller glia cells in postmitotic retinas. Loss of CRB1 and CRB2 in the retina results in dysregulation of target genes for the Notch1 and YAP/Hippo signaling pathways and increased levels of P120-catenin. Loss of CRB1 and CRB2 result in altered progenitor cell cycle distribution with a decrease in number of late progenitors in G1 and an increase in S and G2/M phase. These findings suggest that CRB1 and CRB2 suppress late progenitor pool expansion by regulating multiple proliferative signaling pathways.

Citation: Pellissier LP, Alves CH, Quinn PM, Vos RM, Tanimoto N, et al. (2013) Targeted Ablation of *Crb1* and *Crb2* in Retinal Progenitor Cells Mimics Leber Congenital Amaurosis. PLoS Genet 9(12): e1003976. doi:10.1371/journal.pgen.1003976

Editor: Seth Blackshaw, Johns Hopkins University School of Medicine, United States of America

Received September 10, 2013; **Accepted** October 9, 2013; **Published** December 5, 2013

Funding: This work was supported by Rotterdamse Vereniging Blindenbelangen, Landelijke St. voor Blinden en Slechtzienden, St. Blindenhulp, St. Oogfonds Nederland, St. Retina Nederland, Netherlands Institute for Neuroscience, Foundation Fighting Blindness (TA-GT-0811-0540-NIN), and The Netherlands Organisation for Health Research and Development (ZonMw grant 43200004 to JW), European Union (HEALTH-F2-2008-200234 to ALB MWS JW), The Deutsche Forschungsgemeinschaft (DFG, grants Se837/5-2, Se837/6-1, Se837/6-2, Se837/7-1 to MWS), and the German Ministry of Education and Research (BMBF, grant 0314106 to MWS), The French National Research Agency (ANR n° BLAN07-2-186738 to ALB). The funders had no role in study design, data collection and analysis, decision to publish, or preparation of the manuscript.

Competing Interests: The authors have declared that no competing interests exist.

* E-mail: j.wijnholds@nin.knaw.nl

Introduction

During vertebrate retina development, one type of glial cell and six types of neurons are formed by the orderly generation of post-mitotic cells from a common pool of retinal progenitor cells [1,2]. In this temporally fine-tuned process, ganglion cells are generated first, followed by horizontal cells, cone photoreceptors and early born amacrine cells, rod photoreceptors and late born amacrine cells, and finally bipolar cells and Müller glial cells [2]. Retinal progenitor cells are elongated and polarized cells that extend along the apicobasal axis and connect to adjoining cells by adherens junctions via their apical processes. The proliferation of the progenitors is carefully regulated through a combination of intrinsic and extrinsic signals followed by a complete cessation of cell division around 10 days after birth in mice [3]. Many extrinsic soluble or membrane-bound factors directly promote proliferation activity such as Notch, sonic Hedgehog and Wnt signalling pathways [4]. In addition, intrinsic regulatory genes and transcription factors such as *Chx10* regulate the cell cycle machinery [5].

Recent work suggests that cell adhesion and cell polarity complex proteins play a critical role in the maintenance of the proliferation of the progenitor cells [6]. The polarity proteins that form the Crumbs complex reside at the subapical region adjacent to the adherens junctions between retinal progenitor cells in the developing retina or between photoreceptors and Müller glial cells in mature retinas. The *Crumbs* protein was first identified in *Drosophila* as a key developmental regulator of apical-basal polarity [7]. In mammals, the Crumbs homologue family is composed of three genes, *CRB1*, *CRB2* and *CRB3*. CRB proteins have a large extracellular domain (which is lacking in CRB3) composed of epidermal growth factor and laminin-globular domains, a single transmembrane domain, and an intracellular domain containing FERM and PDZ protein-binding motifs [8]. Through this PDZ motif CRB proteins interact with PALS1, which binds to MUPP1 or PATJ, thus forming the Crumbs complex [8]. Recently, it has been shown that the CRB-interacting partner PALS1 has a role in regulating the proliferation of neural progenitors. Deletion of PALS1 in the developing cortex caused premature exit of

Author Summary

Mutations in the human *CRB1* gene lead to one of the most severe forms of retinal dystrophies, called Leber congenital amaurosis. Here, we report that ablation of CRB1 and the second family member CRB2 are crucial for proper retinal development. These mice display severe impairment of retinal function, abnormal lamination and thickening of the retina mimicking human Leber congenital amaurosis due to loss of *CRB1* function. The thickening of the retina is due to increased cell proliferation during late retinal development leading to an increased number of late-born retinal cells. We describe in these *CRB1* Leber congenital amaurosis mouse models the molecular and cellular events involving CRB proteins during the development of the retina.

progenitors from the cell cycle and massive cell death leading to absence of the cortical structures [9].

Studies suggest a common function of CRB proteins and their partners in regulating growth factor signalling pathways, which orchestrate cell proliferation and cell fate decisions. It has been suggested that *Drosophila Crumbs* and human CRB2 inhibit Notch1 cleavage and signalling by binding to the presenilin complex, inhibiting γ-secretase activity [10,11]. Zebrafish CRB extracellular domains can directly bind to the extracellular domain of Notch1 and inhibit its activation [12]. The Crumbs complex can negatively modulate the mammalian Target of Rapamycin Complex 1 (mTORC1) pathway via the direct interaction between PATJ and the tumour suppressor gene TSC2 and depletion of PALS1 protein results in loss of mTORC1 activity in the murine developing cortex [9,13]. The Hippo pathway is a key regulator of organ size and tumorigenesis in humans and flies [6,14]. *Drosophila Crumbs* has been shown to control the Hippo pathway by direct interaction of its FERM domain [15,16]. Furthermore, PALS1 and PATJ can interact with the effectors of the Hippo pathway Yes-associated Protein (YAP) and transcriptional co-activator with PDZ-binding motif (TAZ) proteins and thus promote their inhibition and retention in the cytoplasm [17].

Mutations in the human *CRB1* gene cause autosomal-recessive progressive retinitis pigmentosa and Leber congenital amaurosis (LCA) [18]. LCA is one of the most severe forms of retinal dystrophy leading to blindness around birth due to defects in the development or maturation of the retina [19]. *CRB1*-LCA retinas are remarkably thick and lack the distinct layers like immature retinas suggesting a developmental defect [20]. The functional roles of CRB proteins during mammalian development remain poorly understood. Both CRB1 and CRB2 are expressed from embryonic day (E)12.5 onwards in the developing murine retina at the subapical region adjacent to adherens junctions in retinal progenitor cells [21–23] suggesting a role of the CRB proteins during the development of the retina. *Crb1* knockout, $Crb1^{C249W/-}$ knockin and the naturally occurring $Crb1^{rd8/rd8}$ mutant mice show mild retinal disorganization in adulthood, limited to the inferior quadrant [24–27]. *Crb2* conditional knockout (cKO) retinas show progressive abnormal lamination of newborn rod photoreceptors and disruption of adherens junctions in postnatal developing retina [22]. Here, we study the effects of loss of CRB1 and CRB2 and their potential overlapping functions during early retinal development. Loss of both CRB1 and CRB2 results in absence of a separate photoreceptor layer, misplaced cell types throughout the retina and loss of retinal function mimicking the phenotype observed in human LCA patients. Our data suggests that the pool of late progenitor cells during retinal development is suppressed by CRB1 and CRB2 through the regulation of mitogenic signaling pathways.

Results

Lack of CRB1 and CRB2 severely impairs retinal function in adult mice

We crossed *Crb1* KO mice with conditionally floxed *Crb2* mice [22,24]. The mice were bred with Chx10*Cre* transgenic mice, which express Cre recombinase fused to GFP throughout the developing retina starting at E11.5 [28]. We showed previously that efficient recombination of the floxed *Crb2* alleles occurred around E12.5 [22]. In this study, double homozygote $Crb1^{-/-}Crb2^{F/F}$Chx10$Cre^{Tg/+}$ conditional knockout retinas (*Crb1Crb2* cKO) were compared to littermate $Crb1^{-/-}Crb2^{F/F}$ and $Crb1^{-/-}Crb2^{F/+}$Chx10$Cre^{Tg/+}$ retinas. $Crb1^{+/-}Crb2^{F/F}$Chx10$Cre^{Tg/+}$ ($Crb1^{+/-}Crb2$ cKO) retinas were compared to littermate double heterozygote $Crb1^{-/+}Crb2^{F/+}$Chx10$Cre^{Tg/+}$ ($Crb1^{+/-}Crb2^{F/+}$ cKO) retinas. We verified the loss of CRB1 and CRB2 proteins in the *Crb1Crb2* cKO at E15.5 and P14 (Figures S4D and S3D).

In vivo functional and structural analysis were performed on 1 to 6 month (M) old *Crb1Crb2* cKO, $Crb1^{+/-}Crb2$ cKO and control mice, using electroretinography, spectral domain optical coherence tomography and scanning laser ophthalmoscopy. Already at 1M, $Crb1^{+/-}Crb2$ cKO and *Crb1Crb2* cKO mice showed more pronounced reduction in amplitudes of electroretinogram responses than *Crb2* cKO mice (Figures 1A and S1A). Both scotopic and photopic responses were affected, which indicate alterations of both rod and cone system components. At 3 and 6M (Figures 1B and S1B C), electroretinogram responses were below detection level, although $Crb1^{+/-}Crb2$ cKO responses were more variable (Figures 1B and S1B).

In vivo imaging analysis revealed changes in $Crb1^{+/-}Crb2$ cKO retinas in fundus appearance as well as in retinal layer morphology in contrast to $Crb1^{+/-}Crb2^{F/+}$ cKO control retinas (Figure S2). With native scanning laser ophthalmoscopy, many spots and patchy areas were visible throughout the retina, corresponding to pseudo-rosettes in the photoreceptor layer and in histological sections (Figures S2B and 2A B). Already at 1M, spectral domain optical coherence tomography revealed an aberrant layering in *Crb1Crb2* cKO retinas (Figure 3E F). The retina consisted of a single inner plexiform layer, an abnormal thick ganglion cell layer and a second broad nuclear layer (Figure 2A B). All retinal cell types appeared to be generated, but a separate photoreceptor nuclear layer, inner and outer segment layer and outer plexiform layer were not formed. Two types of rosettes in the broad nuclear layer could be identified and were primarily formed of photoreceptors or ganglion cells and inner nuclear layer cells (Figure 2A B black arrowheads and asterisks, respectively). Using electron microscopy and immunohistochemistry, we found ectopically localized photoreceptor outer segments, delocalized basal bodies of cilia, adherens junctions and ribbon synapses in the *Crb1Crb2* cKO at 1M (Figures 2E F and S3A,C).

The retina thickness in the *Crb1Crb2* cKO was significantly increased compared to control retinas at P10 (276.1±13.2 μm vs 199.7±5.4 μm, respectively) and P14 (247.8±6.9 μm vs 211 ±7.7 μm, respectively; Figure 2G). Both *Crb1Crb2* cKO and $Crb1^{+/-}Crb2$ cKO retinas degenerate rapidly after 1M, which was associated with retinal vasculature defects leading to the thinning of the retinas in 3 6M retinas (Figures 2C D, S2 and 3). Quantification of cleaved caspase 3 positive cells showed an increase in the number of apoptotic cells in *Crb1Crb2* cKO retinas at P10, P14 and 3M (Figure 2H). Cleaved caspase 3 positive cells

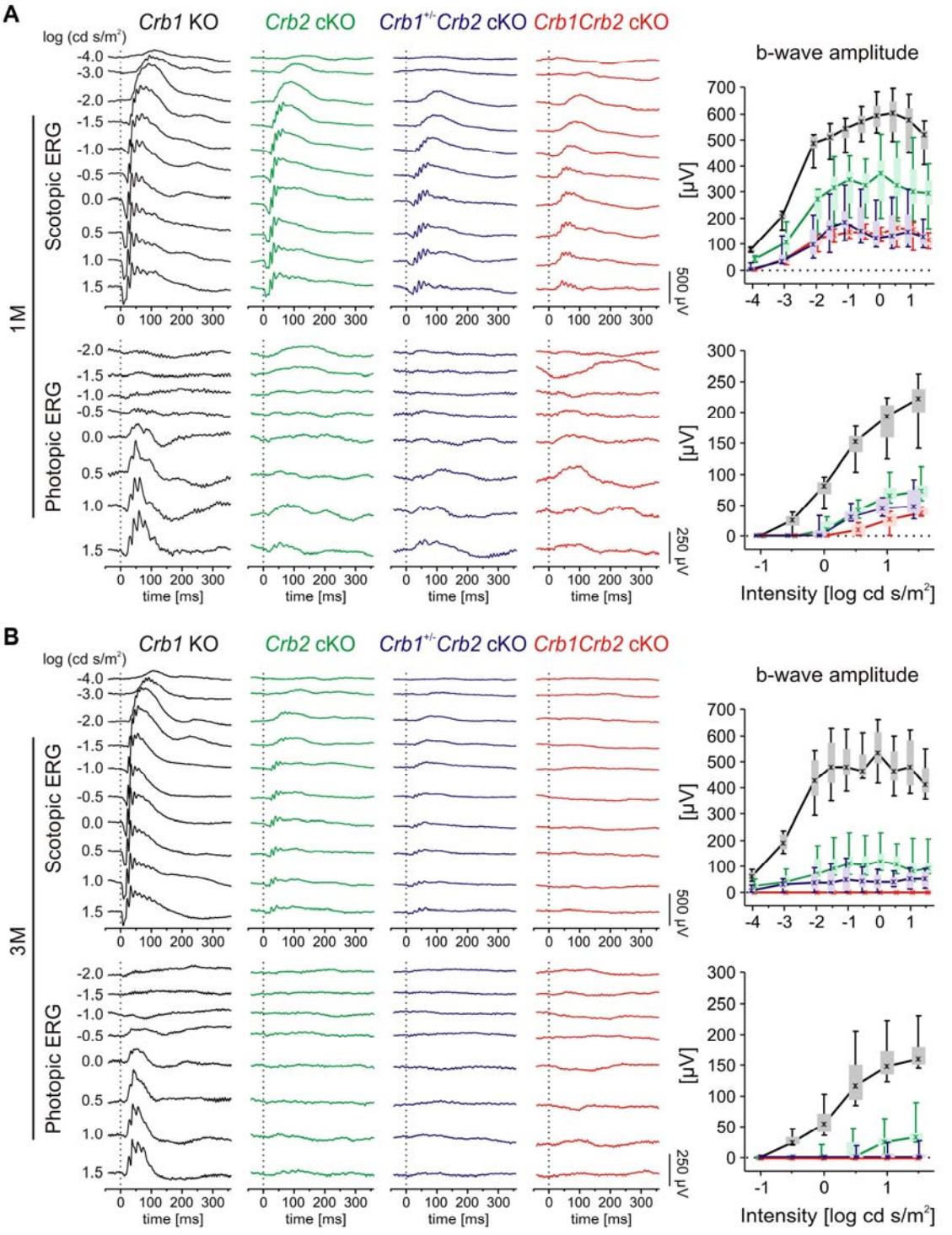

Figure 1. Retinal function in *Crb1Crb2* mutant retinas is severely impaired. Retinal function in *Crb1* KO (black), *Crb2* cKO (green), *Crb1*$^{+/-}$*Crb2* cKO (purple) and *Crb1Crb2* cKO affected mice (red) based on single-flash electroretinogram data from 1M (A), and 3M (B) old animals. (left)

Representative single-flash electroretinogram traces recorded from the indicated genotypes under scotopic (top) and photopic (bottom) conditions. (right) Scotopic (top) and photopic (bottom) b-wave amplitude data plotted as a function of the logarithm of the flash intensity. Boxes indicate the 25% and 75% quantile range, whiskers indicate the 5% and 95% quantiles, and the asterisks indicate the median of the data. In $Crb1^{+/-}Crb2$ cKO and *Crb1Crb2* cKO mice, the b-wave amplitude was already considerably reduced at 1M under both scotopic and photopic conditions, and declined even at 3M compared to *Crb1* KO and *Crb2* cKO.
doi:10.1371/journal.pgen.1003976.g001

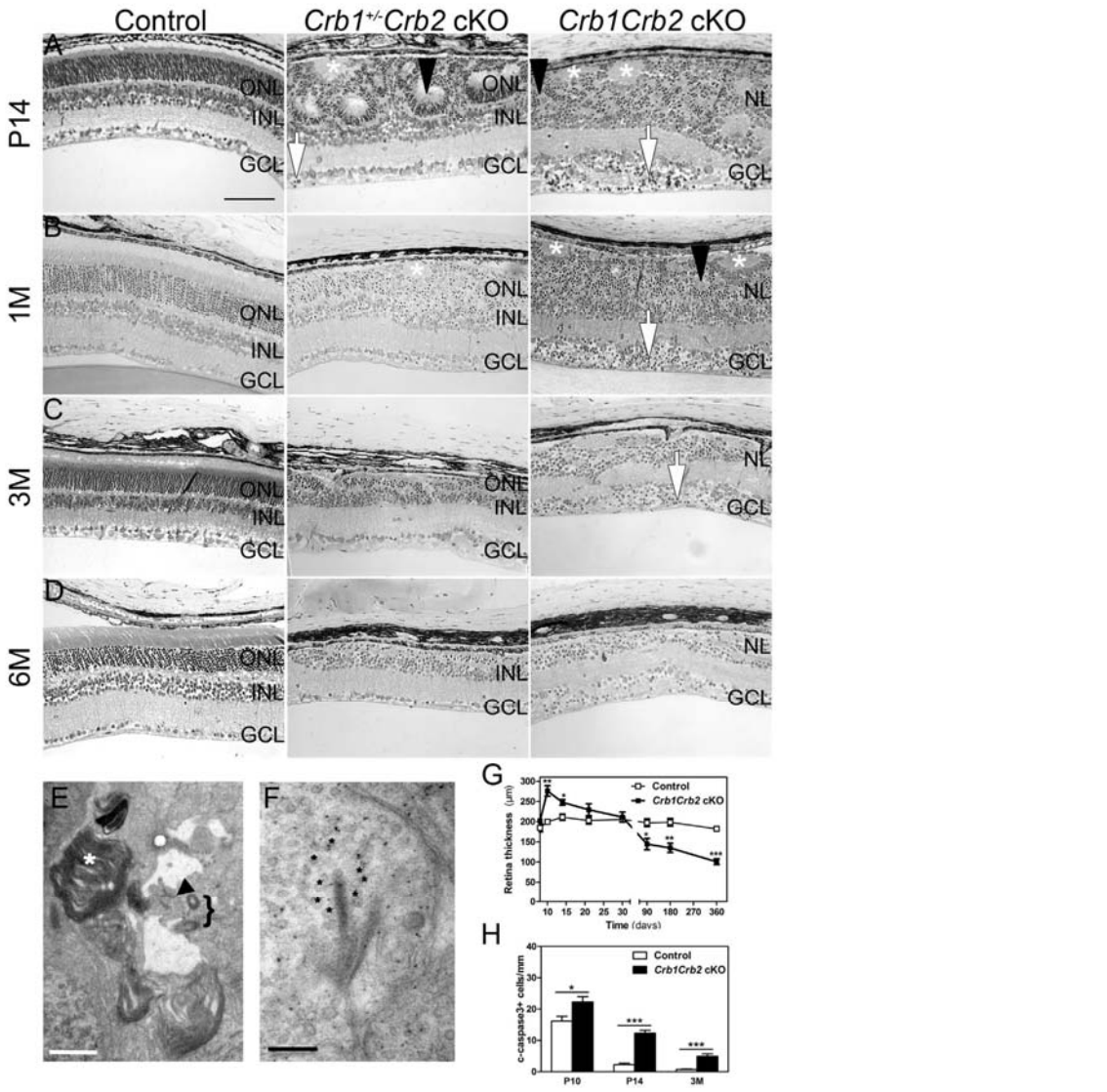

Figure 2. Abnormal layering in *Crb1Crb2* cKO retinas. Histological sections of P14 (A), 1M (B), 3M (C) and 6M (D) old control (left; $Crb1^{+/-}Crb2^{F/+}$ cKO), $Crb1^{+/-}Crb2$ cKO (middle) and *Crb1Crb2* cKO (right). *Crb1Crb2* cKO retinas had a thick ganglion cell layer and a second broad nuclear layer separated by the inner plexiform layer. $Crb1^{+/-}Crb2$ cKO had perturbed outer and inner nuclear layers. Ectopic localization of dark-pigmented photoreceptors (white arrows), ganglion/inner nuclear layer cells (white asterisks) and rosettes of photoreceptors (black arrowheads) was visible in the two mutant retinas (Figure S5B,D). Both mutant retinas degenerated rapidly with age. GCL, ganglion cell layer; INL, inner nuclear layer; ONL, outer nuclear layer; (E,F) Electron microscopic pictures of 1M old *Crb1Crb2* cKO retinas. Some complete segments (E, white asterix), adherens junctions (E, black arrow) and centrioles of cilium (E, bracket) or ribbon synapses with vesicles on the two sides of the cleft (F, black asterix) were identified but in ectopic locations. (G) The thickness of 4–5 control and *Crb1Crb2* cKO retinas from P8 to P360. *Crb1Crb2* cKO retinas had a thicker retina than littermate controls at P10 and P14, followed by progressive thinning and degeneration. (H) The cleaved caspase 3 positive apoptotic cells were counted at P10, P14 and 3M from 20–30 sections of 3 littermate controls and *Crb1Crb2* cKO whole retinas. Mutant retinas showed an increase in the number of apoptotic cells. Data are presented as mean ± s.e.m. *P<0.05; **P<0.01; ***P<0.001. Scale bar, 100 μm (A–D); 1 μm (E,F).
doi:10.1371/journal.pgen.1003976.g002

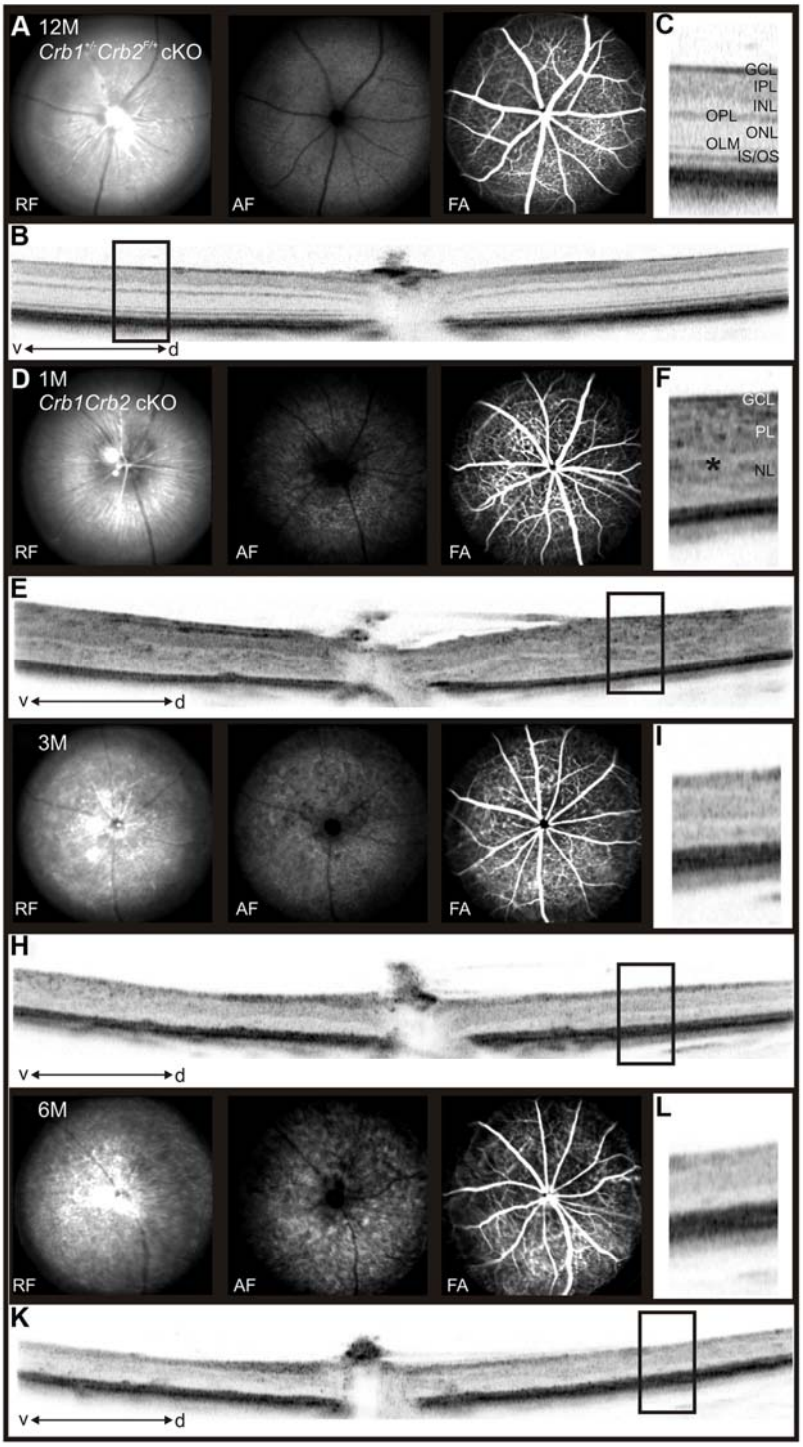

Figure 3. ***In vivo*** **retinal imaging in** ***Crb1Crb2*** **cKO mice.** 12M old control $Crb1^{+/-}Crb2^{F/+}$ cKO (A–C) and 1M (D–F), 3M (G–I) and 6M (J–L) old *Crb1Crb2* cKO mice were subjected to scanning laser ophthalmoscopy (A,D,G,J) and vertical spectral domain optical coherence tomography (B, E, H,

K). C, F, I and L are magnifications of the boxes in B, E, H, and K respectively. At 1M, a disorganized retina with an abnormally thick ganglion cell layer, one plexiform and one nuclear layer was observed (E, asterisk in F). At 3M (G–I) and 6M (J–L), an obvious loss in the retinal thickness was ascertained as well as several fundus alterations (G,J). Abbreviations: AF, autofluorescence; d, dorsal; FA, Fluorescein angiography; GCL, ganglion cell layer; INL, inner nuclear layer; IPL, inner plexiform layer; IS/OS, inner segment/outer segment border; OLM, outer limiting membrane; ONL, outer nuclear layer; OPL, outer plexiform layer; RF, Red-free; v, ventral.
doi:10.1371/journal.pgen.1003976.g003

at P10 and P14 were identified as rod photoreceptor cells and at 3M mainly as bipolar cells (Figure S3E F).

CRB1 and CRB2 are essential for proper retinal development

As CRB1 and CRB2 are expressed in the retinal progenitor cells from E12.5 onwards at the subapical region adjacent to adherens junctions [21 22] and due to the severe disorganization of these retinas in adult, we analyzed control, *Crb1*$^{+/-}$*Crb2* cKO and *Crb1Crb2* cKO mice from E11.5 to P5. Whereas no visible defects were observed at E11.5 and E12.5, perturbations at the outer limiting membrane and cellular mislocalizations near the retinal pigment epithelium were visible at E13.5 in *Crb1Crb2* cKO retinas (Figure 4A, black arrowhead). Between E15.5 and E17.5 in *Crb1Crb2* cKO, the adherens junctions were gradually lost and the nuclei of the retinal progenitors showed abnormal orientation, whereas in control retinas, progenitors were arranged radially along the apical-basal axis (Figures 4B C and S4B). Electron microscopic analyses showed loss of adherens junctions in the neural retina and ectopic nuclei close to the retinal pigment epithelium (Figures 4F G and S4E F). During retinogenesis, the photoreceptor layer and the outer plexiform layer formed at P5. However, in the *Crb1Crb2* cKO, this process never ensued, as no distinct photoreceptor layer was formed (Figure 4E).

In *Crb1*$^{+/-}$*Crb2* cKO, perturbations at the outer limiting membrane started at the periphery of the retina at E15.5 (Figure 4B, black arrowhead). It progressively extended to the centre of the retinas where rosettes also formed (Figure 4C E). In late developmental stages, in addition to photoreceptor rosettes, ganglion cell nuclei and inner nuclear layer cells were found in the outer nuclear layer and some photoreceptor nuclei were found in the ganglion cell layer (Figure 2A). These retinas display intermediate phenotypes between the *Crb2* cKO [22] and *Crb1Crb2* cKO.

Increased number and mislocalization of late born cells in *Crb1Crb2* cKO retinas

Due to the severe disorganisation of the retinas, we further investigated whether all retinal cell types formed in the absence of CRB1 and CRB2. Using specific markers for the different cell types, we found that all the different cell types formed and there were no indications for hybrid retinal cell types (Figure S5 and data not shown). Several of the retinal cell types appeared to localize ectopically. To further analyze this, we compared the localization of the cell nuclei in the top and bottom parts of the broad nuclear layer in *Crb1Crb2* cKO mice to the outer and inner nuclear layer in control retinas (Figures 5A F and S5A F). The localization of the earliest born cell types, ganglion cells (marked by Brn3b), cone photoreceptors (Cone arrestin), horizontal cells (Calbindin) and the earliest born amacrine cells (ChAT) was less affected than the late born cell types, rod photoreceptors (Rhodopsin), Müller cells (Sox9 and glutamine synthetase) and bipolar cells (PKCα or *Cre-GFP* under the Chx10 promoter). In *Crb1*$^{+/-}$*Crb2* cKO retinas, rods, cones and bipolar cells localized ectopically in the ganglion cell layer (Figure S5G H), and amacrine and ganglion cells surrounded by bipolar cells formed pseudo-rosettes in the photoreceptor layer (Figure S5I J). These results suggest that all cell types are generated in retinas that lack CRB1 and CRB2 but their normal migration/localization is affected.

To test whether retinal cell types formed in normal numbers, we counted the different cell types at P14 (Figure 5G). The number of early born cells was unchanged whereas the number of late born cells was increased compared to control retinas: GABAergic amacrine cells (19.4±1.6 versus 14.8±0.6 cells/100 μm), late born GlyT1 positive amacrine (38.9±2.8 versus 20.9±1.4 cells/100 μm), Chx10^{+} bipolar cells (77.2±5.0 versus 46.7±2.8 cells/100 μm) and Sox9^{+} Müller cells (44.3±1.8 versus 18.8± 0.6 cells/100 μm). At P14, the number of rod photoreceptors was not significantly increased due to ongoing apoptosis (Figures 3H and S3E). We found at P10 an increase in number of rods (695±44 in *Crb1Crb2* cKO and 412±17 cells/100 μm in control; Figure 5H). This finding suggests that CRB1 and CRB2 may play a role in regulating the proliferation of the retinal progenitors.

Increased cell proliferation and apoptosis in developing *Crb1Crb2* cKO retinas

In the *Crb1Crb2* cKO retinas, the increased number of late born cells might be due to overproliferation of progenitors or reduced apoptosis. Therefore, in control, *Crb1*$^{+/-}$*Crb2* cKO and *Crb1Crb2* cKO retinas from E13.5 to P5 animals, we analysed the number of phospho-Histone H3 (pH3) positive cells and cleaved caspase 3 positive cells, which are markers for mitotic cells and apoptotic cells respectively (Figures 6A B and S6C D). From E15.5 onwards, the number of M-phase cells was significantly increased in *Crb1Crb2* cKO retinas, and the number of apoptotic cells was increased at E13.5 and E17.5 onwards. These data showed an increase in both mitosis and apoptosis in retinas lacking CRB1 and CRB2. Furthermore, cells in M-phase are normally located at the apical region in control retinas. However, in E17.5 *Crb1Crb2* cKO retinas, where the apical region was almost completely lost, the cells in M-phase localized randomly throughout the entire thickness of the retina (Figure S6C D). To test whether precursor cells formed in normal numbers, we counted at E17.5 early and late-born precursor cells. The number of Islet1^{+} early-born precursor cells (ganglion and amacrine cells) is unchanged in contrast to an increased number of Otx2^{+} late-born precursor cells (photoreceptors and bipolar cells; 139.3±5 cells/100 μm in *Crb1Crb2* cKO retinas versus 110.9±4.1 cells/100 μm in control; Figure 6D).

At E17.5, in *Crb1*$^{+/-}$*Crb2* cKO retinas, the number of mitotic and apoptotic cells was increased like in *Crb1Crb2* cKO retinas (Figure S6A B). However, at P5 an increased number of mitotic cells and a decreased number of apoptotic cells were observed like in *Crb2* cKO [22], indicating that the *Crb1*$^{+/-}$*Crb2* cKO showed intermediate features between *Crb2* and *Crb1Crb2* cKO.

Dysregulation of the cell cycle in *Crb1Crb2* cKO retinas

We further investigated, at E17.5, which phases of the cell cycle were affected using a combination of 30 min pulse labelling with BrdU for the S-phase, phospho-Histone H3 (pH3) for the M-phase and Ki67 labelling, a marker for M, G2, S and late G1 phases of the cell cycle (Figures 6C, S6C and S6E). This showed that in *Crb1Crb2* cKO retinas the number of pH3^{+} (6.1±0.2 in control

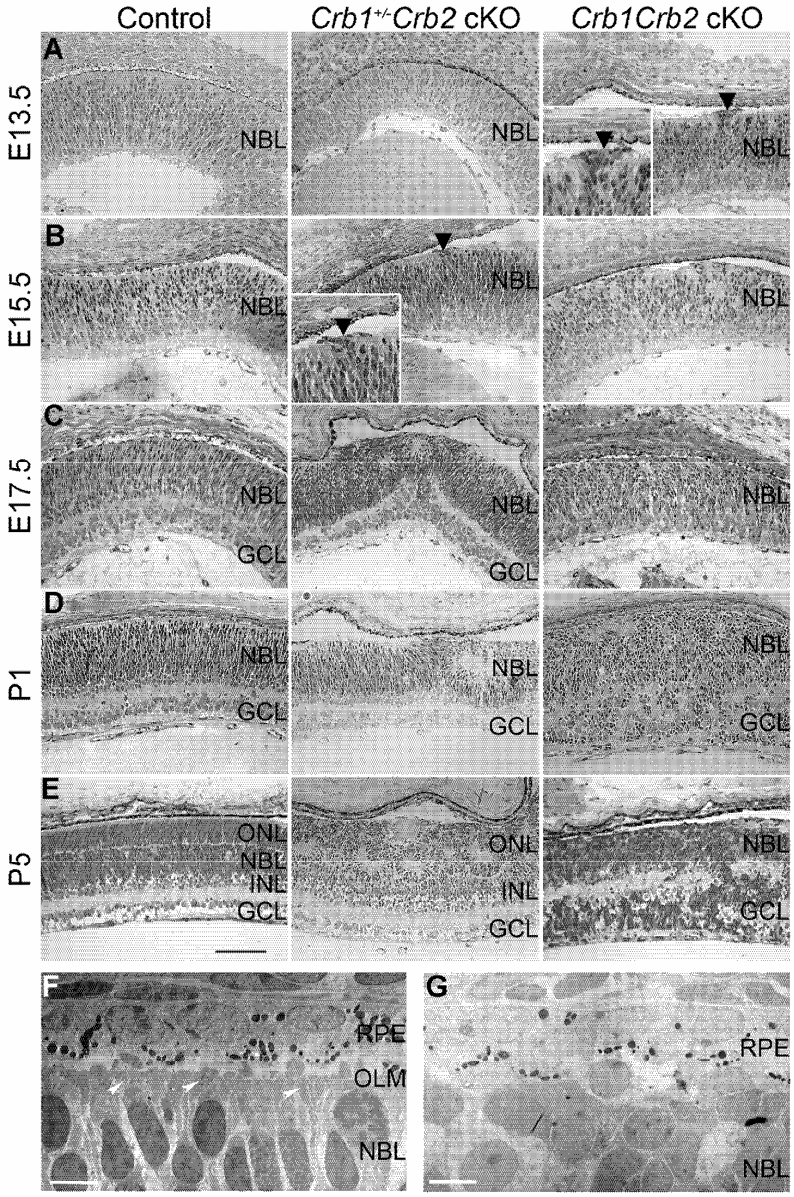

Figure 4. Retinal development is impaired in *Crb1Crb2* cKO. (A–E) Histological sections from E13.5 to P5 control (left), *Crb1*$^{+/-}$*Crb2* cKO (middle) and *Crb1Crb2* cKO (right). From E13.5 onwards, disruption of the outer limiting membrane (A right, black arrowhead) accompanied with ectopic localization of cells extended in *Crb1Crb2* cKO developing retinas (A,B right). At E17.5 and P1, in contrast to control retinas no proper ganglion cell layer was formed (C,D). The separation of the outer nuclear/photoreceptor layer formed around P5, which never happened in the *Crb1Crb2* cKO retinas (E). *Crb1*$^{+/-}$*Crb2* cKO retinas showed the first disruption in the outer limiting membrane at the periphery at E15.5 (B middle, black arrowhead), which progressively extended to the centre accompanied with rosette formation (B–E middle). Electron microscopic pictures from E17.5 littermate control (F) and *Crb1Crb2* cKO (G) retinas. Control retinas showed an organized outer limiting membrane with adherens junctions (white arrowheads), retinal pigment epithelium and retinal nuclei alignments. *Crb1Crb2* cKO retinas showed absence of layer organization and adherens junctions. GCL, ganglion cell layer; INL, inner nuclear layer; NBL, neuroblast layer; ONL, outer nuclear layer; RPE, retinal pigmented epithelium. Scale bar, 100 μm (A–E); 5 μm (F,G).
doi:10.1371/journal.pgen.1003976.g004

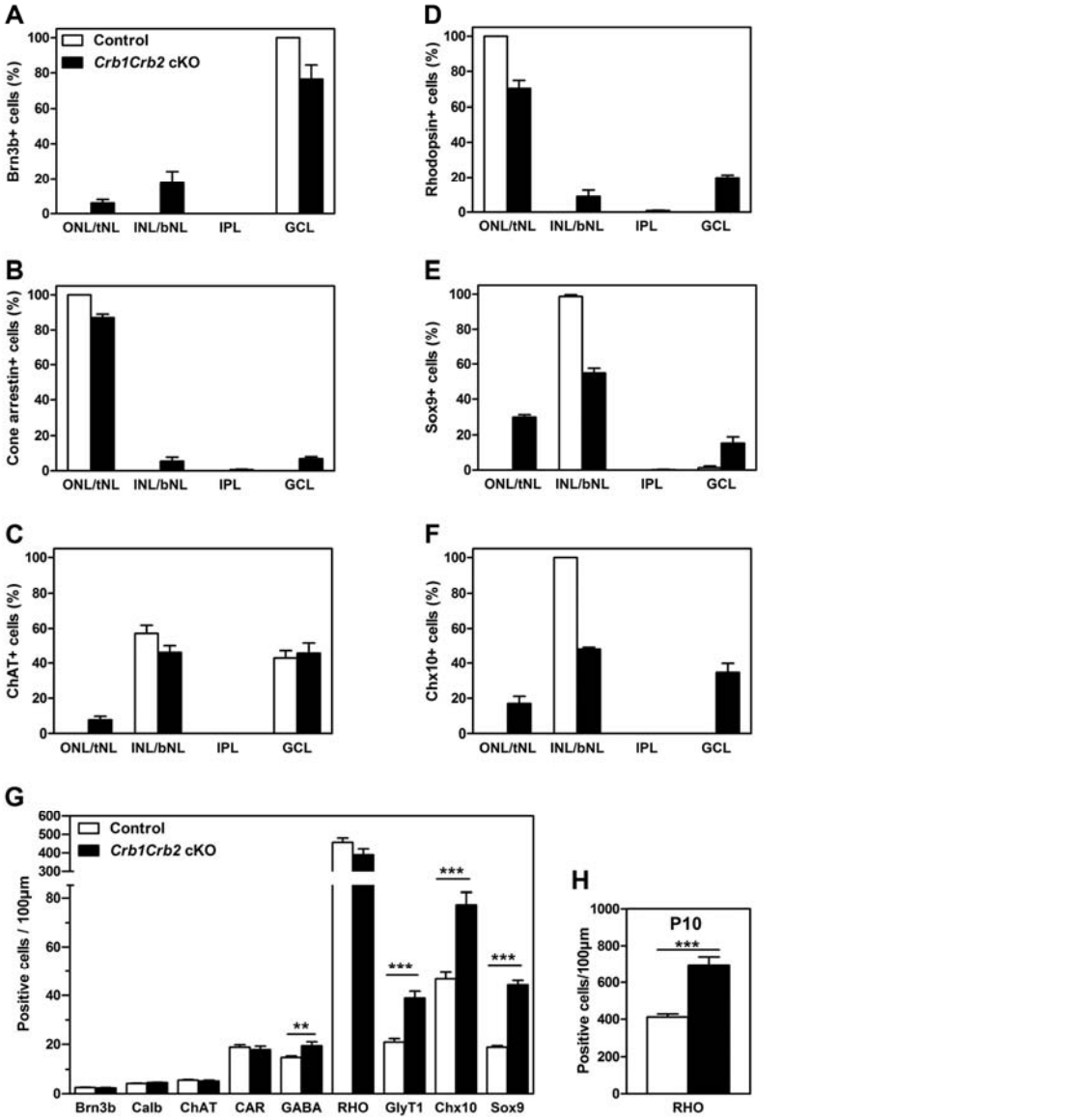

Figure 5. The number of late born cell types is increased in *Crb1Crb2* cKO retinas. The distribution of early (A–C) and late born (D–F) cell types in the three layers was quantified as a percentage of each cell type in outer, inner and ganglion cell nuclear layer in the control (white bars), and top and bottom half of nuclear layer (tNL and bNL) and ganglion cell layer in the *Crb1Crb2* cKO (black bars) retinas at P14 (3–4 different animals/genotype). The distribution of early-born ganglion cells (Brn3b), cone photoreceptors (cone arrestin) and cholinergic amacrine cells (choline acetyltransferase, ChAT) was slightly affected in contrast to late-born rod photoreceptors (rhodopsin), Müller cells (Sox9) and bipolar cells (Chx10), which were to a larger extent wrongly distributed in the two nuclear layers. (G,H) The number of cells for each cell types was quantified at P14 (G) and the rods at P10 (H) in 3–4 retinas of control and *Crb1Crb2* cKO, and represented by the mean ± s.e.m. The number of early born cells was not affected whereas the number of late born cells was increased in *Crb1Crb2* cKO compared to control retinas at P14 and the rods at P10. bNL, bottom nuclear layer; Calb, calbindin positive horizontal cells; CAR, cone arrestin; GCL, ganglion cell layer; GlyT1, glycinergic amacrine cells; INL, inner nuclear layer; IPL, Inner plexiform layer; ONL, outer nuclear layer; RHO, Rhodopsin; tNL, top nuclear layer. **P<0.01; ***P<0.001.
doi:10.1371/journal.pgen.1003976.g005

versus 8.4±0.4 cells/100 µm in cKO retinas), $BrdU^+$ (185.9±12.1 in control versus 238.8±17.5 cells/100 µm in cKO retinas) and $Ki67^+$ cells (329±8.3 in control versus 384.5±15 cells/100 µm in cKO retinas) were increased. In mice, the proportion of dividing cells decreases dramatically at the centre of the retinas from P5 onwards, whereas the progenitors at the periphery of the retina

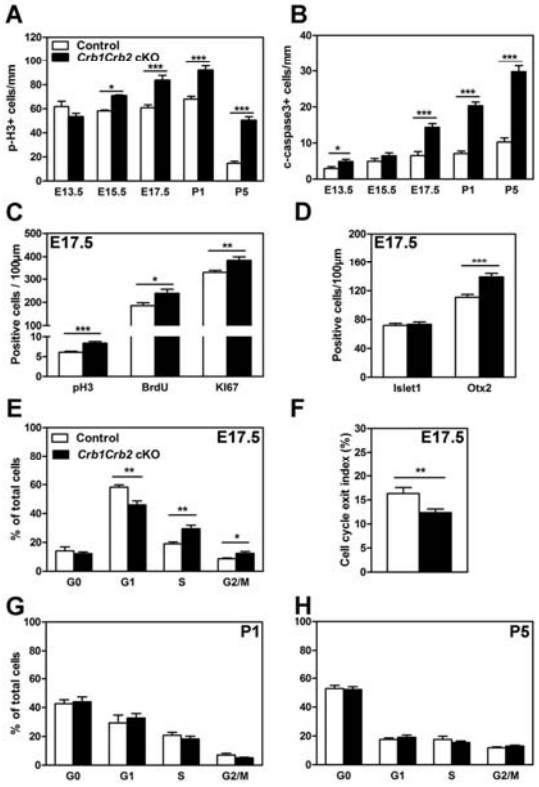

Figure 6. Loss of CRB1 and CRB2 leads to cell cycle defects, increased proliferation and apoptosis. The number of mitotic cells immunostained with anti phospho Histone H3 (pH3; A) and apoptotic cells immunostained with cleaved caspase 3 (B) were quantified from E13.5 to P5. *Crb1Crb2* cKO retinas showed a significant increased number of mitotic and apoptotic cells from E15.5 and E17.5 respectively in comparison to control retinas. At E17.5, the number of mitotic cells in the cell cycle using pH3 (M-phase), 30 min-pulse BrdU labelling (S-phase) and Ki67 immunostaining (all phases) was increased in *Crb1Crb2* cKO retinas (C). Quantification at E17.5 showed that the number of early-born (Islet1, amacrine and ganglion cells) progenitor cells was not affected whereas late-born (Otx2, photoreceptors) progenitor cells was increased in *Crb1Crb2* cKO compared to control retinas (D). Cell cycle exit index (F) was determined as the ratio of $BrdU^+/Ki67^-$ cells (no longer dividing) to total (24 hours) $BrdU^+$ cells. In *Crb1Crb2* cKO retinas less cells exit the cell cycle in the BrdU labelled population. Data from 20 representative sections/pictures of whole retinas from 3–5 control and *Crb1Crb2* cKO retinas are presented as mean ± s.e.m. Flow cytometry analysis of cell cycle in *Crb1Crb2* cKO and control retinas at E17.5 (E), P1 (G) and P5 (H) revealed that only at E17.5 the proportion of cells in the different cell cycle phases is changed compared to control. *P<0.05; **P<0.01; ***P<0.001.
doi:10.1371/journal.pgen.1003976.g006

still proliferate. Ultimately, mitosis is finished at the centre at P6 and at the periphery at P10 [3]. Surprisingly, in *Crb1Crb2* cKO retinas the number of cells in M-phase ($pH3^+$) was higher compared to the controls (Figure 6A). We further investigated this phenomenon using the Ki67 marker to analyse the proliferating cells in all phases of the cell cycle (Figure S6D,F) and found that the total number of cells was increased by a factor of two both in the centre and at the periphery at P5 (Figure S6H). In contrast to the control, some Ki67 positive cells were still present at the periphery of the retina at P10 in *Crb1Crb2* cKO retinas (data not shown). These results suggest that active proliferating cells in *Crb1Crb2* cKO retinas may reside longer than those in control retinas.

We performed flow cytometry analysis based on the DNA content and KI67 labelling at E17.5, P1 and P5 to study the proportion of cells at G1, S and G2/M phases of the cell cycle or which already exited the cell cycle in G0 (Figures 6E, G, H and S6G). At E17.5, the proportion of cells in G1 was reduced whereas the proportion of cells in S and G2/M was increased and G0 unchanged. At P1 and P5, the proportion of cells in *Crb1Crb2* cKO returned to control proportion. In addition, levels of *cyclin D1*, cyclin *E* and *c-myc* transcripts (Figure 7A) were changed suggesting also an aberrant regulation of the cell cycle in *Crb1Crb2* cKO retinas at E17.5.

We examined how the cell cycle exit was affected in the mutants by injecting BrdU at E16.5 and analysing 24 hours later (Figures 6F and S6F) [29–30]. The proportion of cells which exit the cell cycle ($BrdU^+KI67^-$) in the total population of BrdU labelled cells was significantly decreased in *Crb1Crb2* cKO retinas (12.3±0.7%) compared to control (16.3±1.3%). However, the number of $BrdU^+KI67^-$ cells per 100 µm is not significantly different (40.2±2.9) compared to control (35.3±1.8). In summary, our data suggest that the increased population of late progenitor cells and late born cells is due to dysregulation of the cell cycle at E17.5.

CRB1 and CRB2 restrain the overproliferation of the progenitors via the regulation of mitogenic signaling pathways

We investigated which proliferative signalling pathway(s) might be involved in the overproliferation of the murine progenitors in *Crb1Crb2* cKO retinas at E17.5 and in early postnatal days.

The phospho-S6 ribosomal protein (pS6RB), a downstream target of mTOR signalling, localised in the post-mitotic cells in the retina and the number of the pS6RB positive cells or pS6RB protein levels at E17.5 and P1 were unchanged in *Crb1Crb2* cKO retinas, suggesting that mTOR signalling is not affected in the retina upon removal of CRB1 and CRB2 (Figure S7D and data not shown).

No differences were observed in the primary downstream targets Gli1 and Ptch1 of sonic hedgehog signalling (Figure 7A). The downregulation of Smoothened and Gli2 might be due to a secondary effect of the loss of CRB proteins. The sonic hedgehog signalling seemed to not be directly involved in the increased number of progenitors.

In E17.5 and P1 retinas, whereas no difference in the amount of cleaved active intracellular form of Notch1 protein was detected, the transcript levels of Notch1 and its primary downstream targets Hey1 and Heyl were reduced in *Crb1Crb2* cKO compared to control (Figures 7 and S7). The Notch1 signalling might be affected following loss of CRB1 and CRB2.

The role of Wnt-β-catenin canonical signalling in retinal proliferation remains controversial. In E17.5 control retinas, P120-catenin and β-catenin localized mainly in the adherens junctions at the subapical region whereas in the *Crb1Crb2* cKO the adherens junctions were disrupted and the catenins are membrane-associated (Figure S7A–B, white arrowheads). At E17.5, levels of P120-catenin proteins were increased in *Crb1Crb2* cKO retinas, in contrast to β-catenin, whereas transcript levels were unchanged (Figures 7 and S7E–F). Furthermore, we showed that the zinc finger protein Kaiso was expressed in E17.5 and P1 developing retinas, but that its protein levels were not affected in *Crb1Crb2* cKO mice (Figures 7 and S7E). The presence of Kaiso in

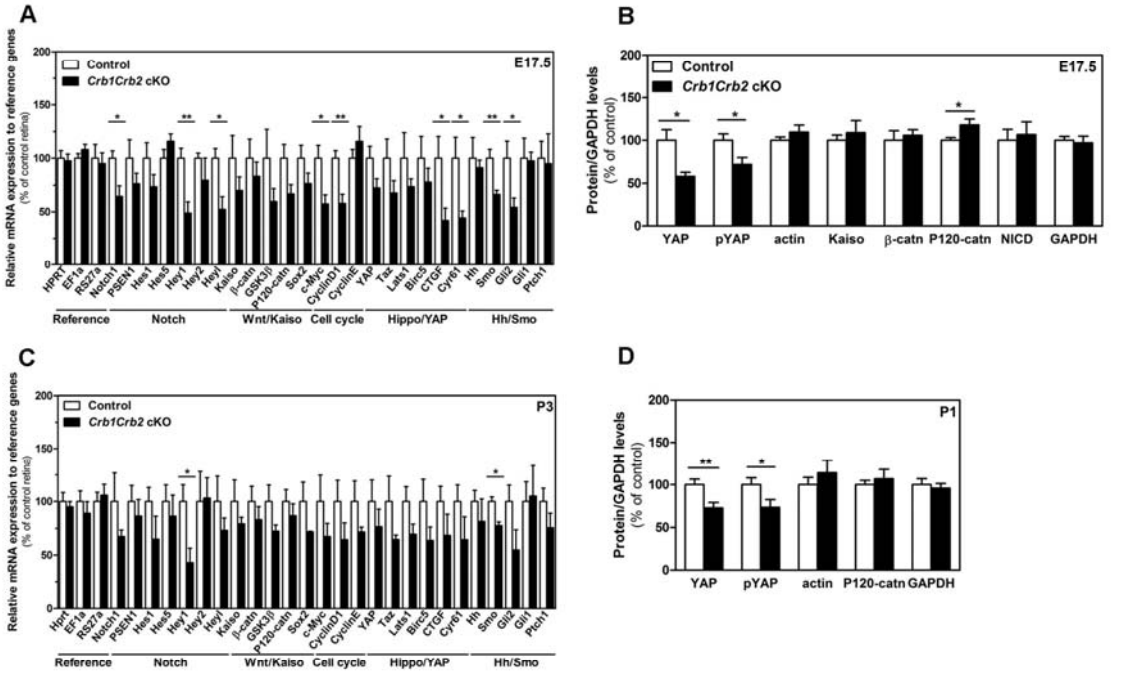

Figure 7. CRB1 and CRB2 acts on the proliferative signalling pathways. Transcript levels measured by quantitative PCR at E17.5 (A) and P3 (C) in 3–6 control and *Crb1Crb2* cKO retinas showed changes in Notch1, YAP, sonic hedgehogs and cell cycle genes at E17,5 whereas at P1 these genes were not significantly changed except Hey1 and Smoothened. Quantification of protein levels of control and *Crb1Crb2* cKO retinal lysates (N = 3–5 for each Western blot and Western blots were repeated 2–4 times) at E17.5 (B) and P1 (D). Protein levels of YAP and pYAP were reduced at E17.5 and P1 whereas P120-catenin was increased and β-catenin and Kaiso unchanged at E17.5. Data are presented as mean ± s.e.m *P<0.05; **P<0.01.
doi:10.1371/journal.pgen.1003976.g007

the retina and the increased levels of P120-catenin proteins are of interest as the inhibition of Kaiso on Wnt signalling is blocked through its interaction with P120-catenin (Figure 7E) [31,32].

Only recently, YAP, the downstream effector of the Hippo pathway, has been reported to promote the proliferation of the murine progenitors in postnatal retinas, followed by downregulation around P5 during neuronal differentiation [33]. In control mice, YAP protein was detected in progenitor nuclei, overlapping with Chx10*Cre-GFP* localization (Figure S7C). YAP localized also at the apical region where the adherens junctions and the CRB complex were located. In the *Crb1Crb2* cKO retinas, YAP localized at the remaining subapical region and only in the cytoplasm of the progenitors (Figure S7C). Phosphorylation of YAP causes its retention in the cytoplasm and binding to the adherens junctions, thus inactivating the protein [14]. Both YAP and phospho-YAP (pYAP) protein levels and the transcripts of the direct downstream targets genes CTGF and Cyr61 were reduced in *Crb1Crb2* cKO retinas at E17.5 and P1 (Figure 7B,D). The YAP signalling is affected by the loss of CRB1 and CRB2.

Discussion

One key element in the construction of the retina during development is the tight control of the proliferation and differentiation of the retinal progenitor cells by a combination of extrinsic and intrinsic influences [2]. In this study, we analyzed the effect of ablation of CRB1 and CRB2 in the murine retina and showed that levels of CRB protein control the lamination and proliferation of the progenitors. Complete loss of CRB1 and CRB2 proteins in the mouse retina mimics human LCA due to mutations in the *CRB1* gene.

The adherens junctions play a critical role in the migration of post-mitotic cells from the apical surface to their final destination [34]. Ganglion, bipolar and photoreceptor cells extend basal processes that guide nucleus translocation to their final destination. Bipolar and ganglion cells relinquish their apical attachment when translocation is complete whereas photoreceptors maintain adherens junctions with Müller glial cells. Amacrine and horizontal cells by contrast display active cellular migration without apical attachment by sensing their local environment [34]. Disruption of the apical adherens junctions/subapical region in $Crb1^{+/-}Crb2$ cKO retinas at E15.5 leads to ectopic localization of some photoreceptor and bipolar cells in the ganglion cell layer and vice versa, ganglion, amacrine and bipolar cells in the outer nuclear layer. In *Crb1Crb2* cKO mice, where the disruption occurs two days earlier, the lack of apico-basal axis leads to distribution of all the cell types in two nuclear layers and lack of a separate photoreceptor layer. Photoreceptor, ganglion and bipolar cells may undergo misguided migration due to the lack of apical attachment. The localization of the earliest born cells remains less affected, probably due to completion of migration prior to adherens junction disruption.

Apart from the role in orchestration of migration, we suggest a direct role of CRB proteins in regulation of proliferation of retinal

progenitors. *Crb1* KO retinas do not show an obvious developmental phenotype [24], and *Crb2* cKO retinas show an increase in the number of progenitors only at P3 [22]. However, the *Crb1Crb2* cKO showed increased number of mitotic cells from E15.5 to P10 and $Crb1^{+/-}Crb2$ cKO retinas at E17.5 and P5. Thus, the uncontrolled proliferation of progenitors is proportional to the lack of CRB1 and CRB2 proteins. A study on CRB-interacting protein PALS1 has shown that the CRB complex might be involved in the control of progenitor proliferation in the developing mouse cortex [9]. However, in mouse retinas, conditional knockout or knockdown of *Pals1* does not lead to increased proliferation of retinal progenitor cells [35,36]. The role of CRB protein on the proliferation of the progenitors may be independent of PALS1 and involve other partners. Ablation of CRB1 and CRB2 proteins leads to an increased number of proliferating cells and abnormalities in the cell cycle. Hence, CRB proteins restrain the proliferation acting on the cell cycle machinery. Additionally, the lack of the apical CRB1 and CRB2 had an effect on the cell cycle exit potentially directing the decision to re-enter the cell cycle and explaining the increased number of progenitors. The reduced number of cells withdrawing the cell cycle may explain why retinal progenitor cells in *Crb1Crb2* cKO retinas undergo several more cell cycles compared to control retinas, leading to an increase in number of late-born cell types and significant thickening of the retina.

Here, we report that CRB1 and CRB2 act on the proliferation of the retinal progenitor cells through dysregulation of the proliferative signalling pathways such as Notch1 and YAP/Hippo. In addition, we report the presence of Kaiso in the retina and increased level of P120-catenin at E17.5. We hypothesize that the lack of CRB1 and CRB2 leads to disruption of the adherens junction complex and release of available β- and P120-catenins in the cytoplasm and nuclei of progenitors. P120-catenin may retain Kaiso in the cytoplasm leading to the loss of inhibition of the Wnt target genes. Overexpression of P120-catenin and Kaiso has been linked to aberrant mitosis in cancer cells [37,38]. Lack of CRB proteins affects the YAP/Hippo pathway. Despite its direct role on proliferation, YAP promotes cell survival by inhibiting apoptotic pathways [14]. The decrease in YAP signalling at E17.5 and P1 in *Crb1Crb2* cKO might explain the increase in apoptosis observed.

Mutations in the *CRB1* gene cause progressive autosomal-recessive retinitis pigmentosa and LCA. *CRB1*-LCA retinas are remarkably thick and lack distinct layers as detected by optical coherence tomography [20]. Mice lacking CRB1 function show limited and mild retinal disorganization in the inferior quadrant [24 27]. Prominent differences were found between the severe loss of retinal function in humans and the mild phenotype in mice [39]. In contrast, *Crb2* cKO mice display a severe phenotype with progressive loss of photoreceptors and retinal activity mimicking *CRB1*-related retinitis pigmentosa [22]. Many genes involved in retinal dystrophies have been reported to show difference in temporal and spatial expression patterns and in their localization inside the retina [40,41]. Furthermore, compensation by other members of the same protein family occurs frequently in mice and humans such as the tumor suppressor genes during retinal development [42]. Further investigations on CRB1 and CRB2 would be needed to completely understand the difference between mice and humans.

From *Crb2* cKO, $Crb1^{+/-}Crb2$ cKO and *Crb1Crb2* cKO retina studies, the severity of the retinal disease is inversely proportional to the amount of CRB1 and CRB2 proteins which seemed to be critical for the development of the retina. As no genotype-phenotype correlation in *CRB1* retinal dystrophies has been identified [43], additional down-regulation of CRB2 function in human *CRB1*-mutant retinas might range from *CRB1*-retinitis pigmentosa to *CRB1*-LCA. Several polymorphisms in highly conserved residues have been identified in the *CRB2* gene but not directly linked to retinal dystrophies [44]. Further investigations on possible mutations in CRB complex member genes in *CRB1*-LCA versus *CRB1*-RP patients might address the question of the genotype-phenotype correlation.

Here, we report that *Crb1Crb2* retinas display a thicker retina due to excessive proliferation of late-born retinal progenitor cells and also immature layering. Moreover, *Crb1Crb2* and $Crb1^{+/-}Crb2$ cKO animals show severe loss of retinal function. *Crb1Crb2* and $Crb1^{+/-}Crb2$ cKO retinas exhibit the characteristics of human *CRB1*-LCA retinopathies, and are therefore mouse LCA models for the development of therapeutic drugs.

Materials and Methods

Animals

Animal care and use of mice was in accordance with protocols approved by the Animal Care and Use Committee of the Royal Netherlands Academy of Arts and Sciences (KNAW). All mice used were maintained on a 50% C57BL/6JOlaHsd and 50% 129/Ola genetic background. Animals were maintained on a 12 h dark/dim light cycle and supplied with food and water *ad libitum*. *Crb1* KO mice [24] and $Crb2^{F/F}$Chx10$Cre^{Tg/+}$ clone P1E9 (*Crb2* cKO) generated previously [22] were crossed to generate $Crb1^{+/-}Crb2^{F/F}$Chx10$Cre^{Tg/+}$ ($Crb1^{+/-}Crb2$ cKO) and $Crb1^{-/-}Crb2^{F/F}$Chx10$Cre^{Tg/+}$ (*Crb1Crb2* cKO). *Crb1Crb2* cKO retinas were compared to littermate $Crb1^{-/-}Crb2^{F/F}$ and $Crb1^{-/-}Crb2^{F/+}$Chx10$Cre^{Tg/+}$ retinas and $Crb1^{+/-}Crb2$ cKO to littermate $Crb1^{+/-}Crb2^{F/+}$ cKO. Chromosomal DNA isolation and genotyping were performed as previously described [22].

In vivo analysis

Scanning laser ophthalmoscopy (SLO), spectral domain optical coherence tomography (SD-OCT) and electroretinography (ERG) measurements were performed at 1, 3, 6 and 12 month in 4 to 6 animals of each genotype. Electroretinograms were recorded binocularly as described previously [45]. Single-flash responses were obtained under scotopic (dark-adapted overnight) and photopic (light-adapted with a background illumination of 30 cd/m^2 starting 10 minutes before recording) conditions. Single white-flash stimuli ranged from −4 to 1.5 log cd s/m^2 under scotopic and from −2 to 1.5 log cd s/m^2 under photopic conditions. Ten responses were averaged with inter-stimulus intervals of 5 s (for −4 to −0.5 log cd s/m^2) or 17 s (for 0 to 1.5 log cd s/m^2). Retinal morphology of the anesthetized animals was visualized via SLO imaging with a HRA 1 and HRA 2 (Heidelberg Engineering, Heidelberg, Germany) according to previously described procedures (Text S1) [46]. SD-OCT imaging was performed with a commercially available Spectralis HRA+OCT device from Heidelberg Engineering. This equipment features a broadband superluminescent diode at $\lambda = 870$ nm as low coherent light source (Text S1) [47].

Morphological analysis

Eyes were collected from embryonic day E11.5 to 12M (n = 3 5/age/group) and were fixed at room temperature with 4% paraformaldehyde in PBS. Eyes were dehydrated in ethanol and embedded in Technovit 7100 (Kulzer, Wehrheim, Germany) and sectioned (3 μm). Slides were dried, counterstained with 0.5% toluidine blue and mounted under coverslips using Entellan (Merk, Darmstadt, Germany). The thickness of the retina in *Crb1Crb2* cKO mice from P8 to 12M was measured from the outer limiting

membrane to the inner limiting membrane (from top to bottom of *Crb1Crb2* cKO retinas) at exactly 1 mm apart from the optic nerve and the average of the ventral and dorsal measurement was compared to the dorsal measurement of control mice.

Standard transmission electron microscopy

E17.5 and 1M old mice were perfused with 4% paraformaldehyde, 2% glutaraldehyde in 0.1 M cacodylate buffer pH 7.4. After the retinas were dissected free, they were post-fixed in 1% osmium tetroxide. Tissues were thoroughly rinsed and stained with 2% uranyl acetate in 70% ethanol. Samples were then dehydrated in a graded series of ethanol and embedded in epon 812 (Polysciences). Ultrathin sections were examined with a Zeiss 912 electron microscope.

Quantification of apoptotic, proliferating and retinal cells

Positive cells (Table S1) from 20 30 representative sections of the whole retina from 3 5 different control or experimental animals were manually counted and corrected by the length of each section (measured using ImageJ software fiji-win32). Retina sections of E13.5 to P5 were stained with cleaved Caspase 3 (cCasp3; marker for apoptotic cells) and phospho-Histone H3 (pH3; marker for M-phase mitotic cells) antibodies.

To examine the proportion of progenitors in S-phase, pregnant females were injected with BrdU (50 µg/g body weight) at E17.5 and embryos were collected 30 min after BrdU injection. To examine the number of progenitors which exit the cell cycle, pregnant females were injected with BrdU at E16.5 and embryos were collected 24 h later. The number of $BrdU^{+}Ki67^{-}$ cells represents the number of cells which have exited the cell cycle. The number of retinal cells at P14 was counted on 20 30 representative pictures of retinas stained with specific antibodies for each cell type. Cones, rods, horizontal, Müller and ganglion cells were counted using cone arrestin, rhodopsin, calbindin, Sox9/glutamine synthetase and Brn3B antibodies, respectively. Bipolar cells were counted using PKCα staining and *Cre-GFP* expression (GFP is fused to the Cre in Chx10*Cre* mouse line). Subsets of amacrine cell types were stained using choline acetyltransferase (ChAT), GABA, and GlyT1 antibodies.

Flow cytometry

These experiments were performed similarly to [29]. Retinas from at least 4 controls and *Crb1Crb2* cKO were isolated and mechanically dissociated with colagenase/DNAse I (370 U) at 37°C. Cells were fixed with 4% paraformaldehyde in PBS for 5 minutes followed by fixation in ethanol 70% one hour at 4°C. Cells were labelled with KI67 antibody diluted 1/50 in PBS-0.5% Tween-20-BSA 0.1% (PBS-TB) overnight at 4°C followed by goat anti-mouse-Alexa 488 antibody diluted 1/500 in PBS-TB. DNA content was labelled with PBS-TB containing 100 µg/ml RNase A 30 minutes at 37°C followed by 100 µg/ml propidium iodide 30 minutes. Cells analysis was performed using the flow cytometer BD LSR Fortessa. See more details about the analysis in Text S1.

Western blotting

The E17.5 and P1 retinas from at least 3 *Crb1Crb2* cKO or control littermate mice were isolated, homogenized and incubated on ice in 20 µL of lysis buffer (10% glycerol, 150 mM NaCl, 1 mM EGTA, 0.5% Triton x-100, 1 mM PMSF, 1.5 mM $MgCl_2$, 10 µg/µL aprotin, 50 mM Hepes pH 7.4 and protease inhibitor cocktail). Retina extracts from 3 independent control and *Crb1Crb2* cKO animals were fractionated by SDS-PAGE electrophoresis, using 4 12% precast gels (NuPage Novex Bis-Tris Mini Gels, Invitrogen). After transfer to nitrocellulose membrane and blocking in 5% BSA in T-TBS buffer (Tris-HCL 50 mM pH7.5, 200 mM NaCl, 0.05% Tween-20), the primary antibodies (table S1) were diluted 1/1000 in T-TBS-5% BSA and incubated overnight at 4°C. After washing, they were incubated with the appropriate secondary antibodies (conjugated to DyLight Dye-800, Li-COR Odyssey or to cyanine 5) diluted 1/5000 in T-TBS buffer. After washing, the blots were then scanned using LI-COR Odyssey IR Imager. Densitometry of bands was performed in ImageJ. The densitometry for each band was subtracted to the background and normalized with GAPDH densitometry from the same sample.

Real-time quantitative PCR

RNA was isolated from 3 6 control and *Crb1Crb2* cKO retinas using TRIZOL reagent (Gibco life technologies), according to the manufacturer manual, and after the final precipitation dissolved in RNase-free water. After genomic DNA degradation with RNase-free DNase I (New England Biolabs), 1 µg of total RNA was reverse transcribed into first-strand cDNA with Superscript III Plus RNase H-Reverse Transcriptase (Invitrogen) and 50 ng random hexamer primers, during 50 min at 50°C in a total volume of 20 µl. To the resulting cDNA sample, 14 µl of 10 mM Tris, 1 mM EDTA was added. From all samples, a 1:20 dilution was made and used for qPCR analysis. For this analysis, primer pairs were designed with a melting temperature of 60 62°C, giving rise to an amplicon of 80 110 bp. Real-time qPCR was based on the real-time monitoring of SYBR Green I dye fluorescence on a ABI Prism 7300 Sequence Detection System (Applied Biosystems, Nieuwekerk a/d IJssel, The Netherlands). The PCR conditions were as follows: 12.5 µL SYBR Green PCR 2× mastermix (Applied Biosystems), 20 pmol of primers, and 2 µl of the diluted cDNA (ca 3 ng total RNA input). An initial step of 50°C for 2 min was used for AmpErase incubation followed by 15 min at 95°C to inactivate AmpErase and to activate the AmpliTaq. Cycling conditions were as follows: melting step at 95°C for 1 min, annealing at 58°C for 1 min and elongation at 72°C, for 40 cycles. At the end of the PCR run, a dissociation curve was determined by ramping the temperature of the sample from 60 to 95°C while continuously collecting fluorescence data. Non template controls were included for each primer pair to check for any significant levels of contaminants. Values were normalized by the mean of the 3 reference genes hypoxanthine-guanine phosphoribosyltransferase, elongation factor 1-a and ribosomal protein S27a.

Statistical analysis

Normality of the distribution was tested by Kolmogorov-Smirnov test. Statistical significance was calculated by using *t*-test of 3 5 independent retinas (20 sections)/genotype/age. Values are expressed as mean ± s.e.m. Values of $^{*}P<0.05$, $^{**}P<0.01$, $^{***}P<0.001$ were considered to be statistically significant. Calculations and graphs were generated using GraphPad Prism 5.

Supporting Information

Figure S1 Retinal activity in *Crb1Crb2* mutant retinas is severely impaired. (A C) Single-flash electroretinogram age series in double heterozygote $Crb1^{+/-}Crb2^{F/+}$ cKO (blue), $Crb1^{+/-}Crb2$ cKO (purple) and *Crb1Crb2* cKO mice (red) at 1M (A), 3M (B) and 6M (C). Scotopic b-wave amplitudes were plotted as a function of the logarithm of the flash intensity. Boxes indicate the 25% and 75% quantile range, whiskers indicate the 5% and 95% quantiles, and solid lines connect the medians of the data. In affected $Crb1^{+/}$

$^{-}$*Crb2* cKO and *Crb1Crb2* cKO mice, the b-wave amplitude was already considerably reduced at the age of 1M under both scotopic and photopic conditions, and declined even at 3M and 6M to a flat electroretinogram.
(TIF)

Figure S2 *In vivo* retinal imaging in $Crb1^{+/-}Crb2$ cKO mice. $Crb1^{+/-}Crb2$ cKO mice were examined with scanning laser ophthalmoscopy (A,D,G), spectral domain optical coherence tomography (B,C,E,F,H,I) at the age of 1M (A C). 3M (D F) and 6M (G I). Due to the fact that younger mice from this genotype did not show morphological alterations (data not shown), 12M $Crb1^{+/-}Crb2^{F/+}$ cKO were used as controls, and even here no abnormalities were found neither in the native fundus image, nor in the autofluorescence or the retinal vasculature (Figure 3). The retinal organization was also unaffected, as observed by optical coherence tomography analysis (Figure 3). $Crb1^{+/-}Crb2$ cKO animals already at 1M showed a spotty fundus, as well as several degeneration sites represented by the presence of fluorescent material detectable at 488 nm (A). In the optical coherence tomography analysis, a decrease in the retinal thickness was observed as well as a wavy appearance of the outer plexiform layer together with the formation of structures like rosettes located in the outer nuclear layer (B,C). At 3M, the retinal thickness was further decreased, specially at the level of the outer nuclear layer (E,F). In the autofluorescence image, many hyper and hypo fluorescent regions as well as a several vascular changes indicating neovascularization processes were observed (D). Six month old individuals presented a more severe degeneration ascertained by scanning laser ophthalmoscopy (G) and optical coherence tomography (H,I). Abbreviations: AF, autofluorescence; d, dorsal; FA, fluorescein angiography; RF, red free; v, ventral.
(TIF)

Figure S3 Loss of Crumbs complex and adherens junctions, ectopic synapses and cell death in *Crb1Crb2* cKO retina. Confocal immunohistofluorescent representative pictures of CRB1 and CRB2, adherens junction marker (Nectin1), Crumbs complex members (PALS1 and MUPP1), OPL ribbon synapse markers (PSD95 and PKCα for bipolar cells) in control (left panel) and *Crb1Crb2* cKO (right panel) retinas at P14 (A D). Adherens junctions and CRB complex proteins were totally absent in the subapical region, except in photoreceptor rosettes which contained few wild type cells still expressing CRB2 in *Crb1Crb2* cKO (A B, D; white arrowheads). The synapses between photoreceptor and bipolar cells located normally in the OPL were found ectopically localized throughout the retina thickness in *Crb1Crb2* cKO (C; white arrowheads). Confocal immunohistofluorescent representative pictures of apoptotic cells (cCaspase 3) in the nuclear layer of *Crb1Crb2* cKO at P14 (E) and 3M (F). Cleaved caspase 3 positive cells were rods (Rhodopsin) at P14 and mainly bipolar cells (Chx10*Cre-GFP*) at 3M. GCL, ganglion cell layer; INL, inner nuclear layer; NL, nuclear layer; ONL, outer nuclear layer; OPL, outer plexiform layer; RPE, retinal pigmented epithelium; SAR, subapical region. Scale bar: 50 μm (A D); 25 μm (E F).
(TIF)

Figure S4 Loss of adherens junctions, CRB and PAR complexes in embryonic *Crb1Crb2* cKO retina. Confocal immunohistofluorescent representative pictures of CRB2 (D), adherens junction marker (Nectin1, B), CRB complex member (PALS1, A) and PAR complex member (PAR3, C) of control (left panel) and *Crb1Crb2* cKO (right panel) retinas at E15.5. Areas with completely disrupted outer limiting membrane showed loss of expression of adherens junction, CRB and PAR complex markers, except in pseudo-rosettes of progenitor cells which contained few wild type cells still expressing CRB2. Electron microscopic zoom pictures at the adherens junctions of E17.5 littermate control (E) and *Crb1Crb2* cKO (F) retinas. *Crb1Crb2* cKO retinas showed completely absence of adherens junctions at the outer limiting membrane. GCL, ganglion cell layer; NBL, neuroblast layer; RPE, retinal pigmented epithelium; SAR, subapical region. Scale bar: 50 μm (A D); 1 μm (E F).
(TIF)

Figure S5 Ectopic localization of cell types in $Crb1^{+/-}Crb2$ cKO and *Crb1Crb2* cKO retinas. The cell types were immunostained with Brn3b for ganglion cells (A), cone arrestin (CAR) for cone photoreceptors (B), choline acetyltransferase for early born cholinergic amacrine cells (C), Sox9 and glutamine synthetase for Müller cells (E) and PKCα and nuclear *Cre-GFP* under the Chx10 promoter for bipolar cells (F) at P14 and Rhodopsin for rod photoreceptors at P10 (D) in control and *Crb1Crb2* cKO. Some ectopic ganglion and cholinergic-amacrine cells localize in rosettes in the vicinity of the retinal pigment epithelium and established dendrites in the lumen. Few ectopic cone photoreceptors are found in the ganglion cell layer. In contrast, the late born rod photoreceptors, Müller glial cells and bipolar cells localize in the two thick nuclear layers. Retinal sections are stained with rhodopsin for rods and cone arrestin for cones and the presence of nuclear GFP for bipolar cells is due to the *Cre-GFP* under the Chx10 promoter in the Chx10*Cre* transgenic line in $Crb1^{+/-}Crb2$ cKO retinas at P10 (G H). Rod and cone photoreceptors are present in the rosettes and segments are present in the lumen. The cells that ectopically localize in the ganglion cell layer in these mutant mice are rod and cone photoreceptors and bipolar cells (H). Retinal sections are stained with calretinin for ganglion and amacrine cells and bipolar cells with the nuclear Cre- GFP in $Crb1^{+/-}Crb2$ cKO retinas at P10 (I J). The second type of rosettes is formed of ganglion and amacrine cells surrounded by bipolar cells. GCL, ganglion cell layer; INL, inner nuclear layer; NL, nuclear layer; ONL, outer nuclear layer. Scale bar: 50 μm.
(TIF)

Figure S6 Overproliferation of retinal progenitor cells in $Crb1^{+/-}Crb2$ cKO and *Crb1Crb2* cKO retinas. The number of mitotic cells immunostained with anti-phospho-Histone H3 (pH3; A) and apoptotic cells immunostained with cleaved caspase 3 (B) were quantified from E15.5 to P5 in 10 15 representative pictures of whole retinas from 3 5 control and $Crb1^{+/-}Crb2$ cKO retinas. Mutant retinas showed a significant increase in the number of mitotic and apoptotic cells at E17.5. At P5 an increase in the number of mitotic and a decrease in the number of apoptotic cells are observed. Mitotic cells were immunostained with pH3 immunostaining (M-phase) and Ki67 immunostaining (M, G2, S and late G1 phases) and counterstained with DAPI in representative pictures of control (left panel) and *Crb1Crb2* cKO (right panel) retinas at E17.5 (C) and in the center of the retina at P5 (D). The mitotic cells displayed an aberrant distribution in *Crb1Crb2* cKO retinas, especially the M-phase cells in E17.5 retina, which in the control localized at the outer limiting membrane whereas in *Crb1Crb2* cKO retina these cells had a scattered distribution throughout the whole neuroblast layer (C). At P5 in the centre of the retina few $Ki67^{+}$ cells were detected, whereas in *Crb1Crb2* cKO retina many cells were still dividing especially in M-phase (D). Immunostaining of E17.5 retinal sections of control and *Crb1Crb2* cKO was performed with Ki67 and BrdU antibodies after 30 min pulse (E) or 24 hours (F) of BrdU labelling and counterstained with DAPI for nuclear staining. Ki67 and BrdU positive cells localized through the entire thickness of *Crb1Crb2* cKO. Flow cytometry

profiles of control and *Crb1Crb2* cKO retinal cells at E17.5 (G) based on Ki67 labelling and DNA content. The number of total proliferating cells using Ki67 immunostaining is increased by a factor two in *Crb1Crb2* cKO retinas at P5 (H). Scale bar: 50 μm. ***P<0.001.
(TIF)

Figure S7 CRB1 and CRB2 act on proliferative signalling pathways. Representative pictures of P120-catenin (A), β-catenin (B) and YAP with *Chx10Cre-GFP* (C) of control and *Crb1Crb2* cKO retinas at E17.5. P120- and β-catenins, which normally localized at the adherens junctions were found in ectopic rosette structures (white arrowheads). YAP protein normally localized at the subapical region adjacent to adherens junctions and in the nuclei of the retinal progenitors (colocalization with Chx10*Cre-GFP*) whereas YAP was found only in ectopic rosette structures (white arrowheads) similarly to the catenins and in the cytoplasm of the retinal progenitors in *Crb1Crb2* cKO retinas. Quantification of the number of phospho-ribosomal protein positive cells (D) showed no difference between control and *Crb1Crb2* cKO retinas at E17.5 and P1. Representative Western Blot of YAP, pYAP, Notch intracellular domain (NICD), Kaiso, β-catenin (β-catn), P120-catenin (P120-catn), actin and Glyceraldehyde 3-phosphate dehydrogenase (GAPDH) at E17.5 (E) and P1 (F). Scale bar: 50 μm. Values are presented as mean ± s.e.m.
(TIF)

Table S1 Antibody list and dilution used for immunohistochemistry.
(DOC)

Text S1 Detailed Materials and Methods of *In vivo* analysis, immunohistochemical analysis and flow cytometry.
(DOC)

Acknowledgments

The authors thank Penny Hartsuiker, Feline Spiering, Christian Kerker, Oswald Kraaikamp and Mathilde Hoogerwerf for technical assistance, and Lisa-Milou Bouma for contributing data. The authors also thank Robert M. Hoek for advice on the manuscript.

Author Contributions

Conceived and designed the experiments: LPP JW MWS ALB. Performed the experiments: LPP CHA PMQ RMV DMSL JJD NT SCB GH VS MGG FR. Analyzed the data: LPP CHA PMQ RMV DMSL JJD JW NT SCB GH VS MGG MWS FR ALB. Contributed reagents/materials/analysis tools: BH. Wrote the paper: LPP JW.

References

1. Andreazzoli M. (2009) Molecular regulation of vertebrate retina cell fate. Birth Defects Res C Embryo Today 87: 284 295.
2. Livesey FJ, Cepko CL. (2001) Vertebrate neural cell-fate determination: lessons from the retina. Nat Rev Neurosci 2: 109 118.
3. Young RW. (1985) Cell differentiation in the retina of the mouse. Anat Rec 212: 199 205.
4. Agathocleous M, Harris WA. (2009) From progenitors to differentiated cells in the vertebrate retina. Annu Rev Cell Dev Biol 25: 45 69.
5. Burmeister M, Novak J, Liang MY, Basu S, Ploder L, et al. (1996) Ocular retardation mouse caused by Chx10 homeobox null allele: impaired retinal progenitor proliferation and bipolar cell differentiation. Nat Genet 12: 376 384.
6. Martin-Belmonte F, Perez-Moreno M. (2011) Epithelial cell polarity, stem cells and cancer. Nat Rev Cancer 12: 23 38
7. Tepass U, Theres C, Knust E. (1990) crumbs encodes an EGF-like protein expressed on apical membranes of Drosophila epithelial cells and required for organization of epithelia. Cell 61:787 799.
8. Bulgakova NA, Knust E. (1990) The Crumbs complex: from epithelial-cell polarity to retinal degeneration. J Cell Sci 122: 2587 2596.
9. Kim S, Lehtinen MK, Sessa A, Zappaterra MW, Cho SH, et al. (2010) The apical complex couples cell fate and cell survival to cerebral cortical development. Neuron 66: 69 84.
10. Herranz H, Stamataki E, Feiguin F, Milán M. (2006) Self-refinement of Notch activity through the transmembrane protein Crumbs: modulation of gamma-secretase activity. EMBO Rep 7: 297 302.
11. Mitsuishi Y, Hasegawa H, Matsuo A, Araki W, Suzuki T, et al. (2010) Human CRB2 inhibits gamma-secretase cleavage of amyloid precursor protein by binding to the presenilin complex. J Biol Chem 285: 14920 14931.
12. Ohata S, Aoki R, Kinoshita S, Yamaguchi M, Tsuruoka-Kinoshita S, et al. (2011) Dual roles of Notch in regulation of apically restricted mitosis and apicobasal polarity of neuroepithelial cells. Neuron 69: 215 230.
13. Massey-Harroche D, Delgrossi MH, Lane-Guermonprez L, Arsanto JP, Borg JP, et al. (2007) Evidence for a molecular link between the tuberous sclerosis complex and the Crumbs complex. Hum Mol Genet 16: 529 536.
14. Zhao B, Tumaneng K, Guan KL. (2011) The Hippo pathway in organ size control, tissue regeneration and stem cell self-renewal. Nat Cell Biol 13: 877 883.
15. Chen CL, Gajewski KM, Hamaratoglu F, Bossuyt W, Sansores-Garcia L, et al. (2010) The apical-basal cell polarity determinant Crumbs regulates Hippo signaling in Drosophila. Proc Natl Acad Sci U S A 107: 15810 15815.
16. Robinson BS, Huang J, Hong Y, Moberg KH. (2010) Crumbs regulates Salvador/Warts/Hippo signaling in Drosophila via the FERM-domain protein Expanded. Curr Biol 20: 582 590.
17. Varelas X, Samavarchi-Tehrani P, Narimatsu M, Weiss A, Cockburn K, et al. (2010) The Crumbs complex couples cell density sensing to Hippo-dependent control of the TGF-β-SMAD pathway. Dev Cell 19: 831 844.
18. Richard M, Roepman R, Aartsen WM, van Rossum AG, den Hollander AI, et al. (2006) Towards understanding CRUMBS function in retinal dystrophies. Hum Mol Genet 15: 235 243.
19. den Hollander AI, Roepman R, Koenekoop RK, Cremers FP. (2008) Leber congenital amaurosis: genes, proteins and disease mechanisms. Prog Retin Eye Res 27: 391 419.
20. Jacobson SG, Cideciyan AV, Aleman TS, Pianta MJ, Sumaroka A, et al. (2003) Crumbs homolog 1 (*CRB1*) mutations result in a thick human retina with abnormal lamination. Hum Mol Genet 12: 1073 1078.
21. den Hollander AI, Ghiani M, de Kok YJ, Wijnholds J, Ballabio A, et al. (2002) Isolation of *Crb1*, a mouse homologue of Drosophila crumbs, and analysis of its expression pattern in eye and brain. Mech Dev 110: 203 207.
22. Alves CH, Sanz Sanz A, Park B, Pellissier LP, Tanimoto N, et al. (2013) Loss of CRB2 in the mouse retina mimics human Retinitis Pigmentosa due to mutations in the *CRB1* gene. Hum Mol Genet 22: 35 50.
23. van Rossum AG, Aartsen WM, Meuleman J, Klooster J, Malysheva A, et al. (2006) Pals1/Mpp5 is required for correct localization of *Crb1* at the subapical region in polarized Muller glia cells. Hum Mol Genet 15: 2659 2672.
24. van de Pavert SA, Kantardzhieva A, Malysheva A, Meuleman J, Versteeg I, et al. (2004) Crumbs homologue 1 is required for maintenance of photoreceptor cell polarization and adhesion during light exposure. J Cell Sci 117: 4169 4177.
25. van de Pavert SA, Sanz AS, Aartsen WM, Vos RM, Versteeg I, et al. (2007) *Crb1* is a determinant of retinal apical Müller glia cell features. Glia 55: 1486 1497.
26. van de Pavert SA, Meuleman J, Malysheva A, Aartsen WM, Versteeg I, et al. (2007) A single amino acid substitution (Cys249Trp) in *Crb1* causes retinal degeneration and deregulates expression of pituitary tumor transforming gene Pttg1. J Neurosci 27: 564 573.
27. Mehalow AK, Kameya S, Smith RS, Hawes NL, Denegre JM, et al. (2003) *CRB1* is essential for external limiting membrane integrity and photoreceptor morphogenesis in the mammalian retina. Hum Mol Genet 12: 2179 2189.
28. Rowan S, Cepko CL. (2004) Genetic analysis of the homeodomain transcription factor Chx10 in the retina using a novel multifunctional BAC transgenic mouse reporter. Dev Biol 271: 388 402.
29. Sakagami K, Gan L, Yang XJ. (2009) Distinct effects of Hedgehog signaling on neuronal fate specification and cell cycle progression in the embryonic mouse retina. J Neurosci 29: 6932 6944.
30. Das G, Choi Y, Sicinski P, Levine EM. (2009) Cyclin D1 fine-tunes the neurogenic output of embryonic retinal progenitor cells. Neural Dev 4: 15.
31. Park JI, Kim SW, Lyons JP, Ji H, Nguyen TT, et al. (2005) Kaiso/p120-catenin and TCF/beta-catenin complexes coordinately regulate canonical Wnt gene targets. Dev Cell 8: 843 854.
32. Park JI, Ji H, Jun S, Gu D, Hikasa H, et al. (2006) Frodo links Dishevelled to the p120-catenin/Kaiso pathway: distinct catenin subfamilies promote Wnt signals. Dev Cell 11: 683 695.
33. Zhang H, Deo M, Thompson RC, Uhler MD, Turner DL. (2012) Negative regulation of Yap during neuronal differentiation. Dev Biol 361: 103 115.
34. Reese BE. (2011) Development of the retina and optic pathway. Vision Res 51: 613 632.
35. Cho SH, Kim JY, Simons DL, Song JY, Le JH, et al. (2012) Genetic ablation of Pals1 in retinal progenitor cells models the retinal pathology of Leber congenital amaurosis. Hum Mol Genet 21: 2663 2676.

36. Park B, Alves CH, Lundvig DM, Tanimoto N, Beck SC, et al. (2011) PALS1 is essential for retinal pigment epithelium structure and neural retina stratification. J Neurosci 31: 17230 17241.
37. Chartier NT, Oddou CI, Lainé MG, Ducarouge B, Marie CA, et al. (2007) Cyclin-dependent kinase 2/cyclin E complex is involved in p120 catenin (p120ctn)-dependent cell growth control: a new role for p120ctn in cancer. Cancer Res 67: 9781 9790.
38. Jiang G, Wang Y, Dai S, Liu Y, Stoecker M, et al. (2012) P120-catenin isoforms 1 and 3 regulate proliferation and cell cycle of lung cancer cells via β-catenin and Kaiso respectively. PLoS One 7:e30303.
39. Aleman TS, Cideciyan AV, Aguirre GK, Huang WC, Mullins CL, et al. (2011) Human *CRB1*-associated retinal degeneration: comparison with the rd8 *Crb1*-mutant mouse model. Invest Ophthalmol Vis Sci 52: 6898 6910.
40. Trifunovic D, Karali M, Camposampiero D, Ponzin D, Banfi S, et al. (2008) A high-resolution RNA expression atlas of retinitis pigmentosa genes in human and mouse retinas. Invest Ophthalmol Vis Sci 49: 2330 2336.
41. Bibb LC, Holt JK, Tarttelin EE, Hodges MD, Gregory-Evans K, et al. (2001) Temporal and spatial expression patterns of the CRX transcription factor and its downstream targets. Critical differences during human and mouse eye development. Hum Mol Genet 10: 1571 1579.
42. Donovan SL, Schweers B, Martins R, Johnson D, Dyer MA. (2006) Compensation by tumor suppressor genes during retinal development in mice and humans. BMC Biol 4: 14.
43. Bujakowska K, Audo I, Mohand-Saïd S, Lancelot ME, Antonio A, et al. (2012) *CRB1* mutations in inherited retinal dystrophies. Hum Mutat 33: 306 315.
44. van den Hurk JA, Rashbass P, Roepman R, Davis J, Voesenek KE, et al. (2005) Characterization of the Crumbs homolog 2 (CRB2) gene and analysis of its role in retinitis pigmentosa and Leber congenital amaurosis. Mol Vis 11: 263 273.
45. Tanimoto N, Muehlfriedel RL, Fischer MD, Fahl E, Humphries P, et al. (2009) Vision tests in the mouse: functional phenotyping with electroretinography. Front Biosci 14: 2730 2737.
46. Seeliger MW, Beck SC, Pereyra-Muñoz N, Dangel S, Tsai JY, et al. (2005) In vivo confocal imaging of the retina in animal models using scanning laser ophthalmoscopy. Vision Res 45: 3512 3519.
47. Fischer MD, Huber G, Beck SC, Tanimoto N, Muehlfriedel R, et al. (2009) Non invasive, in vivo assessment of mouse retinal structure using optical coherence tomography. PLoS One 4:e7507.

Chapter 24

Optimized Technique for Subretinal Injections in Mice

Regine Mühlfriedel, Stylianos Michalakis, Marina Garcia Garrido, Martin Biel, and Mathias W. Seeliger

Abstract

Subretinal injections in mice become increasingly important. Currently, the most prominent application is in gene therapy of inherited eye diseases by means of viral vector delivery to photoreceptors or the retinal pigment epithelium (RPE). Since there are no large animal models for most of these diseases, genetically modified mouse models are commonly used in preclinical proof-of-concept studies. However, because of the relatively small mouse eye, adverse effects of the subretinal delivery procedure itself may interfere with the therapeutic outcome. The protocol described here concerns a transscleral *pars plana* subretinal injection in small eyes, and may be used for but not limited to virus-mediated gene transfer.

Key words: Recombinant adeno-associated virus, Gene delivery, Subretinal injection, Transscleral *pars plana* injection, Retina, Mouse eye, Ablation, Bleb formation, Photoreceptor cell

1. Introduction

Recombinant, replication-deficient adeno-associated viral (rAAV) vectors are increasingly used in gene therapy trials in the central nervous system (1–3) and are a promising tool for human gene therapy of hereditary retinal diseases (4–6). As many such vision-threatening disorders are caused by mutations in photoreceptor and/or retinal pigment epithelium (RPE) genes, the currently best strategy for gene therapy is by local viral vector delivery via subretinal injection. The subretinal space is particularly well suited for transfection because injected material gets in direct contact with both photoreceptors (PhR) and RPE cells. Up to now, different routes of injection were described: (a) subretinal injections via a transcorneal route passing lens and vitreous (7–9) as well as (b) transscleral route entering *pars plana* at the limbus or *ora serrata* (10, 11). Recently, rAAVs have been successfully applied in experimental studies for the treatment of retinal dysfunctions or retinal

Bernhard H.F. Weber and Thomas Langmann (eds.), *Retinal Degeneration: Methods and Protocols*, Methods in Molecular Biology, vol. 935, DOI 10.1007/978-1-62703-080-9_24, © Springer Science+Business Media, LLC 2013

degenerative diseases (12–17). However, there are studies that have not succeeded to restore function in other cases (18, 19). Apart from disease model-specific causes, an important factor that may influence the outcome is the quality of vector administration. Despite recent improvements in the development of specific promoters and viral capsids, little efforts have been made so far to study and potentially optimize the procedures for subretinal delivery (20, 21). The injection technique described here bases on our experience with successfully treated gene-deficient mouse lines (22).

2. Materials

2.1. Anesthesia, Solutions, and Agents

1. Purified virus stored at −80 °C (vector titer: 3×10^8 to 8×10^9 vector genomes/µl).
2. Mixture of ketamine (working solution: 66.7 mg/kg) and xylazine (working solution: 11.7 mg/kg).
3. Tropicamide eye drops (Mydriaticum Stulln, Pharma Stulln GmbH, Germany).
4. Carbomer hydrogel (Vidisic®, Dr. Mann Pharma, Berlin).
5. Dexamethason and Gentamicin ointment (Dexamytrex®, Bausch & Lomb, Berlin).
6. Acetone.

2.2. Surgical Instruments and Supplies

1. Operating microscope (Zeiss, Germany).
2. Glass syringe (WPI Nanofil syringe 10 µl, World Precision Instruments, Berlin).
3. Sterile needles (34-gauges with 25° beveled tip, WPI).
4. Sterile curved surgical forceps.
5. Glass cover slips (7–10 mm in diameter).
6. Warming blanket.

3. Methods

3.1. Preparation of the Virus Suspension

1. Centrifuge the purified virus suspension shortly and store the collecting tube on ice.

3.2. Anesthesia and Preparation of Mice

1. Before starting the experiment, sterilize surgical instruments, needles, and syringes by incubating with 70 % ethanol for 10–15 min. Rinse needles three times with sterile water.

2. Anesthetize the mouse by subcutaneous injection of the prepared mixture of ketamin and xylazin. The mouse will develop adequate anesthesia in approximately 5 min.
3. For pupillary mydriasis apply tropic amide eye drops. The pupil is fully dilated within 2–3 min. If necessary, another drop of tropic amide has to be placed on the cornea when the pupil is not adequately dilated up to that point in time. After dilation, it should take <5 min to complete the surgery.

3.3. Injection Procedure

Subretinal injection is performed under direct visualization using an operating microscope.

1. Fill the syringe with 1–2 μl vector suspension. Prevent air bubbles in the solution (see Note 1).
2. Position the mouse with its nose pointing away from the surgeon and its right eye facing up toward the ring light and the microscope.
3. Drop the hydrogel on the cornea and cover it with a glass cover slip. Visualize the fundus in such a way that its blood vessels and the optic nerve head can be clearly seen (see Note 2). This serves as a means to assess the condition of the eye before injection and as a control for the postoperative condition of the retina (Fig. 1a). The cover slip is not removed during the surgery.
4. Grasp the *tunica conjunctiva* with the forceps at favored site as desired (e.g., dorsal part) and place the sterile needle at the inferior site of the *ora serrata*. The tip of the needle should be positioned with the aperture turned up (Fig. 1a).
5. Advance the needle *ab externo* transsclerally into the subretinal space. Under manual control, inject the suspension slowly with low pressure as soon as the tip of the needle becomes visible after its passage through the sclera/RPE (more easily in pigmented mice). The injection in the subretinal space results in a visible retinal detachment due to the bleb formation (Fig. 1b, see Notes 3 and 4). A 34-gauge needle may be reused about ten times before replacement.
6. Withdraw the needle slowly. Rinse the needle two times with sterile water and acetone. Sterilize the needle with 70 % ethanol by rinsing several times and wash again with sterile, desalinated water.
7. Optional: Monitoring and assessment of the quality of subretinal injection, retinal morphology, size of ablation as well as injection site using the in vivo imaging techniques (e.g., cSLO and SD-OCT, Fig. 2).
8. Place the animal on a warming blanket. Apply ointment to the corneas to prevent drying eyes while the animal recovers from anesthesia.
9. Note injection site, volume, virus titre, bleb formation as well as any side effects.

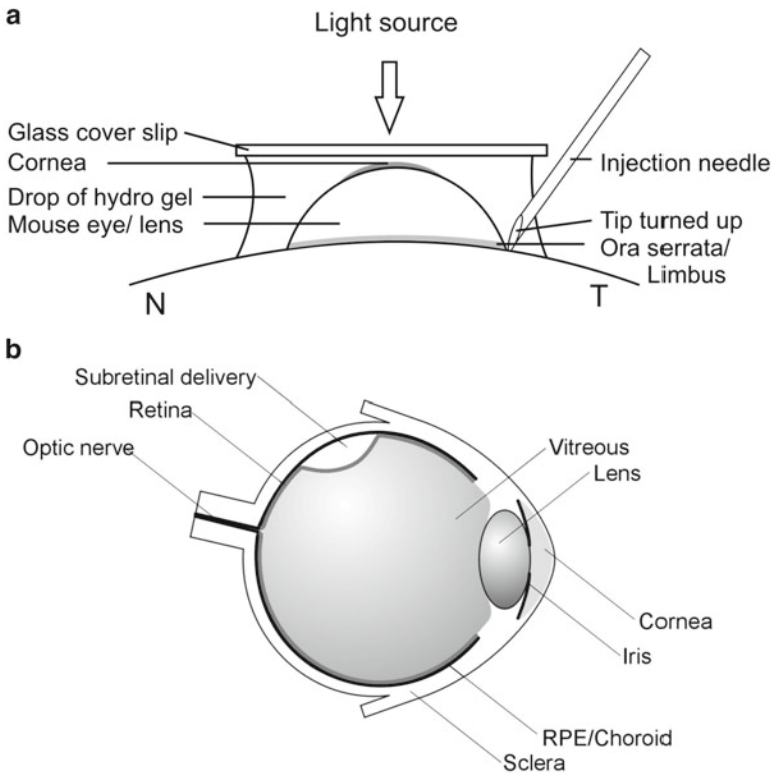

Fig. 1. Sketch of the subretinal injection technique described here. (**a**) Technical setup for the intraocular injection. The fundus is visualized by means of a "contact lens" consisting of a drop of a hydrogel on the cornea, covered with a glass cover slip. The tangential position of the 34-gauge beveled needle is shown just before transscleral passage at the site of the *ora serrata*. N = nasal, T = temporal. (**b**) Schematic view of the cavity following a transscleral injection to the subretinal space, which has formed between the retina and the RPE at the dorsal part of the eye.

3.4. Postoperative Treatment

1. Provide antibiotic ointment two times daily for 48 h. Opacity of the eye is mostly due to injuries of the lens and/or cornea via the needle tip. Animals should be excluded from further studies (see Notes 5 and 6).

4. Notes

1. Air bubbles in the vector solution can be avoided by rinsing (slowly) the needle several times with sterile water and replacing the water with the vector suspension before starting the experiment.
2. Because of the small size of the mouse eye, the success of a subretinal injection is not easy to evaluate, particularly for less experienced investigators. A surgery microscope offers the best

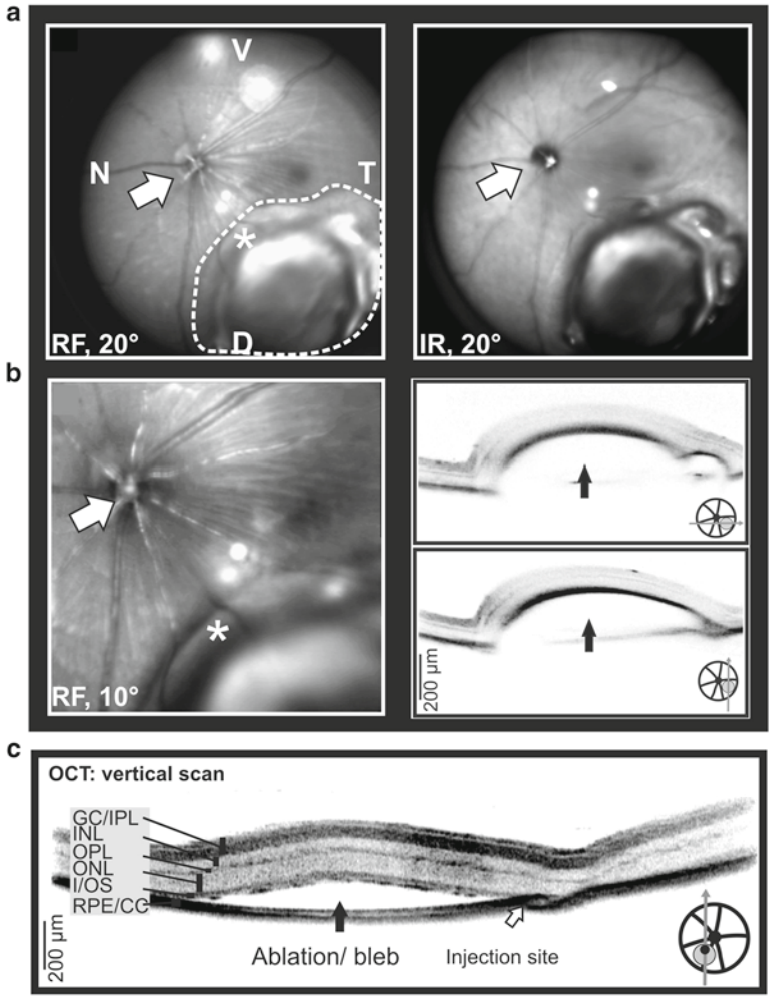

Fig. 2. Quality control of the retinal detachment immediately after subretinal injection by a combination of cSLO and SD-OCT. (**a**) Fundus images of the injection site in relation to landmarks of the murine retinal morphology (vessels, optic nerve head (*open arrows*)). *Left*: Surface-enhanced view at 514 nm laser wavelength (*green*, labeled RF). The *broken line* indicates the position of the subretinal injection cavity. *Asterisks* indicate a site where retinal vessels are pushed apart by the bleb. Also, their continuation on top of the bleb is well visible. *Right*: Depth-enhanced view at 830 nm laser wavelength (infrared, labeled IR). (**b**) *Left*: Higher magnification detail (10°) of the 514 nm image in (**a**). *Right*: SD-OCT images reveal the detachment of the retina (*filled arrows*) in the injected area in horizontal and in vertical orientation following the intervention. (**c**) Detailed in vivo SD-OCT imaging of the retinal architecture of a subretinally injected eye. The detachment (*filled arrow*) is located between the photoreceptor cell layer (IS/OS) and the RPE. Note the injection site (*open arrow*). D = dorsal, V = ventral, T = temporal, N = nasal, RPE/CC = retinal pigment epithelium/choriocapillaris, I/OS = inner/outer segments, ONL = outer nuclear layer, OPL = outer plexiform layer, INL = inner nuclear layer, GC/IPL = ganglion cells and inner plexiform layer.

view and allows for a well-controlled intraocular procedure. Additionally, in vivo imaging immediately postinjection using cSLO and SD-OCT is very helpful to improve quality of the injection and fine tuning of the surgical procedure. There are several causes of incorrect cargo delivery into the subretinal space.

3. By using the transscleral as well the transcorneal route of administration, retinal and choroidal vessels may be injured by the needle tip resulting in hemorrhages. By using a glass cover slip during the injection, the fundus and the retinal vessels may be well visualized. This information is used to select the optimal combination of the fixation site (where the eye is held with the fine forceps) and the entry position (where the needle passes through the RPE).
4. By using the transscleral as well the transcorneal route of administration, injected material may go suprachoroidally or subchoroidally. This can be avoided by strict control of the position of the tip of the needle as well as by generation of a sufficient retinal detachment by bleb formation.
5. By using the transscleral as well as the transcorneal route of administration, material may end up in the vitreous or the lens, resulting in damages and in incorrect administration of the cargo. Transscleral injection: Overly high pressure during the injection results in fine ruptures of the retinal layers. The tip of the needle may easily pass through the inner retina/ganglion cells, resulting in incorrect injections in the lens or vitreous. The difference between a needle tip located either subretinally or intravitreally may be visualized by the properties of reflectance: when located intravitreally, tips appear more clear and bright than those located subretinally. Transcorneal injection: Premature injection by misinterpretation of the tip position before reaching the subretinal space.
6. The postoperative treatment with antibiotic ointment is important to prevent eyes from drying out and infections resulting in neovascularizations of the cornea. These processes lead to irreversible side effects that may prevent further follow-up examinations.

Acknowledgment

This work was supported by Deutsche Forschungsgemeinschaft (Se837/6-1, Se837/7-1).

References

1. McCown TJ (2005) Adeno-associated virus (AAV) vectors in the CNS. Curr Gene Ther 5:333–338 (Review)
2. Marks WJ Jr, Ostrem JL, Verhagen L et al (2008) Safety and tolerability of intraputaminal delivery of CERE-120 (adeno-associated virus serotype 2-neurturin) to patients with idiopathic Parkinson's disease: an open-label, phase I trial. Lancet Neurol 7:400–408
3. den Hollander AI, Black A, Bennett J (2010) Lighting a candle in the dark: advances in genetics and gene therapy of recessive retinal dystrophies. J Clin Invest 120:3042–3053
4. Bainbridge JW, Smith AJ, Barker SS et al (2008) Effect of gene therapy on visual function in Leber's congenital amaurosis. N Engl J Med 358:2231–2239
5. Bennett J, Ashtari M, Wellman J et al (2012) AAV2 gene therapy readministration in three adults with congenital blindness. Sci Transl Med 4, 120ra15
6. Jacobson SG, Cideciyan AV, Ratnakaram R et al (2012) Gene therapy for leber congenital amaurosis caused by RPE65 mutations: safety and efficacy in 15 children and adults followed up to 3 years. Arch Ophthalmol 130:9–24
7. Timmers AM, Zhang H, Squitieri A et al (2001) Subretinal injections in rodent eyes: effects on electrophysiology and histology of rat retina. Mol Vis 7:131–137
8. Johnson CJ, Berglin L, Chrenek MA et al (2008) Technical brief: subretinal injection and electroporation into adult mouse eyes. Mol Vis 14:2211–2226
9. Busskamp V, Duebel J, Balya D et al (2010) Genetic reactivation of cone photoreceptors restores visual responses in retinitis pigmentosa. Science 329:413–417
10. Price J, Turner D, Cepko C et al (1987) Lineage analysis in the vertebrate nervous system by retrovirus-mediated gene transfer. Proc Natl Acad Sci U S A 84:156–160
11. Schlichtenbrede FC, da Cruz L, Stephens C et al (2003) Long-term evaluation of retinal function in Prph2Rd2/Rd2 mice following AAV-mediated gene replacement therapy. J Gene Med 5:757–764
12. Alexander JJ, Umino Y, Everhart D et al (2007) Restoration of cone vision in a mouse model of achromatopsia. Nat Med 13:685–687
13. Janssen A, Min SH, Molday LL et al (2008) Effect of late-stage therapy on disease progression in AAV-mediated rescue of photoreceptor cells in the retinoschisin-deficient mouse. Mol Ther 16:1010–1017
14. Cideciyan AV, Hauswirth WW, Aleman TS et al (2009) Human RPE65 gene therapy for Leber congenital amaurosis: persistence of early visual improvements and safety at 1 year. Hum Gene Ther 20:999–1004
15. Simonelli F, Maguire AM, Testa F et al (2010) Gene therapy for Leber's congenital amaurosis is safe and effective through 1.5 years after vector administration. Mol Ther 18:643–650
16. Palfi A, Millington-Ward S, Chadderton N et al (2010) Adeno-associated virus-mediated rhodopsin replacement provides therapeutic benefit in mice with a targeted disruption of the rhodopsin gene. Hum Gene Ther 21:311–323
17. Sun X, Pawlyk B, Xu X et al (2010) Gene therapy with a promoter targeting both rods and cones rescues retinal degeneration caused by AIPL1 mutations. Gene Ther 17:117–131
18. Towne C, Setola V, Schneider BL et al (2011) Neuroprotection by gene therapy targeting mutant SOD1 in individual pools of motor neurons does not translate into therapeutic benefit in fALS mice. Mol Ther 19:274–283
19. Lhériteau E, Libeau L, Mendes-Madeira A et al (2010) Regulation of retinal function but non-rescue of vision in RPE65-deficient dogs treated with doxycycline-regulatable AAV vectors. Mol Ther 18:1085–1093
20. Bainbridge JW, Mistry A, Schlichtenbrede FC et al (2003) Stable rAAV-mediated transduction of rod and cone photoreceptors in the canine retina. Gene Ther 10:1336–1344
21. Liang FQ, Anand V, Maguire AM et al (2001) Intraocular delivery of recombinant virus. Methods Mol Med 47:125–139
22. Michalakis S, Mühlfriedel R, Tanimoto N et al (2010) Restoration of cone vision in the CNGA3$^{-/-}$ mouse model for congenital complete lack of cone photoreceptor function. Mol Ther 18:2057–2063

HMG Advance Access published July 30, 2012

Human Molecular Genetics, 2012 **1–11**
doi:10.1093/hmg/dds290

Gene therapy restores vision and delays degeneration in the CNGB1$^{-/-}$ mouse model of retinitis pigmentosa

Susanne Koch[1], Vithiyanjali Sothilingam[2], Marina Garcia Garrido[2], Naoyuki Tanimoto[2], Elvir Becirovic[1], Fred Koch[1], Christina Seide[2], Susanne C. Beck[2], Mathias W. Seeliger[2], Martin Biel[1], Regine Mühlfriedel[2,*] and Stylianos Michalakis[1,*]

[1]Center for Integrated Protein Science Munich (CIPSM), Department of Pharmacy – Center for Drug Research, Ludwig-Maximilians-Universität München, Butenandtstr. 5-13, 81377 Munich, Germany and [2]Division of Ocular Neurodegeneration, Institute for Ophthalmic Research, Centre for Ophthalmology, University of Tübingen, Schleichstr. 4/3, 72076 Tübingen, Germany

Received May 29, 2012; Revised July 9, 2012; Accepted July 11, 2012

Retinitis pigmentosa (RP) is a group of genetically heterogeneous, severe retinal diseases commonly leading to legal blindness. Mutations in the CNGB1a subunit of the rod cyclic nucleotide-gated (CNG) channel have been found to cause RP in patients. Here, we demonstrate the efficacy of gene therapy as a potential treatment for RP by means of recombinant adeno-associated viral (AAV) vectors in the CNGB1 knockout (CNGB1$^{-/-}$) mouse model. To enable efficient packaging and rod-specific expression of the relatively large CNGB1a cDNA (~4 kb), we used an AAV expression cassette with a short rod-specific promoter and short regulatory elements. After injection of therapeutic AAVs into the subretinal space of 2-week-old CNGB1$^{-/-}$ mice, we assessed the restoration of the visual system by analyzing (i) CNG channel expression and localization, (ii) retinal function and morphology and (iii) vision-guided behavior. We found that the treatment not only led to expression of full-length CNGB1a, but also restored normal levels of the previously degraded CNGA1 subunit of the rod CNG channel. Both proteins co-localized in rod outer segments and formed regular CNG channel complexes within the treated area of the CNGB1$^{-/-}$ retina, leading to significant morphological preservation and a delay of retinal degeneration. In the electroretinographic analysis, we also observed restoration of rod-driven light responses. Finally, treated CNGB1$^{-/-}$ mice performed significantly better than untreated mice in a rod-dependent vision-guided behavior test. In summary, this work provides a proof-of-concept for the treatment of rod channelopathy-associated RP by AAV-mediated gene replacement.

INTRODUCTION

Retinitis pigmentosa (RP) is a family of hereditary eye disorders characterized by progressive retinal degeneration (1,2). RP primarily affects rod photoreceptors, but secondary to rods, cone photoreceptors also degenerate. Owing to the lack of rod functionality, patients suffer from night blindness at disease onset. Once cones are affected, the visual field becomes more and more constricted ('tunnel vision') and, finally, central vision is also impaired, leading eventually to complete blindness. Accordingly, clinical key symptoms of RP are night blindness, constricted visual fields, decreased visual acuity and color vision and enhanced glare sensitivity. The typical fundus picture includes dark pigmentary clumps ('bone spicules') and attenuated retinal vessels as well as retinal-pigment epithelium (RPE) atrophy. RP is genetically very heterogeneous and currently >50 RP genes are known. Many of the RP genes are preferentially or even exclusively expressed in rod photoreceptors (1). Only a minor fraction of the RP genes are specific for other retinal cell types, e.g. RPE cells. Early success of gene replacement therapy for

*To whom correspondence should be addressed. Tel: +49-7071-29-87784; Fax: +49-7071-29-4503; Email: regine.muehlfriedel@med.uni-tuebingen.de (R. Mühlfriedel); Tel: +49-89-2180-77325; Fax: +49-89-2180-77326; Email: michalakis@lmu.de (S. Michalakis).

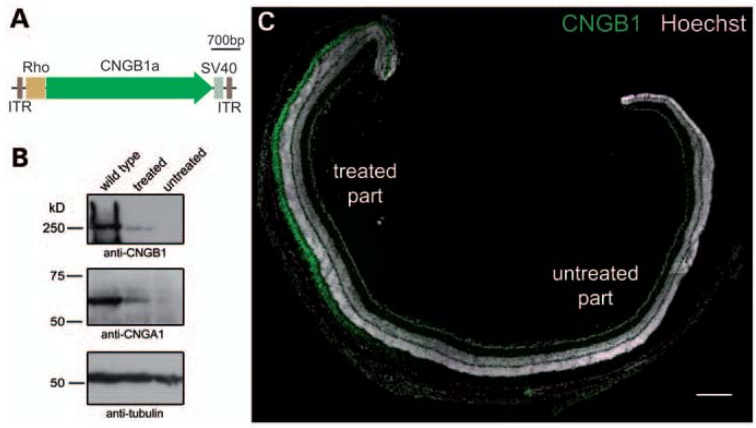

Figure 1. Subretinal delivery of CNGB1a using an optimized AAV vector results in the expression of full-length CNGB1a in photoreceptors. (**A**) Schematic representation of the Rho-CNGB1a AAV vector. The expression cassette within the two inverted terminal repeats (ITRs) includes a 471 bp mouse rhodopsin promoter fragment (Rho), the 3978 bp mouse CNGB1a cDNA and a 221 bp long SV40 polyA sequence. (**B**) Western blot analysis of retinal lysates from wild-type, treated and untreated CNGB1-deficient mice using an antibody against the C-terminus of CNGB1 demonstrates the expression of the CNGB1a (upper panel) and up-regulation of CNGA1 (middle panel) in treated CNGB1$^{-/-}$ mice. (**C**) Overview image showing expression and outer segment localization of CNGB1a in the treated part of a CNGB1$^{-/-}$ retina at 40 days after injection. The retinal slice was immunolabeled with an antibody directed against the C-terminus of CNGB1 (CNGB1, green). The cell nuclei were stained with the nuclear dye Hoechst 33342 (grey). Scale bar in (C) marks 200 μm.

RPE-specific mutations resulted in a number of clinical trials with promising results (3). However, as many of the disease-causing mutations concern (rod) photoreceptor-expressed genes, there is a need to develop treatments for photoreceptor-specific RP genes (1).

Mutations in the genes encoding the two rod cyclic nucleotide-gated (CNG) channel subunits cause autosomal recessive RP (arRP) (4). CNG channels are found in the plasma membrane of rod and cone photoreceptors and translate light-mediated concentration changes of the second messenger cyclic guanosine monophosphate (cGMP) into voltage and calcium signals (4). The rod CNG channel is a heterotetramer comprised of three CNGA1 subunits and one CNGB1 subunit (5). Mutations in CNGB1 (RP45 locus) are found in ~4% of arRP cases (1). Knockout of CNGB1 in mice results in a phenotype that recapitulates the principal pathology of RP patients. In particular, CNGB1 knockout mice lack rod photoreceptor function (6,7). This functional defect is accompanied by a progressive degeneration of rods, and, secondary to this, a degeneration of the cones (6,7). The degeneration progresses rather slow and results in loss of 10 20% of rods at 4 months, 30 50% at 6 months and 80 90% at 1 year of age. Finally, the loss of CNGB1a induces down-regulation of several proteins of the phototransduction cascade and degradation of the CNGA1 subunit (6,7). In the present study, we used CNGB1 knockout mice as a model for RP to evaluate adeno-associated virus (AAV)-mediated gene therapy as a potential treatment of RP caused by rod photoreceptor-specific gene mutations. We show here that our gene replacement approach was able to restore rod CNG channel expression and localization, to improve retinal function and vision-guided behavior and to delay retinal degeneration in CNGB1$^{-/-}$ mice.

RESULTS

Design and subretinal delivery of a gene therapy vector for rod-specific expression of CNGB1a

The relatively small packaging capacity (~5.2 kb) of AAV vectors (8 10) limits their use for the expression of large transgenes such as CNGB1a. Because of the large size of the CNGB1a cDNA (3978 bp), there is only limited space left for *cis*- and *trans*-regulatory elements. To achieve high expression rates at the smallest possible vector genome size, we decided to use only a single 221 bp long SV40 polyA sequence (see Materials and Methods) in combination with a 471 bp mouse rhodopsin promoter (−386 to +86) (11). This vector allowed the incorporation of the full-length CNGB1a cDNA without violating the 5.2 kb packaging limit of AAVs (8 10). We then packaged this construct (Fig. 1A) into viral vector particles with Y733F-modified AAV8 capsid (12) and injected ~10^{11} AAV genomic particles into the subretinal space of 2-week-old CNGB1$^{-/-}$ mice. The retinal site of treatment was monitored *in vivo* directly upon completion of the injection procedure and at subsequent time points using confocal scanning laser ophthalmoscopy (cSLO) (13) and optical coherence tomography (OCT) (14).

Restoration of CNG channel expression in rod outer segments of CNGB1$^{-/-}$ mice

We next analyzed the expression of CNGB1a in the retina of treated CNGB1$^{-/-}$ mice. In a western blot analysis, we confirmed that subretinal delivery of our AAV vector led to expression of the full-length CNGB1a protein migrating at the expected size of ~250 kDa (Fig. 1B, upper panel). In addition, the 63 kDa CNGA1 subunit that is completely degraded in

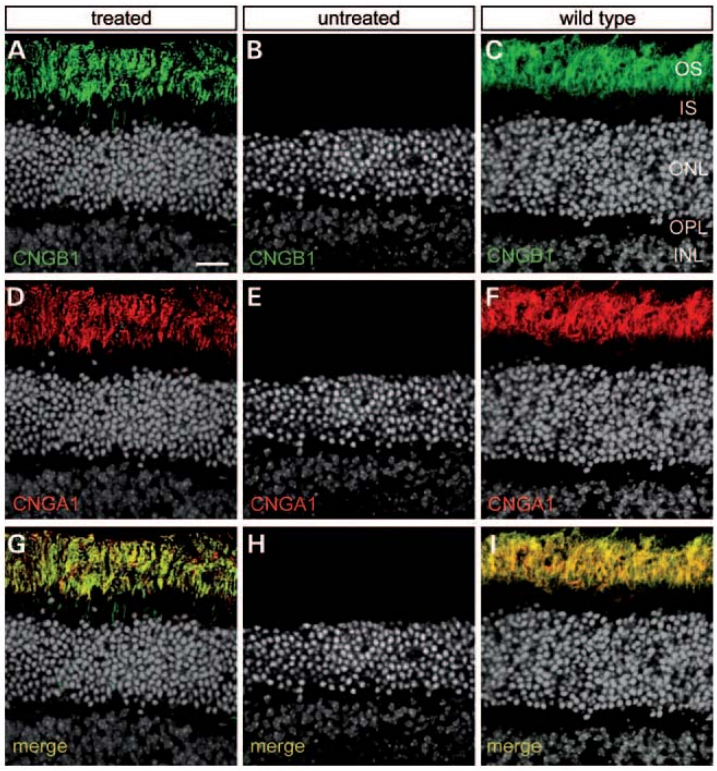

Figure 2. Analysis of CNG channel expression in the treated and untreated CNGB1$^{-/-}$ retina. Confocal scans from retinal slices immunolabeled with antibodies specific for CNGB1a (green) and CNGA1 (red). The treatment results in the expression of CNGB1a in rod outer segments of treated mice (**A**), which is absent in the untreated knockout retina (**B**). The CNGB1a expression levels in the treated knockout are comparable to wild-type (**C**). Viral CNGB1a expression also rescues the expression of CNGA1 in rod outer segments (**D**), which is down-regulated in the untreated knockout retina (**E**). Again, the levels of expression are comparable to wild-type (**F**). (**G**–**I**) Merged images of CNGA1 and CNGB1a signals (yellow). Both proteins co-localized in the outer segments from treated (G) and wild-type mice (I). Cell nuclei were stained with the nuclear dye Hoechst 33342 (grey) in all panels. INL, inner nuclear layer; IS, photoreceptor inner segments; ONL, outer nuclear layer; OPL, outer plexiform layer; OS, photoreceptor outer segments. The scale bar marks 20 μm.

CNGB1$^{-/-}$ mice was readily detectable in the injected retina (Fig. 1B, middle panel). Using immunohistochemistry, we detected virally encoded CNGB1a protein in the treated, but not the untreated part of the retina. Figure 1C shows a representative overview image of a CNGB1$^{-/-}$ retinal slice 40 days after treatment immunolabeled for CNGB1a. The treated area with high levels of CNGB1a expression corresponded to approximately one-third of the retina. The CNGB1a protein localized almost exclusively to rod outer segments, suggesting that transport mechanisms required for proper outer segment targeting of the channel are preserved in the treated knockout (Fig. 1C). Figure 2 shows high-resolution confocal scans from the treated (A, D and G) and untreated regions (B, E and H) of a CNGB1$^{-/-}$ retina as well as from wild-type control retina (C, F and I). Importantly, viral treatment not only restored expression of CNGB1a (Fig. 2A), but also restored levels of the previously missing endogenous CNGA1 protein (Fig. 2D), which now co-localized with CNGB1a in rod outer segments within the treated area (Fig. 2G). This suggests that AAV-mediated delivery of CNGB1a restored the expression of wild-type-like heterotetrameric CNG channels in rod outer segments of treated mice. Moreover, comparison with wild-type mice showed that the treatment led to almost wild-type levels of expression of CNGB1 and CNGA1 in treated CNGB1$^{-/-}$ mice (Fig. 2A, C, D and F). An improvement of photoreceptor outer segment morphology in the treated CNGB1$^{-/-}$ retina could also be detected *in vivo* using OCT (Fig. 3A and B). The typical outer retinal appearance in OCT with horizontal bands associated with the outer limiting membrane and the border between inner and outer segments (14,15) (arrow in Fig. 3A) was preserved in the treated eye (TE), but not in the untreated eye (UE). We also performed confocal microscopy on histological retinal sections labeled with the photoreceptor outer segment marker peripherin-2 to analyze the outer segment morphology in more detail (Fig. 3C and D). The labeling pattern and intensity of the anti-peripherin-2 antibody in the treated CNGB1$^{-/-}$ retina were comparable to the staining in the untreated. However, the length of the peripherin-2-positive outer segments was markedly increased in the treated (Fig. 3C) compared with the untreated (Fig. 3D) part of the CNGB1$^{-/-}$ retina.

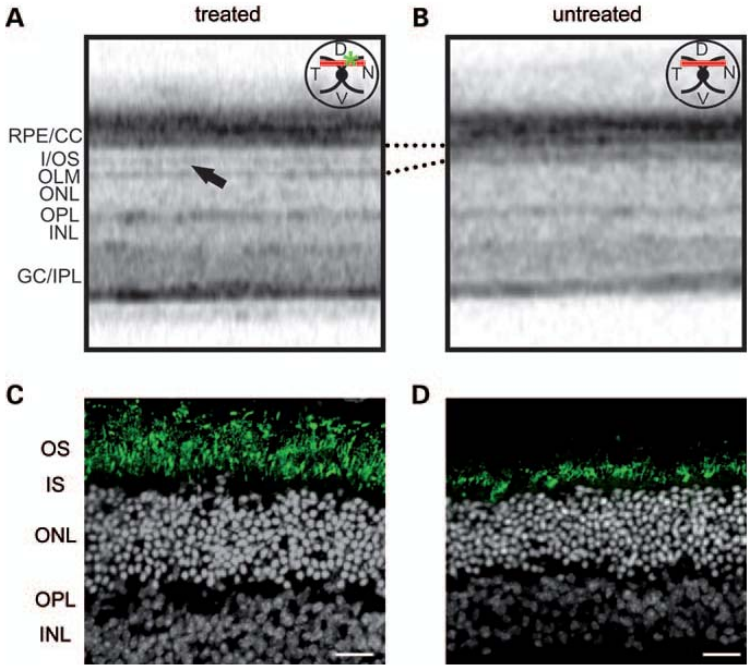

Figure 3. Effect of gene therapy on outer retinal morphology in *CNGB1*$^{-/-}$ mice. (**A**, **B**) Comparison of OCT data from TEs and UEs of the same representative CNGB1$^{-/-}$ mouse 2 months after injection. A schematic drawing of the mouse retina with the position of the injection site (green asterisk) and/or the OCT scan (red line) is shown in (A) and (B). D, dorsal; N, nasal; T, temporal; V, ventral. The typical outer retinal appearance in OCT with horizontal bands associated with the OLM and IS/OS border (marked with an arrow) was preserved in the TE (A), but not in the UE (B). The dotted lines between (A) and (B) mark the position of the lower margin of the RPE/choriocapillaris (CC) layer and the outer limiting membrane (OLM) in the treated (A) and untreated (B) retinas. The space between these two layers is markedly increased in the treated retina, indicating a distinct rescue of rod outer segment organization. (**C**, **D**) Confocal images from the treated (C) and untreated (D) CNGB1$^{-/-}$ retina immunostained with anti-peripherin-2 antibody (green) at 40 days after treatment. The outer segment length is increased in the treated (C) compared with the untreated (D) part. Cell nuclei were stained with the nuclear dye Hoechst 33342 (grey) in (C) and (D). GC/IPL, ganglion cell layer/inner plexiform layer; INL, inner nuclear layer; IS, photoreceptor inner segments; OPL, outer plexiform layer; ONL, outer nuclear layer; I/OS, inner/outer segment border; OS, photoreceptor outer segments. The scale bar in (C and D) marks 20 μm.

Restoration of rod photoreceptor function in treated CNGB1$^{-/-}$ mice

As expected, non-injected eyes (UEs) of 8-week-old CNGB1$^{-/-}$ mice did not show the usual responses to dim light stimuli in dark-adapted (scotopic) Ganzfeld electroretinography (ERG), reflecting a lack of regular rod system activity (Fig. 4A, middle panel). In contrast, distinct responses were present in eyes of CNGB1$^{-/-}$ mice that had received injections of CNGB1a AAV vector (TEs) (Fig. 4A, left panel and overlay in Fig. 4A, right panel). Figure 4B shows a statistical analysis of the ERG b-wave amplitude (which reflects mainly the activity of bipolar cells) for six TEs and UEs. It is again obvious that, in contrast to the controls, treated mice show substantial b-wave amplitudes, particularly at low light intensities (-4.0 to -2.0 log cd*s/m^2) where responses are entirely rod-driven.

For completeness, it should be mentioned that in a few cases, very small, irregular rod responses were present in CNGB1$^{-/-}$ mice as previously described (5), which are attributed to homomeric CNGA1 channels that have escaped degradation. This fact is, however, mainly of theoretical interest as these contributions were too small to have any perceivable impact on the results shown.

To further probe whether the responses of the rod to repetitive stimuli were also restored, a scotopic flicker flash intensity series was done (Fig. 4C and D). Contrary to UEs, a recovery of the rod-driven flicker ERG responses was observed in AAV TEs. In accordance with the approximate size of the treated area (about one-third of the total retina), rod-specific ERG amplitudes were about one-third of that in age-matched controls (Fig. 4E). It should further be noted that injections of CNGB1a AAVs had no effect on the light-adapted photopic ERG of CNGB1$^{-/-}$, indicating that the treatment including the technical procedure had no adverse effects on the cone system (data not shown).

AAV treatment restores rod-mediated vision-guided behavior in CNGB1$^{-/-}$ mice

Having shown by ERG that treated CNGB1$^{-/-}$ mice acquired the ability to generate rod-specific light-evoked signals and to activate rod bipolar cells, we asked whether this improvement on a retinal level might establish vision-guided behavior of the rod. We therefore used a simple water maze test to assess visual responsivity (see Materials and Methods). The mice were tested for five consecutive days in a cued water maze

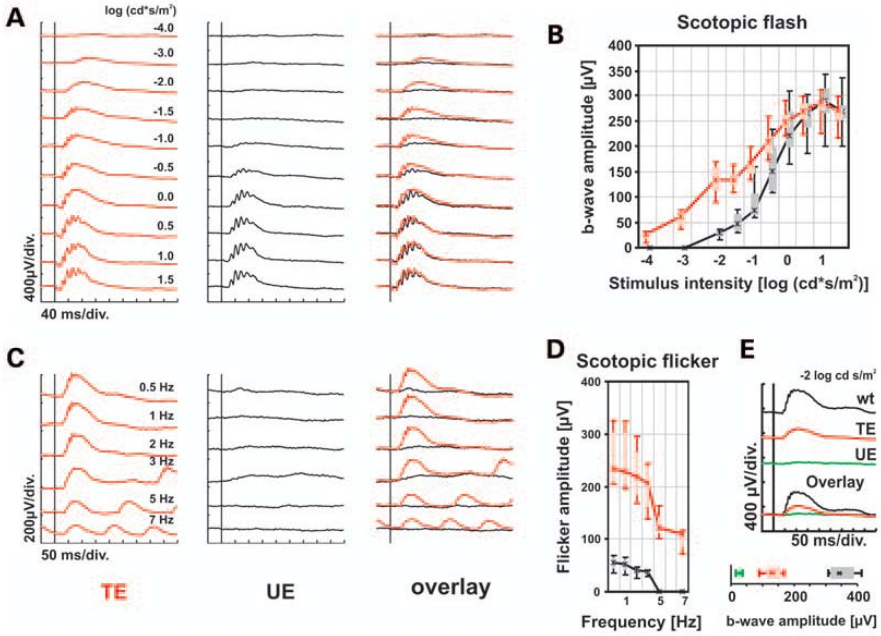

Figure 4. Effect of gene therapy on visual function in CNGB1$^{-/-}$ mice. Comparison of ERG data from TEs and UEs of the same individual CNGB1$^{-/-}$ mice ($n = 6$) treated at postnatal week 2 (PW 2). (**A**) Dark-adapted (scotopic) single-flash ERG intensity series of the treated (TE, red) and the untreated fellow eye (UE, black) of a representative CNGB1$^{-/-}$ mouse at 2 months after injection, together with a superposition to enhance visibility of differences (right column). The vertical line indicates the timing of the light stimulus in each panel. (**C**) Scotopic flicker ERG responses at a fixed rod-specific intensity (-2 log cd*s/m^2) from 0.5 to 7 Hz and the corresponding overlay. (**B**, **D**) The quantitative data of the entire group are shown as Box-and-Whisker plots, i.e. boxes indicate the 25 and 75% quantile range, whiskers indicate the 5 and 95% quantiles, and the asterisks indicate the median of the data. The amplitude data are plotted as a function of the logarithm of the flash intensity (B) and as a function of flash frequency (D). (**E**, top) Representative scotopic single-flash ERG responses at -2 log cd*s/m^2 recorded from a wild-type (wt) eye, TE, UE and a superposition. (E, bottom) The quantitative data of each group are shown as Box-and-Whisker plots as specified above. The results indicate a distinct rescue of rod functionality.

for their ability to navigate to a visible escape platform. On Days 1 3, the experiment was performed at dim light conditions (see Materials and Methods) to ensure that vision is totally conferred to the rod system. On Day 1, wild-type control mice needed 47.9 ± 10.6 s to navigate to the escape platform, but gradually improved their performance to 7.3 ± 1.1 s on Day 3 [$P = 0.0009$, one-way analysis of variance (ANOVA)] (Fig. 5A). An example swim path for a wild-type mouse on Day 3 is shown in Figure 5C. Based on the swimming abilities of the mice (mean swimming speed: 19.0 ± 1.8 cm/s) and the diameter (120 cm) of the water-filled tank, the swimming performance on Day 3 can be considered as the best achievable one. Untreated CNGB1$^{-/-}$ mice needed significantly longer than wild-type mice ($P < 0.001$, two-way ANOVA) and were not able to improve their performance significantly during the three test days (Day 1: 90.4 ± 8.1 s; Day 3: 67.9 ± 10.8 s; $P = 0.2660$, one-way ANOVA) (Fig. 5A; example swim path in Fig. 5C). In contrast, treated CNGB1$^{-/-}$ mice were clearly able to improve during the three test days (Day 1: 59.7 ± 11.0 s; Day 3: 23.1 ± 4.7 s; $P = 0.0127$, one-way ANOVA) and performed significantly better than untreated CNGB1$^{-/-}$ mice ($P = 0.0123$, two-way ANOVA) (Fig. 5A; example swim path in Fig. 5D). Treated mice showed slightly longer escape latencies than the wild-type mice, but did not significantly differ from wild-type in their overall performance ($P = 0.0834$, two-way ANOVA) (Fig. 5A). Also, the learning curves from treated and wild-type mice developed in parallel and had similar slopes (wild-type: −21.5 ± 5.4, treated: −18.3 ± 6.8; $P = 0.725$, *t*-test). Taken together, these findings suggest that treated CNGB1$^{-/-}$ mice gained the ability to navigate using information provided by the rod visual system.

We performed the test on Days 4 and 5 under normal light conditions (see Materials and Methods). Vision under these light conditions is mainly conferred by cone photoreceptors. As CNGB1$^{-/-}$ mice have preserved cone function until 6 months of age (6), we expected all animal groups to be able to navigate under these test conditions. Wild-type and treated CNGB1$^{-/-}$ mice performed better than untreated CNGB1$^{-/-}$ mice on Day 4, because they already learned the task under dim light conditions. However, untreated mice also started improving their performance until they reached similar levels of escape latencies like wild-type and treated mice on Day 5 (Fig. 5A).

During all tests, the mice were allowed to swim for up to 120 s. If a mouse did not find the platform within 120 s, it was considered as an 'error of omission'. Wild-type mice showed no (Day 3) or almost no (Day 2: 0.2 ± 0.2%) errors

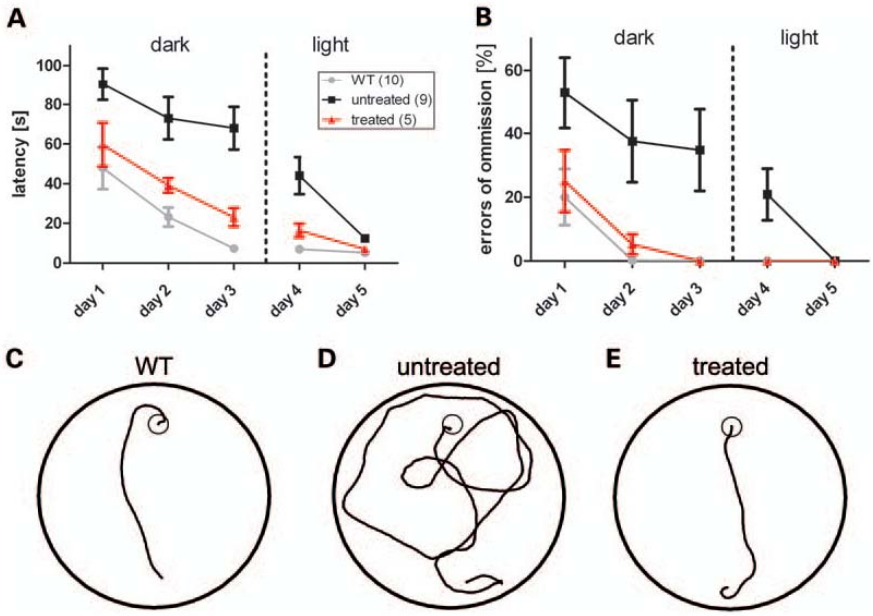

Figure 5. Effect of gene therapy on vision-guided behavior in CNGB1$^{-/-}$ mice. Treated mice show improved learning curves in a visual water maze that tests rod-mediated vision. (**A, B**) Latency to locate a swimming escape platform (A) and errors of omission (B) under dark (Days 1 3) and normal (Days 4 and 5) light conditions. In contrast to untreated CNGB1$^{-/-}$ mice (black), treated CNGB1$^{-/-}$ mice (red) significantly improved their performance during the first three test days in the dark. All treated mice successfully located the escape platform (e.g. performed without errors of omission) on Day 3. Their performance did not significantly differ from wild-type control mice (grey). On Days 4 and 5, the mice were tested under normal light conditions. As cone function is not impaired in young untreated CNGB1$^{-/-}$ mice (6), they were also able to improve their performance to the level of wild-type and treated CNGB1$^{-/-}$ mice on Day 5. (**C E**) Example swim paths from wild-type (C), treated (D) and untreated (E) mice on Day 3.

of omission from the second test day onward (Fig. 5B). In contrast, untreated CNGB1$^{-/-}$ mice made errors of omission throughout the low-light condition test phase (Days 1 3) and the first day under normal light conditions (Day 4), and only improved to no more errors of omission on the second day under normal light conditions (Day 5) (Fig. 5B). As a clear indication for an improvement of rod-mediated vision, treated CNGB1$^{-/-}$ mice performed without any error of omission on Day 3 and had only 5.2 $\pm$ 3.2% errors of omission on Day 2 (Fig. 5B).

Gene therapy delays retinal degeneration in CNGB1$^{-/-}$ mice

RP patients and CNGB1$^{-/-}$ mice display a progressive retinal degeneration due to the loss of rod and cone photoreceptors, which needs to be ameliorated or halted in order to achieve long-term beneficial effects on vision. Having shown that our gene replacement therapy was able to restore rod photoreceptor function in ERG and to improve rod-mediated vision in the behavioral test, the question remained to what extent the treatment could also delay photoreceptor degeneration. Specifically, the progressive photoreceptor degeneration in CNGB1$^{-/-}$ mice results in thinning of the outer nuclear layer to about half the size of wild-type control mice at 6 months of age and to 1 2 rows of photoreceptors at 1 year (6). The wild-type retina contains 11 12 rows of photoreceptors. To test whether the treatment was able to delay the retinal degeneration, we isolated the retina at 12 months after injection and analyzed the retinal histology. Figure 6A shows an overview image from a representative retinal slice of a treated knockout mouse at 12 months after treatment labeled with a CNGB1-specific antibody and the nuclear dye Hoechst 33342. The region with no CNGB1a expression revealed the expected thinning of the outer nuclear layer. However, in the treated part with high levels of CNGB1a expression, 7 8 rows of photoreceptors remained, indicating that the treatment significantly delayed photoreceptor cell loss (Fig. 6A). In the untreated CNGB1$^{-/-}$ retina, Müller cells are activated and show high levels of glial fibrillary acidic protein (GFAP) immunoreactivity (Fig 6B) (6). In support of a beneficial effect on retinal degeneration, we observed a reduction of the GFAP signal to wild-type levels at 12 months after treatment (Fig. 6C and D). An overview image from a treated CNGB1$^{-/-}$ retina illustrating the treatment effect on Müller gliosis is shown in Figure 6E. The beneficial effects on retinal degeneration go along with the normalization of cGMP metabolism in the CNGB1$^{-/-}$ retina (Fig. 6G). Within the untreated part of the retina, a profound accumulation of cGMP can be detected in photoreceptors (Fig. 6F). In accordance with the functional data, expression of CNGB1a also lowered cGMP in photoreceptors to levels comparable to wild-type (Fig. 6G and H). As is typical for RP and its models, cone photoreceptors also start to

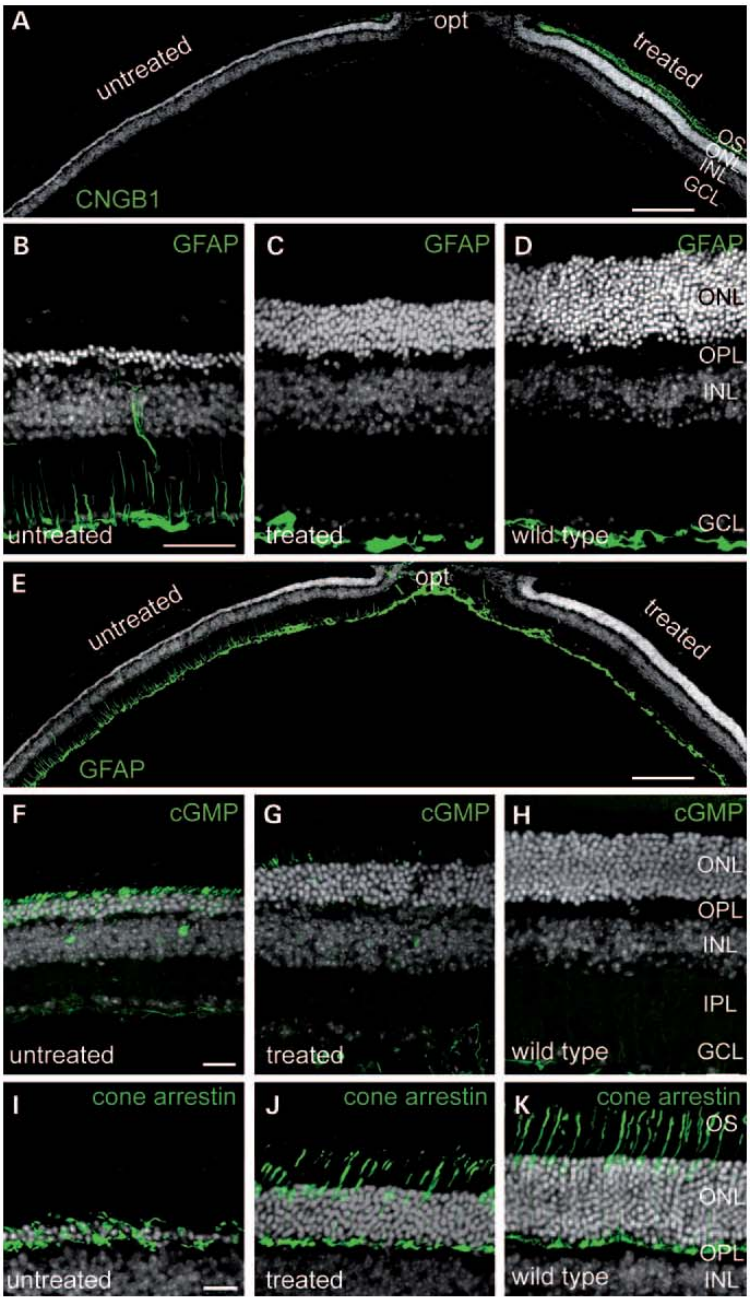

Figure 6. Effect of gene therapy on photoreceptor degeneration in CNGB1$^{-/-}$ mice at 12 months after treatment. (**A**) Expression of CNGB1a protein (green) in the CNGB1$^{-/-}$ retina delayed photoreceptor cell loss and thinning of outer nuclear layer (ONL) at 12 months after treatment. (**B**–**D**) Representative confocal images from untreated (B), treated (C) CNGB1$^{-/-}$ and wild-type (D) retinas immunolabeled for GFAP (green). The treatment decreased the activation of Müller glia cells (C) to levels comparable to wild-type (D). (**E**) Overview image spanning a larger portion of a treated CNGB1$^{-/-}$ retina showing the different levels of GFAP (green) in the treated and untreated parts. (**F**–**H**) Viral CNGB1a expression also lowered presumably deleterious levels of cGMP (green) in photoreceptors of treated mice 6 months after treatment (G) to levels comparable to wild-type (H). (**I**–**K**) Confocal scans from retinal slices immunolabeld for the specific 'cone marker' cone arrestin demonstrate the positive effect on cone morphology at 12 months after treatment (I–K). Cell nuclei were stained with the nuclear dye Hoechst 33342 (grey) in all panels. The scale bar marks 100 μm in (A) and (E), 50 μm in (B–D) and 20 μm in (F–K). GCL, ganglion cell layer; INL, inner nuclear layer; IPL, inner plexiform layer; OPL, outer plexiform layer; opt, optic nerve; ONL, outer nuclear layer; OS, photoreceptor outer segments.

degenerate in the CNGB1 $^{-/-}$ mouse secondary to rods although they are primarily unaffected. In untreated mice, cone degeneration becomes evident after 6 months of age (6). To test for the beneficial effect of the treatment on cone photoreceptors, we stained the treated and untreated CNGB1 $^{-/-}$ retina with the cone marker cone arrestin (16) at 12 months after injection. We found that in the treated CNGB1-deficient retina, the morphology of cones was positively affected (Fig. 6I–K).

DISCUSSION

RP is a family of hereditary eye diseases that affects the function and viability of rod photoreceptors resulting in night blindness and progressive retinal degeneration (1,2). The secondary degeneration of cone photoreceptors produces a corresponding loss of high-acuity vision that can eventually lead to complete blindness (1,2). Until recently, RP has been considered to be incurable. With the advent of AAV-mediated gene replacement therapy, several groups succeeded in restoration of retinal function in RP animal models (17,18). For one form of RP, Leber's congenital amaurosis caused by mutations in the RPE-specific gene RPE65, a gene replacement approach has already been translated from animal into clinical studies (19–21). For other forms of RP caused by mutations in photoreceptor-specific genes, the success rate of gene replacement therapy varied from modest, short-term effects to more pronounced and more stable therapeutic effects (17,18). This variability may be explained by the interaction of multiple factors such as the type of AAV (e.g. serotype, single- or double-stranded vector), the type of target cell (e.g. RPE, photoreceptors), the animal model in which the treatment is being tested, the rate of degeneration, the time point of treatment and the species specificity of the therapeutic transgenes, as well as the structure, localization and molecular function of the gene product (e.g. enzyme, receptor, ion channel). Another important consideration refers to the dosage of transgene expression. A minimum level of expression in the target cell is essential to achieve a therapeutic effect. However, overexpression of the therapeutic gene may also cause degeneration and cell death. For instance, gene therapy studies in RP mouse models with mutations in genes encoding the rod photoreceptor-specific phosphodiesterase have shown variable success rates ranging from partial rescue to more definite therapeutic effects (22–25). Due to the high degree of signal amplification and multi-facetted regulation of the phototransduction cascade (26), even subtle changes in expression levels may cause severe functional defects that influence the outcome of gene therapy. Thus, it appears that success rates of gene therapies for genes encoding proteins involved in the photoreceptor signal transduction cascade may require well-balanced transgene expression.

In this study, we present data on the successful restoration of vision in the CNGB1 knockout mouse model of RP using AAV-mediated gene therapy. The treatment resulted in efficient expression of high levels of full-length CNGB1a protein in rod photoreceptors that almost exclusively localized to outer segments. Importantly, this also resulted in the restoration of the previously degraded endogenous CNGA1 protein, which is the second subunit of the native rod CNG channel (5). Following treatment, both proteins co-localized in rod outer segments and formed regular CNG channel complexes in the transduced area of the CNGB1 $^{-/-}$ retina. We have previously shown that the vast majority of homomeric CNG channels (e.g. CNGA1 or CNGA3 only) cannot be transported into the photoreceptor outer segments and are rapidly degraded (6,16,27). Only a minor fraction of CNGB1 $^{-/-}$ rods (3 out of 35 recorded cells) (6) showed small (10–15% of wild-type) light responses. Accordingly, the levels of endogenous CNGA1 transcript and protein that are available for assembly with virally expressed CNGB1a seems to be the limiting factor that defines the amount of CNG channel complexes in the treated rod outer segments. Thus, the endogenous CNGA1 transcript levels act as an intrinsic safety barrier to ensure that the amounts of outer segment rod CNG channels cannot exceed wild-type levels, which may prevent deleterious changes in photoreceptor Ca^{2+} levels or membrane potential. In line with this, our treatment showed no adverse effects and revealed a prolonged preservation of photoreceptors up to the end of the follow-up period of 12 months.

In summary, the present study represents the first successful approach of restoration of vision in a retinal channelopathy model of RP. Importantly, we were able to demonstrate the restoration of visual system integrity and functionality by *in vivo* and *in vitro* analyses of retinal function and morphology, as well as vision-guided behavior. Our data are very encouraging to launch AAV-based gene therapy studies in human patients suffering from CNG channelopathies.

MATERIALS AND METHODS

Animals

Animals were housed under standard white cyclic lighting (200 lux), had free access to food and water and were used irrespective of gender. Lighting conditions were consistent across all groups and/or treatments. All procedures concerning animals were performed with permission of local authorities (Regierungspräsidium Tübingen and Regierung von Oberbayern) and in accordance with the ARVO Statement for the Use of Animals in Ophthalmic and Vision Research.

Cloning and production of rAAV vectors

Cloning and mutagenesis were performed by standard techniques. All sequence manipulations were confirmed by sequencing. To construct pAAV2.1-Rho-CNGB1a-SV40, we inserted a polymerase chain reaction (PCR)-amplified mouse Rhodopsin promoter (RhoF: 5′-GATCCTTAAGATGTGGAG AAG TGAATTTAGGGCCCAA-3′ and RhoR: 5′-GTATGTC GA CCACTGCGGCTGCTCGAAGGGGCTCCGCA-3′, PCR template: mouse genomic DNA) and a PCR-amplified SV40 late Poly A fragment [SV40F: 5′-TGTAGCGGCCGCAG ACATGATAAGATACATTGATGAGTT-3′, SV40R: 5′-TG TACTCGAGTACCACATTTGTAGAGGTTTTACTTGCT-3′, PCR template: psiCHECK-2 (Promega, Mannheim, Germany)] and PCR-amplified (mB1F: 5′-CCGGTACCGCCACCATG TTGGGCTGGGTCCAAAGG-3′, mB1R: 5′-GATCGCGGCC GCTCATGCACCTCACTCCGCC-3′, PCR template: mouse

retinal cDNA) full-length mouse CNGB1a cDNA into pAAV2.1-mcs (27). pAAV2/8 Y733F (12) encoding a Y733F-modified AAV8 capsid was obtained by site-directed mutagenesis (YF8F: 5′-GCCCCATTGGCACCCGTTTCCTCA CCCGTAATCTGTAATTG-3′, YF8R: 5′-CAATTACAGAT TACGGGTGAGGAAACGGGTGCCAATGGGGC-3′) using pAAV2/8 (28) as a template. Single-strand AAV vectors were produced by triple calcium phosphate transfection of 293T cells with pAdDeltaF6 (29), pAAV2/8Y733F and pAAV2.1-Rho-CNGB1a-SV40 plasmids followed by iodixanol gradient (30) purification. The 40–60% iodixanol interface was further purified and concentrated by ion exchange chromatography on a 5 ml HiTrap Q Sepharose column using an ÄKTA Basic FPLC system (GE Healthcare, Munich, Germany) according to previously described procedures, followed by further concentration using Amicon Ultra-4 Centrifugal Filter Units (Millipore, Schwalbach, Germany). Physical titers (in genome copies/ml) were determined by quantitative PCR of CNGB1 (B1aqF: 5′-GAACTGGAACTGCTGGCTGAT-3′\xEF\x80 and B1aqR: 5′-TGGAACACGGTGATGTCCAGGA-3′) using a LightCycler 480 (Roche Applied Science, Mannheim, Germany).

Subretinal rAAV injections

As previously described (27), mice were anesthetized by subcutaneous injection of ketamine (66.7 mg/kg) and xylazine (11.7 mg/kg), and their pupils were dilated with tropicamide eye drops (Mydriaticum Stulln; Pharma Stulln GmbH, Germany). One microliter of rAAV particles was injected into the subretinal space using the NanoFil Subretinal Injection Kit (WPI, Germany) equipped with a 34 gauge beveled needle. The injection was performed free hand under a surgical microscope (Carl Zeiss, Germany). Special care was taken to avoid damage of the lens. The success of the procedure was monitored immediately following the injections using SLO (13) and OCT (14). If the procedure was not successful (severe damage like a full retinal detachment), the mice were excluded from further analysis. At the given age, this concerned about one eye out of five.

Electroretinograms

ERG analysis was performed at 6 weeks to 4 months after injection according to the procedures described elsewhere (31,32). Single-flash intensity and flicker frequency series data were available from 11 animals (one eye treated, one eye untreated). Scotopic flicker ERG series data were available from 11 animals (one eye treated, one eye untreated).

Scanning laser ophthalmoscopy

Retinal structures were visualized via a cSLO [Heidelberg Retina Angiograph (HRA I)] according to previously described procedures (13). The HRA features two argon wavelengths (488 and 514 nm) in the short-wavelength range and two infrared diode lasers (795 and 830 nm) in the long-wavelength range. Laser wavelengths used for fundus visualization were: 514 nm (red-free channel) and 488 nm for autofluorescent images, with a barrier filter at 500 nm.

Spectral domain optical coherence tomography

Spectrum domain optical coherence tomography imaging was done with a commercially available Spectralis™ HRA + OCT device (Heidelberg Engineering) featuring a broadband superluminescent diode at 870 nm as low coherent light source. Each two-dimensional B-scan recorded at 30° field of view consists of 1536 A-scans, which are acquired at a speed of 40 000 scans per second. Optical depth resolution is ~7 μm with digital resolution reaching 3.5 μm. Imaging was performed using the proprietary software package Eye Explorer (version 3.2.1.0, Heidelberg Engineering). Retinal thickness was quantified using horizontal slides, located 1500 μm distant from the optic nerve head in the temporal hemisphere.

Immunohistochemistry

Immunohistochemical staining was performed at 40 days to 12 months after injection according to the procedures described previously (16). We used the following primary antibodies: rabbit anti-CNGB1 [C-AbmCNGB1 (6), 1:30 000], mouse anti-CNGA1 [2G11 (33), 1:30], mouse anti-peripherin-2 [Per5H2 (34), 1:1000], sheep anti-cGMP (35) (1:3000), Cy3-coupled anti-GFAP (16) (Sigma, Germany, 1:1000) and rabbit anti-cone arrestin (36) (1:300). Laser scanning confocal micrographs were taken using an LSM 510 meta microscope (Carl Zeiss, Germany) and images are presented as collapsed confocal z-stacks. Stainings were reproduced in ≥3 independent experiments.

Western blot

For protein isolation from mouse retinas, the retinas were homogenized using a mortar and suspended in homogenization buffer [2% sodium dodecyl sulfate (SDS), 50 mM Tris and proteinase inhibitor cocktail mix]. After heating at 95°C for 15 min followed by centrifugation at 1000*g* for 10 min at 4°C, the resulting supernatant was used in western blot analysis as previously described (16). The proteins were separated by 10% SDS-polyacrylamide gel electrophoresis followed by western blot analysis according to the standard procedures. The following antibodies were used: mouse anti-CNGB1 [1B4 (37), 1:30], mouse anti-CNGA1 [2G11 (33), 1:30] and mouse anti-Tubulin (1:2000; Dianova, Hamburg, Germany).

Visual water maze task

The Morris water maze test was originally described as a test for hippocampus-dependent learning (38) and used later with modifications as a test for vision-guided behavior (39). Mice were housed separately in an inverse 12 h light/dark cycle. The experiment was performed in dark. Mice were trained for 3 days (eight trials a day) to locate a stable platform (10 cm in diameter) at dim light conditions of 0.32 cd/m^2 to ensure that vision is totally conferred to the rod system. The platform was placed in a circular swimming pool (120 cm in diameter, 70 cm high, white plastic) filled with water. The starting position of the mouse was changed from trial to trial in a pseudorandom order, whereas the platform was kept in a constant location. Distal cues in the testing room and the

water maze, such as patterned cardboards, were provided as spatial references. Trials were terminated if the mouse climbed onto the platform or when it swam for 2 min. If the mouse did not find the platform, it was gently placed on the stable platform. After each trial, the mouse was left on the platform for 10 s undisturbed before warmed using a heating lamp and transferred to the home cage. On Days 4 and 5, the experiment was performed under light conditions (29.04 cd/m^2) to test cone vision-mediated behavior. The experiment was performed and analyzed blindly to the animal genotype.

Statistics

All values are given as mean ± SE, and N is the number of animals. Unless stated otherwise, an unpaired Student's t-test was performed for the comparison between two groups. Values of $P < 0.05$ were considered significant.

ACKNOWLEDGEMENTS

We thank Gudrun Utz, Pia Lacroix, Jennifer Schmidt and Elisabeth Schulze for excellent technical help, Dr Hildegard Büning for helpful discussion on AAV vectors, Drs James M. Wilson (University of Pennsylvania) and Alberto Auricchio (TIGEM) for the gift of AAV plasmids and Drs Robert Molday (University of British Columbia), Jan de Vente (University of Maastricht), Brigitte Pfeiffer-Guglielmi (University of Tübingen) and Wolfgang Baehr (University of Utah) for the gift of antibodies.

Conflict of Interest statement: None declared.

FUNDING

This work was supported by the Deutsche Forschungsgemeinschaft (DFG) (grant numbers Bi484/4-1 to M.B., Mi1238/1-2 to S.M., and Se837/5-2, Se837/6-2, Se837/7-1 to M.W.S.).

REFERENCES

1. Hartong, D.T., Berson, E.L. and Dryja, T.P. (2006) Retinitis pigmentosa. *Lancet*, **368**, 1795–1809.
2. Sahel, J., Bonnel, S., Mrejen, S. and Paques, M. (2010) Retinitis pigmentosa and other dystrophies. *Dev. Ophthalmol.*, **47**, 160–167.
3. Cideciyan, A.V. (2010) Leber congenital amaurosis due to RPE65 mutations and its treatment with gene therapy. *Prog. Retin. Eye Res.*, **29**, 398–427.
4. Biel, M. and Michalakis, S. (2007) Function and dysfunction of CNG channels: insights from channelopathies and mouse models. *Mol. Neurobiol.*, **35**, 266–277.
5. Biel, M. and Michalakis, S. (2009) Cyclic nucleotide-gated channels. *Handb. Exp. Pharmacol.*, **191**, 111–136.
6. Hüttl, S., Michalakis, S., Seeliger, M., Luo, D.G., Acar, N., Geiger, H., Hudl, K., Mader, R., Haverkamp, S., Moser, M. *et al.* (2005) Impaired channel targeting and retinal degeneration in mice lacking the cyclic nucleotide-gated channel subunit CNGB1. *J. Neurosci.*, **25**, 130–138.
7. Zhang, Y., Molday, L.L., Molday, R.S., Sarfare, S.S., Woodruff, M.L., Fain, G.L., Kraft, T.W. and Pittler, S.J. (2009) Knockout of GARPs and the beta-subunit of the rod cGMP-gated channel disrupts disk morphogenesis and rod outer segment structural integrity. *J. Cell Sci.*, **122**, 1192–1200.
8. Wu, Z.J., Yang, H.Y. and Colosi, P. (2010) Effect of genome size on AAV vector packaging. *Mol. Ther.*, **18**, 80–86.
9. Lai, Y., Yue, Y.P. and Duan, D.S. (2010) Evidence for the failure of adeno-associated virus serotype 5 to package a viral genome ≥8.2 kb. *Mol. Ther.*, **18**, 75–79.
10. Dong, B.A., Nakai, H. and Xiao, W.D. (2010) Characterization of genome integrity for oversized recombinant AAV vector. *Mol. Ther.*, **18**, 87–92.
11. Flannery, J.G., Zolotukhin, S., Vaquero, M.I., LaVail, M.M., Muzyczka, N. and Hauswirth, W.W. (1997) Efficient photoreceptor-targeted gene expression *in vivo* by recombinant adeno-associated virus. *Proc. Natl Acad. Sci. USA*, **94**, 6916–6921.
12. Petrs-Silva, H., Dinculescu, A., Li, Q., Min, S.H., Chiodo, V., Pang, J.J., Zhong, L., Zolotukhin, S., Srivastava, A., Lewin, A.S. *et al.* (2009) High-efficiency transduction of the mouse retina by tyrosine-mutant AAV serotype vectors. *Mol. Ther.*, **17**, 463–471.
13. Seeliger, M.W., Beck, S.C., Pereyra-Munoz, N., Dangel, S., Tsai, J.Y., Luhmann, U.F., van de Pavert, S.A., Wijnholds, J., Samardzija, M., Wenzel, A. *et al.* (2005) *In vivo* confocal imaging of the retina in animal models using scanning laser ophthalmoscopy. *Vision Res.*, **45**, 3512–3519.
14. Fischer, M.D., Huber, G., Beck, S.C., Tanimoto, N., Muehlfriedel, R., Fahl, E., Grimm, C., Wenzel, A., Reme, C.E., van de Pavert, S.A. *et al.* (2009) Noninvasive, *in vivo* assessment of mouse retinal structure using optical coherence tomography. *PLoS ONE*, **4**, e7507.
15. Spaide, R.F. and Curcio, C.A. (2011) Anatomical correlates to the bands seen in the outer retina by optical coherence tomography: literature review and model. *Retina*, **31**, 1609–1619.
16. Michalakis, S., Geiger, H., Haverkamp, S., Hofmann, F., Gerstner, A. and Biel, M. (2005) Impaired opsin targeting and cone photoreceptor migration in the retina of mice lacking the cyclic nucleotide-gated channel CNGA3. *Invest. Ophthalmol. Vis. Sci.*, **46**, 1516–1524.
17. den Hollander, A.I., Black, A., Bennett, J. and Cremers, F.P. (2010) Lighting a candle in the dark: advances in genetics and gene therapy of recessive retinal dystrophies. *J. Clin. Invest.*, **120**, 3042–3053.
18. Smith, A.J., Bainbridge, J.W. and Ali, R.R. (2012) Gene supplementation therapy for recessive forms of inherited retinal dystrophies. *Gene Ther.*, **19**, 154–161.
19. Bainbridge, J.W., Smith, A.J., Barker, S.S., Robbie, S., Henderson, R., Balaggan, K., Viswanathan, A., Holder, G.E., Stockman, A., Tyler, N. *et al.* (2008) Effect of gene therapy on visual function in Leber's congenital amaurosis. *N. Engl. J. Med.*, **358**, 2231–2239.
20. Cideciyan, A.V., Aleman, T.S., Boye, S.L., Schwartz, S.B., Kaushal, S., Roman, A.J., Pang, J.J., Sumaroka, A., Windsor, E.A., Wilson, J.M. *et al.* (2008) Human gene therapy for RPE65 isomerase deficiency activates the retinoid cycle of vision but with slow rod kinetics. *Proc. Natl Acad. Sci. USA*, **105**, 15112–15117.
21. Hauswirth, W.W., Aleman, T.S., Kaushal, S., Cideciyan, A.V., Schwartz, S.B., Wang, L., Conlon, T.J., Boye, S.L., Flotte, T.R., Byrne, B.J. *et al.* (2008) Treatment of Leber congenital amaurosis due to RPE65 mutations by ocular subretinal injection of adeno-associated virus gene vector: short-term results of a phase I trial. *Hum. Gene Ther.*, **19**, 979–990.
22. Bennett, J., Tanabe, T., Sun, D., Zeng, Y., Kjeldbye, H., Gouras, P. and Maguire, A.M. (1996) Photoreceptor cell rescue in retinal degeneration (RD) mice by *in vivo* gene therapy. *Nat. Med.*, **2**, 649–654.
23. Jomary, C., Vincent, K.A., Grist, J., Neal, M.J. and Jones, S.E. (1997) Rescue of photoreceptor function by AAV-mediated gene transfer in a mouse model of inherited retinal degeneration. *Gene Ther.*, **4**, 683–690.
24. Pang, J.J., Boye, S.L., Kumar, A., Dinculescu, A., Deng, W., Li, J., Li, Q., Rani, A., Foster, T.C., Chang, B. *et al.* (2008) AAV-mediated gene therapy for retinal degeneration in the rd10 mouse containing a recessive PDEbeta mutation. *Invest. Ophthalmol. Vis. Sci.*, **49**, 4278–4283.
25. Pang, J.J., Dai, X., Boye, S.E., Barone, I., Boye, S.L., Mao, S., Everhart, D., Dinculescu, A., Liu, L., Umino, Y. *et al.* (2011) Long-term retinal function and structure rescue using capsid mutant AAV8 vector in the rd10 mouse, a model of recessive retinitis pigmentosa. *Mol. Ther.*, **19**, 234–242.
26. Luo, D.G., Xue, T. and Yau, K.W. (2008) How vision begins: an odyssey. *Proc. Natl Acad. Sci. USA*, **105**, 9855–9862.
27. Michalakis, S., Mühlfriedel, R., Tanimoto, N., Krishnamoorthy, V., Koch, S., Fischer, M.D., Becirovic, E., Bai, L., Huber, G., Beck, S.C. *et al.* (2010) Restoration of cone vision in the CNGA3$^{-/-}$ mouse model of

congenital complete lack of cone photoreceptor function. *Mol. Ther.*, **18**, 2057–2063.
28. Gao, G.P., Alvira, M.R., Wang, L., Calcedo, R., Johnston, J. and Wilson, J.M. (2002) Novel adeno-associated viruses from rhesus monkeys as vectors for human gene therapy. *Proc. Natl Acad. Sci. USA*, **99**, 11854–11859.
29. Auricchio, A., Hildinger, M., O'Connor, E., Gao, G.P. and Wilson, J.M. (2001) Isolation of highly infectious and pure adeno-associated virus type 2 vectors with a single-step gravity-flow column. *Hum. Gene Ther.*, **12**, 71–76.
30. Grieger, J.C., Choi, V.W. and Samulski, R.J. (2006) Production and characterization of adeno-associated viral vectors. *Nat. Protoc.*, **1**, 1412–1428.
31. Seeliger, M.W., Grimm, C., Stahlberg, F., Friedburg, C., Jaissle, G., Zrenner, E., Guo, H., Reme, C.E., Humphries, P., Hofmann, F. *et al.* (2001) New views on RPE65 deficiency: the rod system is the source of vision in a mouse model of Leber congenital amaurosis. *Nat. Genet.*, **29**, 70–74.
32. Tanimoto, N., Muehlfriedel, R.L., Fischer, M.D., Fahl, E., Humphries, P., Biel, M. and Seeliger, M.W. (2009) Vision tests in the mouse: functional phenotyping with electroretinography. *Front Biosci.*, **14**, 2730–2737.
33. Molday, R.S., Molday, L.L., Dose, A., Clark-Lewis, I., Illing, M., Cook, N.J., Eismann, E. and Kaupp, U.B. (1991) The cGMP-gated channel of the rod photoreceptor cell characterization and orientation of the amino terminus. *J. Biol. Chem.*, **266**, 21917–21922.
34. Connell, G., Bascom, R., Molday, L., Reid, D., McInnes, R.R. and Molday, R.S. (1991) Photoreceptor peripherin is the normal product of the gene responsible for retinal degeneration in the rds mouse. *Proc. Natl Acad. Sci. USA*, **88**, 723–726.
35. Tanaka, J., Markerink-van Ittersum, M., Steinbusch, H.W. and De Vente, J. (1997) Nitric oxide-mediated cGMP synthesis in oligodendrocytes in the developing rat brain. *Glia*, **19**, 286–297.
36. Zhang, T., Baehr, W. and Fu, Y. (2012) Chemical chaperone TUDCA preserves cone photoreceptors in a mouse model of Leber congenital amaurosis. *Invest. Ophthalmol. Vis. Sci.*, **53**, 3349–3356.
37. Poetsch, A., Molday, L.L. and Molday, R.S. (2001) The cGMP-gated channel and related glutamic acid-rich proteins interact with peripherin-2 at the rim region of rod photoreceptor disc membranes. *J. Biol. Chem.*, **276**, 48009–48016.
38. Morris, R. (1984) Developments of a water-maze procedure for studying spatial learning in the rat. *J. Neurosci. Methods*, **11**, 47–60.
39. Pang, J.J., Chang, B., Kumar, A., Nusinowitz, S., Noorwez, S.M., Li, J., Rani, A., Foster, T.C., Chiodo, V.A., Doyle, T. *et al.* (2006) Gene therapy restores vision-dependent behavior as well as retinal structure and function in a mouse model of RPE65 Leber congenital amaurosis. *Mol. Ther.*, **13**, 565–572.

OPEN ACCESS Freely available online

PLOS ONE

Towards a Quantitative OCT Image Analysis

Marina Garcia Garrido[1]*, Susanne C. Beck[1], Regine Mühlfriedel[1], Sylvie Julien[2], Ulrich Schraermeyer[2], Mathias W. Seeliger[1]

1 Division of Ocular Neurodegeneration, Institute for Ophthalmic Research, Centre for Ophthalmology, Tuebingen, Germany, **2** Section of Experimental Vitreoretinal Surgery, Centre for Ophthalmology, Tuebingen, Germany

Abstract

Background: Optical coherence tomography (OCT) is an invaluable diagnostic tool for the detection and follow-up of retinal pathology in patients and experimental disease models. However, as morphological structures and layering in health as well as their alterations in disease are complex, segmentation procedures have not yet reached a satisfactory level of performance. Therefore, raw images and qualitative data are commonly used in clinical and scientific reports. Here, we assess the value of OCT reflectivity profiles as a basis for a quantitative characterization of the retinal status in a cross-species comparative study.

Methods: Spectral-Domain Optical Coherence Tomography (OCT), confocal Scanning-La-ser Ophthalmoscopy (SLO), and Fluorescein Angiography (FA) were performed in mice (*Mus musculus*), gerbils (*Gerbillus perpadillus*), and cynomolgus monkeys (*Macaca fascicularis*) using the Heidelberg Engineering Spectralis system, and additional SLOs and FAs were obtained with the HRA I (same manufacturer). Reflectivity profiles were extracted from 8-bit greyscale OCT images using the ImageJ software package (http://rsb.info.nih.gov/ij/).

Results: Reflectivity profiles obtained from OCT scans of all three animal species correlated well with ex vivo histomorphometric data. Each of the retinal layers showed a typical pattern that varied in relative size and degree of reflectivity across species. In general, plexiform layers showed a higher level of reflectivity than nuclear layers. A comparison of reflectivity profiles from specialized retinal regions (e.g. visual streak in gerbils, fovea in non-human primates) with respective regions of human retina revealed multiple similarities. In a model of Retinitis Pigmentosa (RP), the value of reflectivity profiles for the follow-up of therapeutic interventions was demonstrated.

Conclusions: OCT reflectivity profiles provide a detailed, quantitative description of retinal layers and structures including specialized retinal regions. Our results highlight the potential of this approach in the long-term follow-up of therapeutic strategies.

Citation: Garcia Garrido M, Beck SC, Mühlfriedel R, Julien S, Schraermeyer U, et al. (2014) Towards a Quantitative OCT Image Analysis. PLoS ONE 9(6): e100080. doi:10.1371/journal.pone.0100080

Editor: Knut Stieger, Justus-Liebig-University Giessen, Germany

Received March 11, 2014; **Accepted** May 21, 2014; **Published** June 13, 2014

Data Availability: The authors confirm that all data underlying the findings are fully available without restriction. All relevant data are within the paper and its Supporting Information files.

Funding: This work was supported by the European Union(HEALTH-F2-2008-200234 and HEALTH-F2-2010-242013), Deutsche Forschungsgemeinschaft (DFG, grants Se837/5-2, Se837/6-1, Se837/6-2, Se837/7-1), and the German Ministry of Education and Research (BMBF, HOPE^2 01GM1108A). We acknowledge support by Deutsche Forschungsgemeinschaft and Open Access Publishing Fund of Tuebingen University. The funders had no role in study design, data collection and analysis, decision to publish, or preparation of the manuscript.

Competing Interests: The authors have declared that no competing interests exist.

* E-mail: marina.garcia-garrido@med.uni-tuebingen.de

Introduction

Vision starts in the retina located at the posterior part of the eye. "Rete", the Latin origin of its name standing for "net", connotes with two important properties, a two-dimensional layer structure and a multitude of connections. Indeed, the retina is composed of several heavily interconnected neuronal layers, each with a specific functional property from the light reception to signal processing and data reduction [1].

In contrast to the rather similar principal organization of the retina in layers, its topography varies substantially between mammalian species, presumably due to evolutionary influences of the environmental conditions [2,3]. In humans and non-human primates (NHPs), a central region of high visual acuity, the macula, has evolved, whereas most other species have a more or less clearly expressed visual streak that is usually located at the separation of the upper and the lower retina. This configuration is believed to follow the basic visual needs of each species, namely high-acuity vision of the horizon, low-sensitivity vision of the (bright) sky, and high-sensitivity vision of the (relatively dim) ground.

Traditionally, fundus photography and angiography have been used to assess macroscopic retinal structure and its changes in disease, whereas fine details were merely accessible via *ex vivo* methods like histology and immunohistochemistry. It was a major breakthrough in ophthalmic diagnostics when Optical Coherence Tomography (OCT) was first introduced as a novel tool for *in vivo* visualization of retinal layers [4–6]. The resolution of third

generation models of OCT equipment that became available a few years later finally turned out to be sufficient for use in rodent models of retinal disease [7,8]. A particular asset for experimental research is the option to follow the course of disease and/or monitor the effects of a therapeutic intervention over time in individual eyes [7,9].

Technically, OCT provides cross-sectional images based on the reflective properties of the investigated sample [4,5]. A single measurement of the reflectivity versus depth at one specific location is called A-scan, whereas the composition of an image by alignment of several consecutive A-scans is called B-scan [10].

A typical B-scan shows several, often alternating bands of low and high reflectivity, as plexiform layers have a higher level of reflectivity than nuclear layers [11]. However, these bands and the retinal layers associated with them vary in their extent with the topographical position in the retina, and this is additionally species-dependent as mentioned above. So far, automated segmentation procedures have still not reached a satisfactory level of performance, which is why in the majority of cases simply a qualitative evaluation is performed.

In this work, we use the layer reflectivity in OCT images as a function of scan depth (similar to A-scan data) for a quantitative analysis of the retina of three different species.

Experimental quantifications based on A-scans have been performed in the past, but have not led to a widespread use of respective approaches [12–15]. Nevertheless, we show here that the information contained in A-scan data is very helpful for the robust quantification of changes in health and disease, and that respective parameters have the potential for excellent quantitative biomarkers bypassing the need for an accurate segmentation of the B-scan images.

Materials and Methods

Ethics Statement

All procedures in rodents were performed according to the German laws governing the use of experimental animals and were previously approved by the local authorities (Regierungspraesidium Tuebingen), which are in accordance with the ARVO statement for the Use of Animals in Ophthalmic and Visual Research.

The OCT data from Monkeys was taken from a dataset recorded as part of a separate study at Covance Laboratories (Muenster, Germany).

Animals

The present study includes three animal models, mice, Gerbils, and Cynomolgus monkeys. In the rodent part, four individual animals per line or species were used (pigmented C57BL/6 wild type mice, non-pigmented BALB/c mice, and gerbils (*Gerbillus perpallidus*)). Rodents were kept under a 12 h:12 h light-dark cycle (60 lux) and they had free access to food and water. Mice were anesthetized with ketamine (66,7 mg/kg) and xylazine (11,7 mg/kg) and their pupils were dilated with tropicamide eyedrops (Mydriaticum Stulln; Pharma Stulln, Stulln, Germany) before image acquisition. Gerbils were anesthetized following the indications of a previous study with this specie carried out by our group [16].

The OCT data of five Cynomolgus monkeys (*Macaca fascicularis*, ages 10 to 15 years, supplied by Nafovanny, Vietnam) were recorded as part of a separate study [17], and used here to construct the reflectivity profiles. Primates were anesthetized with ketamine hydrochloride (10 mg/kg, Ketavet; Pharmacia GmbH, Erlangen, Germany) plus xylazine (2 mg/kg, WDT, Garbsen, Germany). Their pupils were dilated (tropicamide, phenylephrine, Novartis, Siemens, Germany) and their corneae anesthetized (oxybuprocainhydrochloride, Novartis).

Scanning-Laser Ophthalmoscopy (SLO)

Retinal structures of the anesthetized animals were visualized via SLO imaging with a HRA 1 and HRA 2 (Heidelberg Engineering, Heidelberg, Germany) according to previously described procedures [18]. Briefly, HRA 1 and HRA 2 systems feature lasers in the short (visible) wavelength range (488 nm in both and 514 nm in HRA 1 only), and also in the long (infrared) wavelength range (795/830 nm and 785/815 nm). The 488 and 795 nm lasers are used for fluorescein (FLA) and indocyanine green (ICG) angiography, respectively.

Spectral Domain Optical Coherence Tomography (SD-OCT)

SD-OCT imaging was performed in the same session as cSLO and it was carried out with a Spectralis HRA+OCT (Heidelberg Engineering GmbH, Heidelberg, Germany). This device features a superluminescent diode at 870 nm as low coherence light source. Scans are acquired at a speed of 40.000 scans per second and each two-dimensional B-scan contains up to 1536 A-scans. [7]. The images were taken with the equipment set of 30° field of view and with the software Heidelberg Eye Explorer (HEYEX version 5.3.3.0, Heidelberg, Germany).

Image Acquisition and Image Analysis

In order to define a reproducible reflectivity profile in mouse and gerbil, the position of the retinal fundus image was standardized. To achieve that, the position of the eye was adapted until the optic disc was exactly in the center of the fundus region visualized with the SLO module of the Spectralis, and all OCT scans were acquired in this position. In analogy, the visual streak in gerbils and the fovea in cynomolgus monkeys was positioned in the center of the retinal image. In cynomolgus monkeys, additional reflectivity profiles were extracted from OCT scans taken from a retinal region rich in nerve fibres [19], close to the optic disc.

OCT scans were exported and converted with Corel Draw X3 (Corel Corporation, Ottawa, ON Canada) into a 8-bit greyscale images. Images were then processed with the ImageJ software package (http://rsb.info.nih.gov/ij/), and reflectivity profiles were extracted from ten adjacent parallel lines which crossed perpendicularly the OCT scan from the upper layer, the ganglion cell layer to the bottom layer, the retinal pigmented epithelium. For a visual representation of the underlying statistics of the data, reference lines indicating the 5, 50 and 95 quantiles were generated.

Ex vivo Analysis of Retinal Morphology

Mice and gerbils were sacrificed upon completion of experiments and their eyes were marked and enucleated for histological analysis. They were fixed in 2,5% glutaraldehyde prepared in 0.1 M cacodylate buffer and processed as previously described [20]. Subsequently, semi-thin sections (0,5 mm) were obtained and counterstained with methylene blue and were posteriorly analyzed using a light microscope (Axiovision, Zeiss, Jena, Germany).

Results

Generation of OCT Reflectivity Profiles

Mammalian retinae differ somewhat in their morphological landmarks. To understand commonalities and differences in

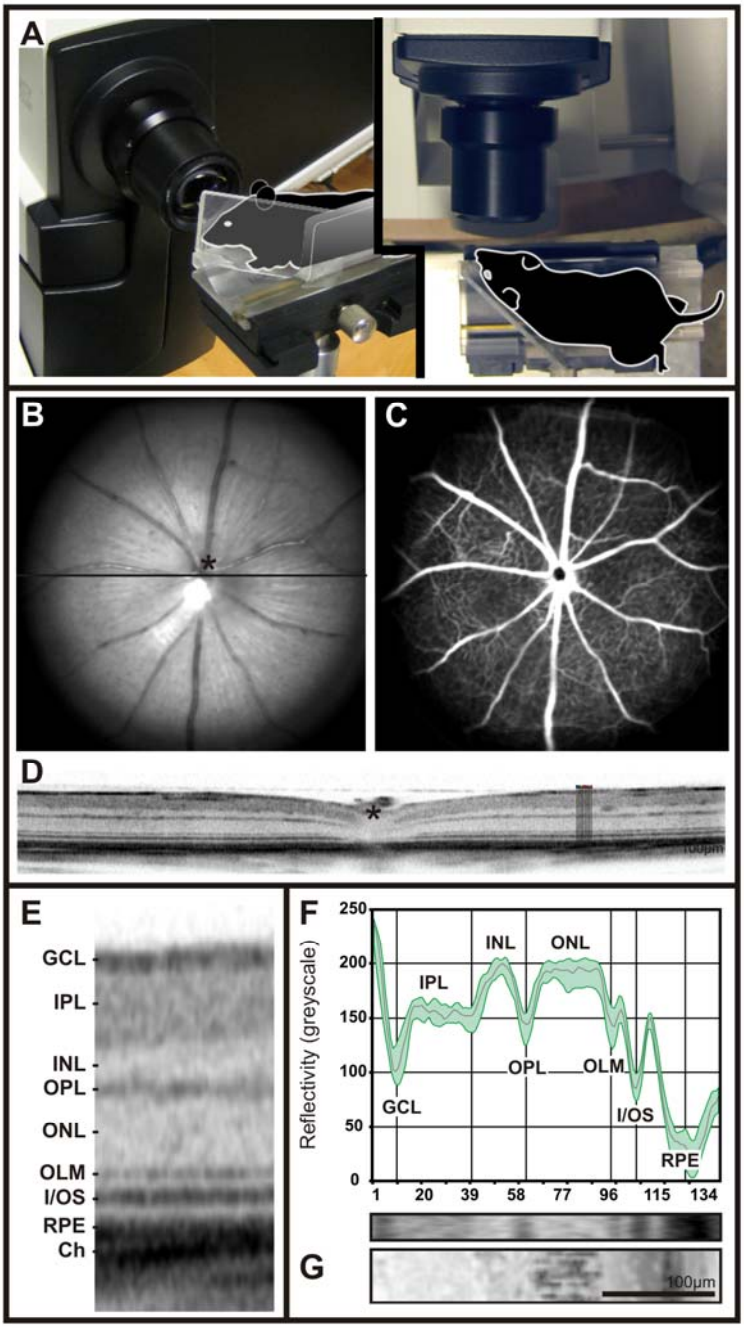

Figure 1. Set-up to visualize the mouse retina: retinal morphology, layer composition and OCT reflectivity profile (A–F). Illustrative representation of the mouse placed in front of the Spectralis camera (**A**). Mouse fundus native image at 513 nm (**B**) and retinal angiography image following fluorescein dye injection using a barrier filter at 488 nm (**C**). Retinal layer composition by means of an OCT horizontal scan through the optic disc (asterisk) and schematic depiction of the 10 longitudinal adjacent pixel lines from which reflectivity profiles were extracted (**D**). Blow up of a section from the OCT scan indicating the retinal layers (**E**). Corresponding OCT reflectivity profiles from "D" and assignation to the different OCT bands as well as correlation with histology (**G**). **Abbreviations:** GCL, ganglion cell layer; IPL, inner plexiform layer; INL, inner nuclear layer; OPL, outer plexiform layer; ONL, outer nuclear layer; I/OS, inner/outer segment border; RPE, retinal pigmented epithelium.
doi:10.1371/journal.pone.0100080.g001

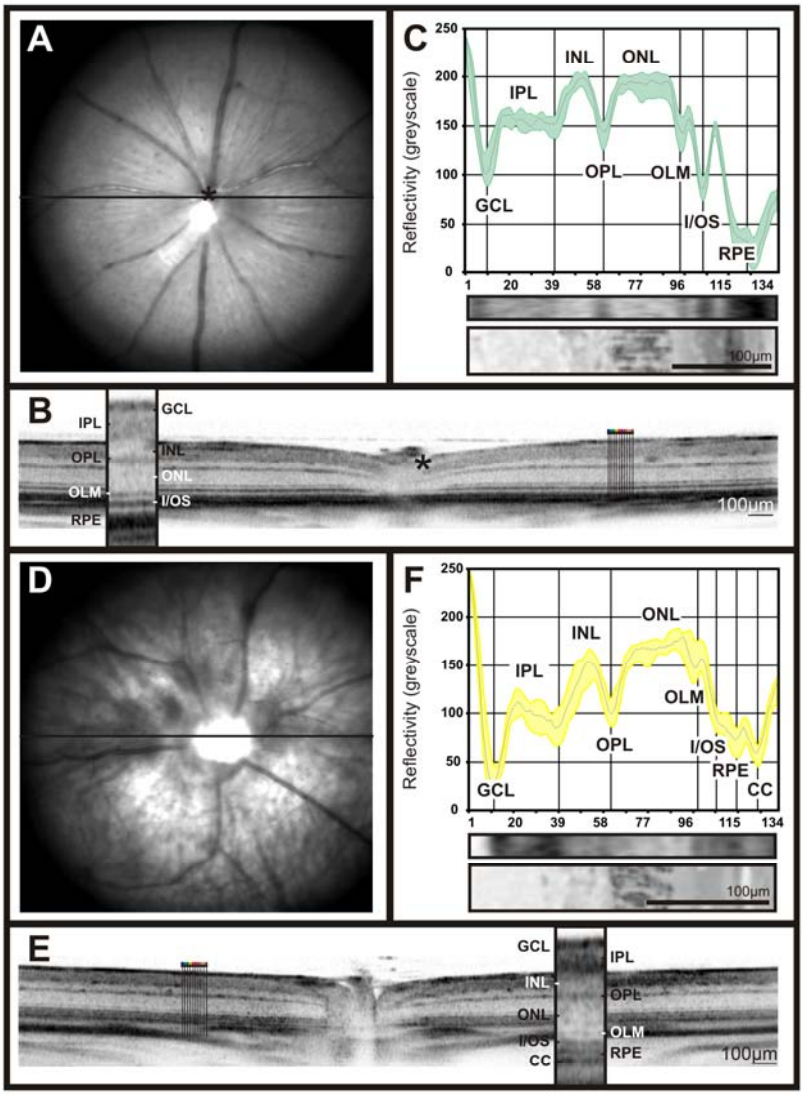

Figure 2. Retinal imaging and OCT reflectivity profiles of two control lines. Fundus native imaging at 514 nm (**A, D**), horizontal OCT scan (**B, E**) and OCT reflectivity profiles were acquired from C57BL/6 pigmented (**A–C**) and BALB/c non pigmented mice (**D–F**).
doi:10.1371/journal.pone.0100080.g002

respective OCT data, a comprehensive in vivo examination using scanning-laser ophthalmoscopy (SLO), fluorescein angiography (FLA), and optical coherence tomography (OCT) was done in three mammalian laboratory species, mice, gerbils and cynomolgus monkeys. OCT reflectivity profiles were then generated by averaging ten adjacent pixel columns from the greyscale image data with the ImageJ software package as described in methods. The SLO examination included the native red-fee (RF; 513 nm), infrared (IR; 830 nm), and autofluorescence (AF; 488 nm) modes. Retinal vasculature was assessed after injection of fluorescein dye via 488 nm wavelength laser with a barrier filter at 500 nm. The results are summarized in the following sections.

OCT Reflectivity Profiles in Mice

Retinal image data using scanning-laser ophthalmoscopy (SLO), fluorescein angiography (FA), and optical coherence tomography (OCT) were obtained from pigmented C57Bl/6 and non-pigmented BALB/c mice. Typically, low greyscale values were found in regions corresponding to the nerve fibre layer (NFL), inner plexiform layer (IPL), outer plexiform layer (OPL), outer limiting membrane (OLM), the border between inner segment and outer segment (I/OS), and the retinal pigmented epithelium (RPE). In contrast, high greyscale values were typical for the inner nuclear layer (INL) and the outer nuclear layer (ONL). In this study, nuclear layer greyscale values in both mouse strains

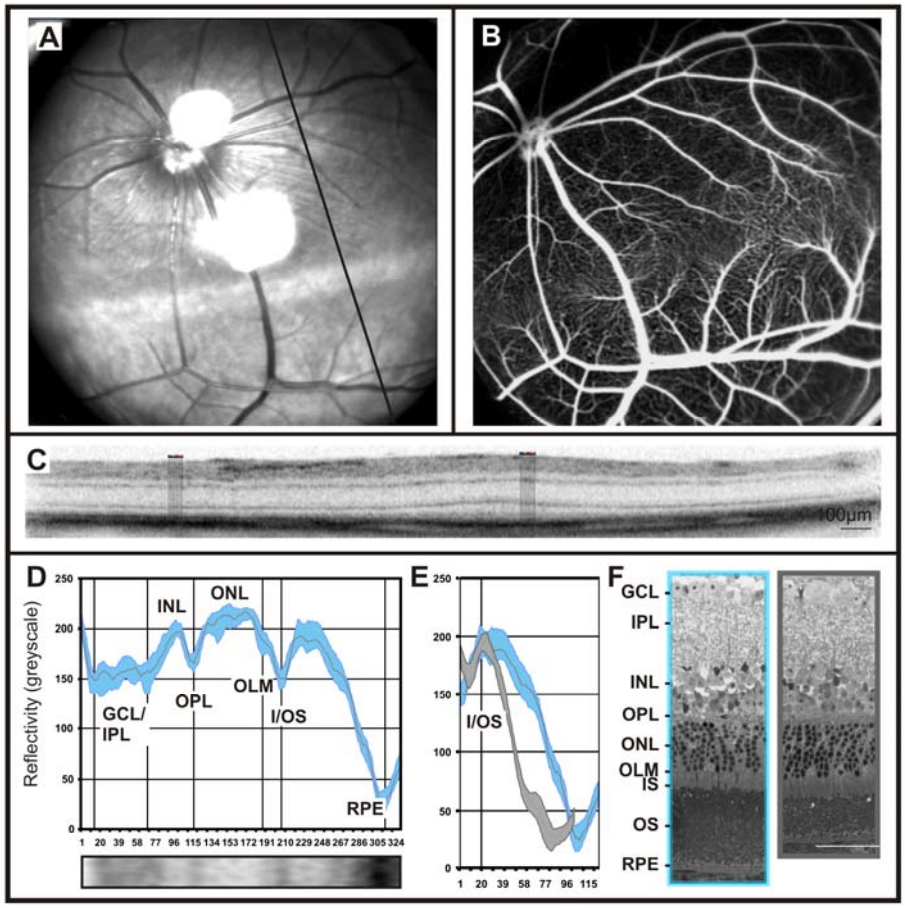

Figure 3. Retinal imaging and OCT reflectivity profile in gerbils. Native fundus image at 514 nm depicts the visual streak as a horizontal hyper reflective structure (**A**). Using fluorescein angiography a characteristic ramification of the capillary net along the visual streak can be observed (**B**). OCT scan through the visual streak reveals changes in the layering in comparison to the rest of the retina (**C**). OCT reflectivity profile from 10 longitudinal adjacent lines at the level of the visual streak and correlation to the retinal layers (**D**). Overlay of the OCT reflectivity profiles extracted from the visual streak (blue) versus the non visual streak regions (grey) (**E**). Histological work-up showing structural differences between the visual streak (blue) and other retinal areas (grey) (**F**).
doi:10.1371/journal.pone.0100080.g003

averaged about 175±15 units, whereas plexiform layers ranged around 150±15 units (Fig. 1F; Fig. 2 C, F).

Although the murine retina appears less topographically structured than that of many other mammals, there are still several structural differences concerning e.g. cell number and distribution, chemical gradients, and visual pigment distribution [3]. To assess whether or not such topographical differences affect OCT reflectivity properties, representative profiles were extracted from OCT scans taken from the dorsal, ventral, nasal and temporal parts of C57BL/6 mouse retinas. However, no substantial differences were found (Fig. S1).

Another important factor in retinal imaging is the degree of pigmentation, as it determines the amount of absorbed light in a wavelength-dependent manner. In this work, we addressed the influence of the degree of pigmentation via a comparison of data from heavily pigmented C57Bl/6 mice, featuring a relatively high melanin content in RPE and choroid, with those from non-pigmented BALB/c mice. As already known from SLO en face imaging work, melanin-rich structures reduce the transmission of light in a wavelength-dependent fashion [18], and although the infrared range is least affected by that, there are still perceivable effects in OCT [8]. The comparison between the two models revealed a generally increased scan depth when pigmentation was low, together with a better differentiation of bands in the outer retina/RPE region (Fig. 2E). These bands are presumably associated with retinal epithelium, choriocapillaris, choroid, and sclera (Fig. 2F).

OCT Reflectivity Profiles in Gerbils

Gerbils are rodents that have a much more topographically structured retina than mice or rats, which has been attributed to their different circadian activity. Retinal image data using scanning-laser ophthalmoscopy (SLO), fluorescein angiography (FA), and optical coherence tomography (OCT) were obtained the same way as in mice. In this study we found that the principal

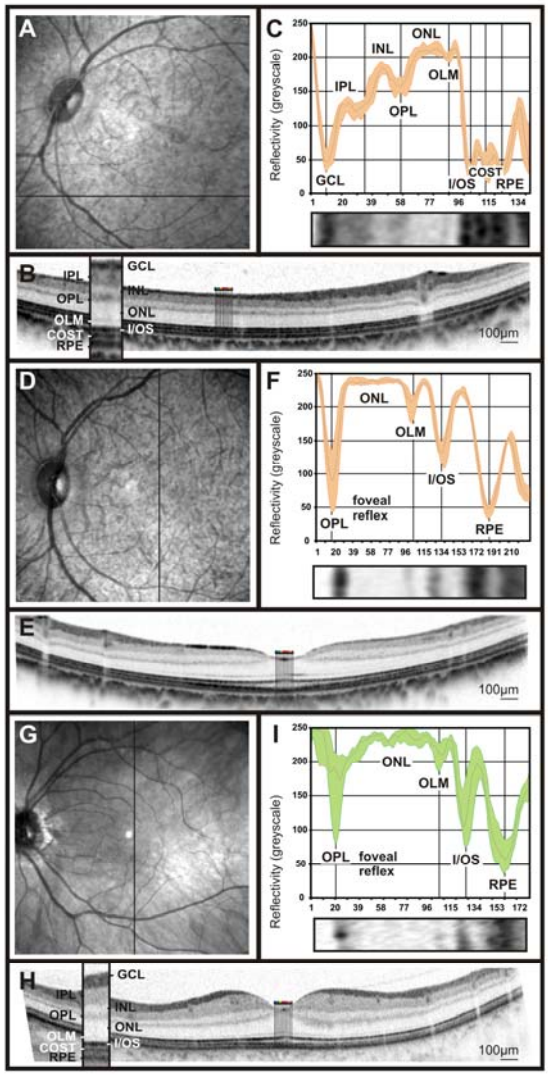

Figure 4. Retinal imaging and OCT reflectivity profile in cynomolgus monkeys and comparison to humans. SLO native fundus imaging in non-human primates (**A**, **D**) and one of the researcher's eye (**G**). The solid bar indicates the origin of the OCT scan. A representative OCT scan taken from the ventral retina (**B**), the fovea of the non-human primate (**F**) and the researcher's eye, (**H**). OCT reflectivity profiles from B, F and H were extracted and assigned to the retinal layers of cynomolgus monkeys fovea and extrafoveal regions (**F** and **C**, respectively) and the human fovea (**I**).
doi:10.1371/journal.pone.0100080.g004

layering structure and the reflectivity profiles were similar to that of most other rodent species, i.e. plexiform layers form zones of higher reflectivity, and nuclear layers bands of lower reflectivity (Fig. 3 D, E). However, there were strong topographical differences in that Gerbils have a strongly expressed visual streak (VS). The VS is, according to current knowledge, an area of increased visual performance for objects on the horizon (Fig. 3A), and thus both morphologically and functionally resembles some features of the human macula. In particular, this includes a characteristic vascular pattern (Fig. 3B), as well as an increased thickness of the photoreceptor layer. Since a similar, but less strongly expressed retinal pattern was found in the unstriped soudanian grass rat (*Arvicanthis ansorgei*) [21], one may speculate that this is common to day active rodents in general.

The recorded OCT reflectivity profiles enabled the quantification and allocation of the corresponding topographical differences in retinal layers, particularly with respect to the visual streak in the dorsal part of the retina (Fig. 3D, E). In this region, the number of photoreceptors is increased, as was confirmed histologically (Fig. 3F). The increased number of photoreceptors is reflected in the OCT reflectivity profile by a much broader extent of the outer segment band when compared to more peripheral regions.

OCT Reflectivity Profiles in Non-human Primates (NHPs)

Non-human primates, due to the presence of a fovea, have an even more topographically structured retina. Again, retinal image data using scanning-laser ophthalmoscopy (SLO), fluorescein angiography (FA), and optical coherence tomography (OCT) were obtained to assess their retinal characteristics. Interestingly, reflectivity profiles from cynomolgus monkeys allowed for a further differentiation of the outer retina, as in extrafoveal regions an additional peak in the reflectivity profile, between the I/OS and the RPE peaks, was detected (Fig. 4C and 5D, G). This peak is thought to belong to the cone outer segment tips (COST) [22,23]. Further, the reflectivity profiles were in accordance with the anatomical changes in the macular area, leading to a reduction and eventually the absence of the bands corresponding to GCL, IPL, and INL. However, the OPL, ONL, I/OS and RPE layers were clearly visible (Fig. 4D–F). When exactly centered on the fovea, the reflectivity curve started with a strong peak representing the foveal reflex (Fig. 4F, [24]). In general, the observed reflectivity profile showed a remarkable resemblance to human data (Fig. 4G–H). Nevertheless, some differences were detected, e.g. the ONL peak was wider in human subjects than in NHPs (Fig. 4I).

The retinal nerve fibre layer (NFL) is mainly formed by ganglion cell axons en route to the optic disc [19]. We gave special attention to the reflectivity pattern of this layer, since alterations in the number of nerve fibres are the basis for several optic dystrophies. Glaucoma is one of the most important diseases in this group, and although there are yet no sufficiently established criteria for detection and monitoring of this disorder, the assessment of NFL thinning is currently a common clinical test [25]. First, we compared the NFL appearance in cynomolgus monkey to that in human subjects (Fig. 5A–C vs. D–F). As part of this comparison, we generated a thickness map from volume scans with 97 B-Scans at 30 µm intervals centred to the fovea, which revealed an increase on the retinal thickness mainly at the sites where major blood vessels are located (Fig. 5A). However, the NFL quantification based vertical OCT scans around the optic disc, together with the reflectivity profiles extracted from them, suggested that a major portion of this thickness is true fibre increase and only a minor portion may be attributed to vessels directly (Fig. 5B & C, E & F). In summary, the comparison of OCT reflectivity profiles between NHPs and human subjects did not reveal major differences, so that this technique is well suited for the follow-up of NHPs in preclinical trials.

Use of Reflectivity Profiles in the Evaluation of Therapeutic Interventions

The progress in molecular therapy of retinal diseases has led to a number of therapeutic approaches, implemented so far mainly in animal disease models and only partly in human clinical trials. In

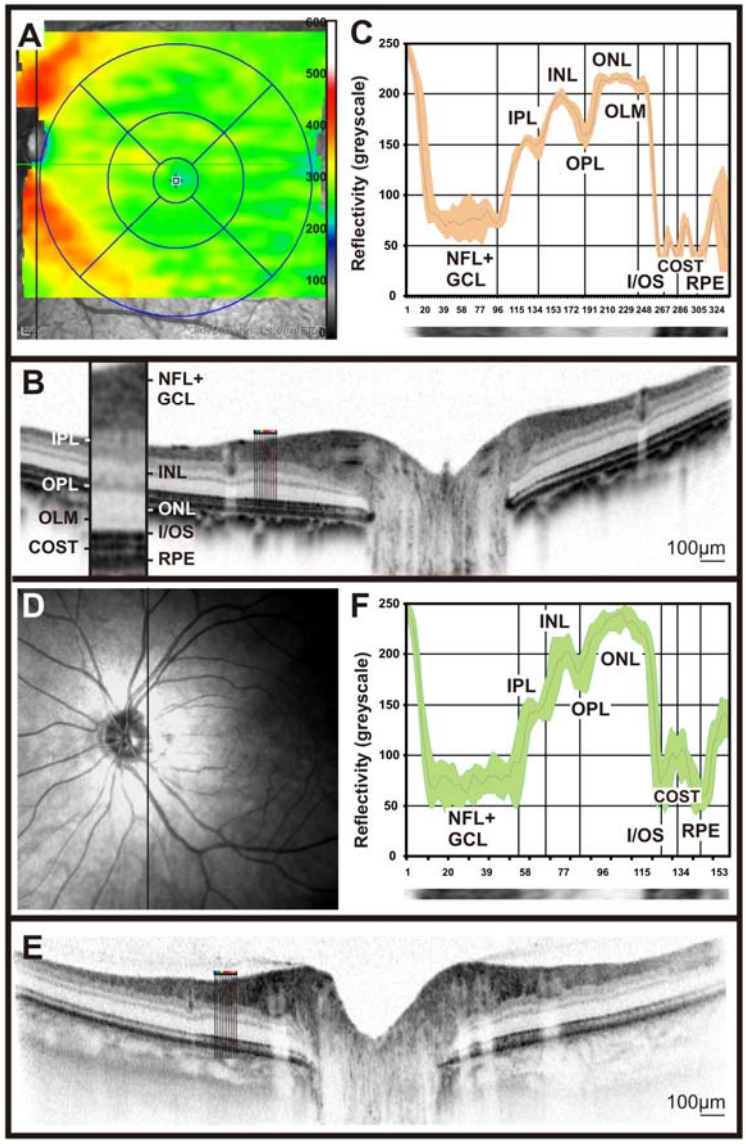

Figure 5. Comparison between the NFL appearance in cynomolgus monkeys and humans by means of OCT reflectivity profiles. Retinal thickness profile map of a cynomolgus monkey indicates where the thickest areas of the retina are located to, presumably due to the abundance of nerve fibers (**A**). SLO imaging in one of the researcher's eye (**D**). Retinal layering via OCT imaging was performed across the central retina in cynomolgus monkeys (**B**) and compared to that of humans (**E**). OCT reflectivity profiles from a region rich in nerve fibers were acquired from cynomolgus monkeys (**C**) and that of human (**F**).
doi:10.1371/journal.pone.0100080.g005

diseases that are accompanied by an alteration or degeneration of tissues, quantification of OCT data may be a valuable biomarker for the post-treatment follow-up. Here, we assessed this follow-up in a model of Retinitis Pigmentosa (RP) lacking the gene encoding the rod nucleotide-gated channel subunit CNGB1 [26]. Like in RP, a knock-out of CNGB1 leads to a mildly progressive degeneration of rods and subsequently of cones [27]. In early stages, rod cells are preserved but do not develop regular outer segments. Recently, we were able to restore morphology and function in the Cngb1 knock-out mouse by means of adeno-associated virus (AAV)-mediated gene therapy [28]. The OCT imaging follow-up of interventions applied in early disease stages (sixty days after injection) revealed that in the treated eye, the injected region (in our approach roughly one third of the retina) showed signs of a substantial rescue, presenting as a persistence of photoreceptor outer segments and maintenance of a regular retinal layering, whereas in the untreated eye no regular outer segment-related layers were found (Fig. 6C vs. A). In OCT

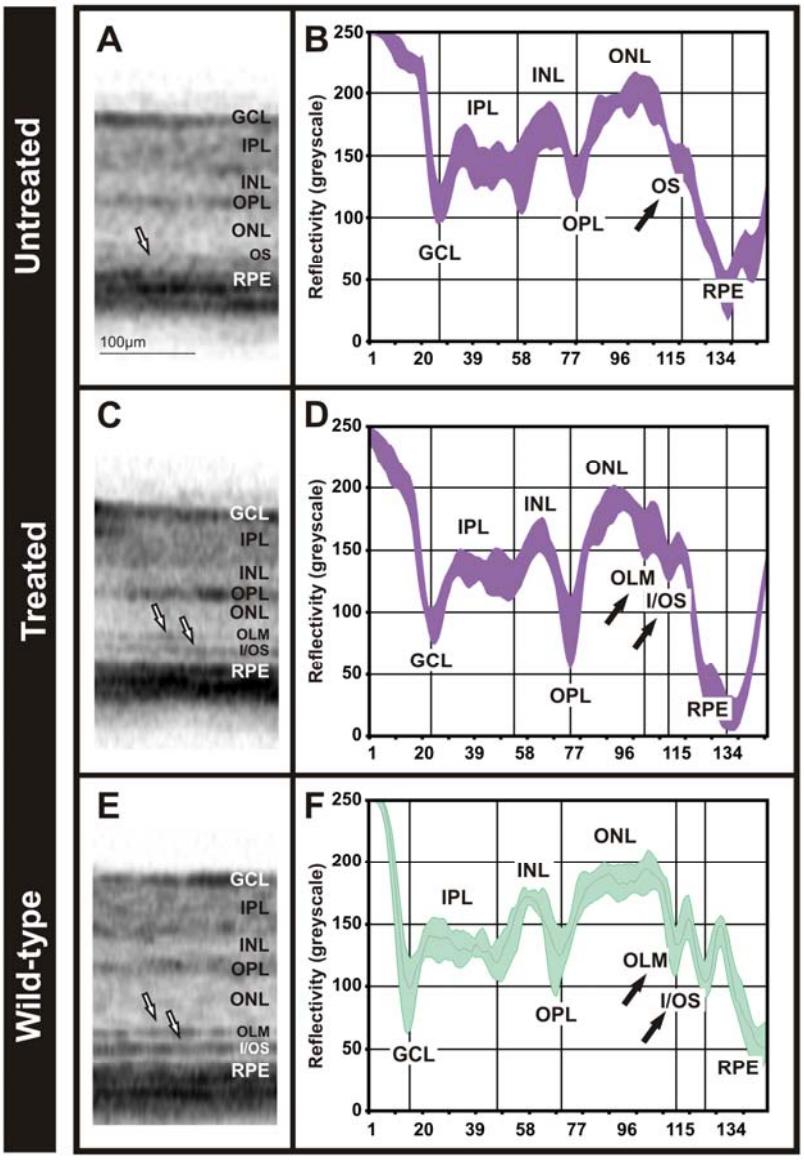

Figure 6. Comparison of retina layer composition and OCT reflectivity profile after a gene therapy approach in the Cngb1 *knock-out* mouse. Representative OCT sections of the untreated eye (**A**), treated (**C**) in the Cngb1 *knock-out* mouse and in a C57BL6 control mouse (**E**). OCT reflectivity profiles from the untreated eye (**B**), treated (**D**) and control (**F**).
doi:10.1371/journal.pone.0100080.g006

reflectivity profiles from those respective areas, substantial differences were found (Fig. 6D vs. B). In the untreated eye, the two peaks corresponding to the OLM and the I/OS border, usually found at approximately 175±9 and 150±7 greyscale units, were absent; merely a minor OLM band remained visible (Fig. 6B, D). However, the regular peaks were present in the treated eye. Our results corroborate the restoration of the rod CNG channel [28], and show the potential for this diagnostic tool as a biomarker in the follow-up of therapeutic trials in retinal diseases.

Discussion

In this work, we assess the potential of OCT reflectivity profiles as a basis for a quantitative characterization of the retinal morphology in vivo. Since we feel this approach may have a general value in the interpretation and quantification of mammalian OCT data, we chose a cross-species comparative study design.

Our results show that such quantitative OCT analyses are very well suited to capture and numeralize similarities and differences in the retina of three laboratory species with a different degree of

topographic structuring (Fig. 1–4). Our work closely relates to human studies [12,13,15,29].

The characteristic pattern of the mammalian reflectivity profiles may also help to better fine-tune automated segmentation algorithms. It is a long-standing problem that, because retinal anatomy and layering in health as well as in disease is complex and variable, automated segmentation procedures have not yet reached a satisfactory level of performance.

As a first step in this study, we generated a basic reflectivity profile of standard mouse lines, the C57BL/6 line representing pigmented strains, and the BALB/c line representing non-pigmented ones. Each part of the profile was matched to a corresponding retinal structure in ex vivo morphology (Fig. 1F and 2F). As presumed, we found that variations in the retinal pigment content do influence the detection of the underlying anatomical structures and their representation in the reflectivity profile (Fig. 2F). By acquiring several reflectivity profiles from different fundus locations, we could demonstrate that the comparatively minor topographical differences across the mouse retina (e.g. cell distribution, opsin gradient) did not substantially manifest in OCT reflectivity profiles (Fig. S1).

In a next step, we recorded a standard reflectivity profile of another rodent model, the gerbil (Fig. 3D, E). Gerbils are primarily diurnal (activity during the day and sleeping at night). Their body size lies between that of mice and rats, but their retinal organisation is very different from those primarily nocturnal species. Most obvious in this regard is the well-expressed visual streak, a specialized retinal region that resembles many features of the human macula [16]. The visual streak is represented in the native fundus image as a high reflective band located to the dorsal part of the retina (Fig. 3A). Based on the reflectivity profile, we were able to show that the visual streak region is characterized by an elongation of the crest corresponding to the photoreceptor outer segments (Fig. 3D, E). Another typical landmark in gerbils is the characteristic pattern of the retinal vasculature (Fig. 3B, further details in [16]). The relatively high similarity of the vascular organization with the human macula may render this class of rodents suitable models for experimental therapies in diseases with a strong vascular component like Diabetes Mellitus.

It is believed that the topographical differences in retinal morphology between different animal species have developed due to evolutionary pressure in their natural habitat. The driving force may be an advantage in the acquirement and processing of specific, vital visual information. Typical patterns associated with such an adaptation may include a difference in the number and type of retinal cells (e.g. photoreceptors, bipolar, or ganglion cells), the distribution and spectral sensitivity of visual pigments, or even variations in the vascular pattern [3]. It is believed that preferential day- or night-activity constitutes a major determina-tive factor in this context, and whether the animal's role is rather prey or predator. Indeed, other day-active species like the unstriped soudanian grass rat (*Arvicanthis ansorgei*) are known to possess a retina rich in cones and a special organisation of those in the ONL [21], very well in agreement with our findings. More details regarding to the visual streak organi-sation in a predator like the cat with a so-called *area centralis* may be found elsewhere [30].

Finally, we turned to even further specialised retinas as found in primates and humans. These retinae are characterized by the presence of a *fovea* conferring high-acuity central vision. Based on Cynomolgus data, we produced a generic OCT reflectivity profile in non-human primates. All layers in foveal and non-foveal regions were successfully matched with the human counterparts (Fig. 4F and 4I). Also, the foveal reflex, featuring a total reflection, was detected in both primates and humans (Fig. 4F, I). The quantification of the retinal nerve fibre layer (RNFL) via reflectivity profiles pointed out a lower density of nerve fibres in cynomolgus monkeys In comparison to human retina (Fig. 5C, F). In diseases where the thickness of the NFL is altered (e.g. glaucoma), the assessment of the RNFL via reflectivity profiles may be a valuable biomarker in the follow-up of the disease.

In conclusion, we present here a way to use OCT reflectivity profiles for a quantitative description of retinal layers and structures including specialized retinal regions. The current developments of molecular therapies, particularly in retinal degenerations, will undoubtedly lead to a large number of clinical trials in the near future. In these imminent studies, the in vivo quantification of therapeutic effects over time will almost certainly include OCT data. In this work, we show that our technique is well applicable in both patients and experimental models. Our approach may in this situation constitute a valuable biomarker for the follow-up of therapeutic interventions in individual eyes.

Supporting Information

Figure S1 OCT reflectivity profiles from a C57BL/6 wild-type mouse. Graphic representation of the layer reflectivity as a function of the scan depth extracted from representative OCT scans acquired from the dorsal, ventral, nasal and temporal parts of the retina and subsequent correspondence to the retinal layering.
(TIF)

Acknowledgments

The authors thank Gudrun Utz and Pia Lacroix for their technical assistance.

Author Contributions

Conceived and designed the experiments: MGG MWS. Performed the experiments: MGG SB RM. Analyzed the data: MGG MWS. Contributed reagents/materials/analysis tools: MGG SB US SJ. Wrote the paper: MGG MWS.

References

1. Masland RH (2012) The neuronal organization of the retina Neuron. 76(2): p. 266 80.
2. Schiviz AN, Ruf T, Kuebber-Heiss A, Schubert C, Ahnelt PK (2008) Retinal cone topography of artiodactyl mammals: influence of body height and habitat J Comp Neurol. 507(3): p. 1336 50.
3. Peichl L (2005) Diversity of mammalian photoreceptor properties: adaptations to habitat and lifestyle? Anat Rec A Discov Mol Cell Evol Biol. 287(1): p. 1001 12.
4. Fujimoto JG, Brezinski ME, Tearney GJ, Boppart SA, Bouma B, et al. (1995) Optical biopsy and imaging using optical coherence tomography Nat Med. 1(9): p. 970 2.
5. Drexler W, Sattmann H, Hermann B, Ko TH, Stur M, et al. (2003) Enhanced visualization of macular pathology with the use of ultrahigh-resolution optical coherence tomography Arch Ophthalmol. 121(5): p. 695 706.
6. Fujimoto JG (2003) Optical coherence tomography for ultrahigh resolution in vivo imaging Nat Biotechnol. 21(11): p. 1361 7.
7. Fischer MD, Huber G, Beck SC, Tanimoto N, Muehlfriedel R, et al. (2009) Noninvasive, in vivo assessment of mouse retinal structure using optical coherence tomography PLoS One. 4(10): p. e7507.
8. Huber G, Beck SC, Grimm C, Sahaboglu-Tekgoz A, Paquet-Durand F, et al. (2009) Spectral domain optical coherence tomography in mouse models of retinal degeneration Invest Ophthalmol Vis Sci. 50(12): p. 5888 95.
9. Ruggeri M, Wehbe H, Jiao S, Gregori G, Jockovich ME, et al. (2007) In vivo three-dimensional high-resolution imaging of rodent retina with spectral-domain optical coherence tomography Invest Ophthalmol Vis Sci. 48(4): p. 1808 14.
10. van Velthoven ME, Faber DJ, Verbraak FD, van Leeuwen TG,de Smet MD (2007) Recent developments in optical coherence tomography for imaging the retina Prog Retin Eye Res. 26(1): p. 57 77.

11. Jacobson SG, Cideciyan AV, Aleman TS, Pianta MJ, Sumaroka A, et al. (2003) Crumbs homolog 1 (CRB1) mutations result in a thick human retina with abnormal lamination Hum Mol Genet. 12(9): p. 1073–8.
12. Barthelmes D, Sutter FK, Kurz-Levin MM, Bosch MM, Helbig H, et al. (2006) Quantitative analysis of OCT characteristics in patients with achromatopsia and blue-cone monochromatism Invest Ophthalmol Vis Sci. 47(3): p. 1161–6.
13. Barthelmes D, Gillies MC, Sutter FK (2008) Quantitative OCT analysis of idiopathic perifoveal telangiectasia Invest Ophthalmol Vis Sci. 49(5): p. 2156–62.
14. Mataftsi A, Schorderet DF, Chachoua L, Boussalah M, Nouri MT, et al. (2007) Novel TULP1 mutation causing leber congenital amaurosis or early onset retinal degeneration Invest Ophthalmol Vis Sci. 48(11): p. 5160–7.
15. Jacobson SG, Aleman TS, Cideciyan AV, Sumaroka A, Schwartz SB, et al. (2009) Leber congenital amaurosis caused by Lebercilin (LCA5) mutation: retained photoreceptors adjacent to retinal disorganization Mol Vis. 15: p. 1098–106.
16. Huber G, Heynen S, Imsand C, vom Hagen F, Muehlfriedel R, et al. (2010) Novel rodent models for macular research PLoS One. 5(10): p. e13403.
17. Schraermeyer U, Julien S (2012) Formation of immune complexes and thrombotic microangiopathy after intravitreal injection of bevacizumab in the primate eye Graefes Arch Clin Exp Ophthalmol. 250(9): p. 1303–13.
18. Seeliger MW, Beck SC, Pereyra-Munoz N, Dangel S, Tsai JY, et al. (2005) In vivo confocal imaging of the retina in animal models using scanning laser ophthalmoscopy Vision Res. 45(28): p. 3512–9.
19. Ogden TE (1983) Nerve fiber layer of the primate retina: thickness and glial content Vision Res. 23(6): p. 581–7.
20. Samardzija M, Wenzel A, Aufenberg S, Thiersch M, Reme C, et al. (2006) Differential role of Jak-STAT signaling in retinal degenerations FASEB J. 20(13): p. 2411–3.
21. Boudard DL, Tanimoto N, Huber G, Beck SC, Seeliger MW, et al. (2010) Cone loss is delayed relative to rod loss during induced retinal degeneration in the diurnal cone-rich rodent Arvicanthis ansorgei Neuroscience. 169(4): p. 1815–30.
22. Spaide RF, Curcio CA (2011) Anatomical correlates to the bands seen in the outer retina by optical coherence tomography: literature review and model Retina. 31(8): p. 1609–19.
23. Dubis AM, Costakos DM, Subramaniam CD, Godara P, Wirostko WJ, et al. (2012) Evaluation of normal human foveal development using optical coherence tomography and histologic examination Arch Ophthalmol. 130(10): p. 1291–300.
24. Ballantyne AJ (1940) The Reflexes of the Fundus Oculi: (Section of Ophthalmology) Proc R Soc Med. 34(1): p. 19–42.
25. Grewal DS, Tanna AP (2013) Diagnosis of glaucoma and detection of glaucoma progression using spectral domain optical coherence tomography Curr Opin Ophthalmol. 24(2): p. 150–61.
26. Biel M, Michalakis S (2007) Function and dysfunction of CNG channels: insights from channelopathies and mouse models Mol Neurobiol. 35(3): p. 266–77.
27. Hüttl S, Michalakis S, Seeliger M, Luo DG, Acar N, et al. (2005) Impaired channel targeting and retinal degeneration in mice lacking the cyclic nucleotide-gated channel subunit CNGB1 J Neurosci. 25(1): p. 130–8.
28. Koch S, Sothilingam V, Garcia Garrido M, Tanimoto N, Becirovic E, et al. (2012) Gene therapy restores vision and delays degeneration in the CNGB1(−/−) mouse model of retinitis pigmentosa Hum Mol Genet. 21(20): p. 4486–96.
29. Jacobson SG, Cideciyan AV, Ratnakaram R, Heon E, Schwartz SB, et al. (2012) Gene therapy for leber congenital amaurosis caused by RPE65 mutations: safety and efficacy in 15 children and adults followed up to 3 years Arch Ophthalmol. 130(1): p. 9–24.
30. Narfström K, Menotti Raymond M, Seeliger M (2011) Characterization of feline hereditary retinal dystrophies using clinical, functional, structural and molecular genetic studies Vet Ophthalmol. 14 Suppl 1: p. 30–6.

Scale adjustments to facilitate two-dimensional measurements in OCT images

Marina Garcia Garrido[1]*, Regine L. Mühlfriedel[1], Susanne C. Beck[1], Christine Wallrapp[2], Mathias W. Seeliger[1].

[1] Division of Ocular Neurodegeneration, Institute for Ophthalmic Research, Centre for Ophthalmology, Tuebingen, Germany.

[2]BTG International Germany GmbH, Alzenau, Germany

*Corresponding author: Marina Garcia Garrido, E-mail: marina.garcia-garrido@med.uni-tuebingen.de, Tel: +49 (0)7071-2987767, Fax: +49 (0)7071-294789

Grant information: This work was supported by the German Ministry of Education and Research (BMBF, HOPE2 01GM1108A) and by the Deutsche Forschungsgemeinschaft and Open Access Publishing Fund of University of Tuebingen. Dr. Susanne C Beck received a grant from Heidelberg Engineering GmbH. The funders provided support in the form of salaries for authors [SCB], but did not have any additional role in the study design, data collection and analysis, decision to publish, or preparation

of the manuscript. This specific roles of these authors are articulated in the 'author contribution' section.

Financial interest: Dr. C. Wallrapp is a paid employee of BTG International Germany GmbH, CellBeads® are a product of BTG International Germany GmbH. This does not alter the author's adherence to all the PLOS ONE policies and sharing data and materials.

ABSTRACT

Purpose: To address the problem of unequal scales for the measurement of two-dimensional structures in OCT images, and demonstrate the use of intraocular objects of known dimensions in the murine eye for the equal calibration of axes.

Methods: The first part of this work describes the mathematical foundation of major distortion effects introduced by X-Y scaling differences. Illustrations were generated with CorelGraph X3 software. The second part bases on image data obtained with a HRA2 Spectralis (Heidelberg Engineering) in *SV129* wild-type mice. Subretinally and intravitreally implanted microbeads, alginate capsules with a diameter of 154±5 µm containing GFP-marked mesenchymal stem cells (CellBeads®), were used as intraocular objects for calibration.

Results: The problems encountered with two-dimensional measurements in cases of unequal scales are demonstrated and an estimation of the resulting errors is provided. Commonly, the Y axis is reliably calibrated using outside standards like histology or manufacturer data. We show here that intraocular objects like dimensionally stable spherical alginate capsules allow for a two-dimensional calibration of the acquired OCT raw images by establishing a relation between X and Y axis data. For our setup, a correction factor of about 3.3 was determined using both epiretinally and subretinally positioned beads (3.350 ± 0.104 and 3.324 ± 0.083, respectively).

Conclusions: In this work, we highlight the distortion-related problems in OCT image analysis induced by unequal X and Y scales. As an exemplary case, we provide data for a two-dimensional *in vivo* OCT image calibration in mice using intraocular alginate capsules. Our results demonstrate the need for a proper two-dimensional calibration of OCT data, and we believe that equal scaling will certainly improve the efficiency of OCT image analysis.

INTRODUCTION

Optical coherence tomography (OCT) has rapidly become an important part of diagnostic imaging in clinical ophthalmology. The continuous advances in spatial resolution have recently also enabled experimental applications in a number of disease models (1, 2). However, little progress has been made in the development of methods for exact calibration of OCT image data. Indeed, interpretation of the data have been complicated within the last years in part due to the variety of OCT manufacturers, as they all provide their own software (3, 4). Additionally, differences in their segmentation algorithms on which retinal thickness measurements based on (5, 6), axial resolution in tissue (7), scan density variations (8) and anatomic variations between individual patients as well as inter-species (9, 10) are the most reported obstacles to deal with in the development of methods for exact calibration of OCT image data. In order to study the influence of some of these effects in OCT images, several studies from our lab and other groups worldwide verified retinal layer thickness in OCT scans, measured along the Y axis of images, on the basis of matching histological sections, and established respective correlation coefficients (2, 11, 12). In OCT data, the Y axis essentially reflects properties of the scan, while the X axis is a product of internal post processing based on a number of inferences. In contrast to those for a histological section, the scales for X and Y in OCT scans are thus not intrinsically identical and need to be calibrated to ensure a system with equal scaling in X and Y (and possibly Z for 'volume scan' 3D stacks). Another approach in the attempt to eliminate intra- and intersubject variabilities is the use of a model eye. Agrawal and other groups worked towards the development of an *in vitro* retina phantom for the evaluation of OCT devices (13,14).

In this work, we were looking for a way to obtain equal scales for X and Y *in vivo* that permit two-dimensional measurements in OCT images that are otherwise distorted.

As a spherical body has equal dimensions along the X, Y and Z axis, it appears to be a suitable gauge for scaling. Thus, we based our approach on dimensionally stable alginate capsules (Cellbeads®) as *in vivo* calibration tool. These beads contain human mesenchymal stem cells transformed to produce green fluorescent protein (GFP) and were placed in the subretinal and intravitreal space of murine eyes as part of the control experiments in a neuroprotection study. The extensive OCT dataset enabled us to estimate the necessary parameters to establish equal X and Y scales, and to provide a mathematical description for the correct measurement of targets contained within an OCT scan in an arbitrary direction. The establishment of equal scales for OCT appears to be essential as it influences both qualitative and quantitative image analysis that often guides diagnosis and treatment in eye diseases (15).

MATERIALS AND METHODS

General remarks

This work is based on data obtained as part of a neuroprotection study. No animal experiments were performed specifically for this project.

Ethics statement

All procedures were performed according to the German laws governing the use of experimental animals and were previously approved by the local authorities (Regierungspraesidium Tuebingen). In addition, the guidelines set by the Association for Research in Vision and Ophthalmology for the Use of Animals in Ophthalmic and Vision Research were followed during experimentation on animal subjects.

Animals

The dataset used in this present study included *SV129* wild type mice (n=12) which were kept under a 12 h: 12 h light-dark cycle (60 lux) and had free access to food and water. They were subcutaneously anesthetized with ketamine (66,7 mg/kg, WDT, Garbsen, Germany) and xylazine (11,7 mg/kg, Bayer, Leverkusen, Germany) and their pupils were dilated with tropicamide eyedrops (Mydriaticum Stulln; Pharma Stulln, Stulln, Germany) prior to microbeads injection and image acquisition.

MicroBeads injections

MicroBeads (CellBeads®, CellMed AG, Alzenau, Germany) are alginate micro-spheres containing human mesenchymal stem cells that may be genetically modified to release therapeutic or marker proteins (16-19). For this study, mice with MicroBeads that produce eGFP as reporting protein were used (20). The miniaturized CellBeads® for use in mice have a diameter of 154 ± 5 µm, each bead containing about 50-70 GFP-secreting cells. Injections were performed as previously reported (21).

Spectral domain optical coherence tomography (SD-OCT)

Retinal structures of the anesthetized animals were visualized via OCT imaging with a Spectralis™ HRA+OCT (Heidelberg Engineering GmbH, Heidelberg, Germany). This device features a superluminescent diode at 870 nm as low coherence light source. Scans are acquired at a speed of 40,000 scans per second and each two-dimensional B-scan contains up to 1536 A-scans (2, 11). The images were taken with the equipment set of 30° field of view and with the software Heidelberg Eye Explorer (HEYEX version 5.3.3.0, Heidelberg, Germany). Resulting images were exported as a 8 bit colour bitmap files and processed with CorelDraw X3 (Corel corporation, Ottawa, ON Canada).

137

138 **Scanning-laser Ophthalmoscopy (SLO)**

139 Eyes were kept moisturized with Methocell (Omnivision, Puchheim, Germany) ac-
140 cording to previously described procedures (22). Briefly, the HRA system features
141 lasers in the short (visible) wavelength range (488 nm and 514 nm), and also in the
142 long (infrared) wavelength range (785/815 nm). The 488 and 795 nm lasers are used
143 for fluorescein (FLA) and indocyanine green (ICG) angiography, respectively. GFP
144 excitation was detected in the autofluorescence mode at 488 nm with a 500 nm bar-
145 rier filter.

146

147 **Statistical analysis**

148 Mean and standard deviation (± SD) values were calculated for the extensions of the
149 microbeads values. The Student's *t*-test was used to analyze statistical significance
150 between epiretinal and subretinal estimated correction factors.

151

152 **RESULTS**

153 In a first part, we introduce some theoretical considerations regarding the distortion of
154 retinal structures if, as it appears to be common in OCT setups, the scales for X and
155 Y axes in OCT scans are not identical. In a second part, we show how the scales
156 may be calibrated based on *in vivo* data to avoid such unwanted distortions.

157

158 **Part I: Theoretical considerations on the subject of image distortion**

159 By design, OCT data consist of many individual scans along the Y axis, while the X
160 axis is a product of internal post processing. Its scaling involves a number of infer-
161 ences and normative data that may not fit well to the actual application, both in clini-
162 cal and experimental work. If X and Y axis are not to the same scale, the resulting

images will show distortion. We demonstrate this effect here with the help of two examples of defined geometrical shapes. First, we address the behaviour of a circular shape **(Fig. 1)**. We assume that the actual object is a circle with the same diameter along X and Y axes (a/b=1). It is obvious that the circle becomes elliptical when the scale of the X axis changes, here shown up to a radio of a/b=5 **(Fig. 1A)**. Respective retinal structures like e.g. vessels would feature a highly elliptical cross section depending on the magnitude of this effect. When attempting to measure the diameter of the structure, this is only straightforward at 0° or 90°, i.e. entirely along the X or Y axis. While in case of the (original) circle the diameter is independent of the angle of the section, this is not so in case of an ellipse **(Fig. 1B)**. Depending on the angle of the section (α) and the ratio between X and Y scales (a/b), the measured result has to be divided by the relative diameter (d_r) to reflect the correct distance. For a derivation of the formula see Appendix 1. A family of curves for different a/b ratios illustrates this behaviour **(Fig. 1B)**.

This effect has to be particularly considered in oblique recordings which are not uncommon in clinical practice. A simple means to avoid any such X-Y distortion and related calculations is to equally calibrate X and Y axes, which we will introduce in a second part below.

The second example is a rectangular shape at an angle of 45°, which could e.g. reflect a vessel running in the X-Y plane **(Fig. 2)**. Again, the scale of the X axis was changed up to ratio a/b=5 **(Fig. 2A)**. It is clear that a change in the scale of X will increase or reduce the angle of the structure; the actual formula for that angle being α=arctan(b/a) **(Fig. 2B)**. This effect will lead to an underestimation of the angle when the X scale is larger than the Y scale, and will be a particular problem for any analysis by visual inspection **(Fig. 5)**.

Part II: Use of well-defined intraocular objects for two-dimensional calibration

As a conclusion from the above results, an equal scaling of X and Y axes appears desirable. Therefore, we assessed the use of well-defined intraocular objects to achieve a two-dimensional calibration of the acquired OCT raw images via an explicit relation between X and Y axis data. We show here that dimensionally stable spherical alginate capsules (CellBeads®, **Fig. 3**) are suitable in this regard due to their robust nature and their known size of 154 ± 5 µm with low production tolerances.

The imaging data were obtained as part of a neuroprotection study that included a comparison between subretinal and epiretinal placement of the beads **(Fig. 3, 4)**. Typically, unprocessed raw data **(Fig. 3C, D)** show a highly elliptical appearance of both subretinal **(Fig. 3C)** and epiretinal beads **(Fig. 3D)**. The original images (.bmp format) acquired with the Heidelberg Eye Explorer software on the Spectralis system were then scaled manually to obtain a spherical shape of the beads **(Fig. 3 G, H)** with the help of a circular template. We found that, despite a dissimilar appearance of the beads in OCT due to the differences in the environment, there was no perceivable difference in their physical extensions. A correction factor of 3.350 ± 0.104 was found for subretinal beads and of 3.324 ± 0.083 for epiretinally located beads **(Fig. 3E, F)**, which were not significantly different (p= 0,57). Once the scaling factor has been reliably determined for a certain population, it may be applied to all similar recordings with the respective setup and species. In case a sample to be tested differs greatly from the one in which the correction factor was determined, it would be good to reassure that the factor is valid also for this population. In the specific equipment used here, X and Z scales were found to be largely identical, as can be estimated from X-Z plane sections generated from a 3D 'volume scan' dataset. We therefore suggest to scale the Y axis of an OCT scan with the correction factor so that X, Y, and Z have identical scales. An example of images with applied correction (i.e. using the prede-

termined factor not derived from that specific image) is shown in **Fig. 4**. The known size of the objects further allows to check the absolute calibration and possibly adapt the scales accordingly.

DISCUSSION

The introduction of the OCT in the clinical practice has without question been one of the major breakthroughs of the recent years. A particular asset of imaging data in general is that a visual inspection is usually sufficient to get an immediate overview of the contained information without the need for an often intransparent numerical analysis. There is a close correlation between OCT data and respective histological sections (2, 10, 23-26) although both are generated quite differently. OCTs are computer-generated images made of a lateral combination of a series of axial reflectivity profiles (A-scans). While the Y axis basically reflects the original A-scans, the X axis is a product of a fitting process based on a number of inferences, so that the scales for X and Y are not intrinsically identical. As scaling properties may be altered by factors like additional lenses in the optical pathway (on the equipment side or on the side of the subject) (27), shape and size of the eye (28), or species differences (in experimental studies) (10, 26), a check of these properties may be required to ensure a system with equal scaling in X and Y (and possibly Z for 'volume scan' 3D stacks). It may be for this reason that two-dimensional measurements in OCT images, in contrast to e.g. ultrasound image data, are not widely used so far in clinical practice. The evaluation of OCT data is in the vast majority of clinical applications done by visual inspection, and to a lesser degree also supported by quantitative analysis. Presumably since unequal scales are not part of the natural environment, our visual system is not well suited to incorporate this in the assessment process. We show here that a number of effects may lead to unwanted distortions if the scales for X and Y are not equal, which may influence any conclusions drawn from such images.

The effect of distorted proportions in a two-dimensional graph is demonstrated here on the basis of two examples **(Fig. 1, 2)**. We show that a circular shape turns into an ellipse if X-Y scaling is not equal **(Fig. 1)**. A two-dimensional measurement of such a

distorted structure would require a correction dependent on the angle of the cross-section as detailed in **Appendix 1**. Further, any rectangular structure will appear at an altered angle in the X-Y plane depending on the amount of scale differences **(Fig. 2)**, according to the formula given that determines the size of this effect and may be used for a correction.

As a conclusion, we propose to establish an equal scaling of the axes to circumvent the need for any correction of distortion, which would both apply to visual inspection as well as to numerical two-dimensional measurements.

To achieve a two-dimensional calibration of the acquired OCT raw images, a relation between X and Y axis data needs to be established, which in our hands is most reliable when using well-defined intraocular objects *in vivo*. Potentially, this can be anything temporary or persistent from surgical equipment tips, syringes, or fluid droplets to implanted devices like slow release containers or retinal prostheses. In this study, we use spherical MicroBeads containing GFP-expressing mesenchymal stem cells placed either sub- or epiretinally in the retina of *Sv129* wild-type mice. We feel that an *in vivo* verification of scaling is the best option to ensure a proper calibration, as the complexity of the different tissues and pathways are hard to fully integrate in theoretical models or fabricated OCT phantoms (14, 15).

For our setup, a correction factor of about 3.35 was determined from that data **(Fig. 3)**. This factor describes the X-Y scaling differences within the same OCT scan and should not be confused with the "conversion constants" between OCT data and histology that have been established in several studies on animal models (2, 11, 12) These studies purely compare the A-Scan data (Y axis) with ex vivo tissue morphometry, whereas the present study is to our best knowledge the first to introduce a method of how a reliable X-Y relationship may be established based on real world data. However, there are limitations in the present study. Although we believe that

these findings may be applicable to other OCT devices, the data presented here were acquired with a single OCT system and a device variance was reported already (3, 4). Additional studies should be needed to confirm this hypothesis.

In summary, we have highlighted the problems in OCT image analysis induced by distortion due to unequal X and Y scales, and we provide an exemplary case for an OCT image calibration based on *in vivo* data using intraocular objects. Our results demonstrate the need for a proper two-dimensional calibration of OCT data, and we expect that the consideration of equal scaling will advance the use of two-dimensional measurements and thereby help to increase the efficiency of OCT image analysis.

ACKNOWLEDGEMENTS

The authors thank Gudrun Utz and Pia Lacroix for their technical assistance.

REFERENCES

1. Fujimoto JG. Optical coherence tomography for ultrahigh resolution in vivo imaging. Nat Biotechnol 2003; 21:1361-7.
2. Fischer MD, Huber, G, Beck, SC, Tanimoto, N, et al. Noninvasive, in vivo assessment of mouse retinal structure using optical coherence tomography. PLoS One 2009; 4:e7507.
3. Wolf-Schnurrbusch UE, Ceklic, L, Brinkmann, CK, Iliev, ME, et al. Macular thickness measurements in healthy eyes using six different optical coherence tomography instruments. Invest Ophthalmol Vis Sci 2009; 50:3432-7.
4. Sull AC, Vuong, LN, Price, LL, Srinivasan, VJ, et al. Comparison of spectral/Fourier domain optical coherence tomography instruments for assessment of normal macular thickness. Retina 2010; 30:235-45.
5. Odell D, Dubis, AM, Lever, JF, Stepien, KE, et al. Assessing Errors Inherent in OCT-Derived Macular Thickness Maps. J Ophthalmol 2011; 2011:692574.
6. Krebs I, Hagen, S, Brannath, W, Haas, P, et al. Repeatability and reproducibility of retinal thickness measurements by optical coherence tomography in age-related macular degeneration. Ophthalmology 2010; 117:1577-84.
7. Folgar FA, Yuan, EL, Farsiu, S, and Toth, CA. Lateral and axial measurement differences between spectral-domain optical coherence tomography systems. J Biomed Opt 2014; 19:16014.
8. Sadda SR, Keane, PA, Ouyang, Y, Updike, JF, et al. Impact of scanning density on measurements from spectral domain optical coherence tomography. Invest Ophthalmol Vis Sci 2010; 51:1071-8.
9. Cook A, White, S, Batterbury, M, and Clark, D. Ocular growth and refractive error development in premature infants with or without retinopathy of prematurity. Invest Ophthalmol Vis Sci 2008; 49:5199-207.
10. Huber G, Heynen, S, Imsand, C, vom Hagen, F, et al. Novel rodent models for macular research. PLoS One 2010; 5:e13403.
11. Huber G, Beck, SC, Grimm, C, Sahaboglu-Tekgoz, A, et al. Spectral domain optical coherence tomography in mouse models of retinal degeneration. Invest Ophthalmol Vis Sci 2009; 50:5888-95.
12. Ferguson LR, Grover, S, Dominguez Ii, JM, Balaiya, S, et al. Retinal thickness measurement obtained with spectral domain optical coherence tomography assisted optical biopsy accurately correlates with ex vivo histology. PLoS One 2014; 9:e111203.
13. Lozano DC and Twa, MD. Development of a rat schematic eye from in vivo biometry and the correction of lateral magnification in SD-OCT imaging. Invest Ophthalmol Vis Sci 2013; 54:6446-55.
14. Agrawal A, Connors, M, Beylin, A, Liang, CP, et al. Characterizing the point spread function of retinal OCT devices with a model eye-based phantom. Biomed Opt Express 2012; 3:1116-26.
15. Baxi J, Calhoun, W, Sepah, YJ, Hammer, DX, et al. Retina-simulating phantom for optical coherence tomography. J Biomed Opt 2014; 19:21106.
16. Weber C, Pohl, S, Poertner, R, Pino-Grace, P, et al. Production process for stem cell based therapeutic implants: expansion of the production cell line and cultivation of encapsulated cells. Adv Biochem Eng Biotechnol 2010; 123:143-62.
17. Heile AM, Wallrapp, C, Klinge, PM, Samii, A, et al. Cerebral transplantation of encapsulated mesenchymal stem cells improves cellular pathology after experimental traumatic brain injury. Neurosci Lett 2009; 463:176-81.
18. Zhang R, Ma, K, Xu, L, Wallrapp, C, et al. Intraocular cell-based production of glucagon-like peptide-1 in the anterior chamber. Acta Ophthalmol 2010; 88:e348-9.
19. Zhang R, Zhang, H, Xu, L, Ma, K, et al. Intravitreal cell-based production of glucagon-like peptide-1. Retina 2011; 31:785-9.

20. Simonsen JL, Rosada, C, Serakinci, N, Justesen, J, et al. Telomerase expression extends the proliferative life-span and maintains the osteogenic potential of human bone marrow stromal cells. Nat Biotechnol 2002; 20:592-6.
21. Fischer MD, Goldmann, T, Wallrapp, C, Muhlfriedel, R, et al. Successful subretinal delivery and monitoring of MicroBeads in mice. PLoS One 2013; 8:e55173.
22. Seeliger MW, Beck, SC, Pereyra-Munoz, N, Dangel, S, et al. In vivo confocal imaging of the retina in animal models using scanning laser ophthalmoscopy. Vision Res 2005; 45:3512-9.
23. Huang Y, Cideciyan, AV, Papastergiou, GI, Banin, E, et al. Relation of optical coherence tomography to microanatomy in normal and rd chickens. Invest Ophthalmol Vis Sci 1998; 39:2405-16.
24. Gloesmann M, Hermann, B, Schubert, C, Sattmann, H, et al. Histologic correlation of pig retina radial stratification with ultrahigh-resolution optical coherence tomography. Invest Ophthalmol Vis Sci 2003; 44:1696-703.
25. Anger EM, Unterhuber, A, Hermann, B, Sattmann, H, et al. Ultrahigh resolution optical coherence tomography of the monkey fovea. Identification of retinal sublayers by correlation with semithin histology sections. Exp Eye Res 2004; 78:1117-25.
26. Garcia Garrido M, Beck, SC, Muhlfriedel, R, Julien, S, et al. Towards a quantitative OCT image analysis. PLoS One 2014; 9:e100080.
27. Patel NB, Garcia, B, and Harwerth, RS. Influence of anterior segment power on the scan path and RNFL thickness using SD-OCT. Invest Ophthalmol Vis Sci 2012; 53:5788-98.
28. Maldonado RS, Izatt, JA, Sarin, N, Wallace, DK, et al. Optimizing hand-held spectral domain optical coherence tomography imaging for neonates, infants, and children. Invest Ophthalmol Vis Sci 2010; 51:2678-85.

Appendix 1: Determination of the diameter of an ellipse

Given: Ellipse with a major axis *a* and a minor axis *b*

Sought: Diameter *d* as a function of the angle α

Approach: If $P(x_1,y_1)$ is the point of intersection between the ellipse and a line through the origin (y=m*x), it follows

$$x_1 = \frac{ab\sqrt{b^2+m^2a^2}}{b^2+m^2a^2}, \text{ and } \quad y_1 = m*x = \frac{mab\sqrt{b^2+m^2a^2}}{b^2+m^2a^2}$$

The radius r (distance between point of origin (0,0) and P) may be calculated as:

$$r = \sqrt{x_1^2+y_1^2} = \sqrt{\left(1+m^2\right)x_1^2} = \pm x_1\sqrt{\left(1+m^2\right)}$$

Insertion of x_1 renders:

$$r = \sqrt{\left(1+m^2\right)\frac{a^2b^2\left(b^2+m^2a^2\right)}{\left(b^2+m^2a^2\right)^2}} = \sqrt{\left(1+m^2\right)\frac{a^2b^2}{b^2+m^2a^2}}$$

The slope *m* in y=m*x is given as:

$$m = \tan(\alpha) = \frac{\sin(\alpha)}{\cos(\alpha)}$$

Insertion results in:

$$r = \sqrt{\left(1+\frac{\sin^2(\alpha)}{\cos^2(\alpha)}\right)\frac{a^2b^2}{b^2+\frac{\sin^2(\alpha)}{\cos^2(\alpha)}a^2}} = \sqrt{\left(\sin^2(\alpha)+\cos^2(\alpha)\right)\frac{a^2b^2}{a^2\sin^2(\alpha)+b^2\cos^2(\alpha)}}$$

$$= \sqrt{\frac{a^2b^2}{a^2\sin^2(\alpha)+b^2\cos^2(\alpha)}} = \frac{ab}{\sqrt{a^2\sin^2(\alpha)+b^2\cos^2(\alpha)}}$$

Substituting $a = n*b$, it follows:

$$r = \frac{nb^2}{\sqrt{n^2b^2\sin^2(\alpha)+b^2\cos^2(\alpha)}} = \frac{nb}{\sqrt{n^2\sin^2(\alpha)+\cos^2(\alpha)}} = \frac{b}{\sqrt{\sin^2(\alpha)+\frac{1}{n^2}\cos^2(\alpha)}}$$

$$\Leftrightarrow$$

$$r = \frac{b}{\sqrt{1+\left(\frac{1}{n^2}-1\right)\cos^2(\alpha)}} \text{ or alternatively, } r = \frac{a}{\sqrt{1+\left(n^2-1\right)\sin^2(\alpha)}}$$

The relative diameter d_r of the ellipse equals the radius *r* divided by the long axis *a*. It depends on the ratio n=a/b and is a function of the angle α if a/b ≠1.

FIGURE LEGENDS

Figure 1. Considerations regarding appearance and cross-section of a circular shape in case of unequal X and Y scales. (A) Illustration of the increasing elliptic appearance of a circle for X/Y ratios above 1. **(B)** Family of curves representing the relative diameter (d_r) of an ellipse as a function of the angle of the section (α) for different a/b ratios. A measurement of a cross-section in an unequal X-Y space may be corrected via a division by the respective d_r.

Figure 2. Considerations regarding appearance of a rectangular shape in case of unequal X and Y scales. (A) Illustration of the increasing distortion of a rectangle for X/Y ratios above 1 and the reduction of the off-axis angle. **(B)** Quantification of the reduction of the off-axis angle for different a/b ratios.

Figure 3. Use of intraocular MicroBeads to determine a correction factor to establish equal X-Y scaling. (A) Schematic drawing of a MicroBead. Encapsulated cells are genetically modified immortalized mesenchymal stem cells which in this case express GFP as a reporter. Scale bar: 100 µm **(B)**. OCT raw images of **(C)** subretinally and **(D)** epiretinally placed beads. Scale bar: 200 µm. **(E, F)** Correction factors to establish X-Y equality for subretinal **(E)** and epiretinal **(F)** beads. Corrected OCT images of **(G)** subretinally and **(H)** epiretinally placed beads. Scale bar: 200 µm. There was no significant difference between **E** and **F** (p=0,57).

Figure 4. Bead visualization after OCT image correction. Localization of GFP-expressing beads in autofluorescence mode **(A, D)** and position of horizontal and

421 vertical OCT scans. Using the predetermined correction factor, both subretinal **(B, C)**
422 and epiretinal beads **(E,F)** show the correct spherical shape. Scale bars: 200 µm.
423
424 **Figure 5. Adjustment of the off-axis angle of a blood vessel running in the X-Y**
425 **plane.** As detailed in Fig. 2, the off-axis angle of a retinal vessel is decreased when
426 the X/Y ratio is increased **(A)**. Establishment of equal X-Y calibration, based on the
427 established correction factor, increases the angle to its presumably correct value **(B)**.
428 Scale bars: 200 µm.

Figure
Click here to download Figure: Figure1f.tif

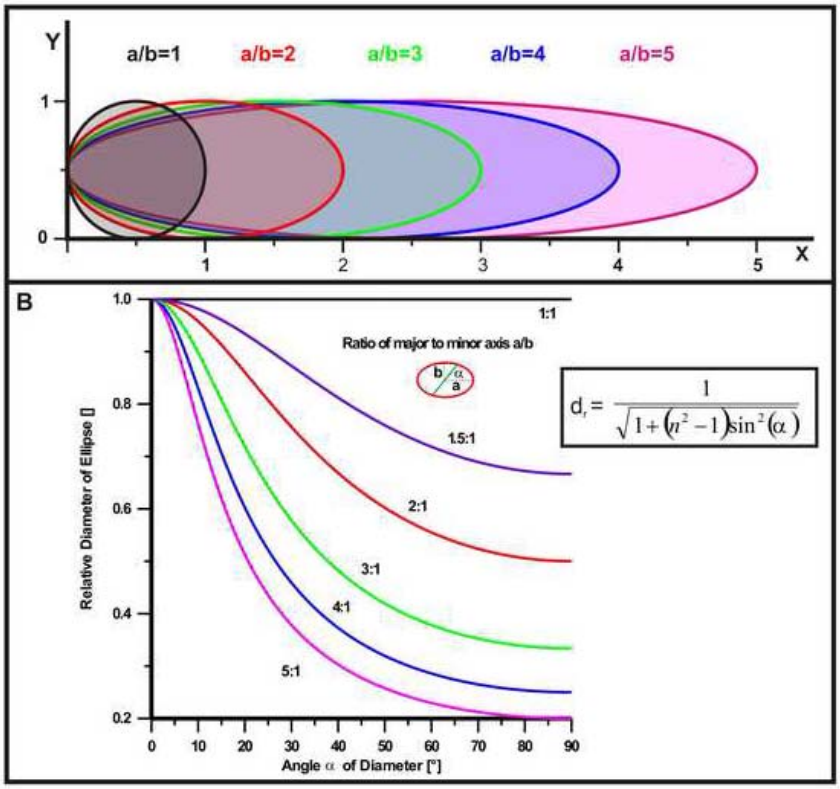

Figure
Click here to download Figure: Figure2f.tif

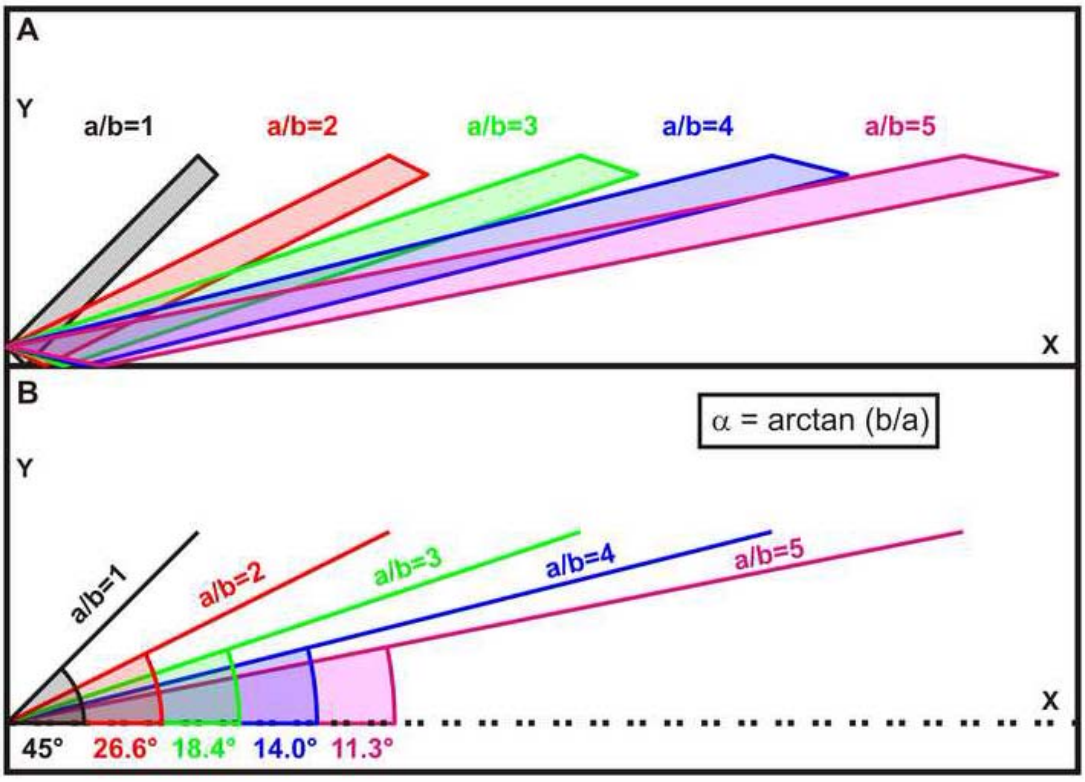

Figure
Click here to download Figure: Figure3f.tif

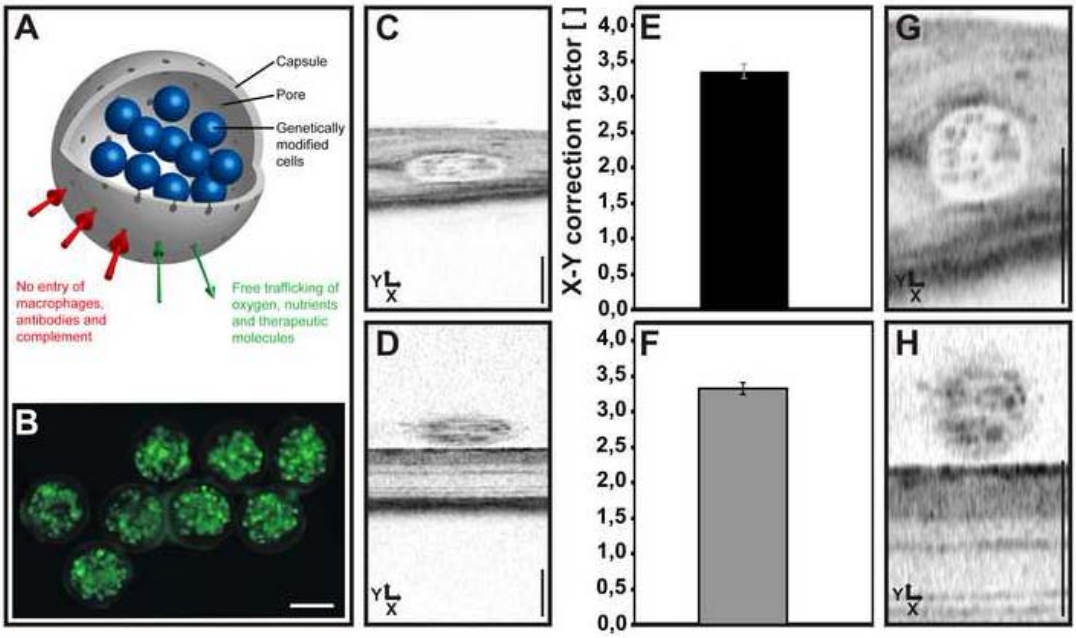

Figure
Click here to download Figure: Figure4f.tif

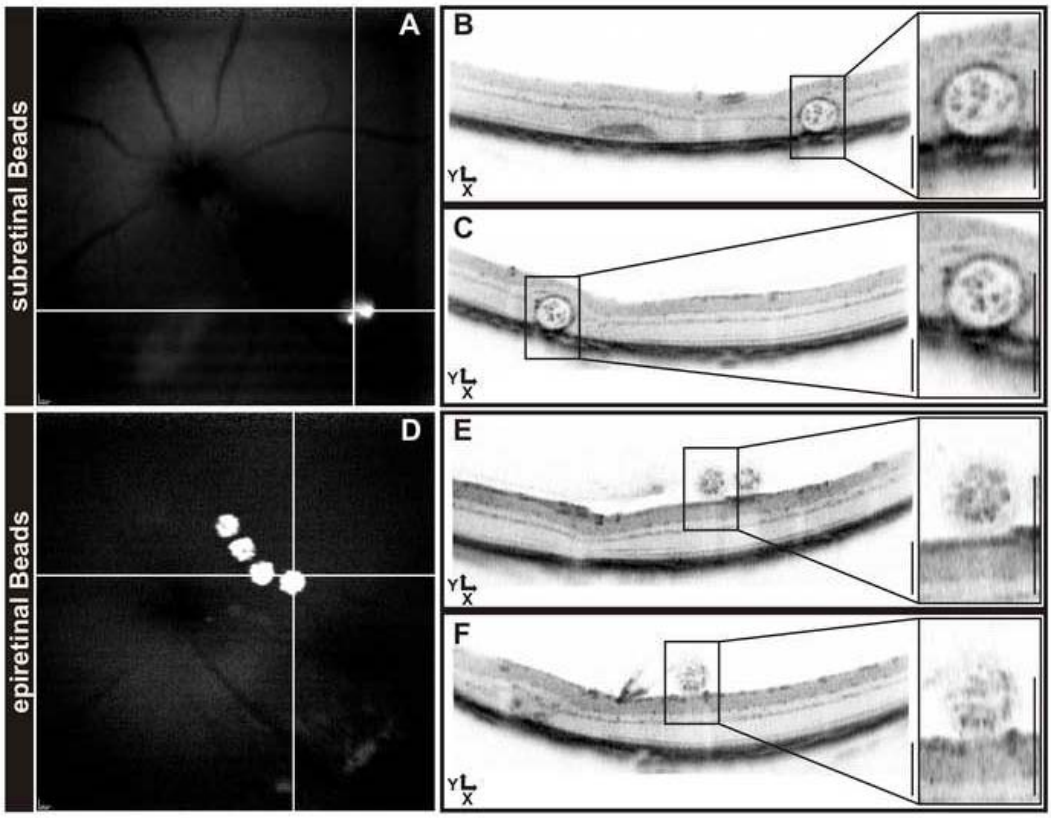

Figure
Click here to download Figure: Figure5f.tif